



UNIVERSITY OF
BIRMINGHAM

TOWARDS THE DESIGN OF
HIERARCHICAL BIOMATERIALS TO
REPLACE CARTILAGE:
DEVELOPMENT AND VALIDATION OF
A LOCALISED CARTILAGE MODEL

by

PIERS C H ALLEN

A thesis submitted to
the University of Birmingham
for the degree of
DOCTOR OF PHILOSOPHY

Department of Mechanical Engineering
College of Engineering and Physical Sciences
University of Birmingham
May 2023

UNIVERSITY OF
BIRMINGHAM

University of Birmingham Research Archive

e-theses repository

This unpublished thesis/dissertation is copyright of the author and/or third parties. The intellectual property rights of the author or third parties in respect of this work are as defined by The Copyright Designs and Patents Act 1988 or as modified by any successor legislation.

Any use made of information contained in this thesis/dissertation must be in accordance with that legislation and must be properly acknowledged. Further distribution or reproduction in any format is prohibited without the permission of the copyright holder.

ABSTRACT

Osteoarthritis (OA) is cited as a key factor for replacement and repair procedures in synovial joints. Osteoarthritis includes damage of the joint's articular cartilage (AC) and sclerosis of its subchondral bone. Better computational and physical models of articular cartilage and its subchondral bone has the potential to enable novel solutions to OA, such as better materials or constructs for replacement. A limitation of many current models is that they ignore the dynamic environment within which articular cartilage is found: specifically, material models often ignore that articular cartilage is not loaded to a state of equilibrium. Indeed, there is scope to exploit additive manufacture (AM) to better mimic the geometric profiles of articular cartilage on bone on a macro and micro scale. This thesis aims to develop the knowledge that is lacking around cartilage's material characterisation and utilise this to further the research into computational and physical AC models. This has been divided into three main components: material model, AM: macro, AM: micro.

Python and Matlab code was used to develop a program that aided in the mechanical modelling of hyper-viscoelastic materials, in our case AC, through the use of finite element analysis (FEA). Human femoral head dynamic mechanical analysis (DMA) data was used as the initial and validation set. The FEA outputs of storage and loss modulus were used as the inputs to a Prony series minimisation problem. Through the use of a cyclic generation and automatic analysis of simulated models, a genetic algorithm was used to minimize the Prony series solution and provide the optimal material parameters for AC. The fitness evaluation for each generation of the genetic algorithm was performed on the simulation results of each

set of models, to allow the models to be the driving source of the parameter value choice.

Macro and micro scale analysis was performed on bovine cartilage samples but using a combination of AM, DMA, and Micro-CT. For macro scale, AM and DMA were exploited to produce a dynamic test set-up used to establish the effect that joint contour has on cartilage material response. Contours that were evaluated were representative of the geometry seen on the tibial plateau. Differences in energy dissipation and viscoelastic properties were highlighted between contours representing the tibial components and the current testing procedures.

The third development was in two parts with the micro scale analysis of cartilage geometry changes pre and post dynamic loading. DMA was applied to osteochondral core samples from bovine humeral heads with micro-CT imaging performed before and after compression, providing micro-scale values of the porosity of the tissue. Statistical significance was not identified pre and post CT, however, distribution in trabecular geometry showed there was a marked change. These values were then used as insight into the AM of prototype replacements tissues utilising PLA as the chosen biomaterial. The AM prototypes were imaged with micro-CT loaded under DMA with all outputs evaluated against tissue values. The findings were then combined to produce a complete osteochondral core with geometric and material response metrics similar to that of the original tissue samples.

Ultimately, the work presented in this thesis has implications for the continued development of cartilage modelling and furthers the aim to create replacement structures and biomaterials which are designed for the dynamic environment within which articular cartilage is found.

ACKNOWLEDGEMENTS

I would firstly like to thank my wonderful supervisors, Dr Sophie Cox, Dr Daniel Espino, and Dr Simon Jones, for providing me with the opportunity to undertake the challenge of the work compiled in this thesis. The constant ongoing guidance, support and expertise resulted in the successful achievement of the work presented in this thesis.

I would like to thank the technical staff of the Mechanical Engineering department at the University of Birmingham, especially Mr Lee Gauntlet, for manufacturing the components required for the experimental work of this thesis.

In addition, thanks to the Biomedical Engineering Research Group of the Mechanical Engineering department at the University of Birmingham, for the available advice as and when required and the friendships made along the way.

Next, I would like to acknowledge the financial support I received from EPSRC as part of the Physical Sciences for Health Doctoral Training Programme (SCI-PHY). I also thank the staff SCIPHY for welcoming me onto the course and your belief in my abilities. A huge thank you to my fellow course mates Laim, Adam, James, Jamie, Katie, Oliver, Sonal, Vicky, and Laura for all their friendship and support throughout the process.

And lastly, I would like to express my everlasting gratitude to my family for their constant love and support throughout my educational journey. Mum, Dad, Patrick, and Barnie, thank you for the constant encouragement and believing in me all the way through. Without all the support I received I know I would not be where I am today.

NOVEL ACADEMIC CONTRIBUTIONS

International Peer-reviewed Journal Publications

Related to Thesis Content:

Sophie E. Mountcastle, Piers Allen, Ben O. L. Mellors, Bernard M. Lawless, Megan E. Cooke, Carolina E. Lavecchia, Natasha L. A. Fell, Daniel M. Espino, Simon W. Jones, and Sophie C. Cox 'Dynamic viscoelastic characterisation of human osteochondral tissue: Understanding the effect of the cartilage-bone interface', BMC Musculoskelet Disord, vol. 20, no. 1, p. 575, Nov. 2019, doi: 10.1186/s12891-019-2959-4.

Ben Mellors, Piers Allen , Carolina E. Lavecchia, Sophie Mountcastle, Megan E. Cooke, Bernard M. Lawless, Sophie C. Cox, Simon Jones, and Daniel M. Espino, 'Development, and experimental validation of a dynamic numerical model for human articular cartilage.' (Current in peer review)

Piers Allen, Sophie C. Cox, Simon Jones, Daniel M. Espino, 'Development of an automated numerical modelling system for the optimisation of hyper-viscoelastic material parameters utilising a genetic algorithm: A comparison of human articular cartilage experimental data to an optimised model.' (Currently in peer review)

Piers Allen, Sophie C. Cox, Simon Jones, Daniel M. Espino, 'An evaluation into how joint contour effects the material characterisation of articular cartilage under when loaded in a dynamic environment.' (In preparation for submission)

Other Publications

Piers Allen, Antonio Calcagni, Anthony G. Robson, Ela Claridge, 'Investigating the potential of Zernike polynomials to characterise spatial distribution of macular pigment', PLOS ONE, vol. 14, no. 5, doi: 10.1371/journal.pone.0217265

Nicola C. Foster, Piers Allen, Alicia J. El Haj, Liam M. Grover, and Richard J. A. Moakes, 'Tailoring Therapeutic Responses via Engineering: Microenvironments with a Novel Synthetic Fluid Gel', *Advanced Healthcare Materials*, vol. 10, no. 16, doi: 10.1002/adhm.202100622.

International Conferences Presentations:

Piers Allen, Sophie C. Cox, Simon Jones, Daniel M. Espino. 'Assessing the feasibility of an optimised modelling framework for articular cartilage'. European Society of Biomechanics General Assembly (GA) 2019 – Vienna, Austria.

Other:

All Code is proprietary and thus is available only on requested access currently on the GitHub repository: <https://github.com/piers-ch-allen/Automated-Modelling-System>.

TABLE OF CONTENTS

CHAPTER 1. INTRODUCTION	1
1.1. THESIS INTRODUCTION	1
1.2. RESEARCH AIMS AND OBJECTIVES	4
1.3. THESIS OVERVIEW	6
CHAPTER 2. BACKGROUND	8
2.1. CHAPTER OVERVIEW	8
2.2. SYNOVIAL JOINTS: TISSUE CONSTITUENTS AND MECHANICS	8
2.3. MECHANICAL TESTING AND MATERIAL CHARACTERISATION	16
2.3.1. MECHANICS OF MATERIALS	16
2.3.2. MATERIAL CHARACTERISATION	19
2.3.3. NUMERICAL MODELLING OF MATERIALS	22
2.4. COMPUTATIONAL MODELLING AND NUMERICAL METHODS	25
2.5. ADDITIVE MANUFACTURING AND ITS USE IN MEDICAL APPLICATIONS	30
2.6. OPEN QUESTIONS IN THE LITERATURE	36
2.7. CHAPTER SUMMARY	38
CHAPTER 3. AUTOMATED NUMERICAL MODELLING SYSTEM FOR THE OPTIMISATION OF HYPER-VISCOELASTIC MATERIAL PARAMETERS	39
3.1. INTRODUCTION	39
3.2. METHODS	43
3.2.1. EXPERIMENTAL TESTING	43
3.2.2. AUTOMATED MODELLING SYSTEM STRUCTURE	45

3.2.3.	ABAQUS MODELLING	49
3.2.4.	MATERIAL APPROXIMATIONS	51
3.2.4.1.	Viscoelastic Material Approximation	52
3.2.5.	PYTHON CONTROL STRUCTURE	54
3.2.6.	MATLAB OPTIMISATION CONTROL SEQUENCE	57
3.2.6.1.	Initial Optimisation (Interior Point)	57
3.2.6.2.	Main Optimisation Sequence Overview (Genetic Algorithm)	58
3.2.6.3.	Genetic operators	59
3.2.6.4.	Fitness Check (Equation Based)	61
3.2.6.5.	Fitness Check (Model Based)	61
3.3.	RESULTS	65
3.4.	DISCUSSION	69
3.5.	CONCLUSION	72

CHAPTER 4. DEVELOPMENT AND EVALUATION OF A JOINT CONTOUR TESTING SYSTEM FOR AC 74

4.1.	INTRODUCTION	74
4.2.	METHODS	78
4.2.1.	CARTILAGE SPECIMEN PREPARATION:	78
4.2.2.	DESIGN AND ADDITIVE MANUFACTURE OF EXPERIMENTAL APPARATUS	81
4.2.3.	DYNAMIC MECHANICAL ANALYSIS OF CARTILAGE ON CURVED SUBSTRATES	86
4.2.4.	STATISTICAL DATA ANALYSIS	89
4.2.5.	HYSTERESIS DATA ANALYSIS	90
4.3.	RESULTS	91
4.3.1.	DMA OF CONTOURED PLATEN TESTS	91
4.3.2.	HYSTERESIS ANALYSIS OF BIOLOGICAL DATA	95
4.4.	DISCUSSION	99

4.5. CONCLUSIONS	105
-------------------------	------------

CHAPTER 5. FEASIBILITY ASSESSMENT OF AN AM OSTEOCHONDRAL CORE REPLACEMENT UNIT – BOVINE TISSUE COMPARISON. **106**

5.1. INTRODUCTION	106
5.2. DMA AND MICRO-CT ANALYSIS OF THE OSTEOCHONDRAL UNIT	109
5.2.1. EXPERIMENTAL OVERVIEW	109
5.2.2. DISSECTION AND SPECIMEN PREPARATION	110
5.2.3. DYNAMIC MECHANICAL ANALYSIS (DMA) OF OSTEOCHONDRAL CORES	111
5.2.4. MICRO-CT SCANNING AND RECONSTRUCTION OF THE OSTEOCHONDRAL UNIT	112
5.2.5. DATA ANALYSIS - STATISTICAL TESTS	115
5.2.6. RESULTS	116
5.2.6.1. DMA Outputs of Osteochondral Cores:	116
5.2.6.2. Micro CT analysis of pre and post DMA	117
5.2.7. KEY FINDINGS	124
5.3. FEASIBILITY STUDY INTO THE AM OF OSTEOCHONDRAL CORES	125
5.3.1. INTRODUCTION	125
5.3.2. METHODS	127
5.3.3. AM PROTOTYPING OF TISSUE SUBSTITUTES.	130
5.3.3.1. Initial unit cell evaluation	131
5.3.3.2. Design and AM of first round prototype cylindrical cores	133
5.3.3.3. DMA of first round prototypes	134
5.3.3.4. First round print viability analysis	138
5.3.3.5. Design and AM of second round prototype cylindrical cores	140
5.3.3.6. DMA of second iteration of AM Prototypes	141
5.3.3.7. Micro-CT Results – Second set of prototypes	150

5.3.3.8. Prototype print viability discussion	155
5.3.4. TOWARDS THE DESIGN OF A BIO-INSPIRED, MULTI-LAYER AM CONSTRUCT	157
5.3.4.1. Tower Specifications	157
5.3.4.2. Tower testing results – Micro CT	159
5.3.4.3. DMA of prototype towers results	163
5.3.4.4. Key findings - Comparison to tissue data	164
5.4. DISCUSSION	165
5.5. CONCLUSION	170
<u>CHAPTER 6. THESIS DISCUSSION AND OVERALL CONCLUSIONS</u>	<u>172</u>
6.1. THESIS DISCUSSION	172
6.2. FUTURE WORK	178
6.3. THESIS CONCLUSIONS	179

List of Figures

FIGURE 1-1: FLOW CHART OF THE PHD THESIS, SHOWING THE DIFFERENT STEPS OF THE STUDY.	5
FIGURE 2-1: IMAGES OF THREE OF THE MAIN SYNOVIAL JOINTS: A) KNEE (TIBIOFEMORAL), B) HIP (ACETABULOFEMORAL) AND C) SHOULDER (GLENOHUMERAL). IMAGE COURTESY OF SADEGHI CC BY- NC-SA 4.0.	8
FIGURE 2-2: SCHEMATIC OF A SYNOVIAL JOINT SHOWING ALL MAJOR COMPONENTS. I (REPRODUCED FROM BC OPEN TEXTBOOK; BETTS, 2019, WHICH IS DISTRIBUTED UNDER THE TERMS OF CC BY-NC-SA 4.0.....	9
FIGURE 2-3: OSTEOCHONDRAL CORE SHOWN IN BOTH HEALTHY AND OSTEOARTHRITIC STATES WITH LABELLED LAYERS FOR THE CONSTITUENT PARTS OF THE TISSUE SEGMENT. IMAGE ORIGINAL PRODUCED BY SILVA ET AL. [41] CC BY-NC-SA 4.0.	9
FIGURE 2-4: MICRO-CT CROSS SECTIONS OF OSTEOCHONDRAL UNIT HIGHLIGHTING THE PORTIONS OF THE OSTEOCHONDRAL CORE. THE DARK REGION AT THE TOP IS THE CARTILAGE LAYER, THEN THE SUBCHONDRAL BONE PLATE (SBP) AND SUBCHONDRAL TRABECULAR BONE (STB). IMAGE SOURCES FROM FELL ET AL. [23] CC BY-NC-SA 4.0.....	10
FIGURE 2-5: BOVINE HUMERAL HEAD WITH CARTILAGE SURFACE ON THE RIGHT SIDE.....	11
FIGURE 2-6: CROSS SECTIONAL SCHEMATIC OF A CARTILAGE TISSUE SEGMENT WITH A) SHOWING THE CELLULAR ORGANISATION OF THE CHONDROCYTES AND B) SHOWING THE FIBRE ORIENTATION OF THE COLLAGEN STRANDS. HIGHLIGHTS THE SUPERFICIAL TANGENTIAL ZONE (STZ), MIDDLE AND DEEP ZONES OF CARTILAGE. ORIGINAL IMAGE FROM FOX ET AL, [3] CC BY-NC-SA 4.0.....	12
FIGURE 2-7: COLLAGEN FIBRE ORIENTATION ANALYSIS: HOW THE ANGLE VARIES WITH RESPECT TO DEPTH AND INITIAL HORIZONTAL 0° ANGLE. A) SECOND HARMONIC GENERATION '(SHG) AND ORIENTATIONJ OVERLAY WITH INSETS HIGHLIGHTING FIBER ORIENTATION ANALYSIS ACROSS ZONES B) CONTINUOUS FIT FROM FACE 1 AND FACE 2 ACROSS THE FULL DEPTH OF THE ARTICULAR CARTILAGE (SHADED REGIONS REPRESENT CONFIDENCE OF FIT) SHOWING DIFFERENCES IN COLLAGEN FIBER ORIENTATION WITH DEPTH BETWEEN FACES AND C) BINNED ZONES WITH 0–20% REPRESENTING SURFACE, 20–60% MIDDLE, 60– 90% DEEP ZONES (BOX PLOT WITH DATA OUTLIERS REMOVED FOR VISUALIZATION).’ IMAGE AND QUOTED PORTION OF CAPTION TEXT OBTAINED FROM FISCHENICH ET AL. [212] CC BY-NC-SA 4.0.....	13
FIGURE 2-8: PHOTOMICROGRAPH OF THE OSTEOCHONDRAL JUNCTION OF A HEALTHY TISSUE DONOR. ABBREVIATIONS WITHIN THE IMAGE ARE AS FOLLOVED: NCC — NON-CALCIFIED CARTILAGE; CC —	

<p>CALCIFIED CARTILAGE; SCB — SUBCHONDRAL BONE; V — VASCULAR CHANNEL. IMAGE COURTESY OF SURI ET AL. [213] CC BY-NC-SA 4.0.</p>	14
<p>FIGURE 2-9: SEM IMAGE OF TRABECULAR BONE SHOWING THE PILLAR STRUCTURES PRESENT. IMAGE COURTESY OF CHAPPARD ET AL. [214] CC BY-NC-SA 4.0.</p>	15
<p>FIGURE 2-10: AN EXAMPLE OF A NON-LINEAR STRESS-STRAIN RELATIONSHIP FROM AN EXPERIMENT PERFORMING IMPACT LOADING ON HUMAN AC. IMAGE COURTESY OF EDELSTEN ET AL. [63]</p>	17
<p>FIGURE 2-11: GENERALISED MAXWELL MODEL SCHEMATIC SHOWING THE SPRINGS (K) AND DASHPOTS (τ) IN SERIES.</p>	19
<p>FIGURE 2-12: ITERATIONS OF DIFFERENT MESHES FOR AN FEA PROBLEM DEFINED WITHIN COMSOL. IMAGE COURTESY OF COMSOL (COMSOL, STOCKHOLM, SWEDEN) CC BY-NC-SA 4.0.</p>	26
<p>FIGURE 2-13: HYPOTHETICAL VALUES ON A GRAPH OF A FUNCTION OF THE FORM $Y = Mx$ WITH M BEING A CONSTANT. DEMONSTRATING THE DIFFERENCE BETWEEN LOCAL AND GLOBAL OF FINDING A SOLUTION FOR M.</p>	28
<p>FIGURE 2-14: A) BASE LAYER PRINT APPLICATION OF AN EXTRUSION BASED AM PRINT ON A PRUSA I3 MK3S (PRUSA RESEARCH A.S., CZECH REPUBLIC). B) THE SAME PRINT AFTER LAYERS HAVE BEEN APPLIED DEMONSTRATING THE REPLICATED CAD MODEL.</p>	32
<p>FIGURE 2-15: CAD MODEL OF COMPONENTS DESIGNED FOR WORK COMPLETED WITHIN CHAPTER 4, SECTION 4.2.2.</p>	33
<p>FIGURE 2-2-16: 'CAD MODELS FOR UNIT CELLS FOR (A) DIAMOND (C) GYROID (E) IWP (G) PRIMITIVE; AND 3D PRINTED TPMS LATTICES FOR (B) DIAMOND (D) GYROID (F) IWP AND (H) PRIMITIVE.' CAPTION TEXT AND IMAGE COURTESY OF QURESHI ET AL [215].</p>	34
<p>FIGURE 3-1: PRODUCED BY MOUNTCASTLE ET AL 2019 / CC BY-NC-SA 4.0. "FLOW DIAGRAM ILLUSTRATING FEMORAL HEAD SPECIMEN PREPARATION AND CORING: A PREPARATION OF SPECIMEN USING A SURGICAL SAW, B EXAMPLE OF CARTILAGE-BONE BLOCK PRIOR TO M-CT ANALYSIS DEMONSTRATING WHERE CORE WAS TAKEN, C CORING OF SPECIMEN, AND D EXAMPLE OF CARTILAGE-BONE CORE PRIOR TO DMA" [37].</p>	43
<p>FIGURE 3-2: FLOW CHART REPRESENTATION OF THE CONTROL STRUCTURE FOR THE AUTOMATION SYSTEM, WITH BOXES REPRESENTING CODE/DATA AND DIAMONDS REPRESENTING QUESTIONS THE SYSTEMS WILL ASK THROUGH ITS ITERATIONS.</p>	46

FIGURE 3-3: FEA MODEL OF THE 2D CROSS-SECTIONAL GEOMETRY OF THE CYLINDRICAL SAMPLE UNDER THE FINAL LOAD APPLIED. THE LOAD IS APPLIED TO THE TOP SURFACE UP TO A MAXIMAL VALUE OF 1.7MPA. THE INDUCED VON MISES STRESS DEFINED IN THE LEGEND. 49

FIGURE 3-4: PYTHON CONTROL NODE CLASS DIAGRAM. THE BOTTOM SET OF BOXES REPRESENT THE DIFFERENT PORTIONS OF THE MODEL CREATION SYSTEM THAT ARE CURRENTLY IMPLEMENTED. THIS CAN BE INCREASED WITH ANY OTHER REQUIREMENTS. 57

FIGURE 3-5: OPTIMISATION SEQUENCE CONTROL STRUCTURE FLOW DIAGRAM REPRESENTATION. 59

FIGURE 3-6: A) AVERAGED EXPERIMENTAL RAMP TEST DATA FIT TO A LOGARITHMIC FUNCTION TO BE USED AS PART OF THE VALIDATION OF THE MODELS PRODUCED IN EACH GENERATION. B) EXAMPLE HYSTERESIS DATA SET PRODUCED FROM THE EXPERIMENTAL DATA AND FITTED TO A LOGARITHMIC AND EXPONENTIAL FUNCTION FOR THE UPPER AND LOWER LINES RESPECTIVELY 64

FIGURE 3-7: A) 50 ITERATION RAMP ERROR OUTPUT, B) 20 ITERATION RAMP ERROR OUTPUT, C) 50 ITERATION LOWER HYSTERESIS ERROR, D) 20 ITERATION LOWER HYSTERESIS ERROR, E) 50 ITERATION UPPER HYSTERESIS ERROR, F) 20 ITERATION UPPER HYSTERESIS ERROR. 68

FIGURE 4-1: ANATOMICAL IMAGE OF A TIBIAL JOINT EPIPHYSIS WITH MAIN GEOMETRIC REGIONS IDENTIFIED. THE TWO TIBIAL PLATEAU SECTIONS (MEDIAL AND LATERAL CONDYLES) AND THE TIBIAL SPINE (MEDIAL AND LATER TUBERCLE). IMAGE COURTESY OF WHITE ET AL [216]. 76

FIGURE 4-2: A) STENCIL FOR SAMPLE ON BOVINE HUMERAL HEAD, B) TISSUE SAMPLES TAKEN FROM SAID JOINT. 78

FIGURE 4-3: A: TIBIAL PLATEAU FROM NIE ET AL [20], CC BY-NC-SA 4.0 USED FOR CALCULATION OF THE STEEP ANGLE PLATEN DESIGN. ADDITIONAL LABELS OF G AND HAND TRIANGLES FOR MEASUREMENTS ARE INCLUDED FOR THE CALCULATIONS OF THE SLOPE ANGLES B: PRINT DESIGN OF 3D COMPONENTS SHOWING INFILL STRUCTURE AND SHELL THICKNESS. C: 3D COMPRESSION AND PLATEN PARTS FROM LEFT TO RIGHT: STEEP 30° ANGLE, SHALLOW 7° ANGLE, BASE FLAT 0° ANGLE. 80

FIGURE 4-4: A: MICRO-CT SLICE OF STEEP SLOPE COMPRESSION PLATE (RED LINE IS SLIPE DEPICTED IN B). B: SINGULAR HORIZONTAL SLICE WITH ROI (RED SQUARE) DEFINED FOR ANALYSIS OF INTERIOR POROSITY OF THE PRINTED SAMPLE. C: CROSS-SECTION OF RECONSTRUCTED MICRO-CT SCAN OF ONE OF THE 3D PRINTED COMPONENT PLATENS DEMONSTRATING INTERIOR DESIGN. 83

FIGURE 4-5: PRELIMINARY A) STORAGE AND B) LOSS MODULUS VALUES FOR CARTILAGE TISSUE MECHANICALLY LOADED UPON THE THREE DIFFERENT ANGULAR PLATENS. 85

FIGURE 4-6: : A: CURRENT TESTING PRACTICE FOR DMA ON CARTILAGE SAMPLES IN PREVIOUS PUBLISHED STUDIES. B: STEEP PLATEN IN-SITU ON THE BOSE TESTING MACHINE WITH A STRIP OF AC HELD IN PLACE WITH TENSION CLAMPS ACROSS THE CONTOURED SURFACE. C: AC SAMPLE UNDER DYNAMIC COMPRESSION IN THE SAME EXPERIMENTAL SET UP AS B..... 87

FIGURE 4-7: CARTILAGE HYSTERESIS LOOPS PRODUCED BY MOUNTCASTLE ET AL [18], CC BY-NC-SA 4.0.
A) EXAMPLE OF A HYSTERESIS LOOP FOR A SINGLE SPECIMEN TESTED AT 30 HZ. B) REPRESENTATION OF HOW THE ENERGY DISSIPATION CALCULATION IS PERFORMED WITHIN THE MATLAB SCRIPT WHEN UTILISING THE TRAPEZOID RULE. Y AXIS LABEL HAS BEEN ALTERED FROM ORIGINAL DUE TO INCORRECT LABEL BEING USED..... 90

FIGURE 4-7: STORAGE STIFFNESS RESULTS OF THE BOVINE HUMERAL TISSUE OF THE THREE DIFFERENT CONTOURS OF TESTING PLATEN PLOTTED AGAINST FREQUENCY RANGING FROM 1 TO 90 HZ. VALUES SHOWN ARE THE MEAN \pm 95% CONFIDENCE INTERVALS (N = 4, N = 15)..... 92

FIGURE 4-8: LOSS STIFFNESS RESULTS OF THE BOVINE HUMERAL TISSUE OF THE THREE DIFFERENT CONTOURS OF TESTING PLATEN PLOTTED AGAINST FREQUENCY RANGING FROM 1 TO 90 HZ. VALUES SHOWN ARE THE MEAN \pm 95% CONFIDENCE INTERVALS (N = 4, N = 1515)..... 94

FIGURE 4-9: EXAMPLE HYSTERESIS LOOPS FROM A RANDOM SAMPLE FOR THE THREE CONTOURS FROM TOP TO BOTTOM: 0°, 7° AND 30° PLATENS AND FROM LEFT TO RIGHT FOR WHEN THE CYCLIC LOADING IS APPLIED AT 1 HZ AND 90 HZ RESPECTIVELY. COLOURS OF THE GRAPHS REPRESENT INDIVIDUAL CYCLES OF THE LOAD. 96

FIGURE 4-10: SINUSOIDALLY VARYING DISPLACEMENT A) AT 1 HZ (EQUIVALENT RISE TIME 500) B) AT 90 HZ (EQUIVALENT RISE TIME 5.4 MS)..... 98

FIGURE 5-1: ARTICULAR CARTILAGE SAMPLES. A) BOVINE HUMERAL HEAD AS RETRIEVED BY SUPPLIERS, B) CAP OF BALL JOINT REMOVED USING HACKSAW, C) SECTIONING OF UNIT OF OSTEOCHONDRAL CORE CLAMPED AND BEING PREPARED FOR DRILLING VIA USE OF A VERTICALLY POSITIONED PILLAR DRILL WITH A BORER ATTACHMENT, D) POST CORING WITH CIRCULAR UNIT REMOVED FROM THE TISSUE..... 110

FIGURE 5-2: SAMPLE MICRO-CT RECONSTRUCTION. A) 3D RECONSTRUCTION OF A COMPLETE OSTEOCHONDRAL CORE. B) CROSS-SECTION OF A SLICE OF THE CORE DEMONSTRATING THE SWARF THAT IS PRESENT IN THE SAMPLE AFTER CORING. C) 3D VISUALISATION OF THE CHOSEN ROI WITHIN THE CORE SAMPLE. D) CROSS SECTION AFTER ROI HAS BEEN APPLIED TO ONLY ANALYSE TRUE TISSUE PARAMETERS. 113

FIGURE 5-3: IMAGE SLICE AS IT PROGRESSES THROUGH THE ANALYSIS AS FOLLOWS: A) GREYSCALE CT IMAGE, B) THRESHOLD APPLIED IMAGE SLICE, C) DESPECKLED IMAGE IN THE 3D DOMAIN SLICE, D) OPEN POROSITY IMAGE SLICE..... 114

FIGURE 5-4: VISUAL REPRESENTATION OF TRABECULAR THICKNESS AND SEPARATION WITH REGARDS TO THE IMAGE DATA SET THAT IS USED WITHIN THIS STUDY. 115

FIGURE 5-5: STORAGE (A) AND LOSS (B) MODULI FOR OSTEOCHONDRAL CORES PLOTTED AGAINST FREQUENCY FROM 1 TO 90 HZ (MEAN \pm 95% CONFIDENCE INTERVAL, (N = 5) WITH NATURAL LOGARITHMIC TRENDLINES). RESULTS ARE DISPLAYED ON A LINEAR SCALE. 116

FIGURE 5-6: 3D RECONSTRUCTION OF THE OSTEOCHONDRAL UNIT, PICTURED IS SAMPLE 1. IN BOTH PICTURES THE BLUE PORTIONS ARE THE TRABECULAE AND RED IS THE PORES THAN RUN THROUGH THE TISSUE..... 117

FIGURE 5-7: MICRO CT GREY SCALE, BINARISED AND OPEN POROSITY SLICE IMAGES OF SAMPLE 2 AND 3 PRE AND POST DMA TESTING. VALUES OF OPEN AND CLOSED POROSITY FOR EACH SAMPLE PRE AND POST DMA ALSO INCLUDED. 119

FIGURE 5-8 DISTRIBUTION OF A) TRABECULAR THICKNESS AND B) TRABECULAR SEPARATION ACROSS ALL SAMPLES ON RECONSTRUCTED 3D IMAGE STACK OF 175 SLICES. BOTH PRE AND POST DMA RESULTS INCLUDED WITH MEAN VALUES \pm STANDARD DEVIATION 123

FIGURE 5-9: EXAMPLE PRINT PROCESS OF THE PRUSA PRINTERS PRODUCING THE SECOND ITERATION OF PROTOTYPES DESCRIBED LATER IN SECTION 4.2.2. 126

FIGURE 5-10: SINGULAR SLICE OF A GYROIDAL UNIT CELL AT INFILL PERCENTAGES OF 50, 25 AND 10 FROM TOP TO BOTTOM AND IN PRUSA SLICER CAD (LEFT) AND RECONSTRUCTED IMAGE (RIGHT). 128

FIGURE 5-11: PRUSASLICER SLICED CAD MODELS OF THE FOUR CHOSEN UNIT CELLS FOR INITIAL ITERATION OF PRINTS. FROM LEFT TO RIGHT REPRESENTS THE UNIT CELL DESIGNS OF: GYROIDAL, TRIANGLE, HONEYCOMB, 3D HONEYCOMB. FROM TOP TO BOTTOM REPRESENTS THE INFIX PERCENTAGES OF 50%, 25% AND 10% FOR EACH OF THE UNIT CELLS ABOVE. 134

FIGURE 5-12: STORAGE MODULUS OUTPUTS FOR THE AM PRINTED CYLINDRICAL UNIT WITH THE FOUR GRAPHS REPRESENTING: A) GYROIDAL UNIT CELL, B) TRIANGULAR UNIT CELL, C) HONEYCOMB UNIT CELL, AND D) 3D HONEYCOMB UNIT CELL. EACH GRAPH CONTAINS THE THREE RESULTS FOR 50%, 25% AND 10% INFILL PERCENTAGE AS WELL..... 135

FIGURE 5-13: ALL STORAGE MODULUS VALUES FROM FIGURE 5-12 COMPARED AGAINST EACH OTHER. ALL SAMPLES ARE SHOWN TO FOLLOW A LOGARITHMIC TREND WITH REGARDS TO FREQUENCY OVER THE RANGE OF 1 TO 90 HZ. 136

FIGURE 5-14: MEAN STORAGE MODULUS FOR EACH PERCENTAGE INFILL COMPARING THE PRODUCED PROTOTYPE UNIT CELLS. 136

FIGURE 5-15: LOSS MODULUS OUTPUTS FOR THE AM PRINTED CYLINDRICAL UNITS FOR ALL OF THE DIFFERENT DESIGNS: GYROIDAL, TRIANGULAR, HONEYCOMB AND 3D HONEYCOMB. SAMPLE ARE LABELLED NUMERICALLY AS DEFINED IN TABLE 4..... 137

FIGURE 5-16: A) HONEY25 PRINT WITH INCOMPLETE HEXAGONS SHOWN AS PART OF THE INTERIOR SLICE. B) TRAIING10 PRINT WHERE THERE ARE NO COMPLETE TRIANGLES PRESENT 138

FIGURE 5-17: PRUSASLICER SLICED CAD MODELS OF THE SECOND ITERATION OF CHOSEN UNIT CELLS. FROM LEFT TO RIGHT REPRESENTS THE UNIT CELL DESIGNS OF: GYROIDAL, HONEYCOMB,3D HONEYCOMB AT 2.6 MM SHELL THICKNESS AND THEN THE SAME AGAIN AT 1.70 MM SHELL THICKNESS. FROM TOP TO BOTTOM REPRESENTS THE INFIX PERCENTAGES OF 50%, 25% AND 10% FOR EACH OF THE CONDITIONS ABOVE. 140

FIGURE 5-18: EXAMPLE SLICE OF IRREGULARITIES FOUND IN A) HONEY_50_2.6 B) GYROID_50_1.7. EXPECTED OUTCOME IN PRINT SPECIFICATION FOR A) HONEY_50_2.6 B) GYROID_50_1.7 141

FIGURE 5-19: TWO EXAMPLE SLICE OF IRREGULARITIES FOUND IN 3DHONEY_10_2.6 (A, B) AND EXPECTED OUTCOME IN PRINT SPECIFICATION FOR 3DHONEY_10_2.6 (C, D)..... 142

FIGURE 5-20: TWO EXAMPLE SLICE OF IRREGULARITIES FOUND IN 3DHONEY_10_1.7 (A, B) AND EXPECTED OUTCOME IN PRINT SPECIFICATION FOR 3DHONEY_10_1.7 (C, D)..... 143

FIGURE 5-21: STORAGE MODULUS OUTPUTS FOR THE AM PRINTED CYLINDRICAL UNIT SORTED ACCORDING TO THEIR SHELL THICKNESS: A) 2.6 MM SHELL AND B) 1.7 MM SHELL..... 144

FIGURE 5-22: STORAGE MODULUS OUTPUTS FOR THE AM PRINTED CYLINDRICAL UNIT WITH THE SIX GRAPHS REPRESENTING: GYROIDAL UNIT CELL WITH A) 2.6MM OR B) 1.70 MM SHELL, HONEYCOMB UNIT CELL WITH EITHER C) 2.6 MM OR D) 1.70 MM SHELL, AND 3D HONEYCOMB UNIT CELL WITH EITHER E) 2.6 MM OR F) 1.70 MM SHELL. EACH GRAPH CONTAINS THE THREE RESULTS FOR 50%, 25% AND 10% INFILL PERCENTAGE AS WELL. 146

FIGURE 5-23: MEAN STORAGE MODULUS SORTED BY PERCENTAGE INFILL WITH MEANS FOR BOTH 2.6 MM AND 1.7 MM IN EACH UNIT CELL DESIGN. ERROR BARS REPRESENT THE 95% CI OVER ALL OF THE FREQUENCIES IN THE FREQUENCY SWEEP..... 147

FIGURE 5-24: LOSS MODULUS OUTPUTS FOR THE SECOND PROTOTYPE OF PRINTED CYLINDRICAL UNIT FOR ALL OF THE ACCEPTED DESIGNS: GYROIDAL, TRIANGULAR, HONEYCOMB AND 3D HONEYCOMB, AND INFILLS: 10, 25 AND 50. VALUES ARE SEPARATED BY SHELL THICKNESS WITH GRAPH A FOR 2.6 MM SHELL AND B FOR 1.7 MM..... 149

FIGURE 5-25: 3D RENDERS OF THE RECONSTRUCTED PROTOTYPES FOR THE FOLLOWING PARAMETER COMBINATIONS: A) GYROID_10_2.6, B) GYROID_25_1.7, C) HONEY_50_1.7, D) HONEY_10_1.7, E) 3DHONEY_25_2.6 AND F) 3DHONEY_50_1.7. EACH IMAGE IS SLICED BY A PLANE TO PROVIDE AN INTERIOR LOOK AT THE SAMPLES..... 150

FIGURE 5-26: MICRO CT IMAGES FOR A 25% INFILL MODEL OF EACH UNIT CELL AND OF BOTH THIN AND THICK OUTER SHELL DIAMETER. FROM TOP TO BOTTOM OF ROWS: GREY SCALE ORIGINAL RECONSTRUCTED IMAGES, THRESHOLDED SLICE IMAGES, BINARISED OPEN PORES DISPLAYED SLICE, BINARISED CLOSED PORES DISPLAYED SLICE. PERCENTAGES FOR POROSITY OF THE INCLUDED IMAGES ARE SHOWN AT THE BOTTOM AS WELL. 151

FIGURE 5-27: CAD DESIGNS, SLICED IN PRUSASLICER, OF THE AM TOWER CONSTRUCT WITH TWO DISCRETE INFILLS, UNIT CELLS AND SHELL THICKNESSES..... 158

FIGURE 5-28: A) RECONSTRUCTED IMAGE OF A TOWER POST CT SCAN PRODUCED IN CT Vox, B) RECONSTRUCTED IMAGE MODEL, AFTER MORPHOLOGICAL OPERATIONS HAVE BEEN PERFORMED ON IT TO CALCULATE THE POROSITY VALUES. 160

FIGURE 5-29: MICRO CT IMAGES, RECONSTRUCTED AND THEN OPEN AND CLOSED POROSITY IMAGE SLICES FOR A 60-SLICE SEGMENT OF THE TOWER DISPLAYED BEFORE, AT AND AFTER THE TRANSITION ZONE OF THE TOWER CONSTRUCT. FROM TOP TO BOTTOM OF ROWS: GREY SCALE ORIGINAL RECONSTRUCTED IMAGES, THRESHOLDED SLICE IMAGES, BINARISED OPEN PORES DISPLAYED SLICE, BINARISED CLOSED PORES DISPLAYED SLICE. PERCENTAGES FOR POROSITY OF THE INCLUDED IMAGES ARE SHOWN AT THE BOTTOM AS WELL. 161

FIGURE 5-30: STORAGE (A) AND LOSS (B) MODULI RESULTS FOR THE THREE PROTOTYPE TOWERS FOR A FREQUENCY SWEEP OF 1 TO 90 HZ. 164

List of Tables

TABLE 3.1: EXAMPLE REQUIRED USED DEFINED PARAMETERS THAT ARE GLOBAL VARIABLES TO ALL THE MODELS PRODUCED. THE DIMENSION VALUES ALL DETERMINE THE GEOMETRIC STRUCTURE OF THE OBJECT UNDERGOING COMPRESSION.	55
TABLE 3.2: OGDEN MATERIAL APPROXIMATION PARAMETER SET USED.	55
TABLE 3.3: MODEL CREATION AND RETRIEVAL OF RESULTS AS PERFORMED IN PYTHON'S INTERACTION WITH ABAQUS.	56
TABLE 3.4: FINAL ERROR VALUES OF EACH SIMULATION AVERAGED ACROSS THE REPEATS WITH SD INCLUDED. THE ERROR VALUES CORRESPOND TO THE DIFFERENCE BETWEEN THE RESULTANT APPROXIMATIONS AND THE EXPERIMENTAL DATA SET AVERAGED ACROSS MULTIPLE SIMULATIONS. DONE FOR A) 50 ITERATIONS AND B) 20 ITERATIONS.	65
TABLE 4.1: MEAN STORAGE STIFFNESS (K') \pm 95% CI FOR THE THREE TESTED CONTOURED PLATENS AT 0°, 7° AND 30° FOR ALL FREQUENCIES IN THE FREQUENCY SWEEP OF 1 – 90 HZ	91
TABLE 4.2: MEAN LOSS STIFFNESS RESULTS (K'') \pm 95% CI FOR THE THREE TESTED CONTOURED PLATENS AT 0°, 7° AND 30° FOR ALL FREQUENCIES IN THE FREQUENCY SWEEP OF 1 – 90 HZ.....	93
TABLE 4.3: ENERGY DISSIPATION RESULTS FOR ALL SAMPLES (N = 4, N = 15) WHEN TESTED OVER ALL CONTOURED PLATENS. RESULTS SHOWN ARE MEAN OUTPUT \pm 95% CI FOR EACH FREQUENCY AND CONTOUR.	97
TABLE 5.1: MICRO-CT MEASUREMENTS TAKEN BEFORE DMA WITH MEAN OF 125, 150 AND 175 IMAGE SLICES ANALYSIS RESULTS FOR EACH OF THE OSTEOCHONDRAL CORES. INCLUDED IS THE MEAN ACROSS ALL THE SAMPLES FOR THE BASELINE COMPARISON.	120
TABLE 5.2: MICRO-CT MEASUREMENTS TAKEN POST DMA WITH MEAN OF 125, 150 AND 175 IMAGE SLICES ANALYSIS RESULTS FOR EACH OF THE OSTEOCHONDRAL CORES. INCLUDED IS THE MEAN ACROSS ALL THE SAMPLES FOR THE BASELINE COMPARISON.....	121
TABLE 5.3: THE 4 UNIT CELLS TO BE EVALUATED AGAINST REQUIRED KEY CHARACTERISTICS.	132
TABLE 5.4: SHORTHAND DEFINITIONS OF TESTING SPECIMENS FOR FUTURE RESULTS.	133
TABLE 5.5: MEAN \pm STD FOR STORAGE MODULUS VALUES OBTAINED FROM THE INITIAL PROTOTYPES. THESE ARE THE SAME VALUES DISPLAYED GRAPHICALLY IN FIGURE 5.12.	135

TABLE 5.6: MEAN VALUES FOR LOSS MODULI OF THE AM SAMPLES WITH SAMPLE 4 EXCLUDED (SD: STANDARD DEVIATION)	137
TABLE 5.7: SCORE ALLOCATION FOR PRINT VIABILITY OF INITIAL PROTOTYPING	138
TABLE 5.8: MEAN ± SD FOR STORAGE MODULUS VALUES OBTAINED FROM THE SECOND ROUND OF PROTOTYPES. THESE ARE THE SAME VALUES DISPLAYED GRAPHICALLY IN FIGURE 5-20.....	147
TABLE 5.9: MEAN VALUES FOR LOSS MODULI OF THE SECOND ROUND OF PROTOTYPE AM SAMPLES.....	148
TABLE 5.10: MICRO-CT RESULTS OF THE SECOND GENERATION OF PROTOTYPES. WITH THE FOLLOWING DATA VALUES INCLUDED: OPEN POROSITY PERCENTAGE, CLOSED POROSITY PERCENTAGE, TRABECULAE THICKNESS (MM) AND TRABECULAE SEPARATION (MM). PREVIOUSLY EXCLUDED SAMPLES ARE MARKED AS NA IN THIS DATA. TISSUE VALUES ARE INCLUDED IN THE LAST COLUMN FOR COMPARISON.	153
TABLE 5.11: LOSS MODULUS COMPARISON OF TISSUE VS LARGEST PRINTED VALUE WITH LARGEST LOSS MODULUS/ WITH COMPARATIVE FACTOR CALCULATED AS $E''(\text{TISSUE})/E''(\text{PRINTED})$	155
TABLE 5.12: STORAGE AND LOSS MODULUS RESULTS FROM THE THREE TOWER PRINTS WITH MEAN AND SD SHOWN FOR EACH FREQUENCY TESTED.....	163

Chapter 1. Introduction

1.1. Thesis introduction

Articular cartilage (AC) is a tissue that is present at the end of all articulating joints and plays a factor in the management of load through these joints. The most commonly researched anatomical joints are the hip and knee [1]–[3] partly due to these areas being prevalent for degenerative diseases such as osteoarthritis (OA)[4], [5]. Damage seen to the AC and thickening of the subchondral bone in these joints can result in progression to early onset OA diagnosis. There are limited medical approaches to treat OA, often replacement of the affected areas is performed through surgery utilising autografts, allografts, and more recently synthetic grafts [6]. This often results in palliative care or pain management being the treatment prescribed until further intervention is required for joint replacement or resurfacing. This outcome is highlighted in the reported by the National Joint registry in 2022 who found that 97.4 % of knee and 91.2% of hip replacements list OA as the primary reason for surgery [7]. Enhancing the biocompatibility and mechanical response representability of these grafts will support the development of further treatment options. This can potentially be achieved through the advancement of currently available computational models and using the mechanical response of biological tissues as a target for synthetic replacements.

The prevalence of OA in the population of the UK was 8.75 million cases between 2004 – 2010 with this value only expected to rise [4] as a result of an increasing and ageing population, and due to the prevalence of diseases such as obesity that effects an estimated 29% of adults[8] and is a known risk factor for OA[9]. When developing synthetic components for the medical industry a key consideration is

biocompatibility. Both allograft and autografts provide a good match for the mechanical properties of the removed tissue; synthetic replacements would benefit from being adapted to match these properties, something that has been lacking in current approaches [10], [11]. Not only biocompatibility, but also bio-integration has become more feasible in AM components. This has become feasible with implants being coated with bioactive substrates [12], [13] or the interior porous networks of certain types of AM parts containing growth supplements to encourage integration [14]. These factors imply that during the design process of the hierarchical structure, the internal geometry is a factor that needs to be accounted for in the design step. In order for a hierarchical design to be successful it would have to mimic the geometric and dynamic mechanical response properties of cartilage effectively.

Cartilage has been characterised with multiple models to represent its mechanical behaviour, with those reported in literature including biphasic and triphasic theory [15], [16]. In particular biphasic states that cartilage has separate constituent parts that provide the viscous and elastic portions of its response to loading. There have, however, been studies that question this classification [17], [18] especially in the need for physiological relevance in the load applied [19], [20]. To accurately gauge the mechanical response of AC and allow it to be mimicked synthetically, dynamic loading experiments are performed to induce a material response that can be modelled into material parameters.

Current literature studies on biphasic material focus on tissue under equilibrium load, rather than the dynamic load being applied through indentation or sinusoidal cycles seen in gait-relevant or non-equilibrium dynamic studies [18], [21]–[24]. The key factor that questions the equilibrium hypothesis of biphasic theory is the loss and the re-imbuing of water during a dynamic loading cycle of cartilage, where the re-imbued

water is less than that extruded due to the permeability of the tissue limiting its speed and therefore the swelling pressure not resulting in at equilibrium[25].

Finite element analysis (FEA) is a technique that can be applied to computational models of biomaterials that experience complicated loading conditions [26] and has been utilised to provide simulations of the theories mentioned previously [27], [28]. A material approximation is required during the calculation of FEA and the solutions employed in most recent studies for cartilage are as a viscoelastic material [18], [23], [29]–[31]. Other approximations used in literature cover linear elasticity and hyper-elasticity [20], [32], [33], however, limited work has applied current material approximations to a dynamic loading environment. In combination with dynamic mechanical analysis (DMA) it can also provide a measure of the ability of a material to store and dissipate energy during dynamic loading. Therefore, it can be used to simulate the aforementioned non-equilibrium loading states and establish more physiologically accurate material response parameters.

Synthetic implants have already seen use in joint replacements at entire joint scale and smaller local replacements. Although entire joint replacements have seen a huge amount of success with 1.42 million performed in 2022 [7], local synthetic replacements are being used and developed but have limits in their capabilities [34], [35]. A key factor many solutions do not account for is the mimicry of the dynamic material response of cartilage/subchondral bone, a key factor to stress shielding occurring in long bone implants[36].

1.2. Research aims and objectives

The aim of this thesis is to develop new techniques for enhancing the material characterisation of cartilage under non-equilibrium loading states, specifically focussing on three key areas of study: creation of an automated process to convert dynamic only data from DMA to FEA-transient output; development of an experimental setup in a dynamic environment to analyse the effect macro-scale variables have on AC characterisation; analyse micro-scale changes seen in AC under dynamic load and utilise these to develop a hierarchical structure exploiting AM. The main questions that are raised within this thesis are subdivided in the flow chart presented in Figure 1-1. To achieve these questions, the thesis has the following objectives:

1. Code a system that can allow the hyper-visco elastic material characterisation of a tissue using DMA output data as an input. Allow the system to be modular so it is not a single impact/use design and can be altered to fit the needs of the user.
2. Develop an algorithm to fit in said system that can optimise the material parameters that will be given as an output.
3. Exploit AM for a dynamic test set-up that enables macro-scale variables, such as joint shape, to be evaluated as a singular experimental variable.
4. Develop a dynamic testing scenario in combination with Micro-CT imaging to identify potential micro-scale changes in material properties and geometric characteristics of cartilage pre and post load.
5. Prototype a hierarchical AM component that represents the constituent sections of an osteochondral unit and then combine into a singular design.

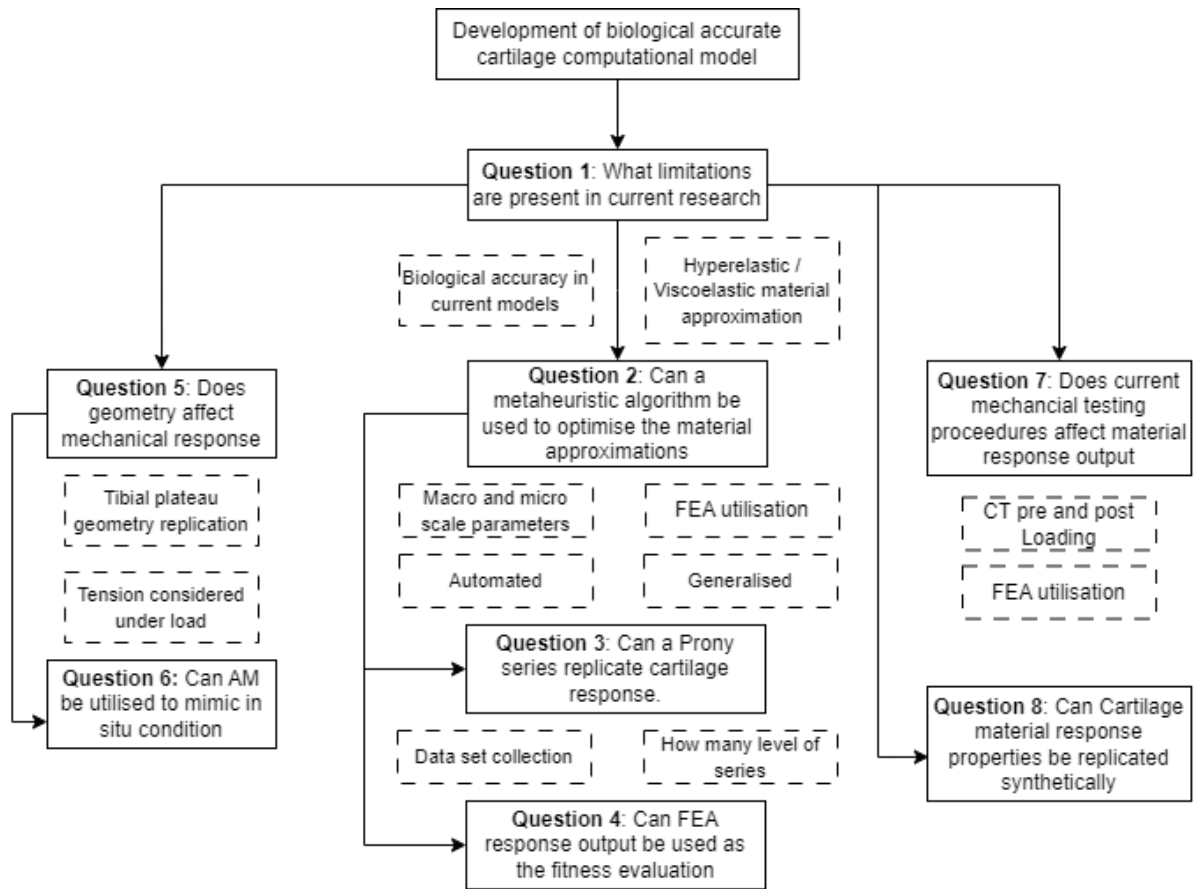


Figure 1-1: Flow chart of the PhD thesis, showing the different steps of the study.

1.3. Thesis overview

Chapter 2 provides the background knowledge needed to understand the experimental chapters within this thesis. It covers synovial joints with a focus on articular cartilage, mechanical testing, and computational modelling of tissue within a dynamic environment, numerical methods for optimisation, and additive manufacturing techniques in the medical industry.

The next three chapters will cover the experimental work which is broken down to cover the main questions raised in Figure 1-1. Each chapter will have its own literature review that covers the scope of the question it is answering. Chapter 3 will answer questions 2,3 and 4, Chapter 4: questions 5 and 6 and Chapter 5: questions 7 and 8. Question 1 which embodies the thesis in its entirety will be inherently covered by all chapters.

Chapter 3 creates, then evaluates an automated modelling system that is designed to provide viscoelastic material approximations in a modular and standardized format by taking data from a dynamic only environment (i.e., DMA) to FEA-transient conditions (i.e., frequency to time domain). The viscoelastic model used is that of the Prony series and it is solved through optimisation using two numerical methods of an interior point and a genetic algorithm. Prony was used due to its previous application in characterising other soft tissue structures [37]–[39]. Articular cartilage data from a previous study was used as a case study to evaluate the system and the results are validated against known tissue data. Chapter 3 provides the framework to start investigating and trying to produce more complicated material models of cartilage under different geometric conditions, such as those that will be investigated in Chapter 4. The data obtained in Chapter 4 will be able to be relayed back in the overall system to increase the accuracy of the models produced.

Chapter 4 investigates how contours within the tibiofemoral joint on the tibial plateau affect articular cartilage properties. In this chapter, a new experimental procedure was defined providing the ability to exploit AM, to design/develop testing approaches that enable geometric variables to be isolated. Specifically, evaluation of the effect of joint contour on material response was analyzed on bovine test samples and evaluated against values recorded in literature and current established testing procedures. Chapter 4 focussed on the macro variables of the joint tissue affect its material properties thus to further the whole picture, Chapter 5 will investigate how micro variables such as internal trabecular components change within the tissue structure.

Chapter 5 investigates the possibility of creating additively manufactured components that mimic the mechanical response and geometric profile of an osteochondral plug. A hierarchical tower will be produced by combining printed profiles established through prototyping, and by varying known parameters that can alter the components mechanical response and interior geometric composition.

Chapter 6 provides the overall thesis discussion and conclusions.

Chapter 2. BACKGROUND

2.1. Chapter Overview

This chapter introduces the fundamental concepts of the topics that are covered within this thesis. There are four main sub sections which will cover the following:

The role of AC on the mechanics of synovial joints, with a focus on the tibiofemoral joint (section 2.2); mechanical properties and the relevant testing used to characterise for material properties (section 2.3), with a focus on dynamic mechanical analysis; computational modelling and numerical methods (section 2.4); and AM with a focused on it medical applications (section 2.5). A more in depth literature review for each chapter is done within their individual introductions.

2.2. Synovial joints: tissue constituents and mechanics

Synovial joints are the connections between bones that control movement and other specific articular functions for a skeletal system. The main synovial joints (Figure 2-1) in the mammalian system are knee (tibiofemoral), hip (acetabulofemoral), elbow (ulnohumeral) and shoulder (glenohumeral) joints. These are all classified as either

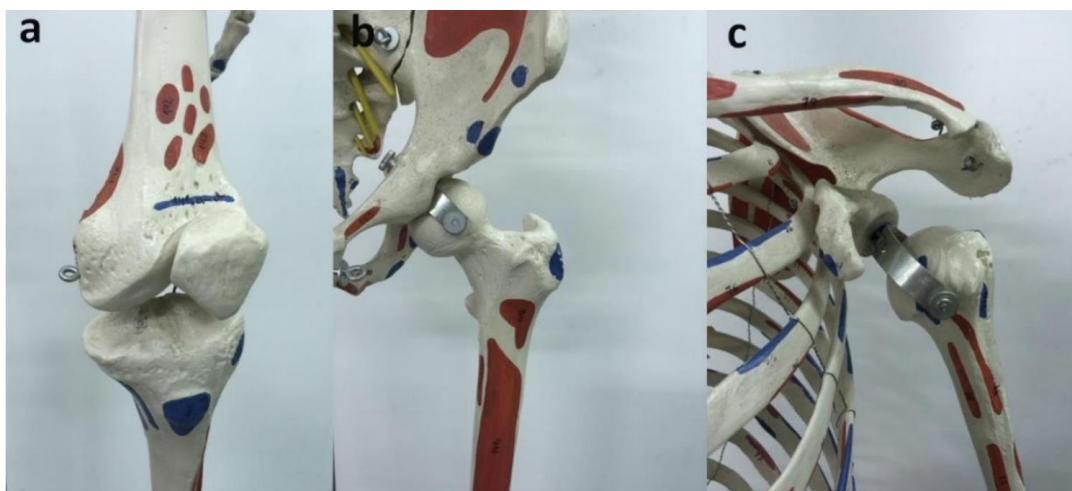


Figure 2-1: Images of three of the main synovial joints: A) knee (tibiofemoral), B) hip (acetabulofemoral) and C) shoulder (glenohumeral). Image courtesy of Sadeghi CC BY-NC-SA 4.0.

hinge or ball and socket joints dependent on the type of movement which they provide and their connection.

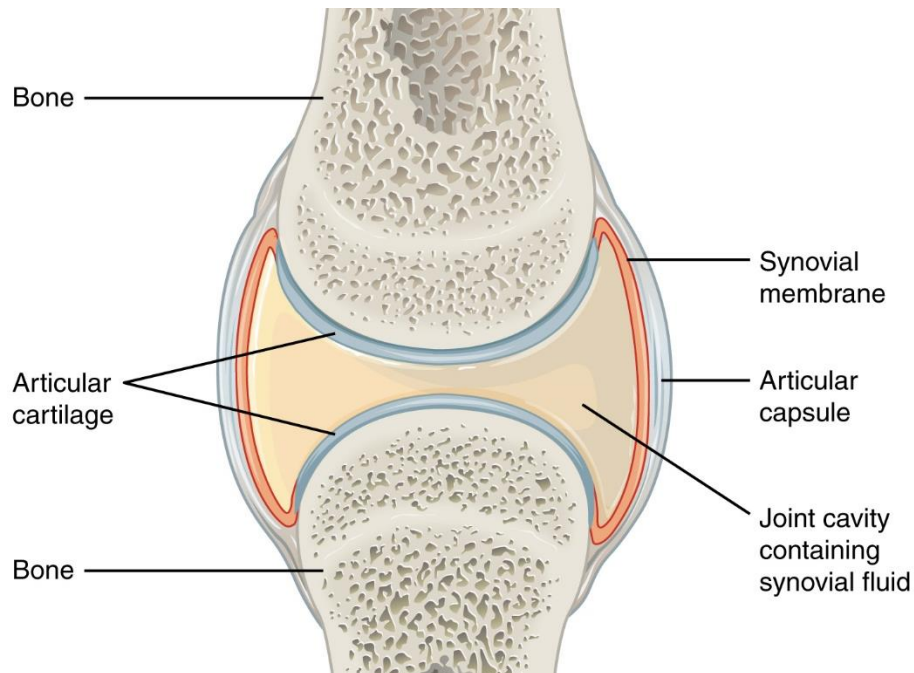


Figure 2-2: Schematic of a synovial joint showing all major components. | (Reproduced from BC Open Textbook; Betts, 2019, which is distributed under the terms of CC BY-NC-SA 4.0.

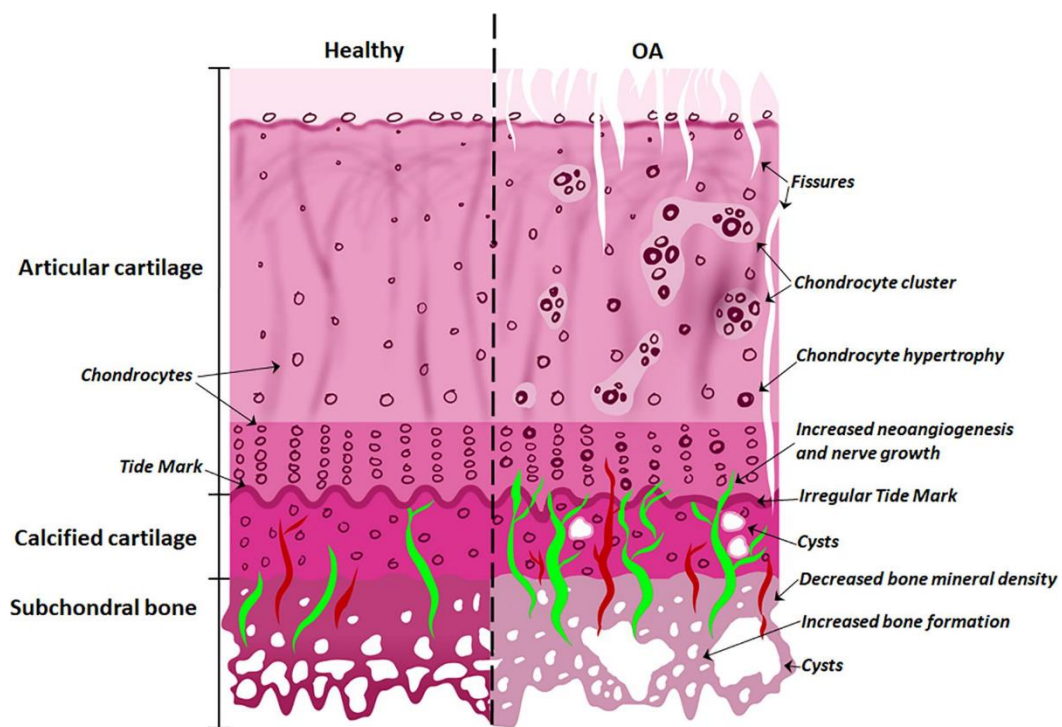


Figure 2-3: Osteochondral core shown in both healthy and osteoarthritic states with labelled layers for the constituent parts of the tissue segment. Image original produced by Silva et al. [41] CC BY-NC-SA 4.0.

The main components of a synovial joint epiphysis are articular cartilage (Figure 2-2) and subchondral bone; commonly referred to in literature as the osteochondral unit (Figure 2-4). It is often defined by layers of these tissues as shown in Figure 2-3 where the cartilage provides the uppermost articulating surface, and the subchondral bone lies below and consists of multiple layers of differing thickness of bone tissue. Within the subchondral bone, there are two main types of bone, cortical and trabecular.

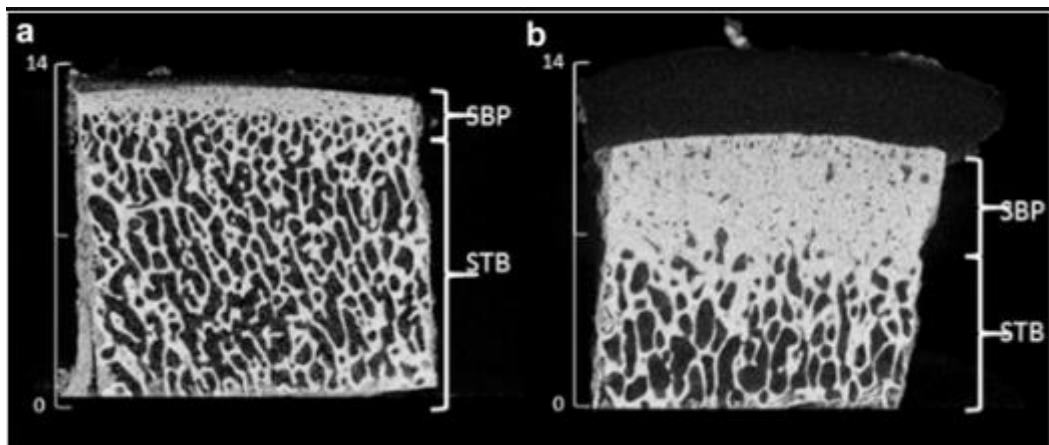


Figure 2-4: Micro-CT cross sections of osteochondral unit highlighting the portions of the osteochondral core. The dark region at the top is the cartilage layer, then the subchondral bone plate (SBP) and subchondral trabecular bone (STB). Image sources from Fell et al. [23] CC BY-NC-SA 4.0.

Articular Cartilage

AC plays a key role in the transmission of forces between the surfaces in articulating joints [3], [40]. It provides a surface on top of the underlying bone in synovial joints that, combined with lubricating factors such as lubricin, provides a surface with a low coefficient of friction which facilitates articular joint movement and prevents direct bone-bone contact. An example of a bovine humeral head with its cartilage surface visible is seen in Figure 2-5. This is important to limit as bone can be viewed as an approximately rigid structure, so direct contact leads to concentrated contact stresses. The most common degeneration of AC comes in the form of osteoarthritis (OA) [4], [5],

[41], which results in a breakdown or complete destruction of the cartilage structure at the articular joint and has been shown to deteriorate the mechanical properties of the tissue [42], [43]. A representation of how the structure breaks down throughout the osteochondral core with OA progression is seen in Figure 2-3.



Figure 2-5: Bovine humeral head with cartilage surface on the right side.

Articular cartilage (AC) is known to be a multilayer construct with its composition differing through the depth of the tissue [3] (Figure 2-6A). It is made up of a dense extra cellular matrix (ECM) but unlike other tissues within the body it has no vacuolisation, nerves, or lymphatic connections [44], [45]. The ECM is mostly comprised water, collagen, proteoglycans, and specialised cells called chondrocytes with other proteins present but in small quantities [45], [46]. Collagen provides between 50%-75% of the dry weight of the ECM and is its main construction component[47].

Proteoglycans are a class of glycoproteins that classified by nature of the glycosaminoglycans (GAGs) chains attached to their core protein with the primary one that is found in the ECM of cartilage being aggrecan. Within the ECM they form proteoglycan aggregates that are the combination of sulphated proteoglycan side chains attached to a hyaluronic acid filament core forming a highly anionic unit. Proteoglycans contribute to the osmotic pressure of cartilage within its fluid state due to the attraction of cations and anions being drawn in, i.e. the Donnan effect, and the additional water than is brought with them. The Donnan effect is where the charged particles are unevenly distributed across a semipermeable membrane. In cartilage the interstitial fluid carries the ions and the proteoglycans within the solid porous matrix of cartilage are the membrane.

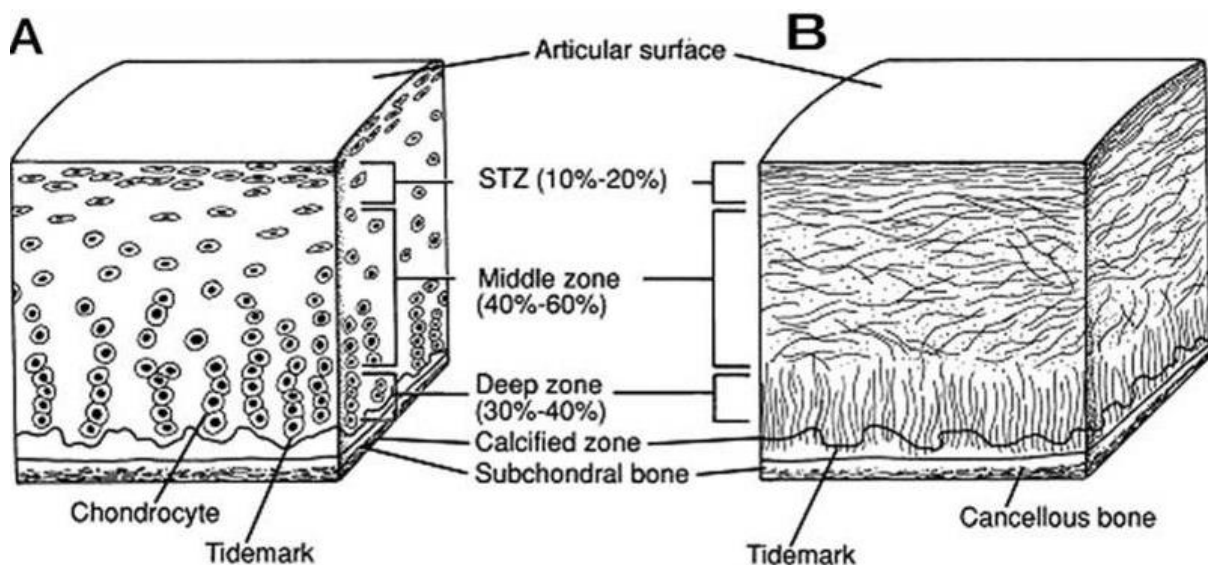


Figure 2-6: Cross sectional schematic of a cartilage tissue segment with A) showing the cellular organisation of the chondrocytes and B) showing the fibre orientation of the collagen strands. Highlights the superficial tangential zone (STZ), middle and deep zones of cartilage. Original image from Fox et al, [3] CC BY-NC-SA 4.0.

As shown on Figure 2-6 and Figure 2-7, AC is commonly split up into 4 zones between the surface and the bone-cartilage interface known as: superficial, transitional, deep, and calcified zones. Across these zones there is a complex collagen fibre network that aids the tissue's ability to support load, and regain its original shape following loading [48], [49] Figure 2-6B. As AC transitions from zone to the other, the fibre-orientation of the collagen changes. For the superficial layer horizontal densely packed fibres are found and cover 10-20% of the total number of layers. The transitional zone is between 40% and 60% of the total tissue and the fibres are seen to orientated between 20 and 70 degrees different to the horizontal fibres seen in the superficial layer. The deep

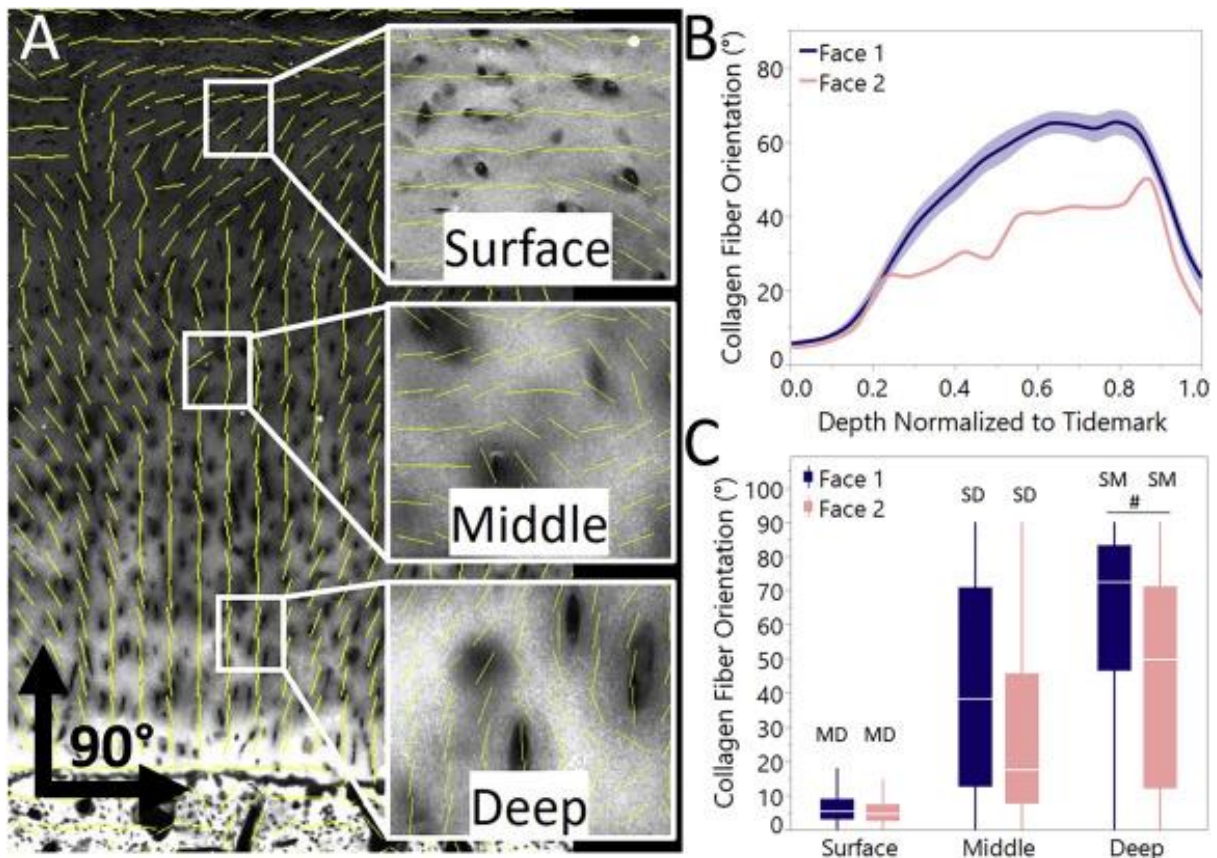


Figure 2-7: Collagen fibre orientation analysis: how the angle varies with respect to depth and initial horizontal 0° angle. A) Second harmonic generation (SHG) and OrientationJ overlay with insets highlighting fiber orientation analysis across zones B) continuous fit from face 1 and face 2 across the full depth of the articular cartilage (shaded regions represent confidence of fit) showing differences in collagen fiber orientation with depth between faces and C) binned zones with 0–20% representing surface, 20–60% middle, 60–90% deep zones (box plot with data outliers removed for visualization). Image and quoted portion of caption text obtained from Fischenich et al. [212] CC BY-NC-SA 4.0.

zone then has fibres that are perpendicular, or 90 degree, to the fibres in the superficial layer and takes up approximately 30% to 40% of the overall thickness. Figure 2-7B and C display this ratio effectively with the relationship of depth to fibre orientation shown in image B demonstrating how this is progressive change rather than immediate.

Subchondral Bone

The other portion of the osteochondral core is the subchondral bone. There are multiple layers to this tissue section as seen in Figure 2-3 and Figure 2-8. It is mainly comprised of 2 components, a thicker exterior shell that comes into direct contact with the cartilage called the subchondral plate, and a deeper more porous subchondral trabecular bone [50], [51]. The sclerosis of subchondral bone is another key symptom of the progression of OA with Figure 2-3 demonstrating the type of change that is seen.

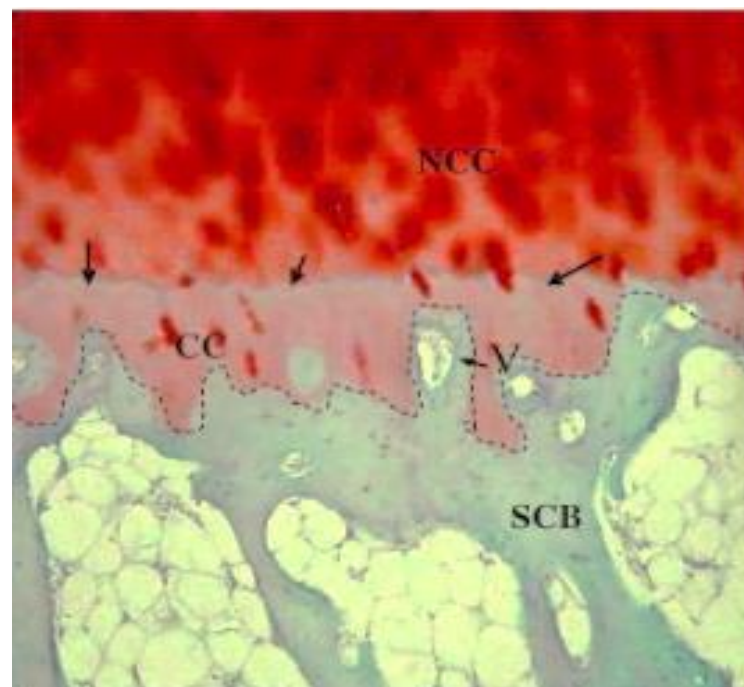


Figure 2-8: Photomicrograph of the osteochondral junction of a healthy tissue donor. Abbreviations within the image are as followed: NCC — non-calcified cartilage; CC — calcified cartilage; SCB — subchondral bone; V — vascular channel. Image courtesy of Suri et al. [213] CC BY-NC-SA 4.0.

Differing to AC, subchondral bone is a vascularised tissue, there are many channels called Volkmann's canal's that run through it that have been shown change in both quantity and distribution based on the patients age and the amount of loading that the tissue has experienced [52]. This is directly contrast to cartilages lack of Vascularization. A results of this is also that bone is able to repair damage that is caused to it. The subchondral bone plate is directly connected to the zone of calcified cartilage and is formed of a thin cortical lamella [52]. This 'plate' has scattered porosity within it.

The other main section is the subchondral trabecular bone, which is made up of a number of trabeculae. These are more easily described as pillars with attachments between them, an example scanning electron microscope (SEM) image of trabecular bone in seen in Figure 2-9. Trabecular bone exhibits supportive, load absorbing qualities that make it important for osteochondral loading. It exhibits structural and mechanical anisotropy, with its preferred orientation being in parallel to length of the bone.

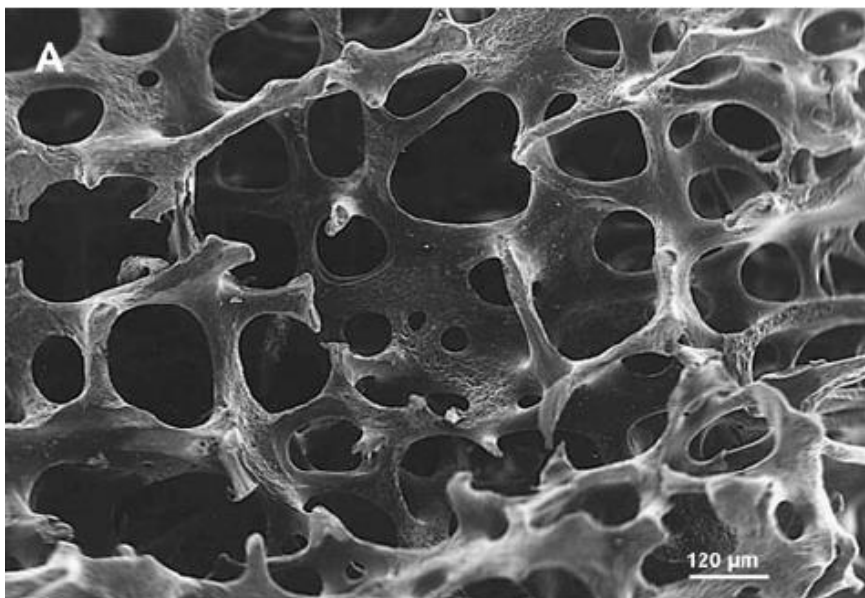


Figure 2-9: SEM image of trabecular bone showing the pillar structures present. Image courtesy of Chappard et al. [214] CC BY-NC-SA 4.0.

2.3. Mechanical testing and material characterisation

2.3.1. Mechanics of materials

When establishing mechanics of materials the two main concepts are the stress (σ) and strain (ϵ) induced in a material sample when it is subjected to a load. The load used to establish these properties can be of different forms such as transverse, axial, and torsional loading.

- Transverse induces a bending effect by applying a load perpendicular to the longitudinal axis of the sample.
- Axial applied a load parallel to the longitudinal axis of the sample to induce a stretch or deformation.
- Torsional induces a twisting motion in the same plane as the axial load.

The main focus of this study will be axial loading. Engineering stress is a measure of the force applied (F) divided by the surface area (A) it is applied to (Eq. 2.1).

$$\sigma = \frac{F}{A} \quad (2.1)$$

Engineering strain is the deformation of a sample under an applied load and can be calculated by taking the change in size a sample experienced (ΔY) and dividing it by the sample's original dimensions (Y) (Eq. 2.2). It is often referred to as a percentage however engineering strain is a dimensionless value.

$$\epsilon = \Delta Y / Y \quad (2.2)$$

Elasticity is used as a term to describe the ability a material has to return to its original shape after a load has been applied to it. When the relationship between stress and strain of a material is linear up until its yield point where permanent deformation occurs, the gradient of this relationship is called the Young's modulus (E). When there

is a non-linear relationship between stress and strain other material models are used such as hyperelastic and viscoelastic.

A Hyperelastic material model is used where the stress – strain relationship of a material derived from a strain energy density function (W) of the form seen in equation 2.3 where F is the deformation gradient and C is the right Cauchy-Green deformation tensor.

$$W = \hat{W}(C) = \hat{W}(F^T \cdot F) \quad (2.3)$$

Many hyperelastic models have been developed to represent materials who don't fit the linear elastic representation such as rubber, and biological tissues [53], [54], an example of such a stress strain relationship is seen in Figure 2-10 Multiple types of models have been created to fit different material responses with some of the more commonly used ones being Neo-Hookean, Mooney-Rivlin, and Ogden[55].

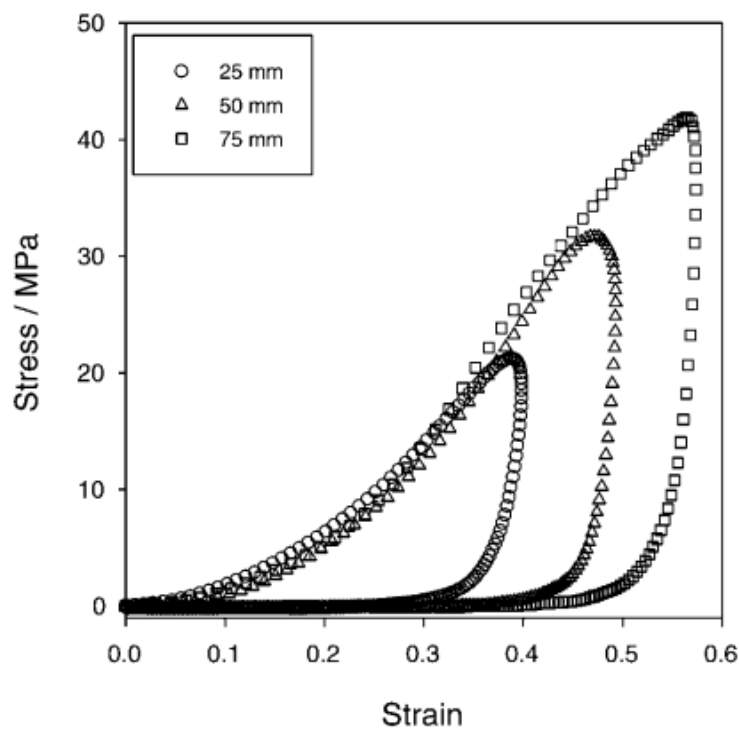


Figure 2-10: An example of a non-linear stress-strain relationship from an experiment performing impact loading on human AC. Image courtesy of Edelsten et al. [63]

An expansion to the hyperelastic approximation is the concept of viscoelasticity, which is where a material exhibits both the characteristics of a viscous and elastic response whilst being deformed. A viscoelastic material will be able to both store potential energy and experience dissipation of energy during a loading cycle. Because this material is viscous it adds a time-dependent factor to the strain rate. During a loading and unloading cycle a viscoelastic material will dissipate energy through heat and this is seen on a hysteresis loop as seen in Figure 2-10. The amount of energy dissipated is calculated as the difference between the area under each of the curves, i.e. the interior section of a loop in Figure 2-10. There are multiple models of viscoelasticity that have been used to represent different materials. Some examples are as follows:

- Maxwell model: Consists of a single elastic spring and viscous damper in series. It is designed to simulate stress decaying exponentially over time and is used often for polymers.
- Kelvin-Voigt: An elastic spring and a Newtonian damper in series to mimic gradual relaxation after a steady-state strain is released. It is often used for organic polymers, rubber, and wood.
- Burgers: A combination of Maxwell and Kelvin-Voigt in parallel and in different configurations. It incorporates viscous flow into the model design.
- Generalised Maxwell model: It is designed to consider the fact that relaxation does not occur at a single moment but across a distribution of time with varying length. It is comprised of many spring-dashpot Maxwell units. A schematic demonstrating this is in Figure 2-11.

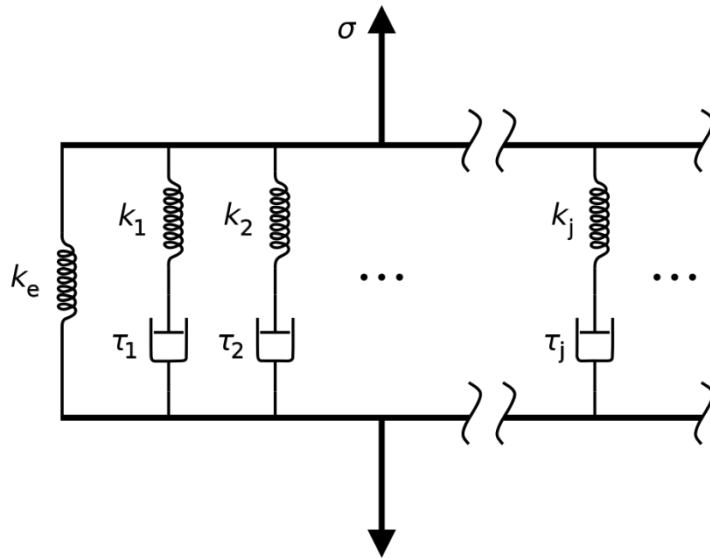


Figure 2-11: Generalised Maxwell model schematic showing the springs (k) and dashpots (τ) in series.

2.3.2. Material Characterisation

Dynamic testing of tissue has been used to characterise material properties [29], [56], [57] with a number of different applications [58], [59]. There are multiple ways of performing dynamic testing which involve techniques such as indentation testing [22] and dynamic mechanical analysis (DMA) amongst others [60].

Hyperelastic materials

Hyperelastic characterisation can use uniaxial compression test data to solve the strain energy density function of the chosen model. The three models mentioned earlier (section 2.3.1) Neo-Hookean, Mooney-Rivlin, and Ogden provide material response parameters through their respective equations (Eq. 2.4, Eq. 2.5, Eq. 2.6).

Neo-Hookean

$$W = C_1(\lambda_1^2 + \lambda_2^2 + \lambda_3^2 - 3) \quad (2.4)$$

Where C_1 is a material constant and λ_i are principal stretch terms.

Mooney-Rivlin:

$$W = C_1(\bar{I}_1 - 3) + C_2(\bar{I}_2 - 3) \quad (2.5)$$

Where C_1 and C_2 are material constants, and \bar{I}_1 and \bar{I}_2 are the first and second invariants of the left Cauchy–Green deformation tensor.

Ogden:

$$W = \sum_{i=1}^N \frac{2 \cdot \mu_i}{\alpha_i^2} (\lambda_1^{\alpha_i} + \lambda_2^{\alpha_i} + \lambda_3^{\alpha_i} - 3) \quad (2.6)$$

Where N is the order of the model, μ_i is a shear term, α_i is a dimensionless constant and λ_i are principal stretch terms.

Viscoelastic materials

Viscoelasticity can be studied using a technique called dynamic mechanical analysis (DMA) which is where an oscillating load (stress (σ)) is applied to the material in axial fashion and the displacement of the tissue is outputted (strain (ϵ)). A dynamic complex modulus (E) is used to describe the relationship of the oscillating stress input to outputted strain (Eq. 2.7). When characterising a viscoelastic material, through DMA, a storage (E') and loss (E'') modulus can be determined (Eq. 2.8, Eq. 2.9, respectively).

$$E = E' + iE'' \quad (2.7)$$

$$E' = \frac{\sigma^0}{\epsilon^0} \cos \delta \quad (2.8)$$

$$E'' = \frac{\sigma^0}{\epsilon^0} \sin \delta \quad (2.9)$$

Where σ^0 and ε^0 are the amplitudes of the stress and strain curves respectively with relation to time, and δ is the phase shift. Storage modulus characterises the ability of the material to store energy for elastic recoil. The loss modulus characterises the ability of the material to dissipate energy during the cycle of loading-unloading.

In an experimental context the load-displacement data of a materials' dynamic modulus is calculated following normalisation for shape. Briefly, the stress (σ) induced and strain (ε) experienced are determined and their data-set length is used to calculate the (dynamics) complex modulus (E) (Eq. 2.7); the data-set length is evaluated from a fast Fourier Transform along with a phase lag between σ and ε waves at each frequency of loading.

AC material characterisation

AC has been shown to exhibit both viscous [61] and elastic [62] mechanical behaviour characteristics and is therefore classed as a viscoelastic structure [19], [24], [31]. The viscoelastic properties of AC have been well documented [63]–[65], with Fulcher et al.[66] showing that it has frequency dependant loading characteristics when tested in the physiological range (1 - 92 Hz [19]) through DMA testing. Cartilage has been subject to both DMA and indentation test procedures with impact testing being used to test failure and instantaneous loading effects on the tissue [67], [68].

Cartilage has been categorised as a singular material [69] as well as a bi-phasic and tri-phasic material. For each of these classifications a specific material parameter model is required, which can be as simple as a linear elastic representation [32] or models with more complexity such as hyperelastic [20], [33], visco elastic [18], [70] or poroelastic [71]. Because cartilage has been shown to have a collagen fibre

component to its material make up (section 2.2) fibre-reinforced approaches has also been researched [72] with the aim of replicating this interior functional structure.

The biphasic model of AC is based on cartilage having a combination of fluid and the interaction between these phases and defines cartilage as a fluid-saturated, fibre-reinforced, porous, permeable composite matrix [15]. It suggests that when cartilage is loaded, the collagen fibres and water component provide elastic and viscous component, respectively. The interactions between these two components are said to be what provides cartilage with its material response to differing loads.

Triphasic theory is another model of AC that postulates that there is a tertiary phase in the tissue. It states that there are two fluid-solid phases that are similar to biphasic theory and then a third ion phase [73]. It combines the physio-chemical theory that focuses on ionic transfer with the biphasic theory that establishes physical components. Another method of characterisation is to use DMA which provides a frequency domain option which enables dynamics within the materials to be accounted for.

Material parameter models such as Neo-hookean and Yeoh hyperelastic approximations were investigated by Robinson et al. but both solutions were highlighted to have limitations with their predictions on contact area [74]. Other hyper elastic models such as Ogden and Mooney-Rivlin were also suggested to be suitable for isotropic assumed incompressible materials such as AC by Wex et al. [54].

2.3.3. Numerical modelling of materials

Computational models have already seen use in medical applications to aid in understanding of areas such as bone tissue engineering [75], computational fluid

dynamics in blood flow [76], cartilage loading [28] and other similar fields.

Regulatory agencies such as the U.S. Food & Drug Administration have supported the use of mechanically accurate computation models of biological systems to back clinical data to enhance device and drug trials and approvals [77].

A numerical technique to generate the storage and loss modulus values was used to convert the values from a DMA output to the frequency domain using a fast Fourier transform (FFT) [31]. This produces the magnitudes of displacement (d^*), the magnitude of load (F^*), the phase lag (δ) and the actual frequency (f). From these values the complex stiffness (k^*), storage stiffness (k') and loss stiffness (k'') values can be calculated (Eq. 2.10, Eq. 2.11, Eq. 2.12).

$$k^* = \frac{F^*}{d^*} \quad (2.10)$$

$$k' = k^* \cos \delta \quad (2.11)$$

$$k'' = k^* \sin \delta \quad (2.12)$$

To calculate the modulus, a shape factor (S) for the test sample is used. This shape factor is calculated from the dimensions of the sample being tested and is unique to its geometry. As an example, for a sample which is geometrically a cylinder the shape factor (S) would be calculated (Eq. 2.13).

$$S = \frac{\pi D^2}{4h} \quad (2.13)$$

Using this shape factor (S) the storage modulus (E') and loss modulus (E'') are both calculated (Eq. 2.14, Eq. 2.15) and allow the removal of the effect the sample dimensions may have been having on the established material properties.

$$E' = \frac{k'}{S} \quad (2.14)$$

$$E'' = \frac{k''}{S} \quad (2.15)$$

A alternative numerical model for viscoelasticity is the Prony series [78]. This has been used for cartilage in a number of comparative studies of material response due to its ability to capture the observed hyper-viscoelastic response [21], [79]. It is a form of the generalised Maxwell model. It is defined as a relaxation test that assumes a sample had an immediate strain applied to it that is kept constant, and then the stress of the sample is measured over the time of the test. It makes the assumption that the initial stress is caused by the materials elastic response and the resulting reduction in stress over time is as a result of the viscous element of the material. The general form of the Prony approximation is:

$$\mu(t) = G_{\infty} + \sum_{i=1}^N g_i \exp\left(-\frac{t}{t'_i}\right) \quad (2.16)$$

Where $\mu(t)$ is the time-dependent relaxation modulus, G_{∞} is the equilibrium modulus, and g_i and t'_i are the spring relaxation modulus and relaxation time of the Prony series for N spring-dashpot pairs or frequency delays. The Prony series viscoelastic approximation is utilised within chapter 3 and will be gone into more detail in section 3.2.4 due to direct connection to the code that is written within that section of the thesis.

2.4. Computational modelling and numerical methods

Numerical methods are widely used across engineering to break down larger problems which are difficult (or impossible) to solve analytically, so as to approximate a solution. This has led to the widespread use of computational modelling across engineering disciplines, including engineering applications to medicine in order to utilise computational solvers. This is partly due to modelling resulting in a reduced use of physical resources, reduced costs for prototyping and reduced time spent in developing experimental set-ups and thus cost. When quantifying mechanical or physical phenomena in such models, these characteristics are normally defined using partial differential equations (PDE) and are often solved using FEA [80], [81].

Finite element analysis

FEA has been used to facilitate the evaluation of experimental conditions, where analysis of the mechanics cannot be obtained either reliably or in a cost-effective manner. For example, a toolbox that generates models for FEA of the mitral heart valve enabling the effect of geometric variables on valve mechanics to be evaluated [82]. To construct effective models, a strong connection between simulations and experimental data needs to be present and reliable for effective results to be obtained [83].

FEA models allow the direct input of materials parameters through various material models depending on the software solution used. FEA is a numerical method that is used to solve partial differential equations in two or three dimensionally bounded problems. The main concept behind it being to reduce the complex original problem

is simpler parts normally done through the creation of a mesh over the model, an example of FEA discretisation of a problem is seen in Figure 2-12.

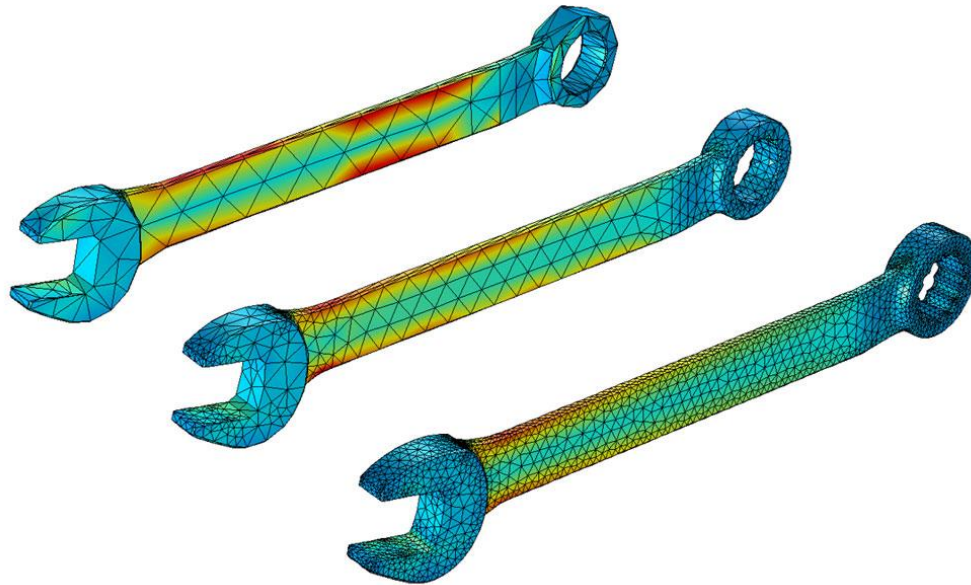


Figure 2-12: Iterations of different meshes for an FEA problem defined within COMSOL. Image courtesy of COMSOL (COMSOL, Stockholm, Sweden) CC BY-NC-SA 4.0.

When approaching an FEA problem there are a few key points need to be addressed. A few key parameters of an FEA problem are the model geometry, mesh, boundary conditions, material properties, and loading conditions. After these are defined, the models are solved depending on the loading condition defined and then the output should be validated in some way, where it be against known data separate from any used within the model construction or some other form of simulation. These concepts are briefly explained below:

- **Geometry:** The dimensional qualities of a model are designed to mimic the real world problem that is trying to be replicated. This can be done through importing a computer-aided design (CAD) model or other techniques.

- Mesh: The meshing of a CAD model is done through the discretisation of the overall system. This is done through splitting up the continuous system into finite elements and nodes that connect these elements. The user can control the level as to which the geometry is discretised as seen in Figure 2-12 through the multiple meshes present. Mesh nodes are used to approximate a solution for a larger continuum.
- Boundary conditions: These are constraints placed on the freedom of movement of a model. Generally, it defines the domain over which the problem is to be solved.
- Material properties: The parameters that define how your model responds to the load that is applied to it. These are taken from material characterisation, some of which are described in section 2.3.2.
- Loading conditions: The main types of loading are force, pressure, and temperature. A load generally contains four components: magnitude, orientation, distribution, and time dependency.

The type of analysis in FEA is normally linked to the load situation that has been defined i.e. stress, thermal or impact as examples. The outputs of a FEA problem will be the displacement or deformation of the dimensions of the original geometrical model. These can be converted to stress, strain, and strain energy density values.

Validation of FEA results are incredibly important to ensure that all the simulation parameters are correct and that the output is representative of the real life situation [84], [85]. Independence in data sets is very important in validation otherwise confirmation bias can result in incorrect assessments of simulations where validation and simulation data are the same. Validation is also very important when it comes to the use of numerical methods for approximating material characterisations.

Optimisation is act of minimising or maximising a mathematical problem to produce the best fitting parameters. A generic representation of an optimisation problem is shown in equation 2.17.

Given: function $f : A \rightarrow \mathbb{R}$ from some set A

There exists: $x_0 \in A$ such that $f(x_0) \leq f(x)$ for all $x \in A$ (minimisation) (2.17)

or such that $f(x_0) \geq f(x)$ for all $x \in A$ (maximisation)

Many of the numerical models and material characterisation explained in 2.3.2 and 2.3.3 are able to have the parameters fitted through the use of optimisation techniques. Hyperelastic material parameters have been obtained through optimisation in a number of industries such as aerospace and the medical industry[86], [87].

The main two types of optimisation algorithms are localised and global techniques. The difference being localised optimised algorithms will find a minimal solution within a specific region of the search space whereas global with the absolute minimum for all possible solutions, a visual representation of which is shown in Figure 2-13.

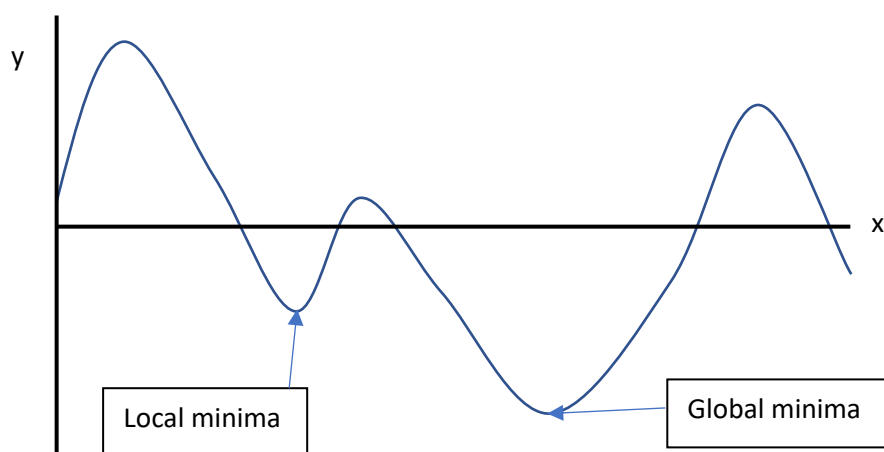


Figure 2-13: hypothetical values on a graph of a function of the form $y = Mx$ with M being a constant. Demonstrating the difference between local and global of finding a solution for M .

The term 'Optimisation' is often misrepresented, being used when parameters are purely varied without the evaluation of a true optimal solution [88], [89]. For example, varying a Young's modulus over 10 values to find a 'best' value is not an optimised solution, but the best of 10 proposed solutions: a common misconception. Further, where a variable range is constrained by a user in this manner, solutions can be stationed within the local minimum rather than the global minima. A related pitfall is overfitting [90], where the solution chosen is specific to a particular dataset and thus might be unsuitable when used to predict future observations.

There are many algorithms for both local and global optimisation that can be utilised for material characterisation and Venter G. produced a review that provides a good overview of the subject matter [91]. The two optimisation techniques that are used within this these are interior point optimisation and a genetic algorithm approach.

These two numerical methods are utilised within the work in chapter 3 and due to the fact that they are implemented within the code base of the work presented it will be further explained in section 3.2.6.

2.5. Additive Manufacturing and its use in medical applications

Additive manufacturing (AM) is a fabrication process of taking a model created using CAD and producing physical components that are built layer-by-layer using multiple printing technologies, the most widely used of which is fused deposition modeling (FDM). It is a hugely customisable technology that provides the ability to make bespoke designs in CAD which otherwise would require more complicated manufacturing process or post processing.

There are 7 different types of AM that all vary in complexity, and technique used. These are classified as follows: vat photopolymerisation, material jetting, binder jetting, material extrusion, powder bed fusion, sheet lamination, and directed energy deposition. Many of the above techniques were not considered due to requirement of specialised technology or not utilising the correct material based on the properties required from the produced designs. The technique focused on for this thesis was material extrusion due to the inexpensive nature of the printing device as its ability to produce high quality finishes on prints.

One of the effective aspects of AM is the ability to perform rapid prototyping [92], [93] of components to fine tune the design, removing constraints of other production techniques (cost, manpower, machining). It does, however, come with its own limitations as well such as size limitations and quality assurance or replicability [94], [95]. This can allow the comparison of many different designs without an addition of huge cost. Certain factors such as build time, structural supports, print resolution and material cost do still need to be accounted for in the overall design cost. This can differ between styles of printing, for example, powder bed titanium prints versus FDM with PLA will have vastly different operating costs. Example just in material cost are

for instance, a spool of polylactic acid (PLA) is priced at £27 per kilo [96] compared to between £280 and £480 per kilo for a titanium print.

Due to the nature of how the components are formed, with a flowing filaments, powder sintering, or other techniques, AM has stochastic element to it. This can cause issues in reliability of the reproduction designs and therefore also in quality assurance. This can be limited in its effect with higher resolution printer quality, but this therefore generally then increases cost and can not necessarily material resolution limitations.

AM is a research field that has been growing in interested in the medical industry. This research is due to its potential to provide customisable medical parts as mentioned previous. This is of particular interest due to the evolution of patient specific medical devices which as seen a surge in interest in all fields of medicine [97]–[99]. AM also provides the ability to customise the geometry and mechanical aptitude of designed components through the variation of the CAD parameters. AM has already been used as a tool for this type of treatment in such areas as orthopaedics [97] and cancer treatments [98]. The most common use of it is for medical implants where it has seen success in dental treatments [99] and has also been explored for use in tissues and biomaterials [100]. AM is a technique that is still evolving, with new methods being developed fast allowing for expansion into more fields of medicine.

The form of AM of particular interest to this thesis is material extrusion, which consists of a hard exterior shell, and an interior lattice structure. The process starts by breaking down a CAD model into a series of triangulated coordinated that are read by the printers and allow it to calculate the positions at which to extrude the material in each layer of the design. A computer controlled nozzle then extrudes the material based on

this defined pattern to create the final unit. An example of a print with the initial layer then the same design mid print is seen in Figure 2-14.

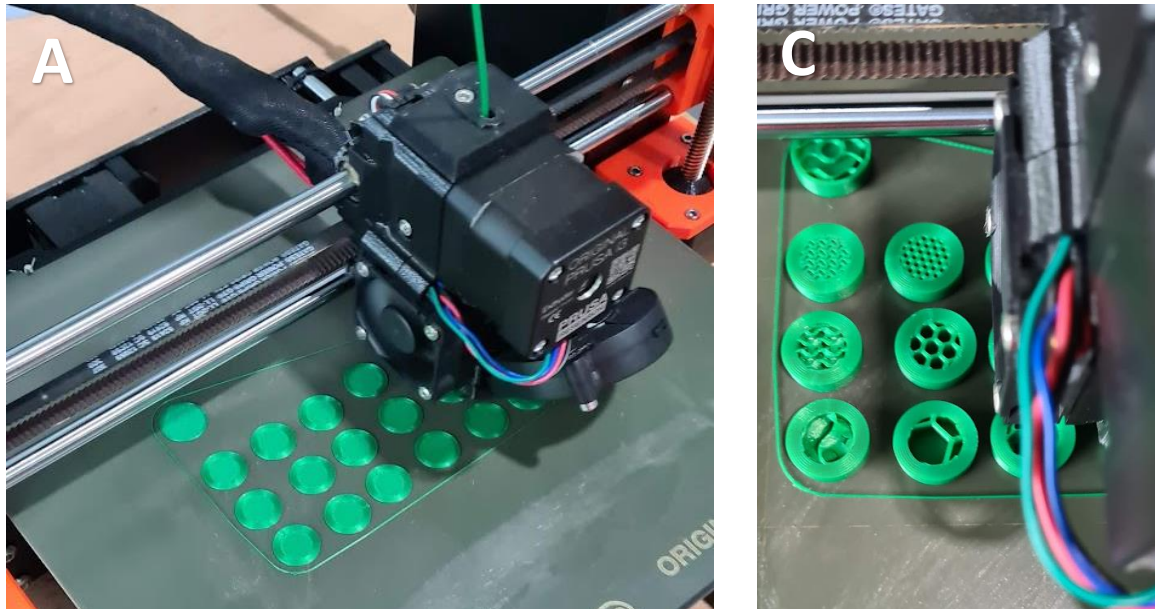


Figure 2-14: A) base layer print application of an extrusion based AM print on a Prusa I3 MK3s (Prusa Research a.s., Czech Republic). B) the same print after layers have been applied demonstrating the replicated CAD model.

Design software and controllable parameters

There are many computational tools available that streamline the design process and have been laid out effectively by Wiberg et al [92]. The two main components to cover within the design process are the CAD model being created and then exported as a Standard Tessellation Language (STL) file format and then the slicing of said file into the G-code required by the 3D printers. The process of creating a CAD model is the stage at which the geometry of the printed component is defined and organised into a 3D computerised object. An example project based on work completed in section 4.2.2 is seen in Figure 2-15. CAD model creation can be done undertaken using software such as Autodesk inventor (Autodesk Inventor. Version 22.0. , CA: Autodesk, San Rafael) or Blender (Blender, Blender Foundation) as examples. Slicing is the other

section of the process for which some printer manufacturers provide their own commercial software such as Prusa Slicer (Prusa Research a.s., Czech Republic) with others opting to allow use of free software such as Slic3r.

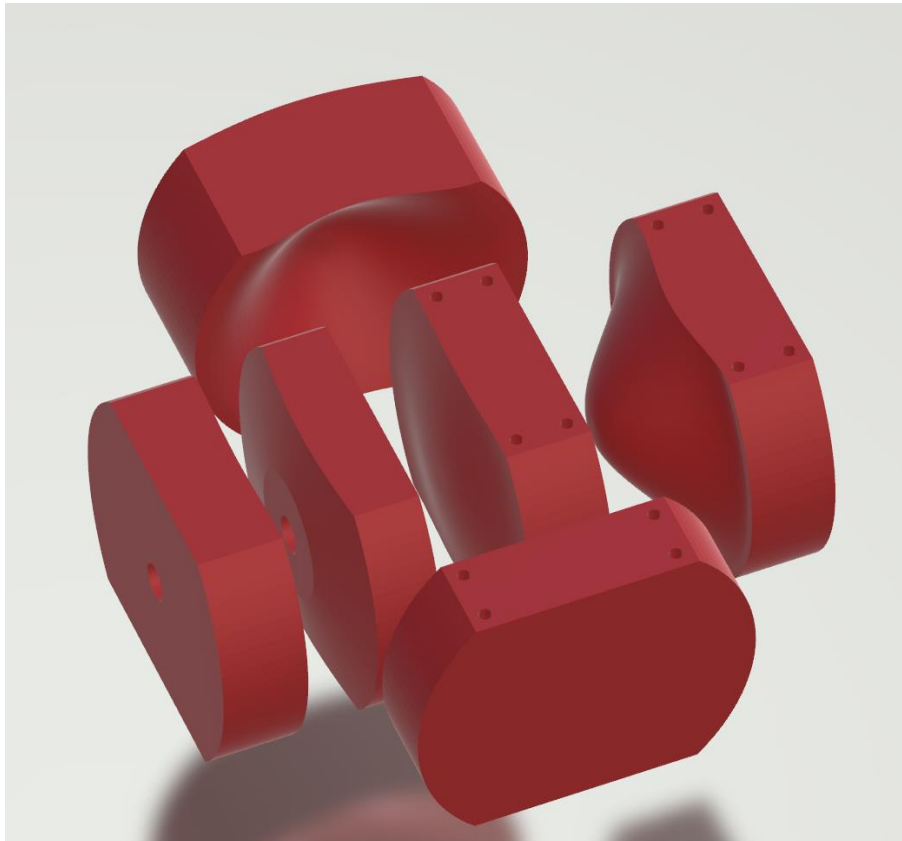


Figure 2-15: CAD model of components designed for work completed within chapter 4, section 4.2.2.

The design of the internal structure of an AM component is called a unit cell and provide a very large portion of the variability seen in printed components after a material is chosen, examples seen in Figure 2-2-16. They are able to provide porous networks, adjustable surface contours and anisotropic or isotropic mechanical response properties. These properties are all very key to the inclusion of AM into the medical field, with each providing different research fields an opportunity for utilisation of the technology. Pores within the unit cells are defined through both the geometry of the shapes used as well as infill percentage. In a medical environment this is of

interest due to this feather seeing use as holding cells for drug delivery[101]–[103], with expansion into promoting bio-integration of printed components utilising growth factor as a catalyst [104]. Surface contour variation provides a large surface area that can be functionalised to improve the bio-integration of any components or for fixation means.

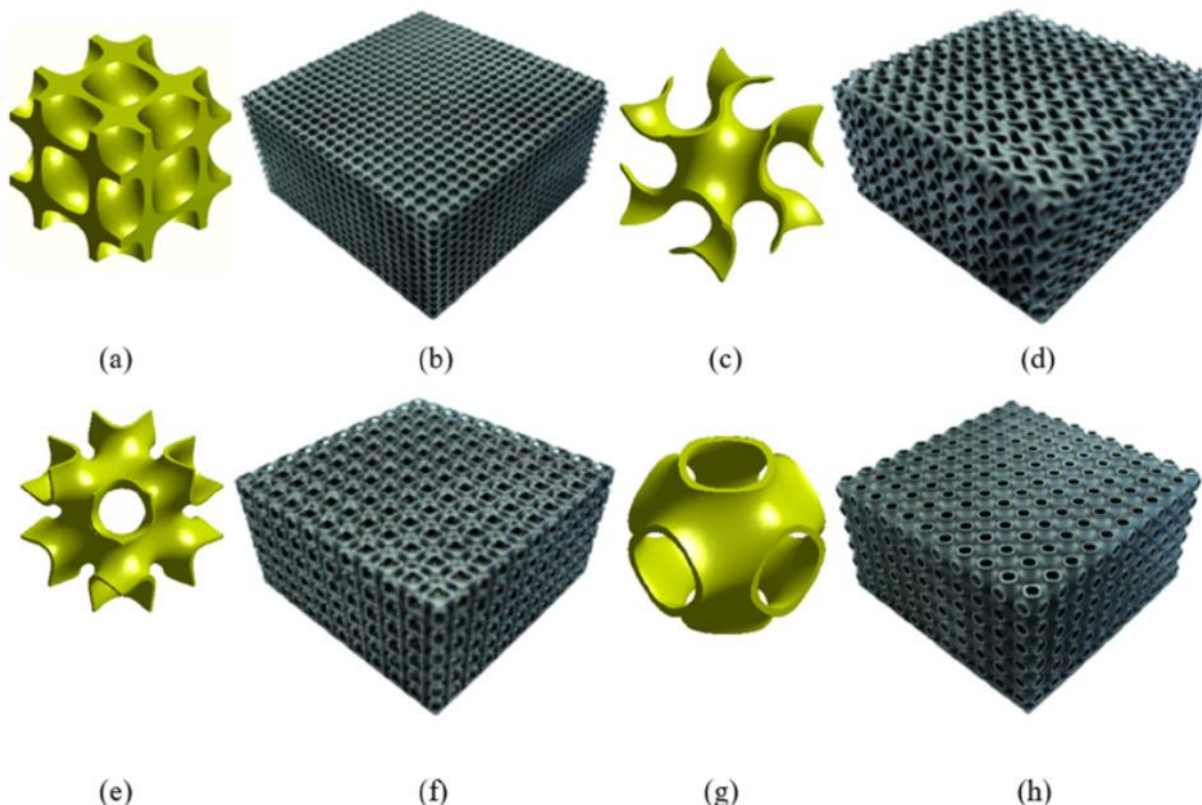


Figure 2-2-16: 'CAD models for unit cells for (a) Diamond (c) Gyroid (e) IWP (g) Primitive; and 3D Printed TPMS lattices for (b) Diamond (d) Gyroid (f) IWP and (h) Primitive.' Caption text and image courtesy of Qureshi et al [215].

The other main parameters that can alter a print are the infill percentage, shell thickness and finally one of the main factors, the material used. The infill percentage controls how densely the unit cell is repeated within a given space. This can be limited by the resolution of the printer that is being used as when the infill is increased the size of each unit cell is decreased thus more accuracy in the print lines is required to gain the same defined structure. The shell thickness is the parameter

that defines the number of layers in the outer wall of the design, this can be varied depending on the structural integrity required but can also change with material and printing technique.

With regards to materials there are many options available. However, the printer technology available to a user will refine the scope of suitable materials. Materials broadly come in three categories, polymers, metals, and others more niche substances. Polymers can be split into soft and hard plastics; soft plastics are those such as polymeric hydrogels [105]–[107] but are not utilised within this study. Hard plastics such as PLA or Polyethylene terephthalate glycol (PETG) both of which are biodegradable, low melting point plastics that are mostly used for at-home and prototype printing [108]–[110]. Metals have been used in the aerospace and medical industries amongst others, however, the earlier mentioned higher cost of material as well as a higher cost of the printer itself, mean that it may not always be suitable for early stages of prototyping.

2.6. Open questions in the literature

When performing material characterisation of AC there are some limitations with current definitions. Some limitations with the biphasic definition of cartilage have been pointed out in more recent studies [24], [111], particularly where the deformation of AC is considered under gait-relevant loads. While some current models have shown it to perform effectively under a state of equilibrium, It has been proposed that the complete separation of the tissue into fluid and solid was one of the deficits of the model[112] as the two components in vivo are mixed at a molecular level[113].

The evolution of biphasic theory, triphasic theory, was also shown to be infeasible due to the fact that it does not fulfil the second law of thermodynamics [17]. Huyghe et al. [17] calculated that as a result of the chemical-expansion term, non-physical free energy was induced during each loading cycle and the value of this energy was estimated to be 20% of the elastic energy stored within the tissue. Therefore, while this model is appealing in terms of including a term for ionic transfer, it would appear to be thermodynamically unreliable.

DMA provides a non-static equilibrium based testing technique to evaluate cartilage and provide dynamic material characteristics of the tissue. The combination of DMA with FEA may be able to provide the ability to model cartilage more accurately. Aim 1 of this thesis investigates this possibility by producing a framework for frequency to time modelling of this hyper-visco material under non-equilibrium conditions.

Testing cartilage at a physiological range of loads [24], [30], [66] has produced results that show that as frequency of load increases the ability of cartilage to store energy also increases. This also highlighted the possibility that cartilage has a higher likelihood of failure with an increased loading frequency. This was suggested to be

different to damage caused to AC through an increased load when applied during static tests [114], [115]. To aid the understanding of cartilage's material response variations, experimenting with how macro and micro scale parameters effect these values could highlight qualities of the tissue that warrant further evaluation.

It has been shown that both the mechanical properties [116], [117] and thickness [30], [118] of knee cartilage vary with its location within the joint space and load dependent [118]. However, the mechanical analysis conducted in these studies perpendicularly applied loads to the tissue samples on top of a flat testing platen, which does not replicate the native joint curvature. There has been a study performed on full rabbit tibial joints, however, this load application is not particularly controlled to specific regional analysis [58]. From this, a hypothesis was formed to test for macro scale variations, can AM be used to develop more customisable test beds (larger scale) & can these results be informative RE: AC mechanics?

The micro scale parameters of cartilage are of interest in the medical field due to them seeing use as holding cells for drug delivery [101]–[103], with expansion into promoting bio-integration of printed components utilising growth factor as a catalyst [104]. Specifically relevant to the aim of chapter 5 is the potential for promoting ossification in osteochondral implants [14], [119]. Current implant options using AM do not necessarily try to mimic the mechanical properties of the tissue around them, this is important to consider because bone degrades when not loaded correctly [120], [121] as might occur during stress shielding. Therefore a hypothesis was set forward as: Can unit cells be exploited to 'design hierarchical' osteochondral units which functionally 'match' healthy AC-on-bone?

2.7. Chapter summary

Articular cartilage is a complicated tissue structure that provides covering of any synovial joint epiphysis. AC mechanical properties have been linked to the tissue below it, the subchondral bone, and the interaction of the constituent parts of the osteochondral core. Dynamic loading and analysis have been used more recently within literature to gather the material properties of AC using frequencies up to 92 Hz. There are multiple mechanical response models of cartilage each with their own limitations reported in literature whether it be in the simplification of the tissue characteristics or accuracy at physiological loading ranges. This condition of testing at a representative physiological load is what allows the models to be relevant for translational use to AM research for the medical industry. The use of additive manufacturing in medical implants has seen success in other medical fields but has not yet been utilised to replicate osteochondral cores.

The work in thesis will focus on advancing the accuracy and complexity of the material models produced to represent osteochondral tissue to those discussed in literature. Literature reviews of currently available studies will be evaluated in each chapter individually. Human and bovine data will be used to perform optimisation of a Prony series at biologically representative loads. To provide additional understanding that is currently missing or incomplete in literature of how cartilage and bone are loaded in vitro and how this should be translated into the geometric models that are produced, new experimental loading situations will be designed and evaluated. Novelty to literature will be provided through new experimental testing procedures and mechanical simulations of biologically representative loading situations associated with cartilage in-vitro mechanics.

Chapter 3. AUTOMATED NUMERICAL MODELLING SYSTEM FOR

THE OPTIMISATION OF HYPER-VISCOELASTIC MATERIAL

PARAMETERS

3.1. Introduction

Numerical methods have been used in various areas of study, for example modelling the musculoskeletal system (MSK) [122], [123] as well as in fluid-structure interaction scenarios [124] amongst others [125]. Due to the complexity of biological systems, many need to be represented at multiple scales, with some studies able to demonstrate the accuracy of the simulations [126]–[128]. These advanced models must not only represent the geometric structure but also its mechanical properties [129] leading to the inclusion of mathematical approximations. This requirement, however, leads to issues with the validation of the output from these types of models; they are used as surrogates for experimental work, but their accuracy must be assured [84].

Sample variability, model robustness, validation-bias and a physiologically representative situation are all factors that need to be accounted for in determining the accuracy of a biological tissue material approximation. A common issue seen in biomechanical research is the low number of unique and independent samples utilised, resulting in a limited representation of the possible biological states when modelling tissues. There is a requirement for a large amount of experimental data in modelling systems [83] with many of them utilising optimisation techniques to develop their material parameters [130]. Less common, but equally necessary, is the need for separate training, testing and validation datasets to ensure robust validation

of any optimisation techniques used; other techniques such as cross validation [131] can be used but this has an even higher data requirement to be effective.

Optimisation is not limited to biomechanical models, with previous applications in fields as diverse as civil engineering structure design [59]. Commercial software that allows optimisation is available, such as the Abaqus topology optimisation module (ATOM) [132] that focuses on structural optimisation; however, these packages often lack the ability to provide complete user-controlled interaction. Other systems provide inbuilt material solving tools that utilise user inputted experimental data (SOLIDWORKS, 2018); however, these are finite solutions and do not allow for model iterations. FEA needs data in a time domain for the range of tests typically conducted (e.g. Abaqus can use E' and E'' but only for things such as modal analysis in a frequency domain data). There are few good methods to 'translate' between the two and this is needed to enable valuable DMA data to be available for FEA modelling more widely.

Optimisation has been utilised to support FEA research before with its application being most effective in the field of material engineering. Kang et al. [133] used mechanical testing data obtained through indentation testing alongside simulation data to optimise the elastic-plastic mechanical properties using a least-squares algorithm. The output FEA load-displacement curves were used as the input data for the optimisation process. A similar approach was taken by Soe et al [134] but with virtual prototyping being to aid the material property definition and a simpler curve fitting process used to optimise their material characterisation. Other examples of optimisation of material properties are seen which utilise FEA either in data collection [135] or in a combinatorial approach [136] A review done by Mulenga et al. [137] highlighted how the combination of these fields have been used in natural fibre

analysis. A limitation of some of the mentioned studies is the separation of the FEA and optimisation procedures. Gentils et al. [136] produced an integrated system for a design optimisation of multicriteria solution however this type of procedure has not been implemented for a non-specialised system, and not yet in the field of biomechanics. The ability of FEA to allow the analysis and checking of material parameters over complex geometries [136], [138] can provide a valuable tool to use a feasibility check on potential material solutions.

The aim of this work presented in this chapter, was to develop an automated process for the generation and analysis of the material properties to fit a given experimental condition, in our case mimicking human AC tissue under physiological loading. It would involve two main components: the automation of the modelling process including creation of the FEA simulation, solving and evaluation; and the development of an algorithm to produce potential material property parameters utilising mathematical optimisation. Experimental data is gathered through compression testing to be used to provide an input for our algorithms and a way to validate the models produced upon each iteration of the automation. It was important that the first component had a low coding knowledge requirement to provide the most accessible system. This would allow it to be transferred for use in other applicable simulations with only minor adjustments to the code base [139]. This enforced the use of abstraction throughout the design of the system, however, the problem specific nature of the second component grounds the development in a real application to a biomaterial. One of the intricacies of the work will be to allow the analysis of the models themselves to define how the parameters are altered on each sequential generation that is created. Similarly, being able to do this autonomously not only reduces the amount of human interaction and/or bias in the establishment of

the fitness of a solution but also will keep it consistent across all models and generations.

The case study of this chapter, and thesis, focuses on Articular Cartilage (AC). It is a particularly pertinent example of a soft connective tissue as the range in the measured material properties varies across 4, if not 5 orders of magnitude according to the experimental method of testing used [140]. Studies such as those by Lawless et al. [29] and Sadeghi et al. [24] exemplify the extent to which the material properties of AC are dependent on loading conditions, particularly physiological stress, and within a frequency domain. There is clear scope for robust optimisation via the use of automated systems for evaluating the mechanical properties of such an unusual material, in the case of human AC this refers to physiological relevance and comparison to appropriate experimental data.

3.2. Methods

3.2.1. Experimental Testing

The initial data set was generated through experimental in a study by Mountcastle et al.[18] , that I co-authored , where human AC specimens were tested. In total, 5 femoral heads were used with 16 unique test samples harvested as seen in Figure 3-1. The femoral heads were donated by patients who had undergone surgery following fracture of the femoral neck. Ethical approval for this study was provided by the United Kingdom National Research Ethics Service (East of Scotland Research Ethics Service; 11/ES/1044) and consent for the use of their tissue for research was given by the patients.

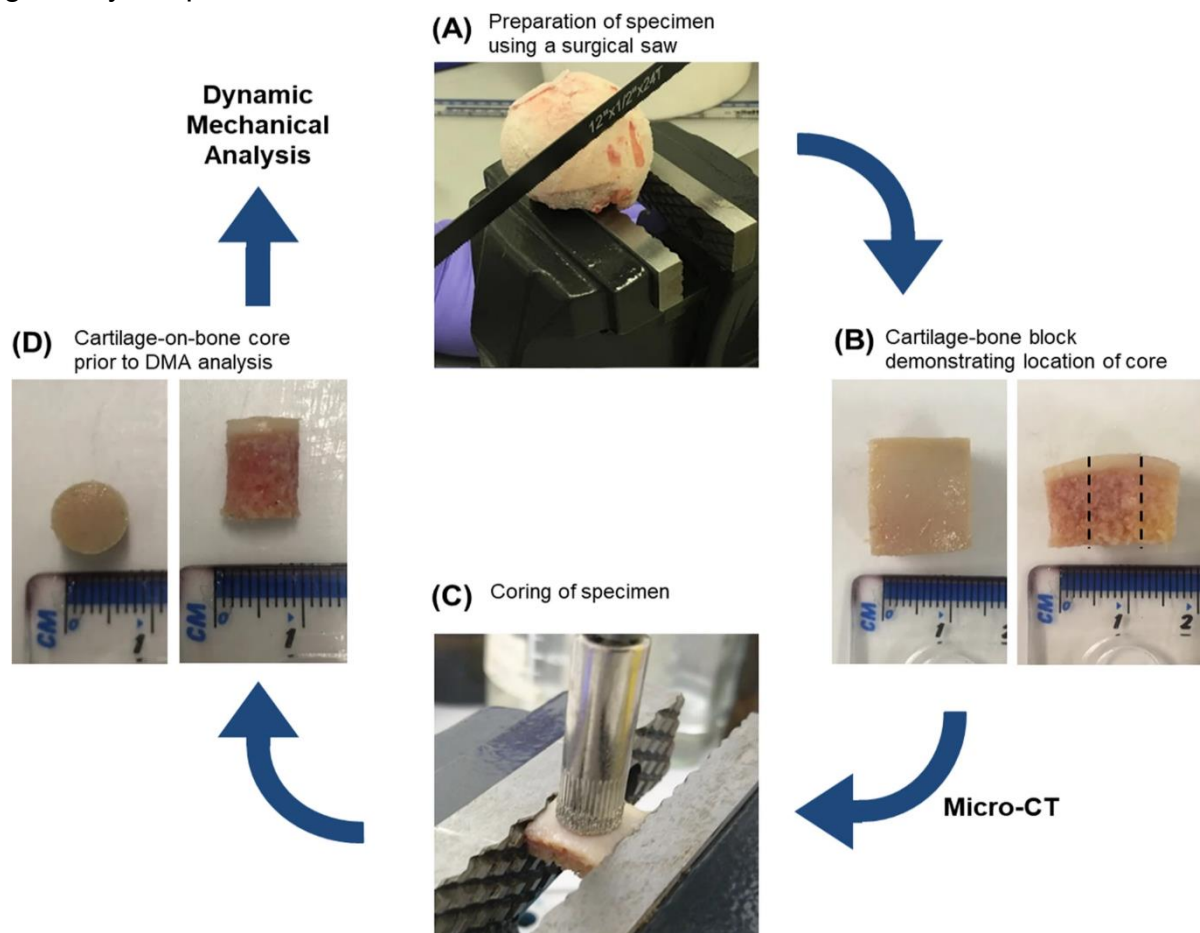


Figure 3-1: Produced by Mountcastle et al 2019 / CC BY-NC-SA 4.0. “Flow diagram illustrating femoral head specimen preparation and coring: a Preparation of specimen using a surgical saw, b Example of cartilage-bone block prior to μ -CT analysis demonstrating where core was taken, c Coring of specimen, and d Example of cartilage-bone core prior to DMA” [37].

Femoral heads were stored at -80°C until 24 hours before testing at which point, they were defrosted in Ringer's solution that has been shown to not affect the viscoelastic properties of the samples [141]. Each sample consisted of an 8 mm cartilage on bone core extracted using a diamond drill bit with the cartilage then being separated using a medical scalpel [29], [142]. This procedure was presented in full by Mountcastle et al [18].

Experimental tests were performed by a Bose ElectroForce 3200 testing machine, controlled using WinTest 4.1 Dynamic Mechanical Analysis (DMA) software (Bose Corporation, Minnesota, USA; now, TA Instruments, New Castle, DE, USA). Two separate loading sequences were performed, a quasi-static ramp compression and Dynamic Mechanical Analysis (DMA). For the first test, a preload of 0.02 N followed by a quasi-static ramp test at a load rate of 3 N/s, to a maximum load of 61.6 N was applied. The subsequent test applied preconditioning loading cycles at 24 Hz and 49 Hz for 1500 and 3000 cycles respectively [143] as it has been shown that AC requires over 1200 [68] and over 2000 [144] cycles to reach a 'dynamic steady state' of the specimens. This was followed by a frequency sweep test at 1, 8, 10, 12, 29, 49, 71 and 88 Hz, which was representative of observed physiological loading rates [143]. These two mechanical tests provided the data set used in the algorithms discussed in 3.6.1 and 3.6.2.

Output data from the mechanical tests was analysed through a Fourier analysis technique previously described by Lawless 2018 [145], seen in section 2.3. In brief, the viscoelastic material was characterised by its complex stiffness (k^*) using the magnitudes of the two main control channels from the DMA (Load & Displacement) after it has the application of a Fast Fourier transform, for each frequency. Using the shape factor (S_F) of the tested specimen's geometry the complex modulus (k^*) can

be computed and then split into the required storage (E') and loss moduli (E'') using the phase lag (δ) between the load and displacement sinusoidal waveforms (Eq. 3.1, Eq. 3.2).

$$E' = \frac{k^* \cos(\delta)}{S_F} \quad (3.1)$$

$$E'' = \frac{k^* \sin(\delta)}{S_F} \quad (3.2)$$

3.2.2. Automated modelling system structure

This is the main portion of the developed code that controls the automation procedure. Two cyclic control structures were developed to work together to allow integration of the optimisation with the modelling software and provide a meaningful output. The two main system components within the main control script are a Python control node and an optimisation control node. All portions of the modelling procedure performed are controlled through the Python node apart from the output analysis which is performed in Matlab (The MathWorks Inc., Natick, Massachusetts, USA). The optimisation of the material parameters is completed in a separate Matlab script. This relationship and the interaction seen is in Figure 3-2. Both nodes are briefly described below with more detail given in sections 3.2.5 (Python node) and 3.2.6 (Matlab node). Before the cycle starts an initial optimisation takes place to create the first parameter set. This is to avoid starting blind and to ensure that some of the initial model set can be solved which is a requirement for the model driven optimisation.

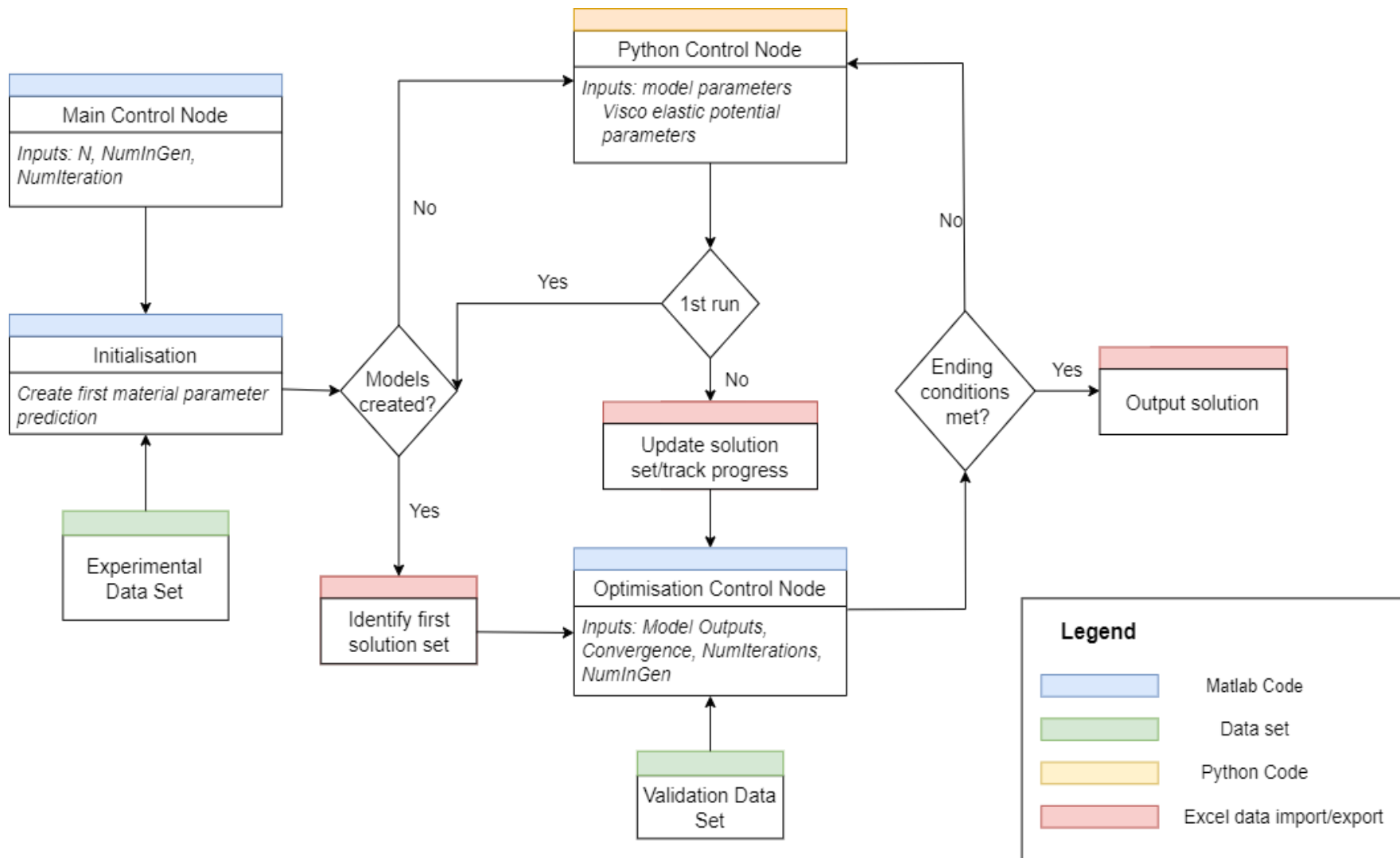


Figure 3-2: Flow chart representation of the control structure for the automation system, with boxes representing code/data and diamonds representing questions the systems will ask through its iterations.

The total data set used has 168 unique data tuples made up of frequency, storage modulus and loss modulus. The frequency values range from 1 to 90 Hz and the storage and loss modulus are of the order of MPa. This data set is split into a training and validation data set of 128 and 40 data points, respectively. This is split randomly on each run of the simulation with mitigations in place to ensure an imbalance of frequency representation is not seen in either data set which could produce bias in the simulations.

This first optimisation is performed using an interior point technique on a partial data set separate from the validation set used within the optimisation node. The overall control system is written in a Matlab script that requires three user inputs (excluding predefined variables defined below): 'N', the degree of the approximation; 'NumIteration', the maximum number of generations the optimisation will complete; and 'NumInGen', the number of models generated per generation. The value for 'NumInGen' has a limit of a minimum of 100 due the requirement of the system to have several models to compare for each generation. Although there is no requirement on the number of generations, the outcome of the solutions is highly sensitive to the number chosen. A limiting factor of this system is the time complexity, which is controlled by the 3 variables above, thus choosing suitable values will impact on the time taken to generate a solution.

The Python control node is self-contained and modular, thus, the code for it does not change for each iteration, only the required inputs are altered. The models are created from a defined set of parameters (provided by the optimisation control node) and then sequentially solved for each combination, providing a range of models to be analysed for efficacy. The lack of required deviations in the code allows for seamless running without the need for user input at this stage. Displacement values are

extracted from the solved jobs and passed through to a Matlab analyser script that compares them to the experimental validation set, allowing the models to control the progression of the material parameter development. This is performed within the optimisation node. After every generation of models, they are stored in back up to track property progression as well as for future investigation of specific models.

In the optimisation node, initially the model outputs are sorted and compared to an evaluation data set that is comprised of three separate displacement profiles representing the ramp test, and then the load and unloading during the sinusoidal sequence. It is then checked to establish whether the ending conditions have been satisfied which could be a number of factors such as: maximum cycles, minimal error, no error change. If they have not, the optimal solutions are then taken and passed into the optimisation module.

A genetic algorithm is used to progress the development of the parameters during optimisation. The mutator utilises cross-over, Gaussian distribution alteration and random mutation to create many possible parameter compositions. These are evaluated against a viability check and then the defined number of models (NumInGen) are passed back to the Python control sequence. The next generation of models created are a combination of the top results from the previous, outputs from the mutator and random possibilities. The inclusion of random values into the parameter data set allows for the algorithm to not be limited to a global minimum.

All Code is proprietary and thus is available only on requested access currently on the GitHub repository: <https://github.com/piers-ch-allen/Automated-Modelling-System>.

3.2.3. Abaqus Modelling

All FEA has been performed using ABAQUS 6.14 (Dassault Systèmes Simulia Corp., Providence, RI, USA), the inbuilt functionality of Python script macros provides the control level required. AC was modelled as a cross-sectional segment of the cylindrical test samples with dimensions matching the sample cores that were tested experimentally. The geometry is set to 8 mm in length (mean), and 1.5 mm in height taken from sample thickness data. The simplification from a cylinder to a cross-sectional segment was deemed appropriate due to the displacement of the sample tissue being negligible in the axis perpendicular to loading (x , and z for this set up). Three options of mesh were defined at 100 μm , 150 μm and 200 μm , providing mesh sizes between 200 – 800 elements to test variation in error amongst mesh conditions. To mimic physical testing two boundary conditions are applied to the model. The base was completely restricted in displacement and rotation, and the top was restricted to only move along the y axis, which has been defined as being perpendicular to the surface of AC test samples and aligned with the direction of load ($-y$ axis). A single FEA rendering of one model output is seen in Figure 3-3. These models are used as input files for the purpose of the automation.

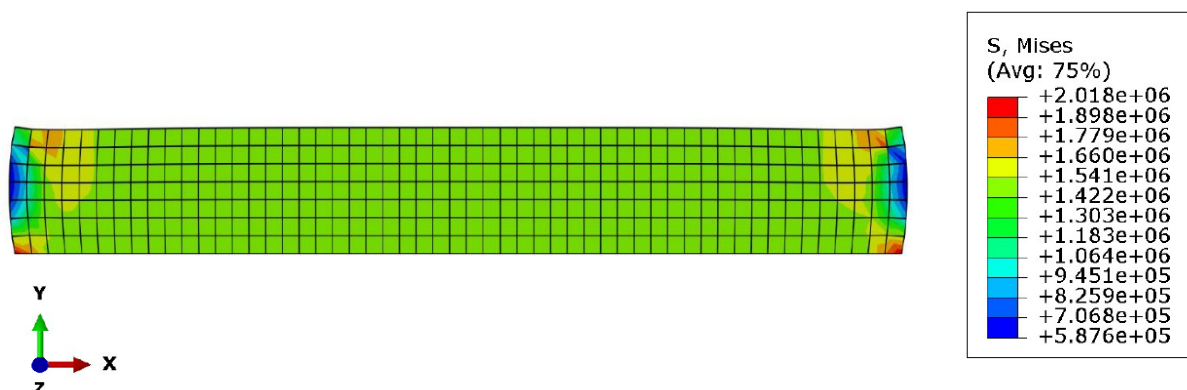


Figure 3-3: FEA model of the 2D cross-sectional geometry of the cylindrical sample under the final load applied. The load is applied to the top surface up to a maximal value of 1.7MPa. The induced von Mises stress defined in the legend.

The models that are being used as seen in Figure 3-3 are currently used to provide a simplistic demonstration of the process of the larger system working. Even though FEA is not necessarily required for a 2D construct as described it checks that the material properties are valid numerically for our situation. When the geometric figures are altered to match the biological topography of the tissues that are being evaluated FEA will play a much larger role in the production of the output parameters as the maths behind will be too complicated to evaluate by hand.

For every possible combination of material properties proposed, an individual model was created and solved with the above definitions, however, staying constant to focus the variability analysis on the parameters of the material definition. For each iteration during the optimisation 1000 viscoelastic potential parameter solutions were created alongside a fixed singular Ogden solution so the total number of models on each iteration was 1000. However, if Ogden optimisation was also included in the parameter variation this would be increased by a factor of how many Ogden solutions were created on each iteration.

For each simulation a uniform load was applied across the top surface of the geometry of 0-1.7 MPa to mimic the experimental testing performed. This was applied in two sequential stages lasting for 1 s. The first section performed a simulated ramp compression step loading from 0 to 1.225 MPa, mimicking the mean induced stress, as a load is initially applied during the ramp test performed *ex vivo in section 3.2.1*. The second portion of the sequence performed a sinusoidal loading step calculated via a time dependent loading conditional (a), frequency of loading (ω), initial step time (t_0) and current step time (t) (Eq.3.3):

$$a = 1.225 + 0.493 \cdot \cos(2 \cdot \pi \cdot \omega \cdot (t - t_0)) \quad (3.3)$$

This amplitude produced a representative 1 Hz sinusoidal stress of 0.7 to 1.7 MPa which is representative of values observed physiologically [146]. Loading was applied uniaxially to the top face of the beam with the displacement of the beam measured in the same axis being recorded.

3.2.4. Material approximations

To simulate AC computationally, a visco-hyper-elastic approximation was used in Abaqus, multiple material definitions were required. A visco-hyper-elastic representation was deemed appropriate due to a Poisson's ratio, hyperelastic and viscoelastic approximation all being utilised to represent the overall material behaviour. The Poisson's ratio was taken to be 0.45 for all produced models, as reported by Bell et al. [32]. The Ogden model [55] was chosen for the hyperelastic approximation as it was demonstrated by Mellors et al. to be a suitable predictor of AC under physiological loading conditions in comparison with other hyperelastic approximations. The strain-energy potential function is defined in equation 3.4, where N is the order of the model, μ_i is a shear term, α_i is a dimensionless material constant and λ_i are principal stretch values evaluated automatically by Abaqus from the experimental data inputted. The second term of equation 3.4 is omitted as it set to 0 in our calculations, which is a good approximation for natural tissues.

$$U = \sum_{i=1}^N \frac{2 \cdot \mu_i}{\alpha_i^2} (\lambda_1^{\alpha_i} + \lambda_2^{\alpha_i} + \lambda_3^{\alpha_i} - 3) \quad (3.4)$$

The values used for the Ogden approximation in our model were taken from a separate study (Mellors B. et al. (under review and co-author of study). They were one of the sets of values introduced in the data start file described in section 3.2.5

and although not varied in this study, the ability to do so is built into the system. The ability to implement other hyperelastic approximations would require minor alterations to the Python data import file.

3.2.4.1. Viscoelastic Material Approximation

The generalised Maxwell model was used here which combines a singular main elastic branch with N spring-dashpot branches. The time-domain viscoelastic response of a tissue can be expressed therefore by the Prony series as explained in section 2.3.3. using this generalised equation the relaxation modulus $\mu(t)$ can be expressed as a discrete set of exponential decays [147] and then, using this, the complex modulus u^* is defined in equation 3.6:

$$u^*(j\omega) = G_\infty + \sum_{i=1}^N g_i \frac{t_i' j\omega}{1 + t_i' j\omega} \quad (3.6)$$

where ω is the angular frequency, and $j = \sqrt{-1}$. This expression is derived as the Laplace form of the equation 3.5. Thus, the Prony series representations of storage and loss modulus in terms of frequency can be defined as equation 3.7 and 3.8 respectively:

$$u'(\omega) = G_\infty + \sum_{k=1}^N g_k \cdot \frac{(\omega\tau_k)^2}{1 + (\omega\tau_k)^2} \quad (3.7)$$

$$u''(\omega) = \sum_{k=1}^N g_k \cdot \frac{(\omega\tau_k)}{1 + (\omega\tau_k)^2} \quad (3.8)$$

Utilising equations 3.7 & 3.8 and parameters for the measured dynamic modulus, u'_i, u''_i at a given frequency ω_i with $u'(\omega_i)$ & $u''(\omega_i)$ being the respective predicted

values a minimisation equation utilising the original generalised Maxwell model can be produced shown in equation 3.9:

$$\min_{\mathbf{g}, \mathbf{t} \in \mathbb{R}^N} F(\mathbf{g}, \mathbf{\tau}) = \sum_{i=1}^N \left(\left(\frac{u'(\omega_i)}{u'_i} - 1 \right)^2 + \left(\frac{G''(\omega_i)}{G''_i} - 1 \right)^2 \right) \quad (3.9)$$

This optimisation problem solves for so-called Prony parameters $(\mathbf{g}, \mathbf{G}_\infty, N, \tau_k)$ so that they simultaneously satisfy experimentally generated storage and loss modulus calculation from DMA tests where $\mathbf{g} = (g_1, \dots, g_N)$ and $\mathbf{\tau} = (\tau_1, \dots, \tau_N)$ for the defined N . These are the parameters that will be manipulated within the multiple models runs in the optimisation.

Prony series have widely been used for viscoelastic material characterisation to analyse the stress and strain within tissue structures [147]. It also has the advantage that it can be defined through experimental data entry or, coefficient representation within Abaqus, our chosen modelling software. The later was chosen to provide additional control and avoid the use of 'black box' systems. The parameters were determined using a two-stage optimisation process within the overall system explained in section 2.6. The following principles were required to be considered during parameter evaluation to ensure they would allow the model to solve effectively. They enforce that sequential time values τ_i are always increasing in value and that the summation of all the equilibrium shear modulus values summate to less than 1, a restriction imposed by Abaqus as defined in equations 3.10, 3.11 and 3.12.

$$\tau_i \leq \tau_{i+1} \quad \forall i \quad (3.10)$$

$$\forall k \sum_{k=1}^N g_k \leq 1, \text{ and } 0 < g_k < 1 \quad (3.11, 3.12)$$

3.2.5. Python Control Structure

All sections of the Python scripts were hierarchically designed for the possibility of future integration of more modelling components as well as providing an ease of understanding the pathway through the system. As there was an expectation to be running FEA models thousands of times (through Abaqus) during a single system run, it was necessary to ensure that the computational load of the design and solving procedure was minimal. To do this effectively, all the design values were predetermined and organised before Abaqus was initialised. Then for each iteration of the automation, one instance of Abaqus was run that sequentially creates and then solves all defined models.

Inputs into the control sequence were defined through two Excel documents controlling the model parameters that are common to all models and then a secondary document that contains the material parameter definition. For the first spreadsheet, an example input for common values is seen in Table 3.1. This defines all the parameters that control the model construction and are unique to the individual overall model being simulated. Only constant variables that are not being altered are inputted into this spreadsheet. However, it can be expanded to include multiple mesh and loading situations so that every iteration is tested for each defined value, but these cannot be applied selectively; thus, all models must be able to be tested under all defined conditions. Also included in this file are the values for the hyperelastic material coefficients as seen in Table 3.2. In this example only one selection of coefficients is supplied, however, akin to loads/meshes, multiple sets of coefficients may be provided, and all combinations of simulations will be produced, with one caveat, that all approximations must be of the same degree of complexity. This means that there must be the same number of material parameter values for

each coefficient set, in this case six points, as a third order model is utilised with α_i and μ_i referring to values in equation 3.4.

Table 3.1: Example required used defined parameters that are global variables to all the models produced. The dimension values all determine the geometric structure of the object undergoing compression.

Dimension Values							
Grid SpaceX1	Grid SpaceX2	XOrigin	Max Width	Grid SpaceY1	Grid SpaceY2	YOrigin	Max Height
0	0.008	0.004	80	0	1e-03	5e-04	80
Loading/Material/Meshing Values							
Elastic Modulus		Poisson Ratio		Load Magnitude (Pa)		Mesh Density	
1e+09		0.45		1255000		1.5e-04	

Table 3.2: Ogden material approximation parameter set used.

μ_1 (Pa)	α_1	μ_2 (Pa)	α_2	μ_3 (Pa)	α_3
-26133000	2.7190	12922000	3.9960	13227000	1.504

The secondary file stores the current iteration of the Prony coefficients that are being tested. These are updated on each iteration and can contain anywhere from 10 to 500 possible combinations depending on the limitations placed by the user on the algorithm. This is an auto-generated file that holds the current sets of coefficients defining the Prony-series being evaluated in the given generation. However, each variation of the file is backed up so that backtracking and analysis of previous solutions is possible. Implementing this was important during the development process of the generation mutators because it allowed analysis of how much or little variation was being produced in the possible solution set. This was also useful in checking how the variables varied across generations and whether specific values held the most or least variation amongst the top solutions and is seen occurring in Figure 3-4.

The spreadsheets are converted to Python variables upon every iteration of new values and then passed into the main class of the Python script. The Excel spreadsheets are converted using a Matlab functionality called ‘fprintf’ which allows direct text to be written in a notepad format. Once converted to notepad the file can be read in by the Python script as a variable file if formatted correctly. It was designed this way to remove the need for the Python workflow to convert file types during the running of Abaqus scripts. This process could be implemented with other FEA software that has scripted access to input files, however, the interfacing scripts would need some reworking. The process for the evaluation and creation of models is defined in Table 3.3 alongside a class diagram depicting its relational schema in Figure 3-4.

Table 3.3: Model creation and retrieval of results as performed in Python's interaction with Abaqus.

Creation of the generation's models
1. Reading in of required variables (2 Excel spreadsheets)
2. Set limitations on number of models to be created based on number of variations in the variables.
3. Create new blank model and job for each combination of variables.
4. Loop through combinations defining model values (loads/material coefficients/meshes etc) based on variations.
Solving and Results collating
1. Model database saved for tracking progress
2. Individual jobs looped through and solved. <ul style="list-style-type: none"> a. Nodal results for displacement and load magnitude saved. b. Results collated into correct folders alongside other tracking information: model database for current generation, variables file, all combinations of variables.
3. Abaqus module closed as analysis occurs within Matlab and to reduce computational usage.

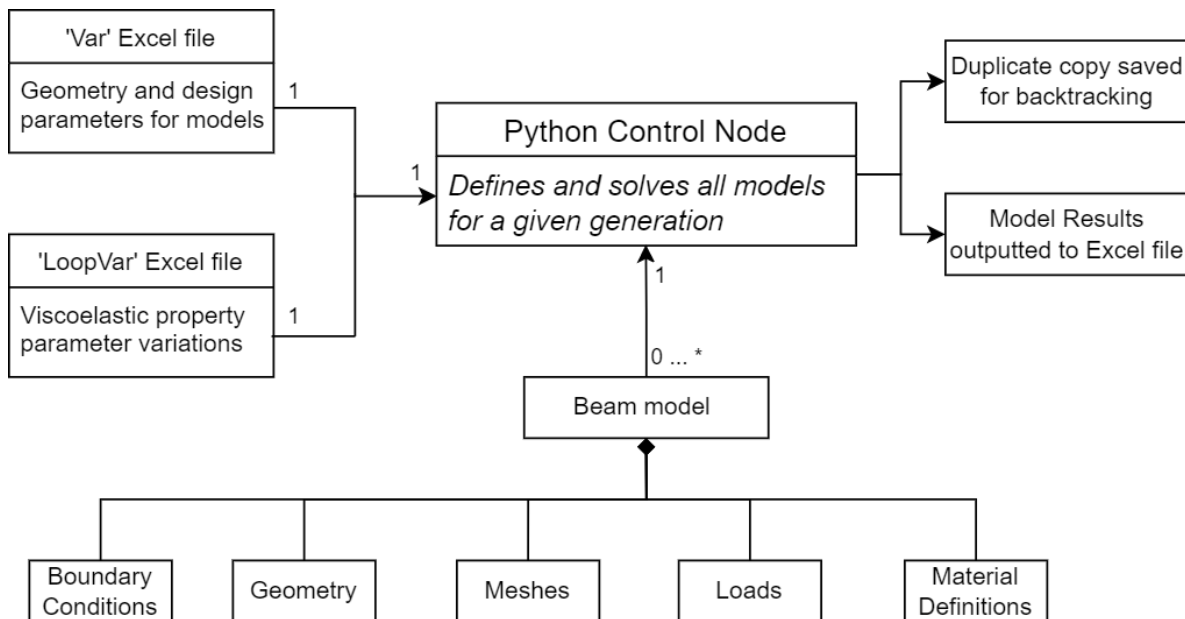


Figure 3-4: Python control node class diagram. The bottom set of boxes represent the different portions of the model creation system that are currently implemented. This can be increased with any other requirements.

3.2.6. Matlab Optimisation Control Sequence

There is a distinct cycle that happens on every iteration of the algorithm which is depicted in the flow diagram (Figure 3-2). The main components of which are: model evaluation and optimal solution identification, data set permutation, genetic mutation, evaluations for model creation, send to modelling node, and restart. Each step is defined in more detail below.

3.2.6.1. Initial Optimisation (Interior Point)

To generate an initial starting point for the genetic algorithm, an interior point optimisation technique is used. Its approach to the optimisation problem is to solve sequential, approximate minimisation problems. Mathematically, if the original minimisation problem is defined in equation 3.13, the approximate solutions are defined as equation 3.14 which has the introduction of as many slack variables s_i as there are inequality constraints $g(x)$. The aim being that as μ trends to 0 so does

the result of $f(x)$. This also includes the addition of a logarithmic term called a barrier function, which provides constraint on the steps taken on the central path of the solution in each approximation.

$$\min_x f(x) \text{ st: } h(x) = 0 \text{ and } g(x) \leq 0 \quad (3.13)$$

$$\forall \mu > 0, \min_{x,s} f_\mu(x,s) = \min_{x,s} f(x) - \mu \sum_i \ln(s_i), \text{ st: } s \geq 0, \\ h(x) = 0 \text{ and } g(x) + s = 0 \quad (3.14)$$

More detail on how interior point optimisation calculates the solution can be found here [148]. To utilise this in practice the ‘fmincon’ tool provided in the optimisation toolbox of Matlab was used in this application, a tool for solving constrained nonlinear multivariable functions. The limits, h , and g were set to the Prony limits previously discussed in equations 3.11 and 3.12. A random seed, defined by the computer time, is used to define the initialisation point of the algorithm with 100 iterations performed to get a range of solutions from unique starting points. The solution set from this first step is what provides the automatic loop with its initial parameter starting point.

3.2.6.2. Main Optimisation Sequence Overview (Genetic Algorithm)

Genetic algorithms are part of a set of algorithms branded as nature-inspired optimisation techniques. This means that they aim to mimic processes that occur in biological lifeforms and in this case are based on the idea of natural selection. The main components of any genetic algorithm are the genetic operators and the fitness check. What is slightly different about this algorithm is that there are two fitness checks that occur to develop the parameter solution. One is based on calculating the error produced by the Prony series equation and the other utilises the model

output and compares that directly to the experimental data set, these are explained further in section 3.2.6.4 and 3.2.6.5. This allows a larger population to be created without hindering the overall efficiency of the system. The cycle of an individual iteration is seen in Figure 3-5.

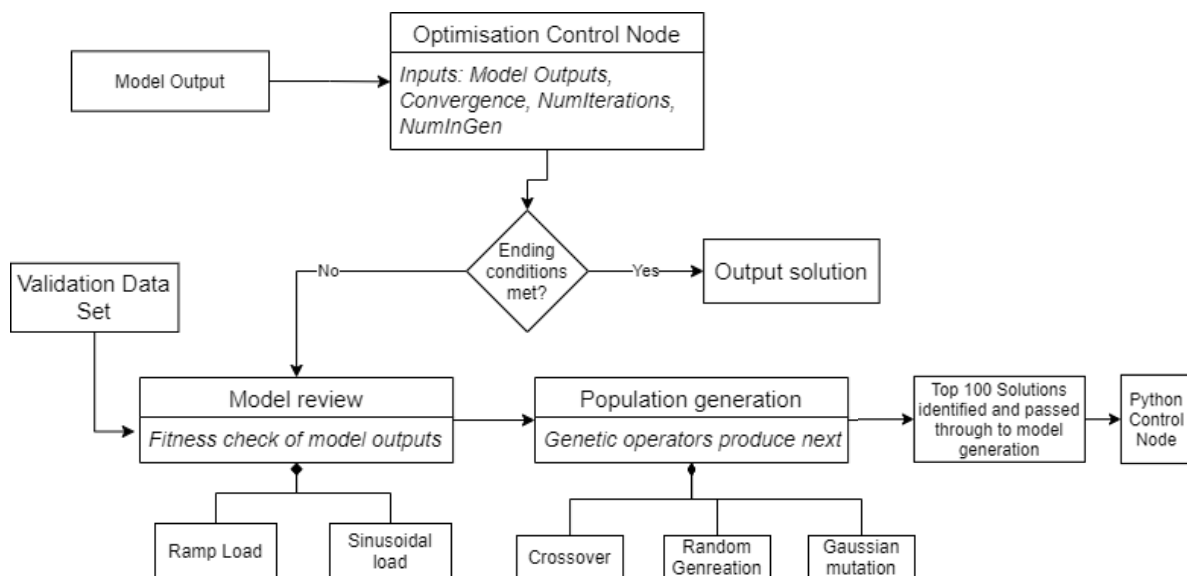


Figure 3-5: Optimisation sequence control structure flow diagram representation.

3.2.6.3. Genetic operators

Upon each generation the new population is created using several genetic operators which are crossover, Gaussian mutation, and random generation, with each of them producing a third of the new generation. The population amount is defined in the code as 'numinpopulation' but is not controllable by the user defined variables. Due to the limits required by the solution (equation 3.11 and 3.12) all children created are checked for validity, this ensures the time values are all sequential and the g values all sum to 1.

Crossover

Both single and K-point crossovers are performed with a 50:50 split of population production. Single point crossover is performed by producing a uniformly distributed random number between one and the length of the solution $(2 \times N) + 1$ where N is the number of series expansions. The parent solutions are split at this point and then recombined to form two new unique solutions. K-point crossover has the same theory, but instead of generating 1 crossover point, a user defined number of crossovers take place. In this case to provide an optimal mutation, for every new child a new k value is randomly generated between 1 and N and used only for that crossover.

Gaussian Mutation

For each element within the parameter solution set a Gaussian distribution is defined representing the variance of each said element across the entire solution set. This is then used to create the new population by altering individual elements of a randomly chosen parent. When a child is defined every parameter has the probability of being altered by $1 / N$, where N is the length of the vector solution. This means an alteration is likely to happen as least once. If a parameter is set to be changed the alteration is defined by a randomly generated value from the distribution that is kept within the bounds of the distribution.

3.2.6.4. Fitness Check (Equation Based)

The evaluation based on the equation is performed as soon as the data set for any given generation is created, ranging from 1000 to 100000 permutations of the parameter set. A data set of 128 unique experimental data points is used to compare against the parameter possibilities. The validation data set of 40 points is stored as storage and loss moduli so utilising equation 3.9 and the parameter values for g_i & τ_i , these data points can be substituted in and thus a difference computed. This is then averaged across all the data points and an 'error' value is produced for each possible solution. Due to the volume of checks that are being computed growing exponentially and being defined by N (Degree of approximation) multiplied by dataSize (Number of comparison points) and GeneticMutations (number of permutations in each generation), ensuring this calculation was computationally efficient was necessary. This was done by reducing the amount of memory allocations and retrievals of data during each calculation and changing how and when the values were retrieved from the computer memory. This fitness check was used solely to thin down solutions already computed from the modelling results reducing the number of models needing to be computed to the value defined by the user as 'NumInGen'.

3.2.6.5. Fitness Check (Model Based)

The values that are used to evaluate which model outputs to continue with are load, time, and displacement. Because of the different loading profiles during the model simulations, this data is split into three portions: ramp test and upper/lower loading profile of sinusoidal load. The ramp data does not require any alterations; however, for the sinusoidal load to be evaluated effectively, the time/displacement data is converted into a hysteresis loop representing the entire time-period. The hysteresis

for every simulation is then split into its upper and lower curve structure. This allows the parameter solutions to be evaluated for how they represent the different loading and unloading material reactions seen in the experimental data. The error values reported are averaged percentage differences across every displacement/force data point produced by the model.

The data set used for validation of the ramp tests was gathered by performing six separate ramp loading sequences without the additional DMA. The six tests were then averaged to provide an overall approximation of the experimental ramp data. To ensure both data sets (experimental and model) are comparable the validation data is approximated by a logarithmic representation with load and displacement as the x and y values respectively. This approximation curve alongside periodic standard deviations of the ramp tests is shown in Figure 3-6A. This allows displacement values for an exact given load in the model data to be compared effectively and a more accurate overall error produced even with the introduced error of the approximated curve. This error introduced by the validation data can be discounted as it is introduced in every solution.

The evaluation of the sinusoidal load used much of the same techniques. Starting with the model output this must firstly be normalised to the lowest displacement value of 0 then split into its upper and lower loop loading profiles. The experimental data was taken from the validation set of DMA experiments referenced earlier. As the experimental data points could not guarantee coverage of the model data points, for comparison a similar approximation function approach was used for each half of the loop.

$$y = a \cdot \log(b \cdot x) \quad (3.15)$$

$$y = a \cdot e^{(b \cdot x)} \quad (3.16)$$

The upper half was approximated using a function of the form displayed in equation 3.15 and the lower half with equation 3.16, with 'a' and 'b' being the optimised variable. For any given load in the simulation data an expected displacement could then be calculated using these functions and compared against. An example hysteresis validation set is shown in Figure 3-6B.

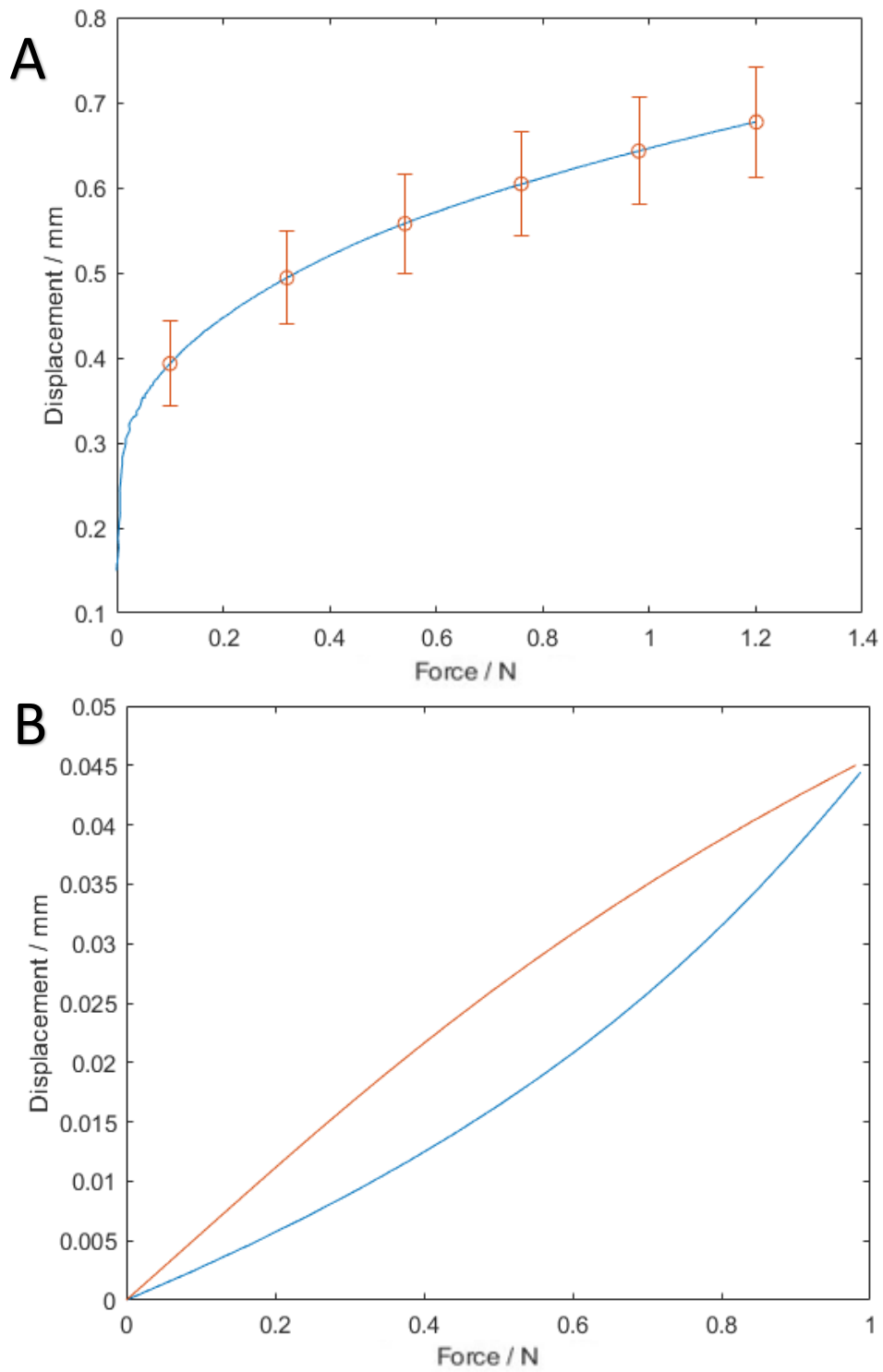


Figure 3-6: A) Averaged experimental ramp test data fit to a logarithmic function to be used as part of the validation of the models produced in each generation. B) Example hysteresis data set produced from the experimental data and fitted to a logarithmic and exponential function for the upper and lower lines respectively.

3.3. Results

The results shown here are based on 30 unique simulations were completed of the automation system. They are composed of three N (order of approximation) values of 1, 3 and 5, and two Iteration lengths of 50 and 20 split into the N values at six 50 runs and four 20 runs. The variation in the value of N allows us to evaluate the need for additional terms in the Prony series approximation. These specific values of N were used so that the order of approximations effect on the progression of the output error across all iterations could be investigated. An additional analysis of whether the extra level of the computational complexity required for a higher order N was a necessity to achieve a suitable error level. The different number of iterations investigation was also used to see how many generations were needed to establish an accurate approximation of the optimisation problem. All initial solutions were derived using the native java rand function utilising the current (at the time of simulation initialisation) computer clock as the seed to ensure no initial bias gave one simulation benefit over the others.

Table 3.4: Final error values of each simulation averaged across the repeats with SD included. The error values correspond to the difference between the resultant approximations and the experimental data set averaged across multiple simulations. Done for A) 50 Iterations and B) 20 Iterations.

A	50 Iterations of the genetic algorithm / % error					
	Ramp		Lower (Unloading)		Upper (loading)	
	Average	SD	Average	SD	Average	SD
N						
1	16.95	0.68	24.60	0.28	20.98	0.81
3	15.79	0.02	19.89	1.80	21.69	1.51
5	15.79	0.02	15.74	0.75	30.69	0.03

B	20 Iterations of the genetic algorithm / % error					
	Ramp		Lower (Unloading)		Upper (loading)	
	Average	SD	Average	SD	Average	SD
N						
1	17.75	1.94	24.59	0.19	21.62	1.30
3	15.79	0.03	19.82	1.95	24.02	4.14
5	15.84	0.04	16.09	0.60	30.73	0.09

From each simulations error values for each ramp, upper hysteresis and lower hysteresis load values were taken on every iteration using the optimal parameter set at that point in progression. These error values are obtained using the method described in section 3.2.6.5. They were then averaged using a mean across their repeats and are displayed in Figure 3-6A and Figure 3-6B. The final error values for all situations are displayed in Table 3.4.

Figure 3-7A and Figure 3-7B displays the results of the ramp load error calculation. For all following statements N refers to the order of Prony approximation used in the genetic algorithm. It was observed that for $N = 1$ the final parameters produced on average more error after both 20 and 50 iterations compared to $N = 3$ & 5. In this result set, produced error when N was defined at 3 and 5 was 2% smaller at $N = 1$ after 20 iterations and still 1% smaller after 50 iterations. An additional feature of both $N = 3$ and 5 was that the deviation amongst the repeats was negligible in both tests with a much larger deviation seen in $N = 1$ results. There is also negligible difference between the data sets produced for $N = 3$ and 5. However there were very small improvements all the way up until 50 iterations as seen in the differences between the final error values of both experiments.

Figure 3-7C and Figure 3-7D presents the lower or unloading portion of the hysteresis loop at 50 and 20 iterations, respectively. The simulations for $N = 1$ perform consistently worse across both sets of simulations with it results in around 5% more error than $N = 3$ and 10% more than $N = 5$. Comparing $N = 3$ and 5, both version plateau after around 20 iterations with $N = 5$ performing around 5% better. $N = 3$ does continue to reduce the error until 50 iterations but at a much more gradual pace demonstrated by the final error value having a large standard deviation.

Figure 3-7E and Figure 3-7F display the loading portion of the hysteresis loop at 50 and 20 iterations, respectively. When $N = 5$, the error was unable to be improved from the initial iteration in both the 20 and 50 iteration runs and produced an overall error value ~10% larger than N values of 1 and 3. Given that the standard deviation was very small in both 20 and 50 iterations it shows that this occurred for every $N = 5$ simulation. It is seen that the error is continued to be reduced up until the point of 50 iterations for both $N = 1$ and $N = 3$ giving an improvement of 1% for both $N = 1$ and 3% for $N = 3$. The convergence across the simulation repetitions also improved as the iteration progressed as shown by the deviation bar values reducing as the later iterations are reached.

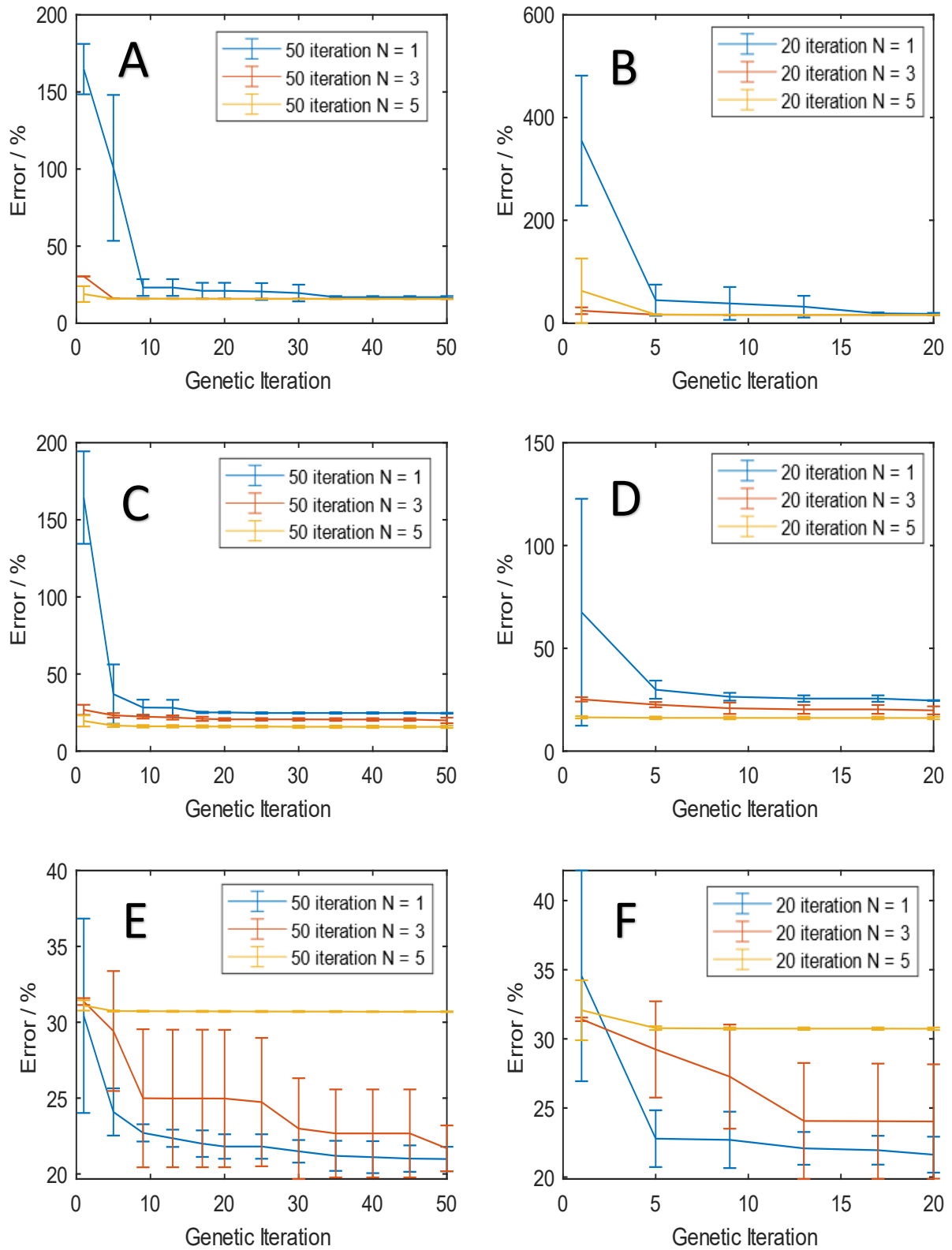


Figure 3-7: A) 50 iteration ramp error output, B) 20 iteration ramp error output, C) 50 iteration lower hysteresis error, D) 20 iteration lower hysteresis error, E) 50 iteration upper hysteresis error, F) 20 iteration upper hysteresis error.

3.4. Discussion

The system developed in this chapter has shown that it is possible to utilise an automatic optimisation approach to characterise the material parameters for a natural biomaterial; the viscoelastic properties for human articular cartilage modelled also as hyper-elastic in this instance. Utilising the model outputs as the driving force for each generations progression allows not only the material approximation to be a factor for the parameters, but the direct comparison of an experimental result to a model's response. In total 30 simulations of the automation system with varying initialisation parameters were run to test the effectiveness of this technique with the aim of showing consistency and effectiveness of said system.

Specific to human AC, the algorithm provided time-domain parameters for a hyper-viscoelastic model, optimised using experimental data gathered in the frequency domain which allows the cartilage to be better represented under dynamic loads. It was seen in all situations that there was a reduction in the error of the models as the iterations of genetic algorithm progressed with varying degrees of success across our different set-ups. Convergence was seen in both ramp and unloading/lower hysteresis error analysis with 20 and 50 iterations respectively, however, there was still significant reduction in the error of the model up to 50 iterations in the loading/upper hysteresis error calculations. Experiments were not continued after 50 iterations, however, doing this would confirm whether the seen trend continues.

Focussing on the ramp section of the error analysis It was seen to be the easiest for the algorithm to converge doing so in just over five iterations across all simulations and producing results within a negligible margin of each other by both 50 and 20 iterations, a difference of 0.01% after 50 iterations for $N = 3$ and 5 and 2% for $N = 1$.

$N = 1$ was seen to be highly ineffective initially, skewing the error dramatically but it did trend to a similar value of error after many more iterations, approximately 50. The hysteresis error variation was more demonstrated the difference between the order of approximation more clearly. The errors seen in both sections show that there is a benefit to progressing the algorithm to 50 iterations, with the error having not converged by this point for both $N = 3$ and $N = 1$. A comparison between the upper and lower approximations shows that there is a flip in what is the optimal degree of approximation. $N = 1$ performs the best for the upper portion and the worst for the lower whereas $N = 5$ is the opposite. Both report in at a about 10% difference from best to worst. $N = 3$ may be the optimal solution for these situations as it results in only a cumulative 5% when compared to both optimal solutions. This added to the reduction in the time complexity of using a 3rd order approximation is also a benefit. It is unclear why $N = 1$ performed so effectively in the upper loop section. However, it could be because this section is the most challenging to approximate; thus, adding more variation with additional parameters results in the additional error seen. The standard deviation of $N = 3$ (Figure 3-7E and Figure 3-7F) shows that for some of the simulations a better solution was indeed found than the best solution in all the $N = 1$ repeats so the limitation mentioned previously can be overcome by allowing the more repeat/iterations of the genetic algorithm.

The use of numerical methods and modelling has seen an uptake in biomedical research over the last 20 years, however, it is still very much in development in its utilisation across the field as demonstrated by Bhattacharya et al [149]. Within this field, an important component is the validation of said numerical methods, to ensure correctness of any given outcomes, as discussed by Henninger et al [150]. A technique was developed to integrate the validation of produced models into the

automatic progression of the generational approximations. Cyclic optimisation of material parameters has been done before [151], however, to the best of our knowledge our work is unique in its application of allowing the simulated mechanical testing results to be a part of the fitness evaluation of the numerical optimisation in self-contained automation. The application of genetic algorithms to optimisation has been demonstrated [152], [153] but has not seen much within the biomedical field. The customisability demonstrated within our system will allow for this to occur, with the additional control over a black box system such as Abaqus or COMSOL.

The system is transferable in its use due to the modular design of its components however the intricacies of the parameters alteration during the optimisation procedures require problem specific definition and thus would require both coding and simulation specific knowledge for an implementation to be utilised effectively for a different material analysis. This would mainly involve changing the fitness characterisation and optimisation equations within the optimisation control node as displayed in the system structure in Figure 3-2.

The technique for in section 3.2.6.5 for model error calculation is seen to effectively provide a basis for the genetic algorithm to rank all the previous solutions as all simulations were able to progress and reduce the error a meaningful amount after the initially optimisation process (3.2.6.1). Part of what could have been hindering the algorithm in some instances is the variation that was seen in the initial data set that was used to create the testing set. This was as a result of the variation seen in the human tissue obtained and its varying level of damage and its donors age, which could have resulted in a less clear view of what the 'ideal' model should be.

Narrowing this down in the future should produce even better results for a similar set of simulations, however it does have its limitations due to the difficulty in obtaining

human tissue of the same standard. Building a validation set of health/un-healthy tissue in the future would be very beneficial to the development of models representing health/damaged cartilage tissue.

3.5. Conclusion

In conclusion, this chapter presents a system that allows the automations of a process to find the optimal material approximation for a given tissue structure using multiple material approximations. A key novelty to the work lies in the use of FEA models during the fitness evaluation procedure of the optimisation rather than a purely equation based approach. When the order of approximation was set to 1, the system underperformed in 2 of the 3 error analyses and only slightly better in the 3rd. When the order was set to 3 and 5 there was minor differences except in the loading hysteresis error value where $N = 3$ performed significantly better. The number of generations being increased to 50 was also shown to be effective in reducing the error in $N = 3$. The model used as the base for the testing of the automation script was a simplistic model comprised of only three material approximation, adding to this by including fibre reinforcement or three-dimensional geometry would increase the time complexity of the system but only require small modifications to the code due to the use of abstraction in its initial design. This would be beneficial due to the models becoming more physiologically representative not only in loading but geometrics as well. The system used here can be useful in furthering the development of physiologically relevant models of not only cartilage, but with small adaptations to the genetic algorithm mutators and input model parameters that are problem specific, any other mechanically modelled systems undergoing dynamic loading.

This chapter has presented an automated method by which to characterise human AC for hyper-viscoelastic modelling. This computational framework is now available here: <https://github.com/piers-ch-allen/Automated-Modelling-System>. The next stage of the work focuses on AM for experimental testing using some of the testing principles of DMA as applied to AC as presented in this chapter. Chapter 4 looks at a macro-scale testing approach, while chapter 5 focuses on the osteochondral cores micro scale geometry. The macro and micro scale analysis of the biological tissue will provide additional information and parameters that can be imported into the work done in the Chapter 3 to better inform them.

Chapter 4. Development and evaluation of a joint contour testing system for AC

4.1. Introduction

Density, joint shape and mechanobiology have all been postulated as affecting the mechanical behaviour of AC. For instance, Humaira et al. [154] demonstrated that with reduced density of a bone substrate in an osteochondral core, there was a significant increase in surface damage of the attached AC when tested at physiologically relevant frequencies. Crolla et al. [155] showing, in addition, that a frequency-dependent viscoelastic response of AC also varied with density of the substrate on which samples were tested (as well as the AC hydration percentage). Separate to this, anatomical regional analysis of knee AC has been conducted by Li et al. [156] and topological quantification performed by Cohen et al. [118] both show that an understanding of the variation in the different areas of the tibiofemoral joint is important to its load response profile. This variation of joint contour is currently yet to be used to influence mechanical testing procedures when analysing joint tissue in literature.

Fell et al. [14] found that a linear relationship between thickness of cartilage and the subchondral bone density exists between bovine AC from the tibial plateau adding to the variation that is seen in the joint's complexity. Adaptations may take place across a joint, whereby loading history may condition the underlying AC and bone [67]; further, there is some evidence that microfractures of the subchondral bone may occur so as to protect its overlying cartilage [67]. Thus, the AC's material properties are altered based on loading history and subchondral density. Further, Espino et al. [30] and Seedhom et al. [2] both demonstrated that the dynamic viscoelasticity of AC

varied with differing regions of the knee joint. While the above studies evidence the role that bone density, tissue thickness, loading history have on a given joint and joint contour, they do not evaluate shape as an independent variable. Hence, it is not clear whether the contour of the joint itself impacts upon the dynamic viscoelasticity measured for AC on a joint, or whether this is purely consequential to loading history and adaptation of the subchondral bone.

To establish a better understand of cartilage *in situ* in the body and its mechanical properties the tibial joint is a location of particular interest due to its joint contour. This is because it contains the tibial plateau, which is approximately flat which is continuous in terms of its articular cartilage and subchondral bone with the tibial spine where the joint orientation changes from approximately 'horizontal' to mostly 'vertical' Figure 4.1[142]. In terms of pathology, damage to the articular cartilage is typically found at specific regions in the AC rather than homogenously distributed across its joint surface [158]. Such examples of this observation across the knee joint include uncovered verses covered meniscus loading [159] and the irregular loading of the patellofemoral joint [160]. When *in situ* the AC on the tibial plateau experiences loads applied at a range of angle due to the changing geometry across its surface [117], [161].

Mechanical testing of cartilage has focused on three configurations: confined, unconfined, and *in situ* compression [162]–[164]. Several studies focus on indentation [162], [165], [166] whilst AC is part of a wider continuum or remove a segment and test without tension removing the replication of pre-stress tissue may experience when on a joint. Many studies have used a flatbed platen and compression plate arrangement to test cartilage (Figure 4-6A); while useful, such studies cannot evaluate whether the angle of the substrate on which the cartilage is loaded affects its mechanical response, as an independent factor. This limitation of current work, if fixed, could affect both how

future mechanical evaluation of tissue is performed in data gathering scenarios, as well as whether computational models should be geometrically formed to more closely represent the goal biological situation.

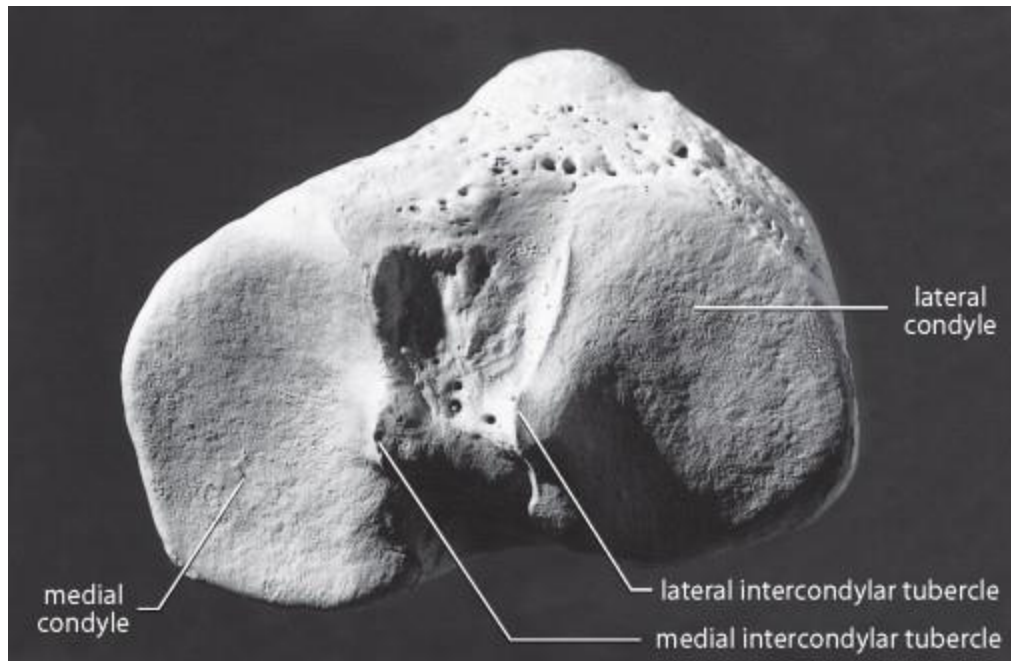


Figure 4-1: Anatomical image of a tibial joint epiphysis with main geometric regions identified. The two tibial plateau sections (medial and lateral condyles) and the tibial spine (medial and lateral tubercle). Image courtesy of White et al [216].

AM was utilised in this chapter due to its ability to enable the evaluation of joint shape as an independent factor. It has been used previously in mimicking body construct [167], an assessment of the suitable options for material was required. With the limitations surrounding the available printer units, the options were polylactic acid (PLA) and Polyethylene terephthalate glycol (PETG). Both of these materials are known to be biocompatible [108]–[110] but have different advantages. PLA was chosen as it enables the production of a higher quality surface finish; a flat contour plane was a major requirement of the printed components [60]. Its operational cost was lower than PETG and was expected to be stiffer, albeit weaker [168].

The aim of this chapter is to evaluate whether the dynamic viscoelastic behaviour of AC is sensitive to the shape of joint contour as an independent variable. Bovine cartilage will be used as it is an accepted model for human cartilage, with similar mechanical properties to human AC [169]. Furthermore, the bovine humeral head enables the harvesting of samples with larger dimensions [24], advantageous to test a wider interconnected cartilage matrix.

The material response data gathered, and joint contour analysis gained through this study will inform the work performed in Chapter 3. The analysis of the joint geometry will be used when the automated system is expanded to a 3D geometry and the additional data will validate or demonstrate changes that need to be made to the data set that is being used to train the genetic algorithm.

Additive manufacturing will be leveraged to produce bespoke geometries compatible with DMA testing to mimic two key contours of the tibial articulating surface of the tibial-femoral joint. DMA will be used to evaluate the dynamic viscoelastic response in terms of storage and loss stiffness as a joint structure. The design will include the ability to test the cartilage continuum under tension to approximate the *in situ* pre-stress which is experienced by AC within its wider continuum. To achieve this study's aim, there are a number of objectives that will be laid out to complete. Firstly it will be required to dissect/harvest a continuum of articular cartilage which can be tested under tension. An CAD model will then be AM that represents the substrate which enables testing of a steep and a shallow contour from the tibial articulating surface. DMA will then be utilised to evaluate the dynamic viscoelastic properties of cartilage upon the different contoured testing platens. Finally, it will be evaluated whether joint contour, as a lone macro-scale factor alters the mechanics of AC within a joint.

The two main novelties of this chapters aim are as follows:

- Mechanically evaluating cartilage tissue over a contoured surface that has anatomically relevant geometry.
- Comparing the tissue mechanical response seen in this study to previous publications that utilised flat platens.

4.2. Methods

4.2.1. Cartilage Specimen Preparation:

Bovine humeral heads (N = 4) were obtained from a supplier (Dissect Supplies, UK) taken from 18 month old livestock. Humeral heads were used because of their large relatively flat area of cartilage that is available on their surface. Humeral heads were visually inspected on receipt to ensure that the surfaces were not damaged and were suitable for testing. After inspection the samples were stored at $-40\text{ }^{\circ}\text{C}$, in heat sealed bags, which has previously been shown to not affect the dynamic viscoelastic

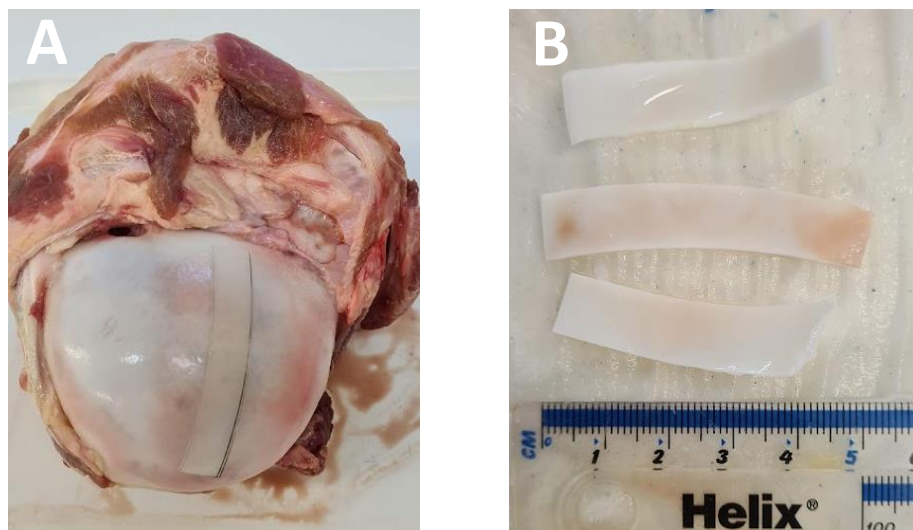


Figure 4-2: A) Stencil for sample on Bovine Humeral Head, B) Tissue samples taken from said joint.

properties of the tissue [141]. Rectangular strips of cartilage with a minimum length of

5 cm and width of 1 cm were required in order for the sample to span the contoured surface of the base platens in the testing experiment (section 4.1.2). The minimum of 5 cm was required due to variable length of the platen that the tissue had to cover, as the angle increased, the surface area that was required also increased. Samples were removed from the freezer 24 hours before testing to allow samples to defrost before they were dissected. Once thawed, test geometries were stencilled onto the joint surface and then dissected using a surgical scalpel and singular planing motion (Figure 4-2A). This ensures a smooth surface on the sample underside reducing the likelihood of instability and errors in the mechanical testing. Fifteen samples of the approximate stencil size (5 x 1 cm; Figure 4-2B) were obtained and stored in Ringer's solution (RINGER tablets, MilliporeSigma, Massachusetts) matching at 4 °C prior to DMA testing, consistent with a previous study [19]. They were allowed to warm up to room temperature prior to the DMA tests occurring to ensure no rigidity as a result of thawing remained.

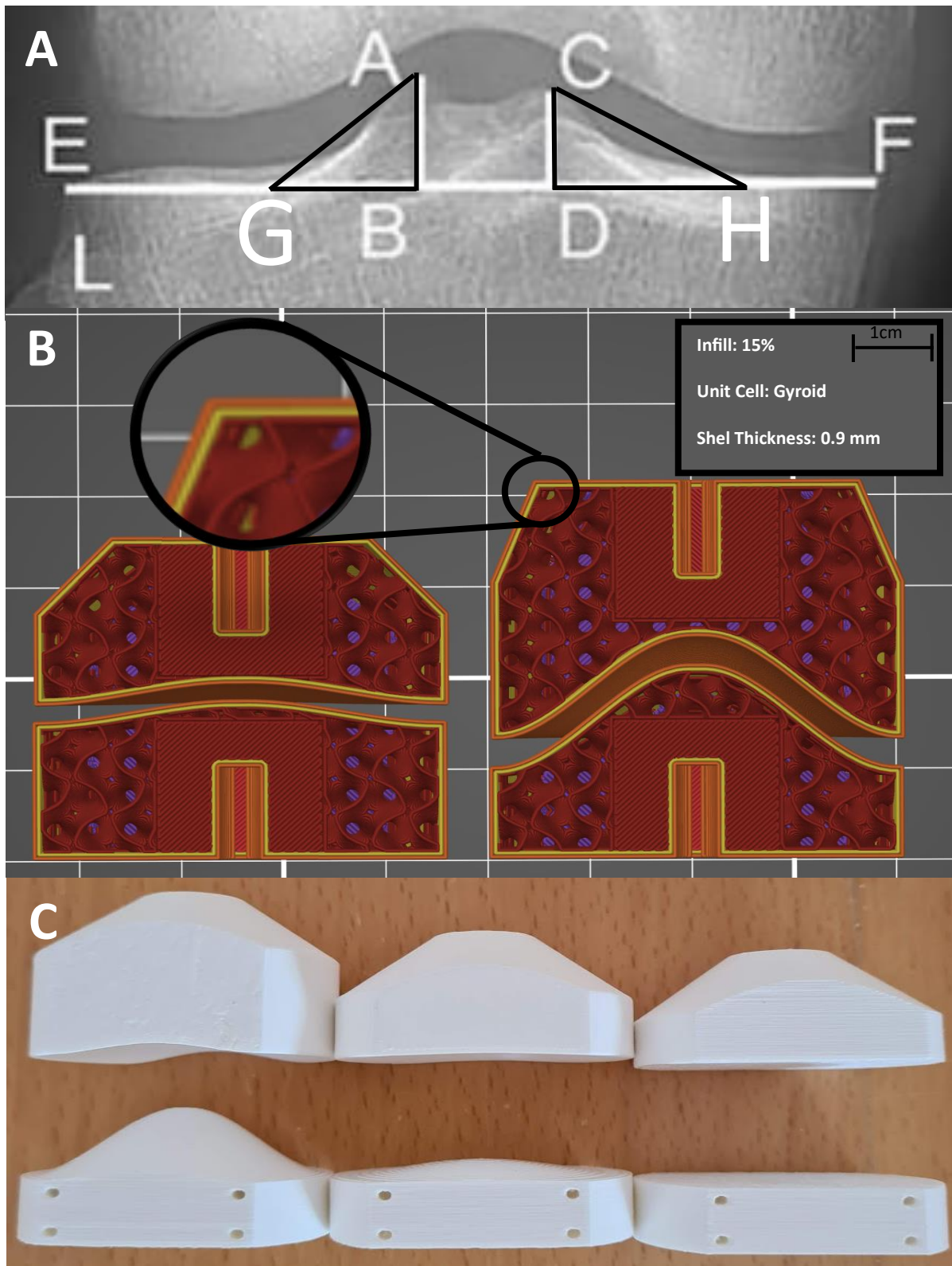


Figure 4-3: A: Tibial plateau from Nie et al [20], CC BY-NC-SA 4.0 used for calculation of the steep angle platen design. Additional labels of G and Hand triangles for measurements are included for the calculations of the slope angles B: Print design of 3D components showing infill structure and shell thickness. C: 3D compression and platen parts from left to right: Steep 30° angle, shallow 7° angle, base flat 0° angle.

4.2.2. Design and additive manufacture of experimental apparatus

The compression base and platen varied depending on the angular test that was being performed. It was decided that there would be three variations of the base platen; flat, to represent the current testing protocols, a shallow angle of 7° and a 30° steep angle. The value of 7° was used to mimic shallow angles across the tibial plateau, taken from the average of medial and lateral tibial slope measurements in a study performed by Hashemi et al. [117]. This value is representative of the portion of the joint between points E and G or H and F in Figure 4-3A where the flatter portion of the plateau is present. The value of a 30° was used to mimic the steeper portions of the tibial spine towards the centre of the tibia and was estimated by analysing X-ray images and measurements reported by Nie et al. [161] (Figure 4-3A). The angles A-G-B and C-H-D were calculated using approximations from where the steepest portion ended (labelled G and H in Figure 4-3A) and known measurements of characteristics of the joint, along with the lateral and medial spine height values. This produced an angle of incline for each spine, which were subsequently averaged to calculate a mean tibial spine steep slope angle at 30°. The three angles represent the two extremes' angles seen biologically in the human tibial plateau that the study is aiming to reproduce *ex vivo* and a flat control platen.

The components were manufactured using a PRUSA i3 Mk3 3D printer (PRUSA i3 Mk3, Prusa Research a.s., Czech Republic) with a 0.15 mm nozzle head and pure PLA prusament filament (Prusa Research a.s., Czech Republic). The CAD models for each of the parts were designed in Autodesk Inventor (Autodesk Inventor. Version 22.0., CA: Autodesk, San Rafael) and then G-code was created in PrusaSlicer 2.5.0 [96] to be fed back into the printer used for additive manufacture. All parts were then

tapped with a 10-32 UNF machining tap to allow attachment to the experimental machine (visible holes that are present in Figure 4-3B). These sets of plates were 3D printed to represent the aforementioned angles of the tibial spine (30°), tibial plateau (7°) and a flat plate (0°), see Figure 4-3C.

A print specification of 0.9 mm shell thickness and an infill lattice set at 15% of a gyroid design was used to ensure structural rigidity of the parts. Each pair of parts were designed so that the base was the convex approximation of the curve, and the platen was its concave inverse ensuring that there is uniform load when the two components are compressed together, this is highlighted in Figure 4-3B. This compression design was set to be similar to the tibial joint articulating against the femoral condyles. They were fixed onto the machine using the same threaded connection that the original parts used and were tested for levelness to ensure correct and uniform compression occurred using a spirit level against the side of the components. All components were printed with an orientation of 90° to the load direction, this was to produce the smoothest finish on the testing surfaces that the cartilage would be in contact with. Printing in this orientation allowed the curved surfaces to be split into more segments, thus reducing the difference between each layer, reducing the 'step' effect.

3D print validation

To ensure the printed parts were produced to the defined specifications, Skyscan 1172 scanner (Bruker Micro-CT, Belgium) was performed on a randomly chosen sample to test its interior structure and how close it matched to the defined CAD model (Figure 4-8). Using CTan data analyser (V1.16.4.1+, Bruker Micro-CT, Belgium) a 3D region of interest was defined on the interior of the sample (red square in Figure 4-4B).

Porosity measurements were taken with an open pore percentage value of 85.04% obtained which matched the 15% defined infill.

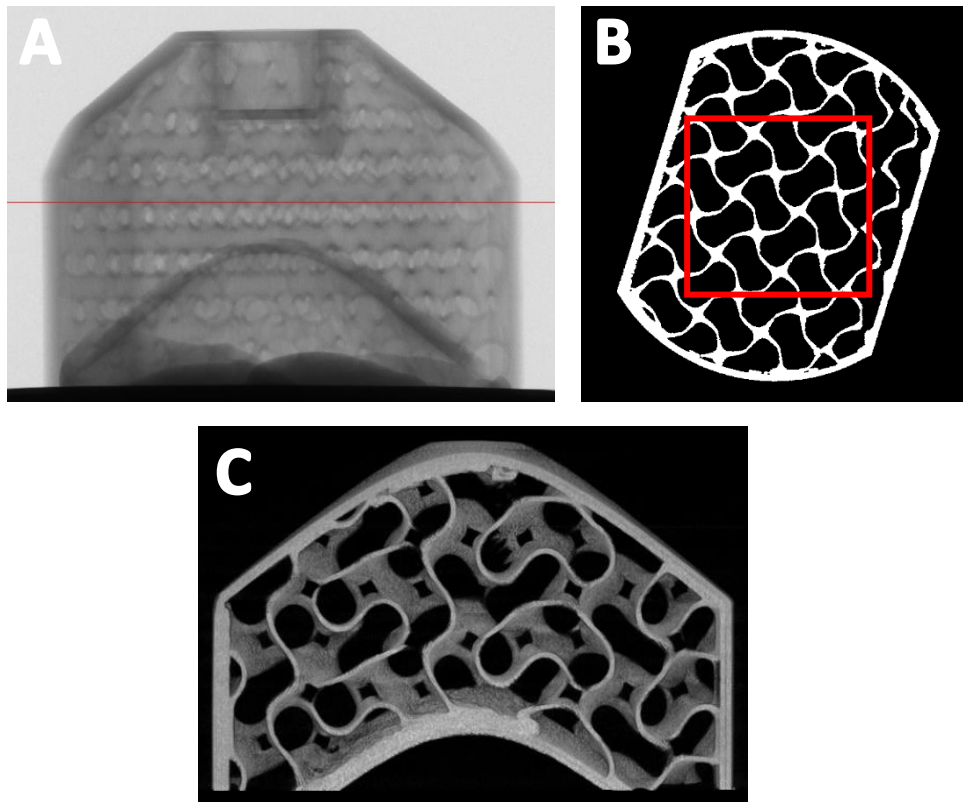


Figure 4-4: A: Micro-CT slice of steep slope compression plate (red line is slice depicted in B). B: Singular horizontal slice with ROI (red square) defined for analysis of interior porosity of the printed sample. C: Cross-section of reconstructed micro-CT scan of one of the 3D printed component platens demonstrating interior design.

A 3D reconstruction of the complete structure was prepared and visually analysed to check for inconsistencies in the print quality, by scanning through the slices. A 3D section is shown in Figure 4-4C demonstrating the interior gyroidal design. The print quality was found to be what we expected with CAD design matching the Micro-CT reconstruction correctly.

As a result of the design conditions, additional porosity was introduced to the platens as the angle increased which had the possibility of creating a more compliant

structure and thus affecting the output results when undergoing testing. In order to ensure this was mitigated as much as possible, preliminary testing was conducted on these components at this point using bovine tissue samples. These tests were performed with same experimental loading setup but without the addition of tension to the system. Five cartilage samples were taken that were of same defined size as in Section 4.2.1 at a minimum length of 5 cm and width of 1 cm and tested across every platen. The preliminary results are displayed in Figure 4-5.

Both the 7° shallow angle platen and 30° steep angle platen reported average storage modulus values that were approximately 10% stiffer than the control surface. Although this is not definitive proof that the interior structure of the 3D printed platens is affecting the material outputs of the tested samples it does provide support in favour of assuming that it does not within our results section. In a repeat of this study, a potential solution to remove all doubt would be to ensure that the interior fill of the components is set at 100% infill to create solid blocks.

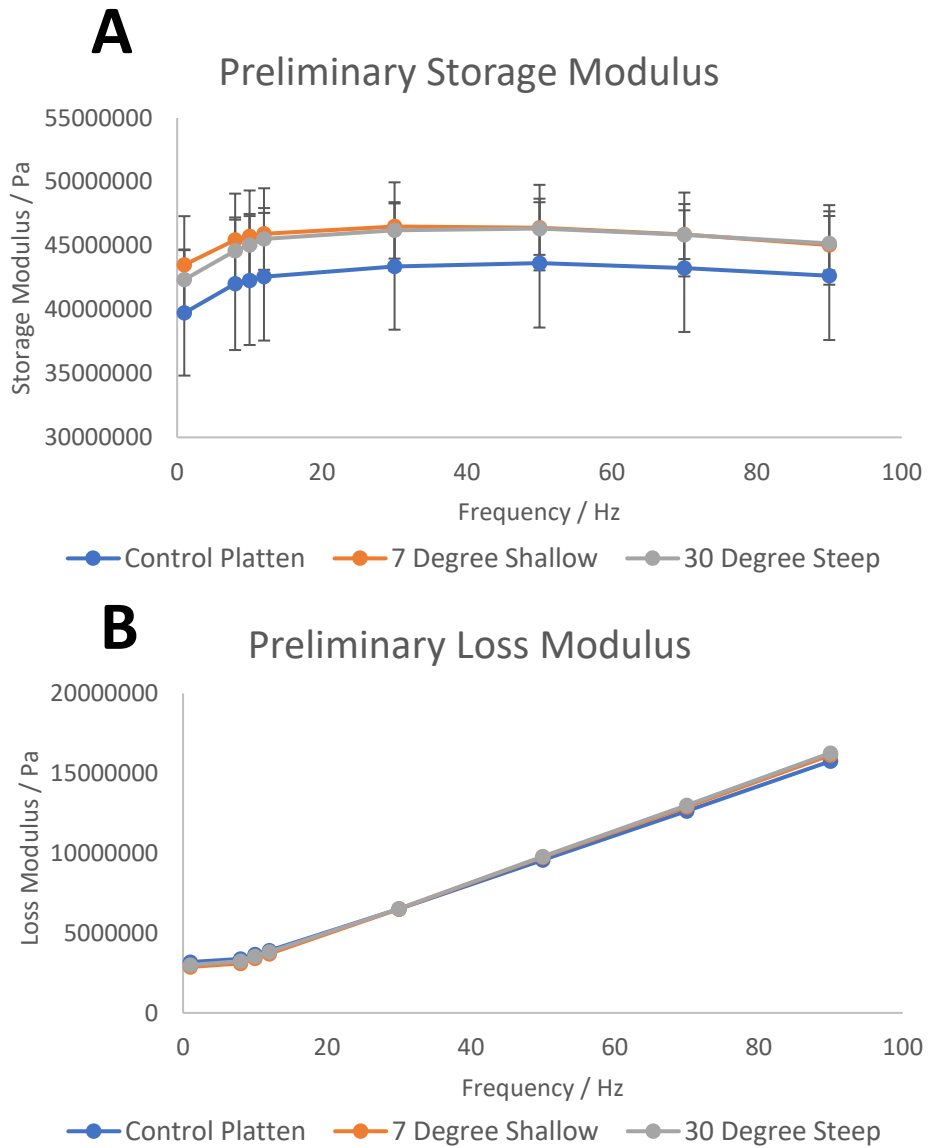


Figure 4-5: Preliminary A) storage and B) loss modulus values for cartilage tissue mechanically loaded upon the three different angular platens.

4.2.3. Dynamic mechanical analysis of cartilage on curved substrates

Dynamic Mechanical Analysis (DMA) was performed on specimens by subjecting these to a sinusoidal load whilst its out-of-phase displacement response was measured. All tests were performed on a Bose ElectroForce 3200 testing machine, running WinTest 4.1 DMA software (Bose Corporation, Minnesota, USA; now, TA Instruments, New Castle, DE, USA). This technique has previously been used to measure the dynamic viscoelastic properties of bovine AC [3] - [5] (section 2.3).

A sinusoidally compressive load ranging between 37.7-85.5 N was applied to all specimens with a preload of 4 N. The loading range equated to an induced stress of 0.75 to 1.7 MPa, matching the peak nominally induced stress in cartilage during ambulatory activities such as walking [27]. The sinusoidal force was applied using a frequency sweep previously established by Fulcher et al. [66] of: 1, 8, 10, 12, 30, 50, 70 and 90 Hz with two frequency pre-loading cycles of 25 and 50 Hz for 1500 and 3000 cycles, respectively.

Each of the 15 test samples were tested once on each of the 0°, 7° and 30° platens, providing three separate mechanical response data sets resulting in a total of 45 unique data sets (15 samples on 3 different platens). The order in which the samples were tested on each platen was random to ensure that there was no bias in which contour of surface was loaded upon first. To avoid dehydration throughout the experiment, between each test the tissue was sandwiched between cloth sheets soaked in Ringers' solutions. A visual inspection of the samples was also performed to ensure no deterioration of the tissue between experiments had occurred. This was immediately obvious if it had occurred due to the cartilage samples excessively curling up, a small amount of curling is a natural response due to the surface tension being

greater on the articulating side of cartilage. However, failure was not expected as all tests were performed within a physiological range and below a failure point normally seen at ~3 MPa [24], [154]. WinTest DMA software was used to perform a fast Fourier transform (FFT) of the load and displacement waves produced at each test frequency, details on this are in section 2.3. All results are displayed against the defined frequencies in the DMA frequency sweep.

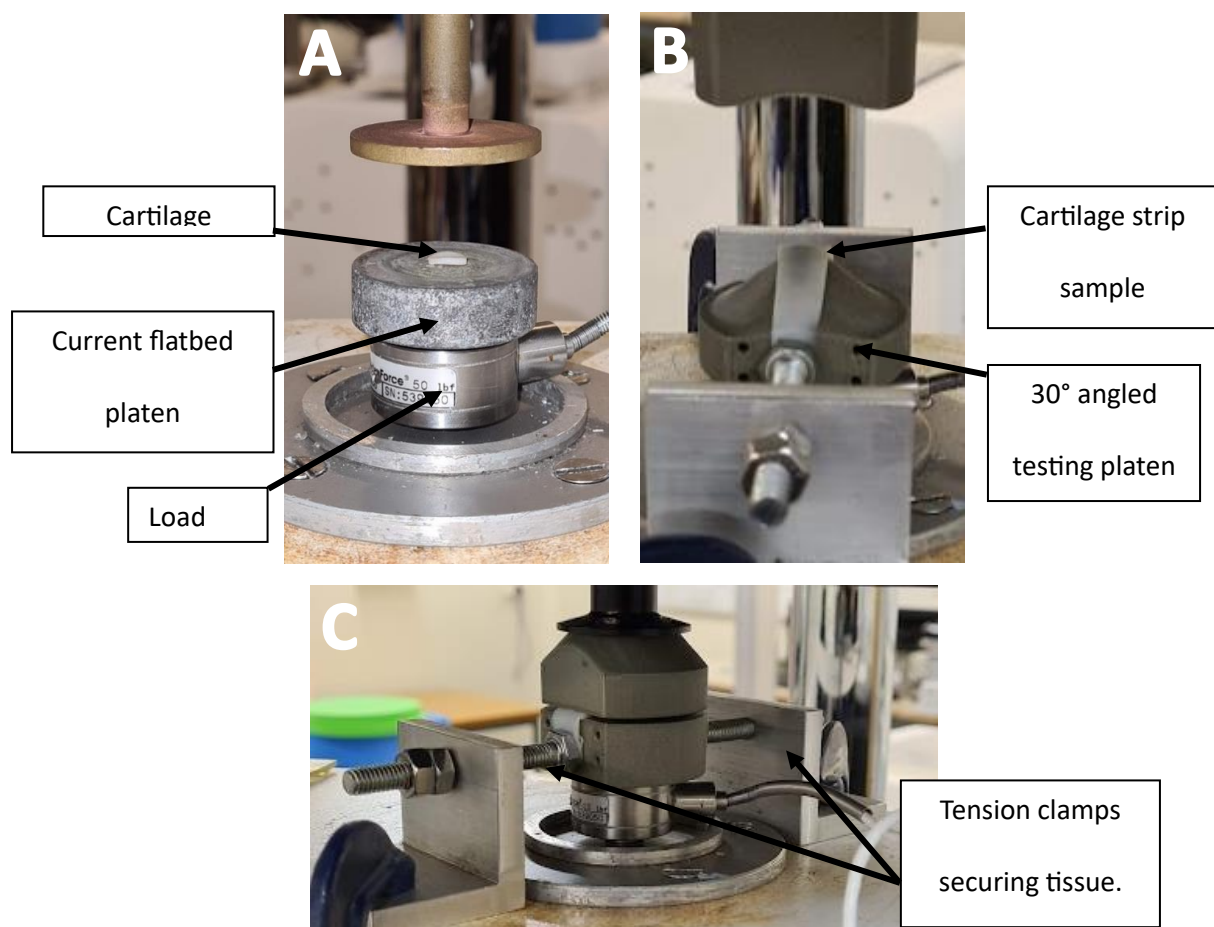


Figure 4-6: : A: Current testing practice for DMA on cartilage samples in previous published studies. B: Steep platen in-situ on the Bose testing machine with a strip of AC held in place with tension clamps across the contoured surface. C: AC sample under dynamic compression in the same experimental set up as B

The contoured platens were fixed to the Bose ElectroForce 3200 running WinTest 4.1 software (Bose ElectroForce Group, New Castle, Delaware, USA, now TA Instruments) having been tapped to the 10 UNF specification in the pre-printed hole (Visible in Figure 4-3B but the space left at the base of the components). This was to ensure no additional lateral movement occurred during the cyclical application of load. Due to the 360° symmetrical design of all of the parts, lining the compression plate and base platen up to ensure uniform coverage was not an issue as they were designed to be direct inverses of each other, the only concession to this was ensuring the tapping was done in the same location otherwise they would not have lined up.

The test set-up included a method to approximate the tension experienced *in situ* by cartilage. This also helped to ensure that the tissue was in direct contact across the width of the curved compression platens, avoiding slippage. Two aluminium braces with adjustable compression heads were designed so that they could be fixed to the test platform of the Bose with G-clamps and then control the position of, and the amount of tension applied to, the tissue on the platen (Figure 4-6B&C). This placed a further requirement on the dimensions of the tissue samples, as they not only needed to cover the platen length but to also have enough tissue either side to allow for adequate fixation. To provide some consistent control over the amount of pre-tension the samples were placed under in the testing rig, they were stretched back to their original length. This original length was measured on the joint sample from the point where the sample slice was removed, by using the stencil visible in Figure 4-2 as a guide tool. This would be better controlled mechanically by a machine to provide absolute consistency, but our solution should adequately provide an approximation of the in-situ tension the tissue was placed under.

4.2.4. Statistical Data Analysis

Statistical analyses were performed using Minitab 21.3 (Minitab, Penn State University, Pennsylvania, USA). 95% confidence intervals were calculated (N = 4, n = 15); Four individual bovine joint samples were obtained, and from those four, 15 total specimen strips were collected. These were 15 independent observations rather than repeat to ensure all data can be compared and no false CIs obtained [170].

Logarithmic and exponential regressions curves (Equations 4.1 and 4.2) were empirically fitted to the relationship of frequency (f) to storage (k') and loss stiffness (k'')[18]. Parameter A of equation 4.1 and equation 4.2 both represent the logarithmic and exponential gradient curve on their respective scales, and parameter B is an offset for k'. A parameter test (Anderson-Darling) was used to assess that the normality of parameter regression curves to ensure $p > 0.05$ for the obtained results. Following this, an ANOVA analysis was performed to compare across frequencies and substrate angulation. A One-way analysis of variance (ANOVA) test was used to test the variances between the fitting parameters of the different testing platforms (0°, 7° shallow, and 30° steep angle) and evaluate whether they were significantly different ($p < 0.05$).

$$k'(A,B) = A \log_e(f) + B \text{ for } 1 \leq f \leq 90 \text{ Hz} \quad (4.1)$$

$$k''(C,D) = C \cdot e^{D \cdot f} \text{ for } 1 \leq f \leq 90 \text{ Hz} \quad (4.2)$$

All parameters (A,B,C,D) of the above equations are unitless as they are comparing the direct value of frequency and stiffness rather than their values with respect to their unit.

4.2.5. Hysteresis Data Analysis

The hysteresis was calculated to directly measure energy dissipation during testing of AC, across the different contoured testing plantens. This was calculated using Matlab R2022a (Matlab R2022a, MathWorks, Inc., Natick, Massachusetts, USA). By plotting force against displacement for a given frequency and specimen a hysteresis loop is produced with an example shown in Figure 4-7A. To work out the energy dissipation, the area between the arcs of each complete loop is calculated using the trapezoid rule (Figure 4-7B). This was done using the same code base which I wrote for a published study which I co-authored but does not otherwise form part of this thesis beyond use of data in chapter 3 [18] where more information can be found on its methodology.

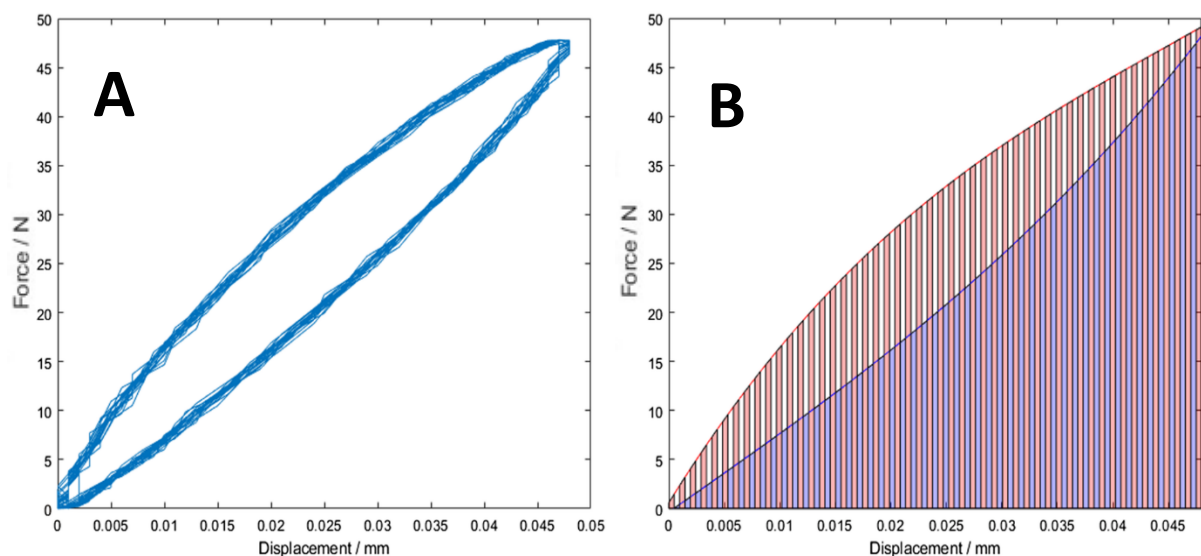


Figure 4-7: Cartilage hysteresis loops produced by Mountcastle et al [18], CC BY-NC-SA 4.0. A) Example of a hysteresis loop for a single specimen tested at 30 Hz. B) Representation of how the energy dissipation calculation is performed within the Matlab script when utilising the trapezoid rule. Y axis label has been altered from original due to incorrect label being used.

4.3. Results

4.3.1. DMA of Contoured Platen Tests

Storage Stiffness (k'):

For all testing conditions the storage stiffness of the tissue increased with respect to the frequency of load. The storage stiffness increased between 11% and 21% across the three platens with the stiffest material response being observed when the shallow platen was used.

For each of the three tests the mean (\pm Confidence Intervals; CI) values for k' across all frequencies with a 95% CI were recorded as follow: 0° platen at 1118.5 ± 36.1 N/mm, 7° shallow angle platen at 1307.9 ± 57.8 N/mm and 30° steep angle platen at 935.7 ± 56.2 N/mm. The complete set of values for each contour are shown numerically in Table 4.1 as well as graphically in Figure 4-8. A logarithmic relationship for k' was observed with respect to frequency, with storage stiffness increasing with relation to frequency up until ~30 Hz and then approximating a plateau with increasing frequency (Figure 4-8).

	Frequency / Hz							
	1	8	10	12	30	50	70	90
0° Flat Platen / N/mm	1031.31 ± 91.2	1104.95 ± 90.4	1115.12 ± 89.3	1124.72 ± 89.6	1148.31 ± 87.4	1150.86 ± 86.1	1132.3 ± 83.2	1140.11 ± 85.8
7° Shallow Platen / N/mm	1170.58 ± 116.5	1284.52 ± 121.2	1297.73 ± 120.3	1311.63 ± 120.1	1348.88 ± 119.5	1357.95 ± 118.1	1343.40 ± 115.8	1348.53 ± 116.1
30° Steep Platen / N/mm	806.79 ± 95.8	909.22 ± 103.8	919.84 ± 104.7	933.04 ± 105.3	969.79 ± 107.4	987.27 ± 107.4	979.28 ± 105.6	980.21 ± 105.0

Table 4.1: Mean Storage stiffness (k') \pm 95% CI for the three tested contoured platens at 0°, 7° and 30° for all frequencies in the frequency sweep of 1 – 90 Hz

When evaluating parameter A (Equation 4.1), the gradient curve of the logarithmic fit, it was seen that the tissue tested on the 0° platen produced a flatter, significantly different mechanical response ($p < 0.001$) to both the 30° steep and 7° shallow platen. This is also visibly seen in Figure 4-8 where the gradient of the 0° platen is flatter than the other 2 results. However, when 30° steep and 7° shallow are compared separately,

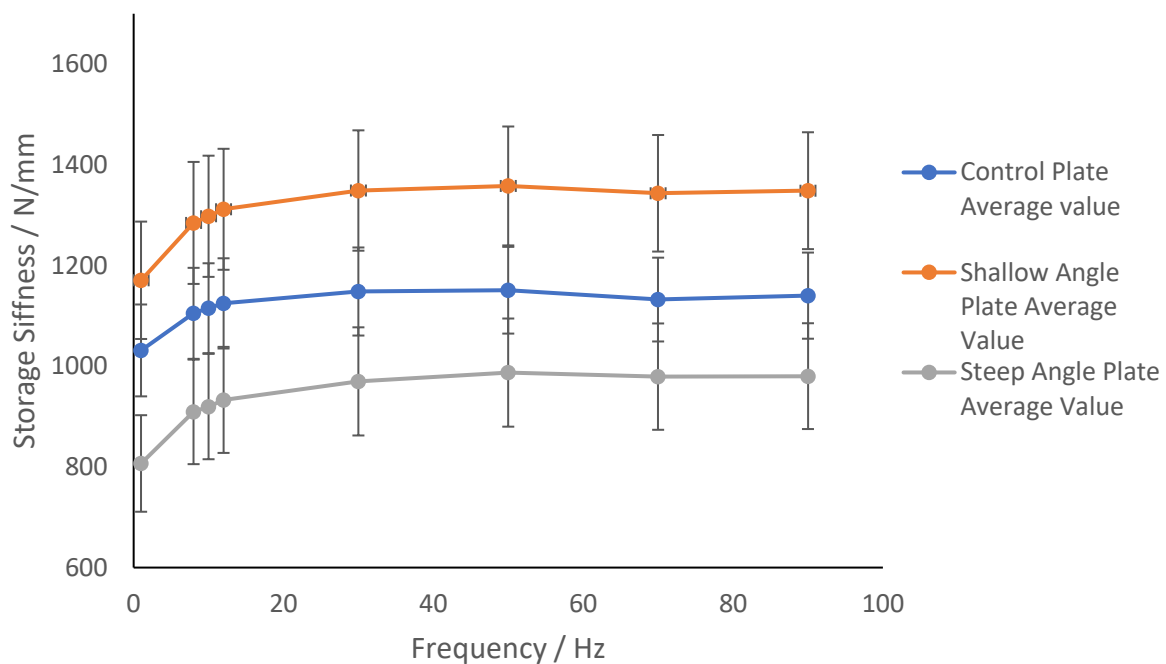


Figure 4-8: Storage Stiffness results of the bovine humeral tissue of the three different contours of testing platen plotted against frequency ranging from 1 to 90 Hz. Values shown are the mean \pm 95% confidence intervals ($N = 4, n = 15$).

no significant difference was recorded ($p > 0.5$). When looking at the second parameter of the approximation (parameter B, eq. 4.1), which represents the offset, it was seen that tissue tested on the 30° steep platen produced a significantly different material response ($p < 0.001$) to both the 0° and 7° shallow platen. The 0° and 7° shallow platen were found to no have a significant difference ($p > 0.5$) in the offset.

Loss Stiffness (k'')

For all testing conditions the loss stiffness of the tissue increased with respect to the frequency of load however the increase was much more consistent compared to the storage stiffness. The stiffness increased between 11% and 21% across the three platens with the stiffest material response being observed when the shallow platen was used. For all of the different contours, the loss stiffness experiences a very shallow increase between 1 to 12 Hz with percentages changes of: 0°; 13.5%, 7°; 7.2% and 30°; 8.3%. This then gradually increases until 90 Hz with distinct values for A for all results.

An exponential relationship for k'' was seen with respect to frequency for all AC samples tested on each platen. The mean values for the exponential fit of parameters C and D (Equation 4.2) for k'' are as follows: For the 0° ($D = 105.1 \pm 15.8$, $C = 0.017 \pm 0.0019$), 7° shallow platen ($B = 135.7 \pm 18.26$, $A = 0.016 \pm 0.0009$) and 30° steep platen ($B = 131.6 \pm 23.17$, $A = 0.014 \pm 0.0008$). The complete set of values for each contour are shown numerically in Table 4.2 as well as graphically in Figure 4-9.

Table 4.2: Mean Loss stiffness results (k'') \pm 95% CI for the three tested contoured platens at 0°, 7° and 30° for all frequencies in the frequency sweep of 1 – 90 Hz.

	Frequency / Hz							
	1	8	10	12	30	50	70	90
0° Flat Platen / N/mm	118.56 \pm 9.8	121.15 \pm 8.2	128.28 \pm 7.7	134.65 \pm 7.7	195.96 \pm 9.2	272.44 \pm 13.1	350.71 \pm 18.0	428.72 \pm 24.0
7° Shallow Platen / N/mm	147.32 \pm 12.4	142.48 \pm 8.8	150.27 \pm 8.8	157.86 \pm 9.0	235.00 \pm 14.1	329.81 \pm 21.1	426.90 \pm 28.8	528.29 \pm 36.4
30° Steep Platen / N/mm	139.16 \pm 13.3	139.61 \pm 11.8	145.34 \pm 12.1	150.66 \pm 12.3	207.93 \pm 16.6	279.31 \pm 22.6	351.03 \pm 29.4	428.48 \pm 36.2

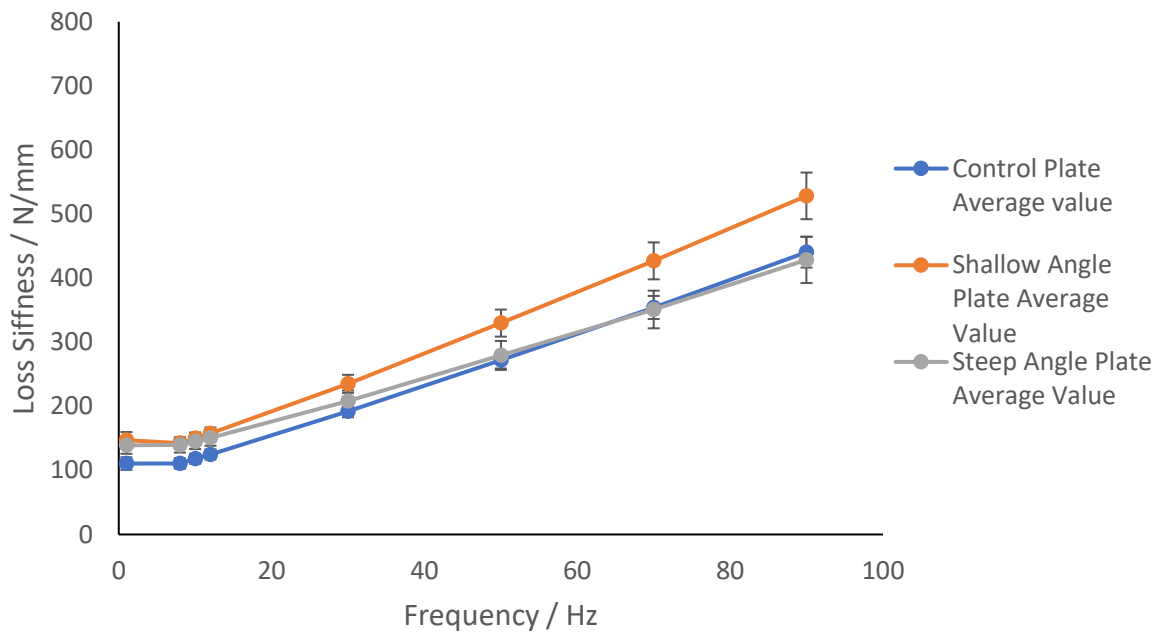


Figure 4-9: Loss Stiffness results of the bovine humeral tissue of the three different contours of testing platen plotted against frequency ranging from 1 to 90 Hz. Values shown are the mean \pm 95% confidence intervals ($N = 4$, $n = 1515$).

Similar to storage stiffness, the 0° platen produced a significantly different response ($p < 0.001$) to both the 30° steep and 7° shallow platen when focussing on parameter C (equation 4.2) with no significant difference seen between the 30° steep and 7° shallow platens ($p > 0.5$). The second parameter (D, Equation 4.2) also showed that the 30° steep platen ($D = 0.014$) produced a significantly different response ($p < 0.001$) to both 0° and 7° shallow platens ($D = 0.017$ and $D = 0.016$, respectively), however, 0° and 7° shallow platens did not produce a significant difference ($p > 0.05$).

4.3.2. Hysteresis Analysis of Biological Data

Figure 4-10 displays the hysteresis loops for a specimen loaded at a frequency of 1 Hz and 90 Hz on the 3 base platens, 0° (A & B), 7° shallow (C & D) and 30° steep (E & F). The peak displacement was observed in the 0° at approximately 0.021 mm (1 Hz) and 0.027 mm (90 Hz); platens with 30° providing values of 0.018 mm (1 Hz) and 0.023 mm (90 Hz). Going just by the visual indicators of Figure 4-10C & D it would seem that the least amount of energy is dissipated when the contour is at 7° as shown by the smallest difference between the loops of the hysteresis, this is confirmed by the values in Table 4.3.

Energy Dissipation was found to be frequency dependent at loads of 10 Hz and higher. This characterisation was mimicked across all three of the contoured platforms as seen in Figure 4-10 and Table 4.3. A significant difference between the 30° and both the 0° and 7° platens was identified (ANOVA, $p < 0.001$). The 30° steep platen consistently dissipated the greatest mean amount of energy at 0.077 mJ, 175% times the values of the 0° flat (0.042 mJ) and 7° shallow platens (0.041 mJ). No significant difference was found between the values of 0° flat and 7° shallow platens ($p > 0.05$).

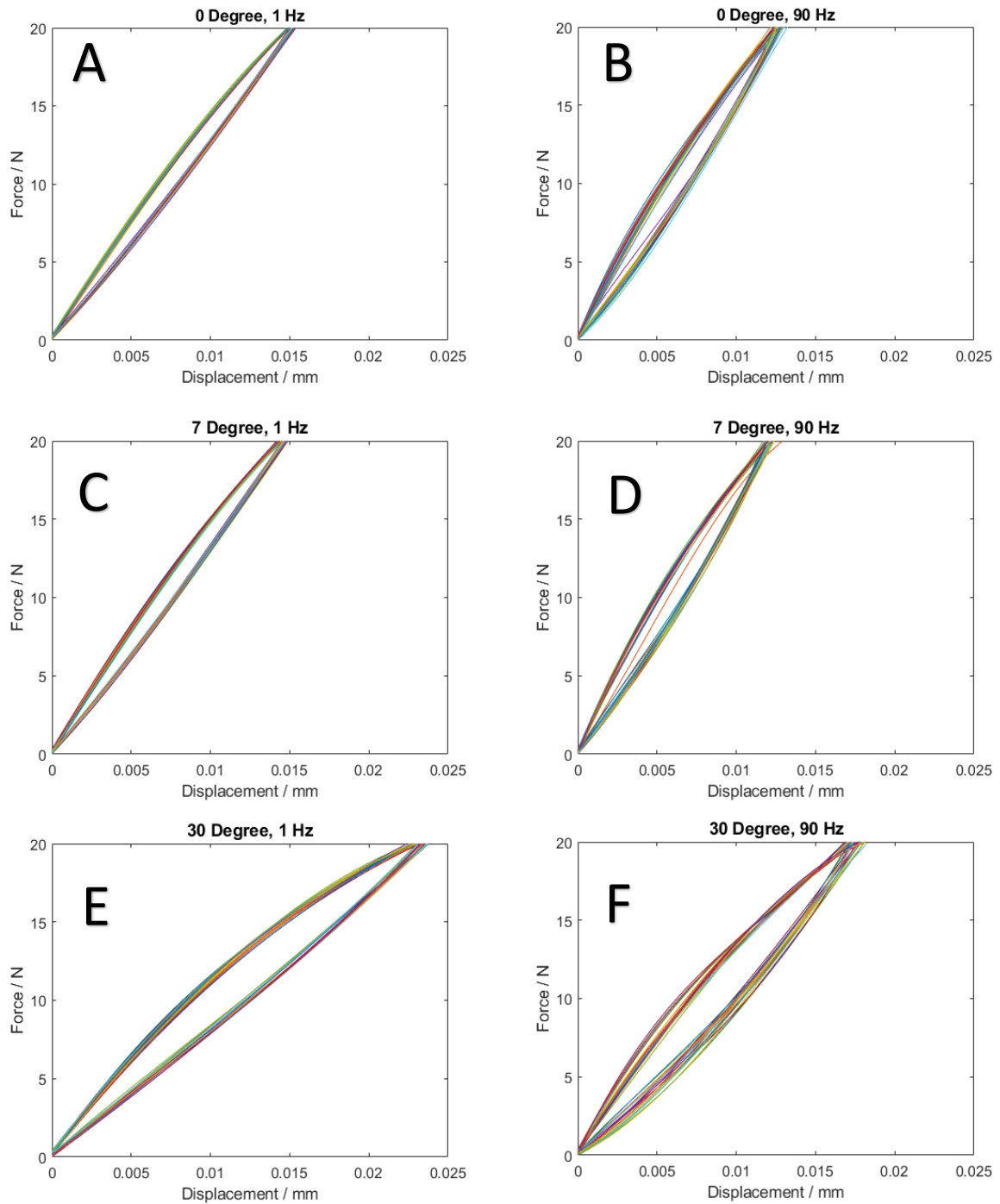


Figure 4-10: Example hysteresis loops from a random sample for the three contours from top to bottom: 0°, 7° and 30° platens and from left to right for when the cyclic loading is applied at 1 Hz and 90 Hz respectively. Colours of the graphs represent individual cycles of the load.

Table 4.3: Energy dissipation results for all samples ($N = 4$, $n = 15$) when tested over all contoured platens. Results shown are mean output \pm 95% CI for each frequency and contour.

Energy Dissipation Results Averages / mJ									
Frequency									
Contour	1	8	10	12	30	50	70	90	Mean
0	0.056 \pm 0.011	0.059 \pm 0.012	0.023 \pm 0.004	0.029 \pm 0.007	0.033 \pm 0.007	0.040 \pm 0.007	0.046 \pm 0.007	0.052 \pm 0.007	0.042 \pm 0.012
7	0.058 \pm 0.008	0.061 \pm 0.008	0.028 \pm 0.006	0.028 \pm 0.005	0.030 \pm 0.006	0.036 \pm 0.006	0.040 \pm 0.007	0.046 \pm 0.007	0.041 \pm 0.012
30	0.111 \pm 0.016	0.122 \pm 0.019	0.056 \pm 0.015	0.056 \pm 0.014	0.058 \pm 0.015	0.065 \pm 0.014	0.071 \pm 0.015	0.077 \pm 0.018	0.077 \pm 0.024

Figure 4-11 displays the how the displacement varies with regards to the time progression of the test for a specific sample at the three contoured platens for both A) 1 Hz and B) 90 Hz. The peak displacement is also shown for all 3 contours decreases when the frequency of load is increased, for the given example at 30° it goes from ~0.0180 mm to ~0.0125 mm at 7° from ~0.0155 mm to ~0.0125 mm and for 0° from ~0.0100 mm to ~0.0900 mm.

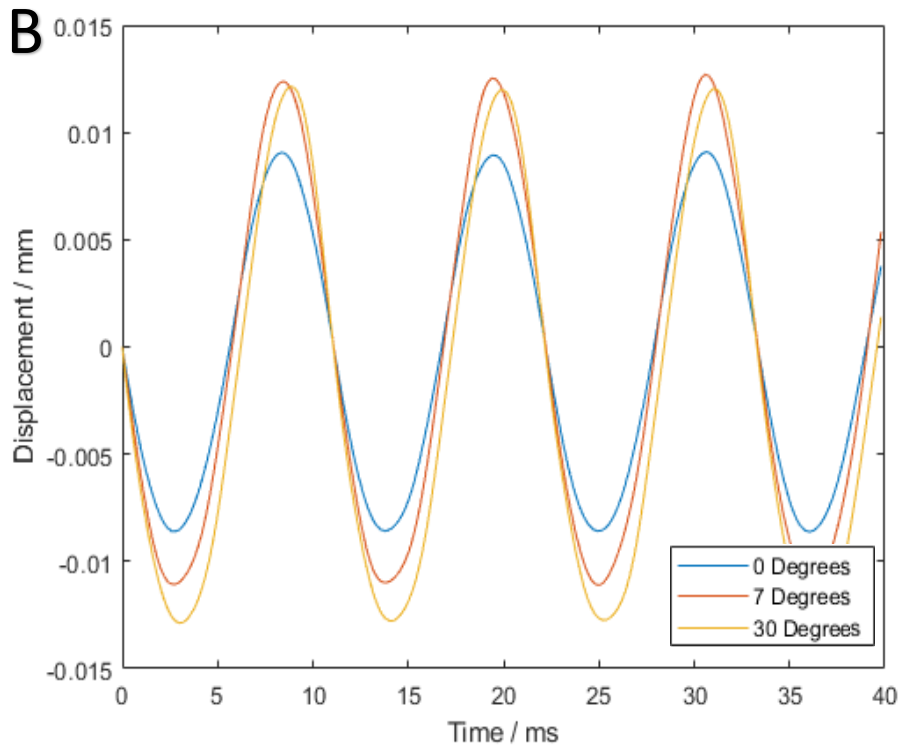
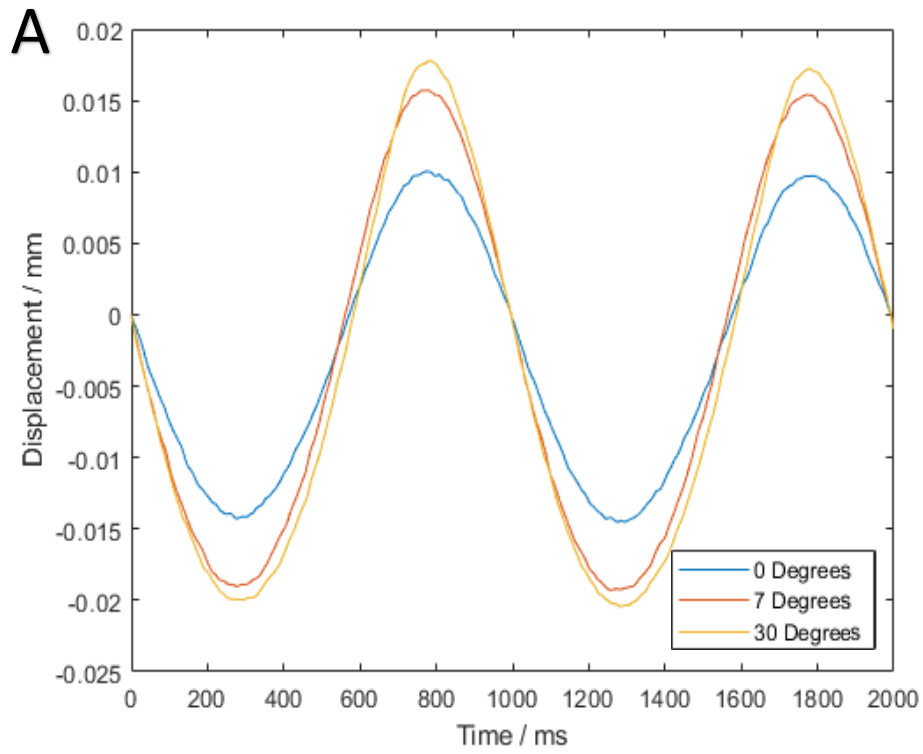


Figure 4-11: Sinusoidally varying displacement A) at 1 Hz (equivalent rise time 500) B) at 90 Hz (equivalent rise time 5.4 ms).

4.4. Discussion

In this chapter, it has been established that the mechanical response of bovine articular cartilage will differ as a structure when compressed using different angles of platen. This is the first study to evaluate how shape alone, under DMA, alters the mechanical response of AC having investigated two inclination angles relevant to a joint contour. Previous studies have focussed on the mechanical response of the tissue samples under a range of conditions, but had not evaluated the effect of the *in situ* joint contour on the mechanical response to loading of the AC. The work has been inspired by the tibiofemoral joint, and specifically the tibial spine and tibial plateau. DMA performed on AC strips at angles representing the tibial spine (30°), tibial plateau (7°) and a control 'flat' plate (0°) have shown that there is a difference in the mechanical response of the tissue under these conditions. It was seen that there was not a direct correlation between an increase in testing angle to mechanical stiffness, rather that the two angled platen resulted in a change of approximately $\pm 20\%$ from the 0° platen for storage stiffness in opposing directions and resulted in a change in curve formation for loss stiffness, as represented in the parameters approximations (Eq. 4.1 & Eq. 4.2). Prior studies of bovine cartilage have shown that both storage and loss stiffness are frequency dependent[31] and these findings have been shown to hold true when the angle of the testing platen is altered. Due to the material of the base platen being altered direct comparison to other studies is not possible without an appropriate adjustment being made. Fell et al. [23] performed similar DMA tests and used the same logarithmic fit as defined in Eq. 4.1 but used a metallic base platen instead (when testing AC off bone). Storage stiffness values were on average approximately 1.5 times greater on a metallic platform than our printed material platens when comparing

purely the 0° platen, 1716.19 ± 109.74 N/mm versus our recorded results of 1118.5 ± 36.1 N/mm.

The loss stiffness trends were different to those reported by Fell et al. and Espino et al. [23], [30]. Instead of the logarithmic relationship between loss stiffness and frequency an exponential one is seen instead. This would most likely be down to the base platen having an effect on the dissipation of the energy. When compared to the average values in [23] the loss modulus results obtained in this study are 1.5 times greater (~ 210 N/mm vs ~ 320 N/mm). Although there was ample variation between the studies the results were still of the same order. This demonstrated that the PLA that was used to print the designed angular platforms provided a similar testing bed to its metallic counterpart, as backed up by the quality of the print and CT data discussed in section (4.1.2). Modulus values are excluded here due to possible bias introduced with the definition of the shape factor over the curved platen surface thus structural stiffness was used as the comparison factor.

AC *in situ* is under confined tension as a result of its attachment to the bone below, however, over two thirds of studies perform unconfined or confined compression with very few testing *in situ* [162]. It was deemed a requirement to enforce the position of the cartilage to be fixed during the DMA reducing the likelihood of errors due to sample movement, also simulated its in-vivo dynamic where they would be no lateral movement possible. By extension of the work by Fell et al. [23] who identified the need to consider the whole osteochondral and the known restrictions that bone provides to the AC [171] the addition of a constraining technique was deemed appropriate. To attempt to replicate the *in situ* tension as perpendicular to the applied load, the compromise was to restore the cartilage to its original *in situ* length across

the base platen. A future improvement to the work would be to measure the tension on each of the tissue samples to allow for consistency during sample preparation.

AC morphology

It should be noted that this study used bovine cartilage as a model for human cartilage. Human cartilage is known to be around 0.3-0.5 mm thicker than bovine cartilage [31], [169] but has been used as a recognised dynamic model for human cartilage with adjustment of around half the respective bovine values [31]. Another allowance that was made was the use of humeral tissue over tibial, however, the thickness differential between the joints has been shown to be minimal with Seedhom et al. [172] classifying tibial cartilage thickness where it is under direct load at ~2.6 mm and Carlson et al. [173] demonstrated humeral AC thickness to be ~1.8 mm.

There is a lot of previous evidence on the subchondral bones effect on AC properties [23], [66], [155] and how these AC properties effect joint congruency[172]. Thus having additional control over the platen that cartilage is tested upon allows further mimicry of physiological condition. If the material properties of the base platen allow, being able to test just cartilage samples on a bone representative AM platen would reduce the need for complete tissue sample. This would make it easier to obtain this type of experimental data due to lack of tissue availability in the field. Adjusting the print specifications of the compression components could allow the cartilage to be tested upon a material that is similar to subchondral bone in its material response. Allowing, cartilage to be tested independently, but still with physiological relevance. This could also be extended to the field of customised medical implants where 3D printing has already seen use [174], [175] by matching the substrates mechanical properties to those known in literature, an idea that will be touched on in chapter 5.

Mechanical response of bovine AC

The difference reported in storage stiffness of the AC for the 30° steep to the 0° platen can be explained through the change in the orientation of the collagen fibres that are being compressed. As reported by Northeast et al [56] the off-axis stiffness k'_a can be modelled by Eq. 4.3:

$$k'_a = k' \cdot \cos^2 \theta \quad (4.3)$$

Where θ is the orientation change and k' is the stiffness of the tissue under original conditions. With our orientation of a 30° angle the expected alteration would be 0.75 and when applied to our experimental results of 1118.5 N/mm an expected value of k'_a would be 838.5 N/mm which is close to the reported value of 935.7 N/mm seen in our results, a 17% difference. This supports not only the case that the angle upon which the load is applied affects the ability of the tissue's response to the load. This is supported by the increase of thickness of AC on the tibial spine reported by Cohen et al. [118], which in turn has been shown to increase the storage stiffness of the tissue.

The change of a 17% increase seen from 0° to 7° shallow platen in storage stiffness is harder to explain. This again, may be a result of collagen fibre orientation within the tissue. It is well reported in the literature that cartilage orientation is perpendicular to the load at the surface layer and as you progress deeper there is a transitional layer [49], [176] where the orientation changed relative to depth to eventually become parallel to the load. As such, it could be the case that the slight angle orientation is allowing some of this transitional layer to change into a perpendicular orientation, allowing for an increase in the stiffness of the tissue.

The loss stiffness of our tissue is seen to follow a different trend to previously reported studies, fitting to an exponential curve rather than logarithmic. Using the bovine-human

adjustment previously calculated the loss stiffness values that were obtained were ~108 N/mm. When this is compared with the previous results obtained in other human tissue studies, 218 N/mm [18] and 106 N/mm [30] our values are seen to be within a reasonable range of results in literature. It was seen that the loss stiffness increased with frequency for all contoured testing platens (0°: 118.56 - 428.72, 7°: 147.32 - 528.29, 30°: 139.16 - 428.48 as frequency changed from 1- 90 Hz) but differed in its ability to dissipate energy based upon the angle of testing. The difference seen between the 0° or 7° shallow angle ($A = 0.017$ and $A = 0.016$ respectively) and 30° steep platen ($A = 0.014$) reported in the ANOVA ($p < 0.001$) highlighted a difference in behaviour of AC when on steeper contoured surface. This demonstrates that the 30° contour that is representative of the tibial spine alters the dissipation of energy, which helps to explain the characteristic increase in the thickness of AC on more angled surfaces [23], [67].

When analysis the hysteresis loops energy dissipation was also shown to vary as the contour increased with the 30° contour dissipating 0.077 J, 175% compared to 0° flat (0.042 mJ) and 7° shallow platens (0.041 mJ). This suggested that when AC is under angled load, such as in the tibial spine, its ability to dissipate energy is greater than at a shallower contour. Both 0° and shallow experiments recorded a larger increase in loss stiffness from the baseline at 1 Hz than the 30° steep angle, as seen by parameter B of equation 5. It could be argued that this is due to the misalignment of the deeper collagen fibres within the tissue and their reduced ability to dissipate energy [56].

Limitations and future work

In this study the location where the cartilage strips were harvested from was not the area that was being intended to be mimicked, i.e. the tibial spine. This was due to the inability to get a large enough strip from the specified locations and the availability of donor tissue. As the thickness of AC is in a consistent range of 1.66 to 2.91 mm consistent across the human tibial plateaus [118] an assumption that the strips taken from the bovine humeral heads would be an accurate substitute was made [177] with aforementioned appropriate adjustments made.

The printed components that were used for this study introduced a new material construct that has to be accounted for. PLA as a full thickness sample, has a storage modulus of approximately 10,000 MPa at room temperature [57] compared to AC reported modulus of 34.4 MPa [18]. However, PLA can be printed as a customisable lattice structure which has been shown to provide varying mechanical properties [178], [179] that could be utilised to mimic the tissue transition from to cartilage to bone in our base platens. The porosity of the platens that are seen in Figure 4-3 and the additional compliance that it could introduce was identified as a possible limitation. However, the preliminary work and results in Section 4.2.2 demonstrated that this should not be of concern. This provides us confidence in the analysis of the results and that the deformation being measured is that of the AC. However, as previously stated, to provide 100% clarity in a repetition of this study the components could be altered to be printed at 100% infill.

The experimental work performed in this chapter identifies the possibility that the simulations in Chapter 3 should also be performed on a similar range of representative angles in future iterations of the study.

4.5. Conclusions

This study has demonstrated that there is a significant difference in the dynamic response of bovine AC when loaded on differently contoured base platens with the angle of contour as an independent variable. A small angle of 7° resulted in an increase of 16% in storage stiffness and for loss stiffness; 29.2% increase of variable A and 15.6% increase of parameter B of the regression equation 5. Whilst an angle of 30° caused a decrease in storage stiffness of 19.5% and a shallower gradient of the incline trend in loss stiffness versus frequency. The frequency dependent nature of AC was conserved under the different testing conditions with the only trend changes being in the 0° flat platen in storage stiffness and in 30° steep angle loss stiffness result. It was also shown that the AC's ability to dissipate energy changes with regards to contour and that tissue structures such as the tibial spine where the contour is larger may have a greater ability to dissipate energy. From these results the importance of replicating physiological testing conditions highlighted not only in the loading frequencies but in the testing platen angle.

Being able to create a physiologically relevant testing platen could see use in future experiments mimicking the *in situ* loading conditions of AC. Overall, this work has demonstrated the need to evaluate the current methodologies of mechanically testing AC and in particular when mimicking the *in situ* joint contours that have been shown to alter the mechanical properties of AC. Having now developed a joint scale test using AM, the next chapter will focus on developing test samples which exploit AM to develop structured osteochondral cores, can the hierarchical AC on bone structure and mechanics be mimicked?

Chapter 5. Feasibility Assessment of an AM osteochondral core replacement unit – Bovine tissue comparison.

5.1. Introduction

Additive manufacture (AM) can be a useful tool to mimic biological conditions and has potential to be further integrated into the mechanical evaluation of tissues. This has been explored on a macro scale in Chapter 3. Within that study the focus was on the geometrical design of the printed components, but mimicking full scale anatomy is only one of the parameters that AM can allow to be investigate. AM has already been utilised in a number of research studies on joints, more specifically as a substitute for implants[174], [175], and other tissue engineering products such as functionalised hydrogel bioinks[106]. This current chapter, instead, focuses on the feasibility of utilising AM in synovial joint replacement surgeries by designing a construct that can mechanically mimic the response of bone and cartilage under physiological loads.

The design of AM unit cells can be exploited to provide porous networks, adjustable surface contours and anisotropic or isotropic mechanical response properties [179], [180]. These physical properties are key to the inclusion of AM into the medical field, with each providing different research fields an opportunity for utilisation of the technology. Pores within the unit cells are defined through both the geometry of the shapes used as well as the infill percentage that controls how densely the unit cell is repeated within a given space.

Two techniques useful to evaluate any AM constructs are Micro-CT and DMA. Micro-CT has been previously used on AM components [181], [182] and tissues samples [183], [184] to provide non-destructive numerical and visual analysis of

specimens. The high resolution that Micro-CT provides of 5–150 μm [185] enables the interior of the sample to be imaged. Given the printed resolution between 10 - 250 μm [186], it will provide the ability to evaluate the quality of the structures within a relative range of dimensions. The output of the micro-CT analysis will provide not only three-dimensional visualisation of the samples, but also values that quantify the porosity and trabeculae dimensions of the bone internal structure and unit cells of the AM parts. DMA will provide values of storage and loss stiffness to evaluation the energy storage and dissipation respectively of all AM and tissue samples. This will be the same as performed in chapter 4 (section 4.2.3) and will provide a similar data set to the one that is utilised with chapter 3 (section 3.1.2).

The first section of this chapter will be focused on evaluating how the internal structures of the osteochondral core change having been loaded by a physiologically relevant load. This will provide valuable insight into how the internal components react to load and whether any lasting effects are present within the structure. It has previously been demonstrated that cartilage has the ability to adapt its properties to its loading situation [30], [117], [187] but less work has been done looking at how the bone in the epiphysis changes and whether permanent changes can occur. Bone has been shown to adapt and remodel [188], [189] in long bone evaluations, however, extending this work to the epiphysis will provide valuable insight into future structural components and material property requirements of implant designs. The effect of DMA with physiologically relevant loads on tissue microscale geometry is a subject that is yet to be explored.

The second section of this study aimed to assess the feasibility of producing an AM component that is mechanically and geometrically similar to bovine osteochondral core tissue samples. This is approached via a progressive analysis of different AM

unit cell designs through rapid prototyping. The focus of the parameters to control in this feasibility study is the orientation of print, the resolution of the print, the infill percentage, and the outer shell diameter. These would all also alter the mechanical properties of the design and have been shown to be effectively optimised before using mechanical response as a decision making tool [190]. The shell is a required component of the design but is not comparable in structure to the tissue samples, thus the focus is on matching the internal structures. Due to the shell providing a lot of the mechanical stiffness we will test to see if there are differences seen in the storage and loss moduli by altering the internal structures of the units. DMA and Micro-CT imaging are to be used for analysis of the storage/loss stiffness and porosity/trabeculae data, respectively. Finally, the feasibility of producing a construct mimicking the tissue cores' hierarchy will be evaluated. Osteochondral cores will be initially tested to gain DMA and Micro-CT for initial validation of proof-of-concept.

5.2. DMA and Micro-CT Analysis of the Osteochondral Unit

5.2.1. Experimental overview

This section presents two experimentation techniques, DMA (Section 5.2.3) and Micro-CT (5.2.4) to investigate the interior geometrical structure of AC and whether loading of the tissue affects this microstructure. This will provide valuable insight into the design parameters that need to be taken forward into the AM work in section 5.3.

The experiment will be laid out as follows to gather the expected data output:

1. Specimen preparation and dissection (Section 5.2.2)
2. Micro-CT imaging of all samples to obtain a set of images and numerical data points based on the geometry of the samples. This will include statistics on: Porosity (Open and Closed), trabecular thickness and trabecular separation.
3. DMA will be performed using physiologically representative loads upon each sample once to gain mechanical response data. This will be used to compare AM constructs in section 5.3. All samples will be checked for damage post testing to confirm viability is intact and no visual changes have occurred.
4. Micro-CT imaging of all the samples a second time to gain the same set of data points but this time post DMA loading.
5. Comparative analysis of pre and post DMA loading Micro-CT image data sets as well as statistical analysis.

5.2.2. Dissection and Specimen Preparation

Bovine humeral heads (Figure 5-1A) taken from 18 month-old livestock, that was otherwise destined for the food chain, were selected as the joint utilised in this study to gain cartilage on bone tissues. The tissue was obtained through a local supplier (R Brown Butchers, Harborne, UK) and on delivery to the lab was frozen at -40° until it was to be used. This joint choice provided a large flat surface from which samples could be harvested and has been to be comparable to human tissue in its mechanical response to physiological load [169].

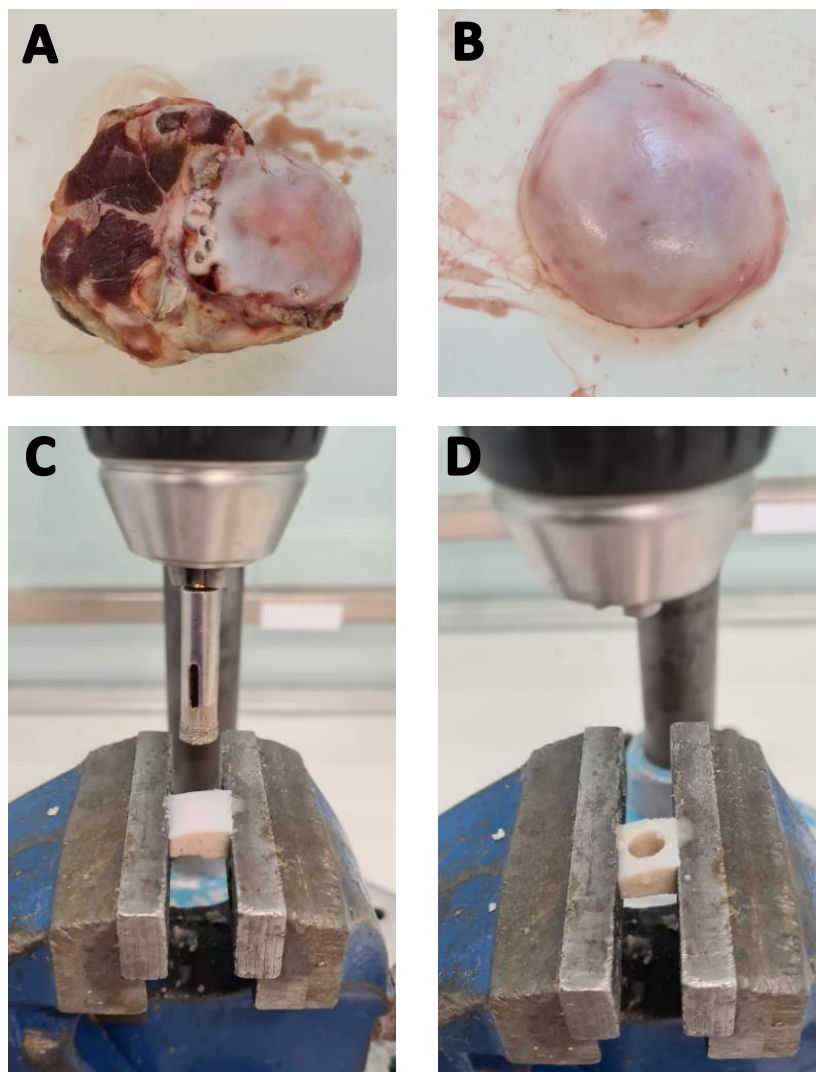


Figure 5-1: Articular Cartilage samples. A) Bovine humeral head as retrieved by suppliers, B) Cap of ball joint removed using hacksaw, C) Sectioning of unit of osteochondral core clamped and being prepared for drilling via use of a vertically positioned pillar drill with a borer attachment, D) post coring with circular unit removed from the tissue.

The cap of the joint samples was removed using a hacksaw (Figure 5-1B), with the joint clamped in a table-top vice but with the surfaces cushioned using disposable cloth. A total of 6 osteochondral units were taken from the joint cap and placed within airtight vials to ensure there was minimal moisture loss. They were then placed in a refrigerator at 4° and removed 3 hours prior to either DMA or micro-CT scanning and returned back to the same storage post experimentation.

Cubic units of dimensions approximately 15 mm × 15 mm × 10 mm were cut from the joint caps using a hand-held hacksaw. These were held in a vice and mounted under a vertical pillar drill that had a diamond-coated drill bit attachment (Figure 5-1C). A cylindrical sample was then drilled using this 'coring' method. The sample consisted of articular cartilage and subchondral bone (Figure 5-1D). These samples were 8 mm in diameter and approximately 10 mm in height. This ensured the same sample size for each tested unit and the removal of exterior tissue damaged as a result of the hand sawing. Each sample was contained within an airtight vial to ensure no movement could occur during future imaging (Section 5.2.5.2). Sample 5 became damaged due to slippage during the boring process and thus was excluded from the rest of the study.

5.2.3. Dynamic Mechanical Analysis (DMA) of Osteochondral Cores

DMA was performed with the same conditions as previously defined in section 4.2.3 and used in the study by Mountcastle et al. [18] when analysing human osteochondral cores. Full details, including calculations of storage and loss moduli, are provided in section 2.3. In brief, DMA was conducted using a Bose ElectroForce

3200 material's testing machine controlled using WinTest 4.1 software (Bose ElectroForce Group, New Castle, Delaware, USA, now TA Instruments).

The test involved applying a sinusoidal compressive load between 37.7 - 85.5 N, following a preload of 4 N. This load range induced a stress of between 0.75 -1.7 MPa. This stress range has been estimated as mimicking the stress induced on the tibial-femoral joint during walking [146]. A frequency sweep was used to apply the sinusoidal loading, which was 1, 8, 10, 12, 30, 50, 70, and 90 Hz, this is the same test set up as in section 4.2.3. A single test was performed on each sample, over this short time dehydration is not expected to occur [29], subsequently, they were returned to the same airtight vial ready for micro-CT analysis.

5.2.4. Micro-CT Scanning and Reconstruction of the Osteochondral Unit

Micro-CT was performed on samples using a Skyscan 1172 scanner (Bruker Micro-CT, Belgium). Each sample was scanned individually using a low X-ray attenuation tube after being fixed in place to ensure no movements occurred during the scan. The same settings were kept as constants for all samples and were set as follows. A 180° scan was performed with 67 Kv maximum X-ray energy and 8 W beam power, using no filter and a pixel size of 9.01 µm. Reconstruction of the CT data was performed with NRecon (V1.6.10.2, Bruker Micro-CT, Belgium) using a beam hardening correction of 71%, a ring artefact correction of 3.0, and a smoothing value of 2.0. Three-dimensional reconstruction of one of the samples is shown in Figure 5-2A with an individual slice of said sample displayed in Figure 5-2B.

Three-dimensional analysis of the reconstructed images was performed using CTan (V1.16.4.1+, Bruker Micro-CT, Belgium). To limit the effect of 'swarf' on the results, a circular region of interest was used for all samples that was 165×165 pixels or $4.46 \text{ mm} \times 4.46 \text{ mm}$ with the number of image slices being 125, 150 or 175. A comparison of an original image slice to a Region of Interest (ROI) restricted image slice is seen in Figure 5-2B and in Figure 5-2D, respectively. A 3D reconstruction of the limited ROI and slices is shown in Figure 5-2C. The settings to perform the imaging were

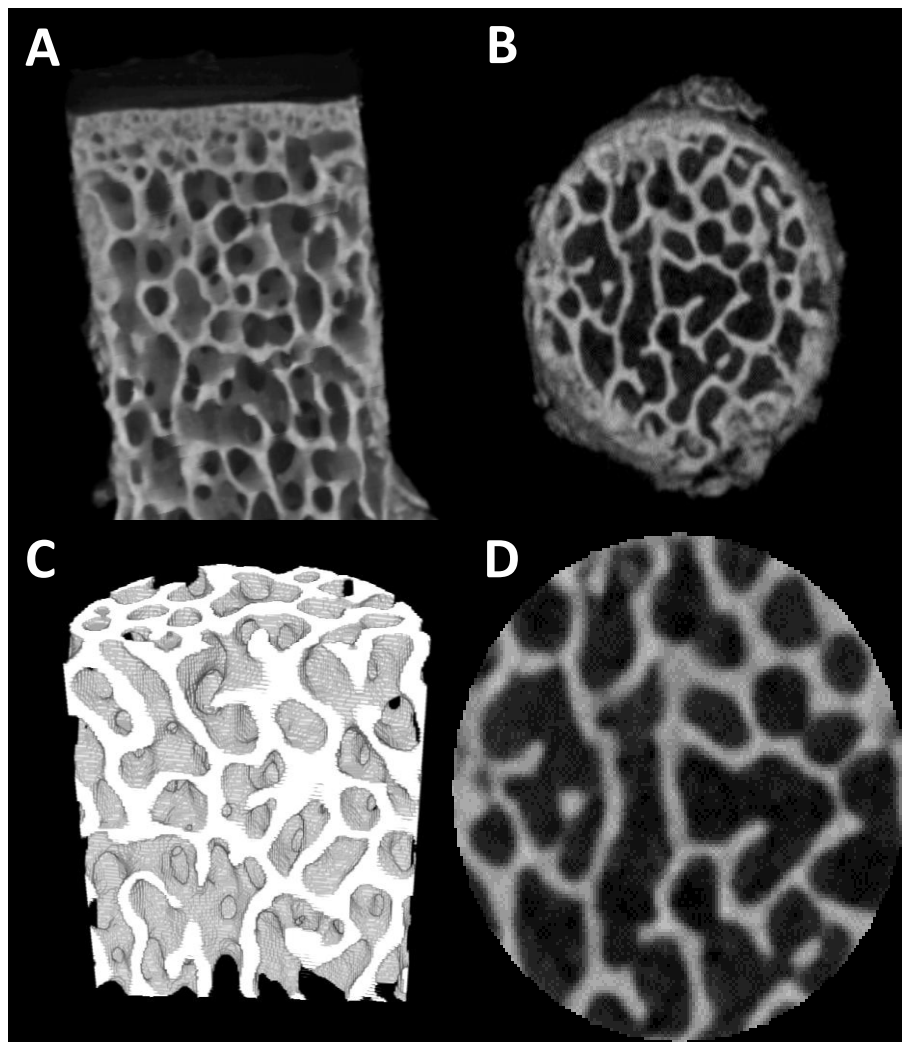


Figure 5-2: Sample micro-CT reconstruction. A) 3D reconstruction of a complete osteochondral core. B) Cross-section of a slice of the core demonstrating the swarf that is present in the sample after coring. C) 3D visualisation of the chosen ROI within the core sample. D) Cross section after ROI has been applied to only analyse true tissue parameters.

determined using a trial and error approach, with the goal of maximising the clarity of the internal structures of the sample.

Images were analysed using morphological tools, applied to each sample in a specific order. Firstly, the image stack was reduced to a binary representation using a threshold, this was set at a lower grey threshold of 72 and higher grey threshold of 255. The despeckle operation was then applied on groups of black pixels of size 50 or below to reduce the noise in the image. A 3D analysis was then performed to gather the open and closed porosity values, trabecular thickness, thickness distribution, separation, and separation distribution. An example set of images was saved at each stage of the process and are displayed in Figure 5-3. This process was then extended to the complete data set for visual analysis. Trabecular thickness related to the mean thickness of the trabeculae or the solid components of the tissue, and trabecular separation measuring the mean gap of the pores in the joint, could be visualised with regards to an image of the data set (Figure 5-4). The same set of analytics was performed pre- and post-DMA testing to allow for comparison of how the load affected the tissue.

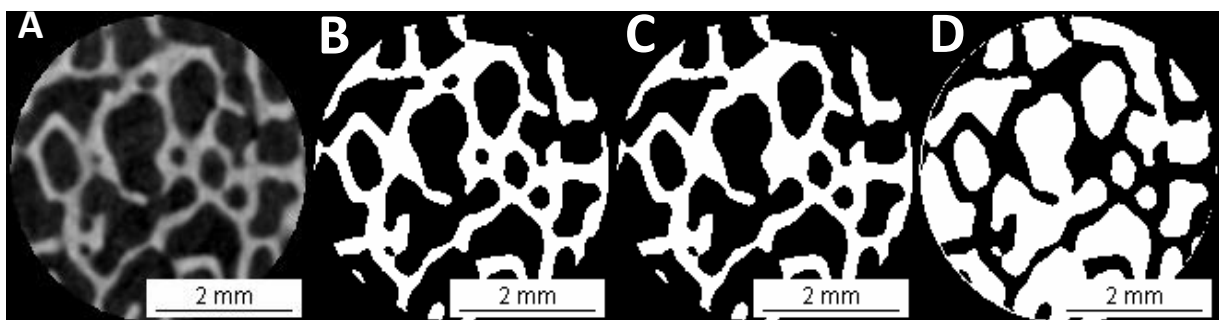


Figure 5-3: Image slice as it progresses through the analysis as follows: A) Greyscale CT image, B) Threshold applied image slice, C) Despeckled image in the 3D domain slice, D) Open porosity image slice.

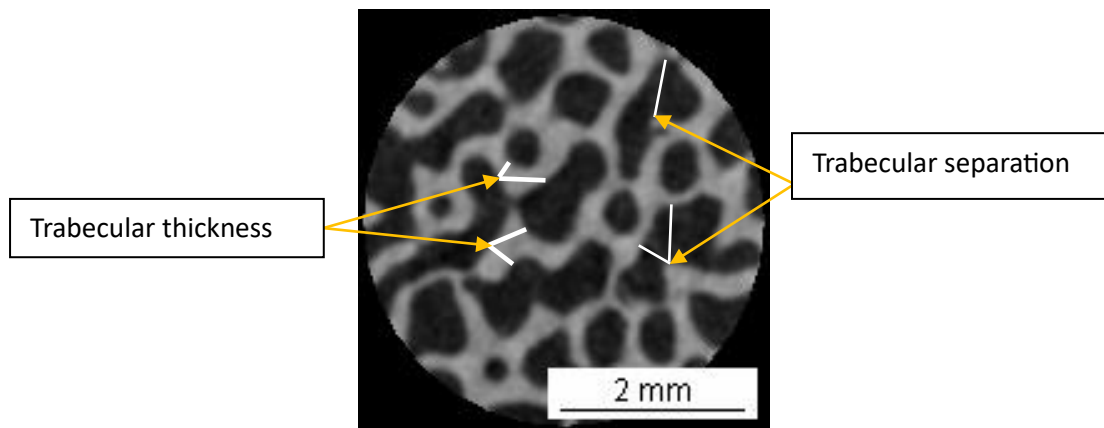


Figure 5-4: Visual representation of trabecular thickness and separation with regards to the image data set that is used within this study.

The methodology demonstrated in Figure 5-4 represents the automated process that CTan (V1.16.4.1+, Bruker Micro-CT, Belgium) goes through to provide the measurements of trabecular thickness and separation. There is no user interaction with how it calculates these values bar the original definition of the ROI, further information can be found in Mys et al [191].

5.2.5. Data analysis - statistical tests

Two types of statistical tests were performed on the results data in section 5.2.5. For values of open and closed porosity and mean trabeculae thickness and separation, paired t-tests were used to evaluate the variation between pre and post tissue characteristics. In order to compare the trabeculae thickness and separation distributions, Q-Q plots were used to compare the values present in each of the quantiles for the two distributions.

5.2.6. Results

5.2.6.1. DMA Outputs of Osteochondral Cores:

Of the 6 samples obtained, five were suitable for testing (see section 5.2.3). All samples were tested utilising the same metal platens for full compression, with results for storage and loss moduli shown in Figure 5-5.

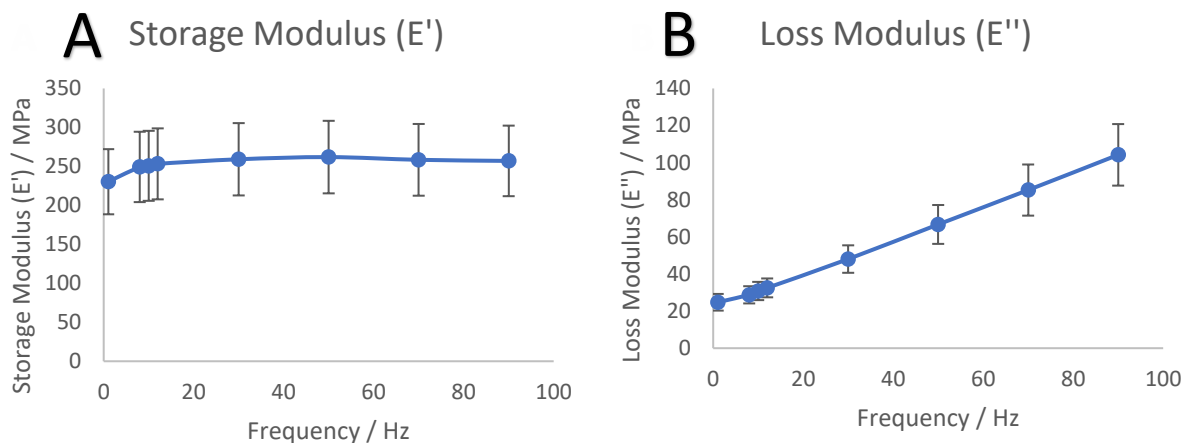


Figure 5-5: Storage (A) and Loss (B) moduli for osteochondral cores plotted against frequency from 1 to 90 Hz (mean \pm 95% confidence interval, (N = 5) with natural logarithmic trendlines). Results are displayed on a linear scale.

Storage Modulus

The mean value for storage modulus, E' was 252 ± 9.32 MPa. An empirical, logarithmic relationship was observed for E' with respect to frequency. There was an increase of storage modulus with respect to a frequency increase of 11.6% between 1 Hz and 90 Hz (Figure 5-5A).

Loss Modulus

Loss modulus was also identified to be frequency dependent with respect to E'' , Figure 5-5B. As E'' increased, the observed loss modulus also increased with an exponential trend. It was also observed that there was more variation between

samples as the frequency was increased to 90 Hz. The mean value for loss modulus was 52.6 ± 27.8 MPa, a large deviation being the results of the trend noted above.

5.2.6.2. Micro CT analysis of pre and post DMA

Segments of 125, 150 and 175 image slices were all tested. This enabled the avoidance of vertical bias within core by performing analysis on whether there was variability in the tissue based on different height segments of the overall core that was extracted from the tissue. The segmented sections were separately run through the analytical script in CTan which produced values for open and closed porosity as well as trabecular thickness and separation for every image slice selection.

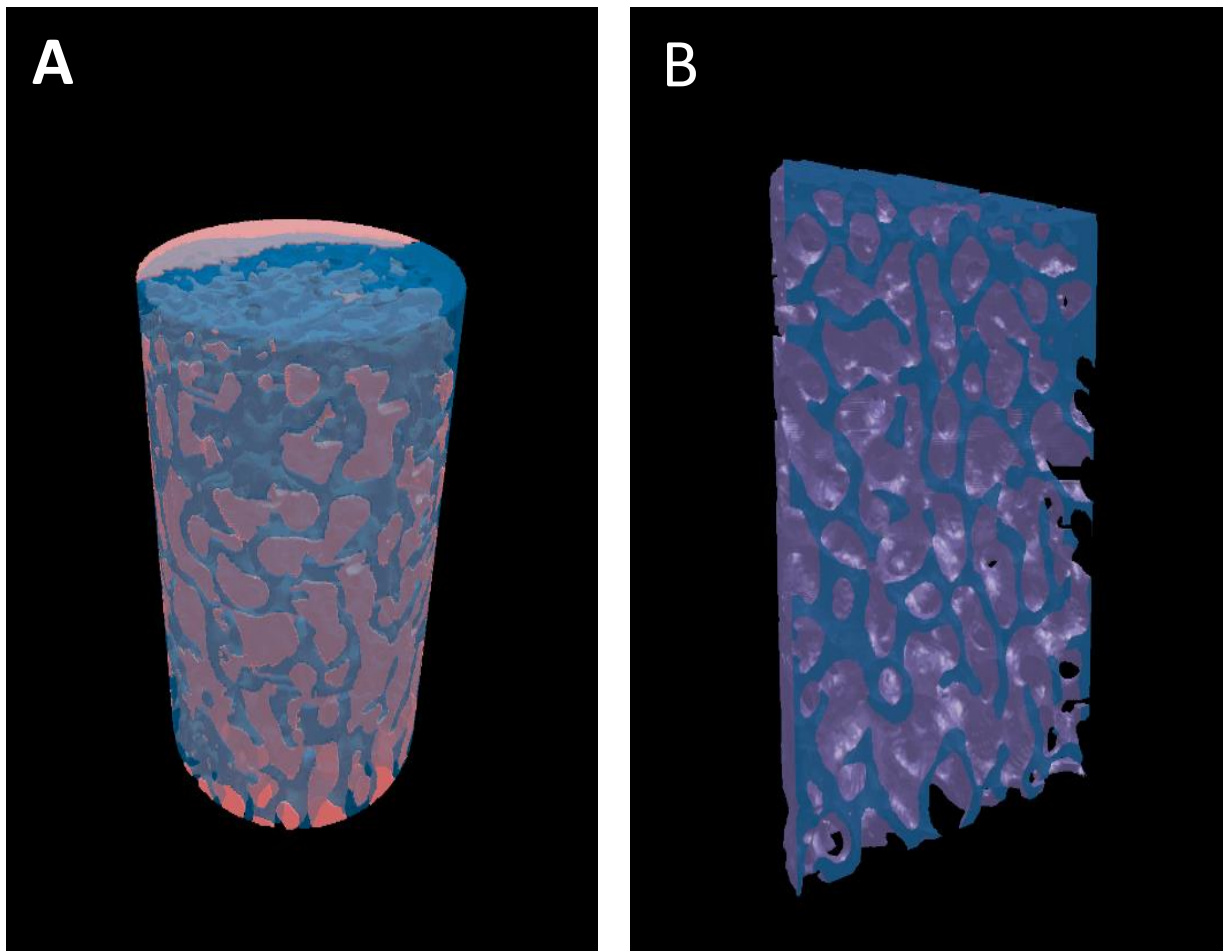


Figure 5-6: 3D reconstruction of the osteochondral unit, pictured is sample 1. In both pictures the blue portions are the trabeculae and red is the pores than run through the tissue.

The reconstructed images were visualised in CTVol to demonstrate the porosity throughout the layers in the tissue samples (Figure 5-6). The Blue segments of Figure 5-6 highlight the trabecular bone that is present in the samples and show the distribution of thickness throughout the height of the sample. We can see from this image that the bone becomes thicker and less porous towards the upper edge of the core where it was in contact with the cartilage. The red portions of Figure 5-6A and highlights in Figure 5-6B demonstrate the 3D aspect of the porosity of the bone tissue, displaying a network of vestibules in both the 2D and 3D visualisation.

Figure 5-7 enables the differences between sample 2 and sample 3 for pre and post DMA testing to be visualised. The thresholding of the images shows what information is lost due to the requirement of performing the same reconstruction on every sample. For instance, in sample 2 post DMA in the grayscale image (Figure 5-7 1st row 3rd column) there are clear sections of bone that are of different colour to the porous portions. However, they are then excluded in the binarised image of the same sample (Figure 5-7 2nd row 3rd column).

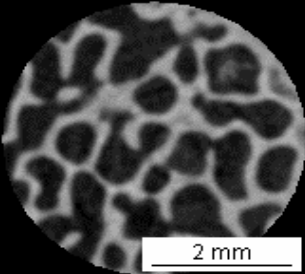
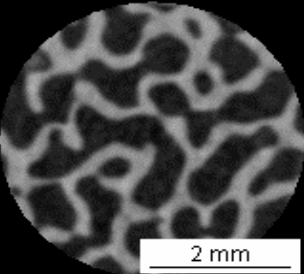
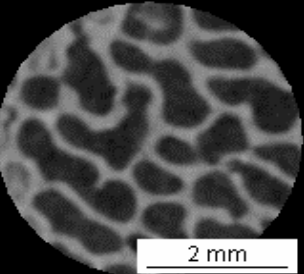
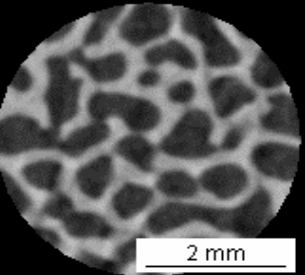
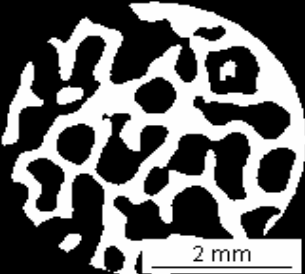
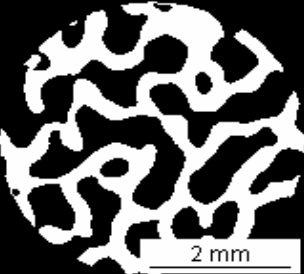
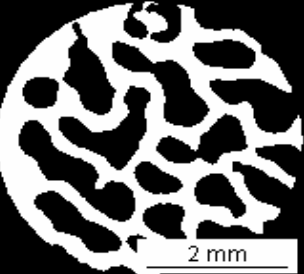
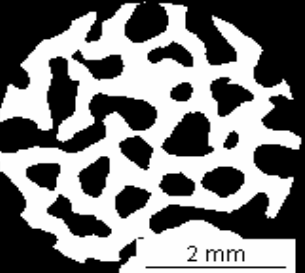
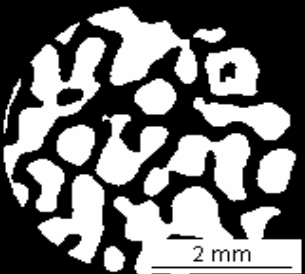
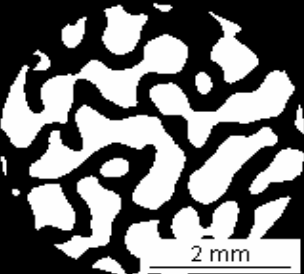
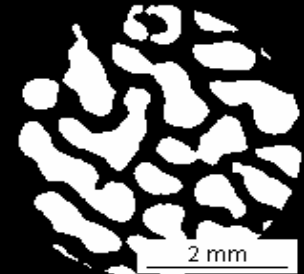
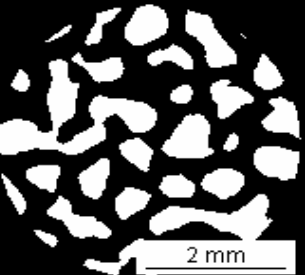
	Before DMA		After DMA	
	Sample 2	Sample 3	Sample 2	Sample 3
Grayscale Bone CT				
Binarised Bone Image				
Binarised Open Porosity				
Total Porosity / %	53.79	41.21	51.04	40.32
Open Porosity / %	53.78	40.49	51.02	40.28
Closed Porosity / %	0.01	0.72	0.02	0.04

Figure 5-7: Micro CT grey scale, binarised and open porosity slice images of sample 2 and 3 pre and post DMA testing. Values of open and closed porosity for each sample pre and post DMA also included.

Pre-DMA Results

Table 5.1: Micro-CT measurements taken before DMA with mean of 125, 150 and 175 image slices analysis results for each of the osteochondral cores. Included is the mean across all the samples for the baseline comparison.

	Sample 1		Sample 2		Sample 3		Sample 4		Sample 6		Mean / 95% CI across samples	
	Mean	95% CI	Mean	95% CI	Mean	95% CI	Mean	95% CI	Mean	95% CI		
Open Porosity %	57.98	0.04	53.78	0.38	40.49	0.67	58.3	0.20	49.2	0.41	51.96	6.62
Closed Porosity %	0.00	0.00	0.01	0.00	0.72	0.10	0.00	0.00	0.02	0.00	0.15	0.28
Trabecular Thickness / μm	239.66	0.27	246.97	2.98	332.17	9.74	205.04	2.16	267.25	0.81	258.22	42.07
Trabecular Separation / μm	446.87	1.35	421.71	1.89	396.28	4.60	389.52	3.52	389.52	3.25	408.78	22.43

All values for pre-DMA testing are displayed in Table 5.1. Individually comparing the samples' mean values across the slice choices, there was minimal variation across both porosity variants (Open at 6.62%, Closed 0.28%). The maximum variation when dependent on number of images analysed was in sample 3's open porosity at a standard deviation of 0.67%. Trabecular thickness and separation also showed very little variation with the maximal 95% confidence interval being 0.36 μm for thickness, a 2.9% variation and 0.17 μm for separation, a 1.1% variation.

Pre-DMA there was negligible closed porosity (median of 0.01% \pm 0.01 and mean of 0.15% \pm 0.28) with one outlier in sample 3 skewing the results. Open porosity, however, produced a mean value of 51.96% \pm 6.62. This is visualised in Figure 5-7 column 1 and 2. Trabecular thickness was measured at 9.55 \pm 1.55 μm and separation measured at 15.13 \pm 0.81 μm .

Post-DMA Results

Table 5.2: Micro-CT measurements taken post DMA with mean of 125, 150 and 175 image slices analysis results for each of the osteochondral cores. Included is the mean across all the samples for the baseline comparison.

	Sample 1		Sample 2		Sample 3		Sample 4		Sample 6		Mean / STD across samples	
	Mean	95% CI	Mean	95% CI	Mean	95% CI	Mean	95% CI	Mean	95% CI		
Open Porosity %	50.15	0.11	51.02	0.34	40.28	0.21	51.65	0.10	51.23	0.50	48.87	4.32
Closed Porosity %	0.01	0.00	0.02	0.00	0.04	0.00	0.01	0.00	0.04	0.01	0.02	0.01
Trabecular Thickness / μm	261.57	1.62	262.39	5.68	331.36	0.54	238.31	2.71	245.88	2.16	267.90	33.04
Trabecular Separation / μm	383.03	1.62	413.87	3.25	373.56	0.27	370.04	4.06	357.87	1.08	379.67	18.90

All Micro-CT data for post-DMA testing are displayed in Table 5.2. The mean open porosity of the tissue measured at $48.87 \pm 4.32\%$, a 4.6% decrease compared to pre-DMA output. The values for closed porosity were low across all samples (maximum values of $0.04 \pm 0.01\%$). Open porosity also had a maximal 95% confidence interval of 0.50, 1% of the mean value. These results along with those taken before the DMA study show there is negligible variation in the extracted parameters depending on the image slice choices during the micro-CT reconstruction process.

Post DMA open porosity was reported at $48.87 \pm 4.32\%$ a 3% decrease to that recorded pre-DMA. However, no significant difference was found ($p > 0.05$) when a paired t-test was performed. Closed porosity was measured as negligible and thus changed between pre and post DMA. No significant difference ($p > 0.05$) was measured in the trabecular thickness with a mean value of $258.22 \pm 42.07 \mu\text{m}$ for pre-DMA data, as compared to $279.90 \pm 33.04 \mu\text{m}$ for post-DMA data. For trabecular separation no significant difference ($p > 0.05$) was measured also

reported with a mean value of $408.78 \pm 22.43 \mu\text{m}$ for pre-DMA data, as compared to $379.67 \pm 18.90 \mu\text{m}$ for post-DMA data.

Trabecular thickness and separation distributions

Due to the 95% CI of each of the individual sample measurements being less than 1% of the total value when comparing between analysis of 120, 150 and 175 slices, we can say with confidence that testing over any range of the total image is suitable. Therefore the distribution measurements were analysed only over the largest data set of 175 images. Trabecular thickness distribution tracks the variability of the trabeculae width throughout the three-dimensional sample reconstruction (Figure 5-8A). Pre DMA the distribution peaked at a value of $243.4 \mu\text{m}$ and post DMA peaked at $270.5 \mu\text{m}$. A statistically non-significant change ($p > 0.05$) but visually present was that post DMA the distribution had shifted to higher values as confirmed by the associated mean value; however, the shape of the normal distribution was consistent between the two data sets.

Trabecular separation distribution tracks the variability of the width of the pores that run through the layers of the 3D sample reconstruction (Figure 5-8B). Trabecular separation did not have the same idealised normal distribution that was seen in the thickness. Pre DMA the distribution peaked at $432.8 \mu\text{m}$ and post DMA at $378.7 \mu\text{m}$. This mirrors the trabeculae thickness changes and suggests that part of the compression of the pores is conserved after DMA resulting in a smaller separation distribution, however it was also deemed statistically non-significant ($p > 0.05$). It is

worth noting that the 95% CI are large for both data sets at the peak portions of the distributions.

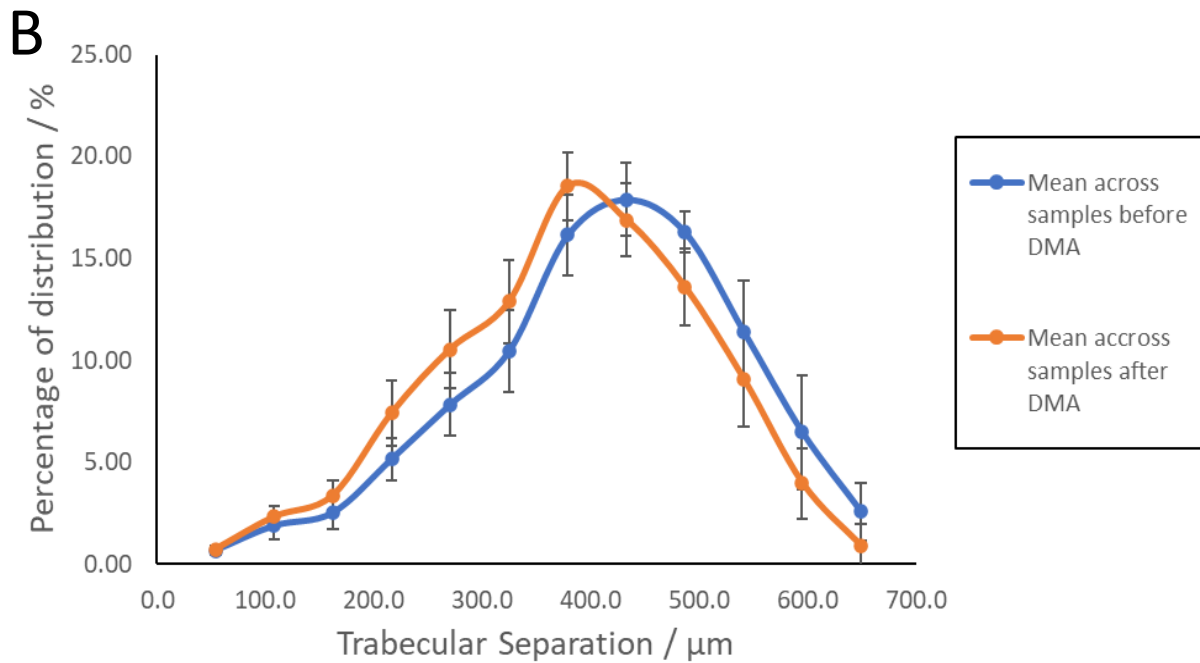
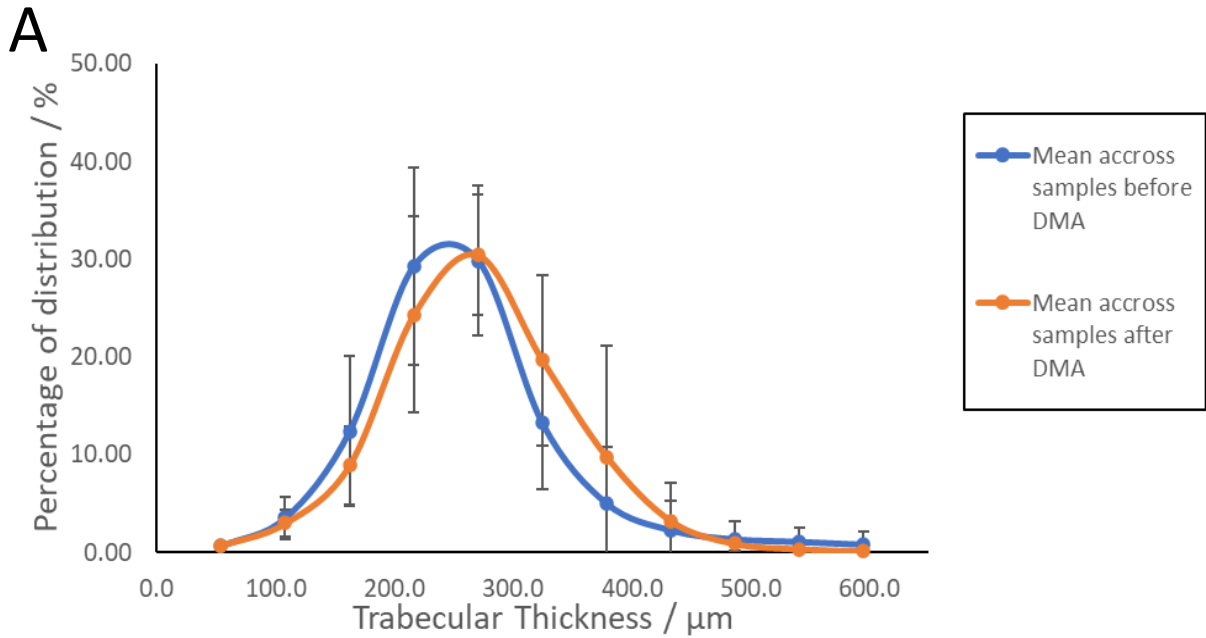


Figure 5-8 Distribution of A) trabecular thickness and B) Trabecular separation across all samples on reconstructed 3D image stack of 175 slices. Both pre and post DMA results included with mean values \pm standard deviation .

5.2.7. Key findings

A brief overview of the key points at the current stage of the chapter are provided here, with a more in-depth discussion being available in section 5.4. From the work done here it has been established that the osteochondral core is approximately a 50% porous structure (51.96% pre-DMA / 48.87% post-DMA) with a high focus on open porosity, this matches with previous studies results [192]. There was no significant difference ($p > 0.05$) in the comparison of pre and post DMA Micro-CT data for any of the parameters that were measured. However, when the trabecular thickness / separation distributions were plotted in Figure 5-8, indications of changes in the trabecular properties were seen with the distributions shifting right and left, respectively. This could indicate that there is some lasting effect on the tissue as results of the loading that was causing the pore size to shrink. Two key limitations were identified as a results of the tissue testing procedures. Firstly, cartilage itself is a curved surface, thus getting a complete contact coverage with the compression plated was tricky to accomplish, this could mean as a results the load was not applied completely even across the tissue samples although this is currently unmeasurable with the set-up as it is designed. Secondly, due to the requirement to remount the tissue samples post DMA it was impossible to obtain the equivalent slice for direct comparison, however, characteristics can still be observed and compared. The first limitation was mitigated during the dissection process by making the base of the sample parallel to the top surface. The second limitation had little effect as seen in Figure 5-7 there are no visual changes in the samples with the porous network into the trabecular bone being preserved. No obvious tissue cracks or damage were identified through when analysing the 3D reconstructions of the samples.

5.3. Feasibility study into the AM of osteochondral cores

5.3.1. Introduction

This section focuses on evaluating how varying AM parameters alter the mechanical and interior structure of CAD components with the final goal of this section being to create a hybrid osteochondral plug construct. The parameters that were focused on are: Unit cell design, interior infill percentage and exterior shell thickness as these were established to be variables that are important to print characteristics in section 2.5. These variables were tested through three stages of prototyping with the following guidelines:

- Firstly, to limit the number of unit cells that would be printed and tested mechanically an initial evaluation was done of the available options provided within the PrusaSlicer software (Prusa Research a.s., Czech Republic).
- Secondly the chosen unit cells will be evaluated against three variations of infill percentage (10%, 25% and 50%). This will show variations in the ability of the unit cells to handle load with small or large representation within the shell.
- Thirdly, the shell thickness will be introduced as a third parameter and will be evaluated against both the chosen unit cells and infill percentages.

Performing the prototyping in stages allows individual parameters to be analysed for their efficacy to the overall main design problem. The printer that was used for this study was the original Prusa I3 Mk3 (Prusa Research a.s., Czech Republic) with a 0.15 mm nozzle head and standard Prusa PLA prusament filament Mk3 (Prusa Research a.s., Czech Republic), with an example print shown in Figure 5-9. One

target of this was to establish whether the printer was able to print a part of sufficient quality when combining the different infills.

To provide a geometrically comparable set of data points to the tissue data that had been obtained, it was decided to create all of our CAD models to mimic the bored osteochondral core dimensions from section 5.2.2, with a diameter and height of 15 mm. To allow for fixation to the load cell of the DMA machine, a bore hole would also be included in the center of one of the ends of the cylinder.

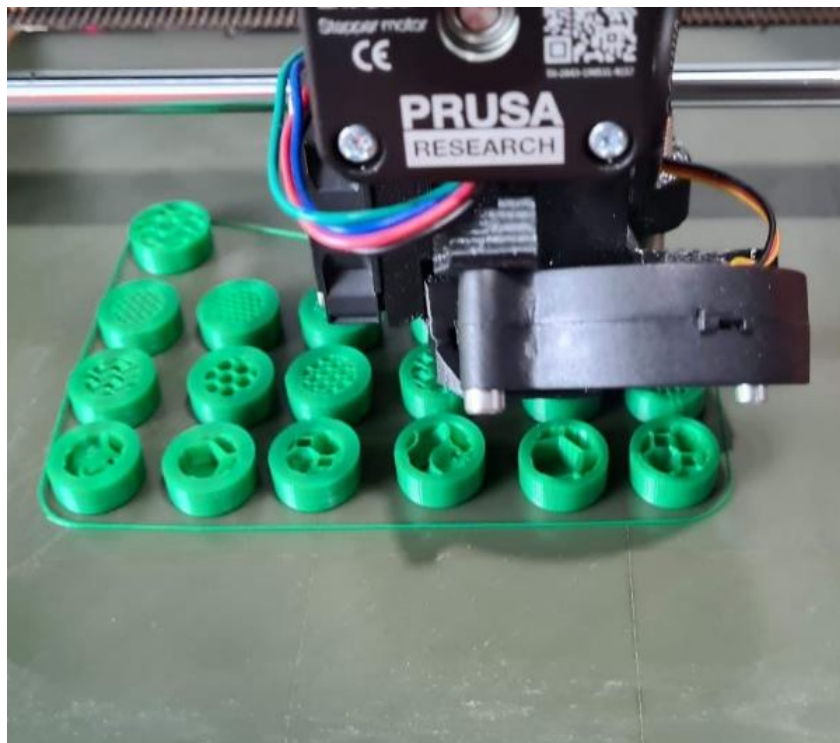


Figure 5-9: Example print process of the Prusa printers producing the second iteration of prototypes described later in section 4.2.2.

5.3.2. Methods

The AM constructs have been evaluated in two main forms. Firstly through DMA matching the experimental setup as described in section 5.2.3 for the tissue cores. This approach allows the direct comparison between the results obtained. The key values are an induced stress of 0.75 to 1.7 MPa applied using a sinusoidal frequency sweep of: 1, 8, 10, 12, 30, 50, 70, and 90 Hz [146] with an additional two preload conditions of 25 Hz for 1500 cycles and 50 Hz for 3000 cycles (for further details see section 2.3, 4.2.3 and 5.2.3).

The second method of evaluation will be through Micro-CT similar to that performed on the tissue cores (section 5.2.5.2) but with altered specifications. This is due to difference in in the required imaging parameters to get clear visuals of the polymer material. Due to a different material being scanned the setting has to be adjusted appropriately to get the desired coverage and quality of image. A 180° scan was performed with 67 Kv maximum X-ray energy and 8 W beam power, using no filter, pixel size of 27.05 µm and 700 ms exposure. Reconstruction of the micro-CT data was performed with NRecon V1.6.10.2 (Bruker Micro-CT, Belgium) using a beam hardening correction of 94%, a ring artefact correction of 80, and smoothing value of 2.0. Two-dimensional slices of sample 10, 11 and 12 are shown as both CAD images and as a reconstructed image segment in Figure 5-10.

The reconstructed 3D images of the printed prototypes were analysed using CTan V1.16.4.1+ (Bruker Micro-CT, Belgium) and singular slices are shown in Figure 5-10 row 1. As there was no concern about swarf due to no exterior damage occurring compared to the tissue samples, the entirety of each unit was able to be contained within the ROI. The region of interest was defined to start above the base layer and

below the top layer to avoid any artefacts due to the fixation to the testing platform. The ROI that was used for all samples was 597×597 pixels or $16.19 \text{ mm} \times 16.19 \text{ mm}$, with the number of image slices observed 420 slices. The difference of 15 mm diameter of the prototypes to the 16.19 mm ROI is to allow for vertical variation in the samples, as it could not be guaranteed that each sample was placed exactly perpendicular to the base platen.

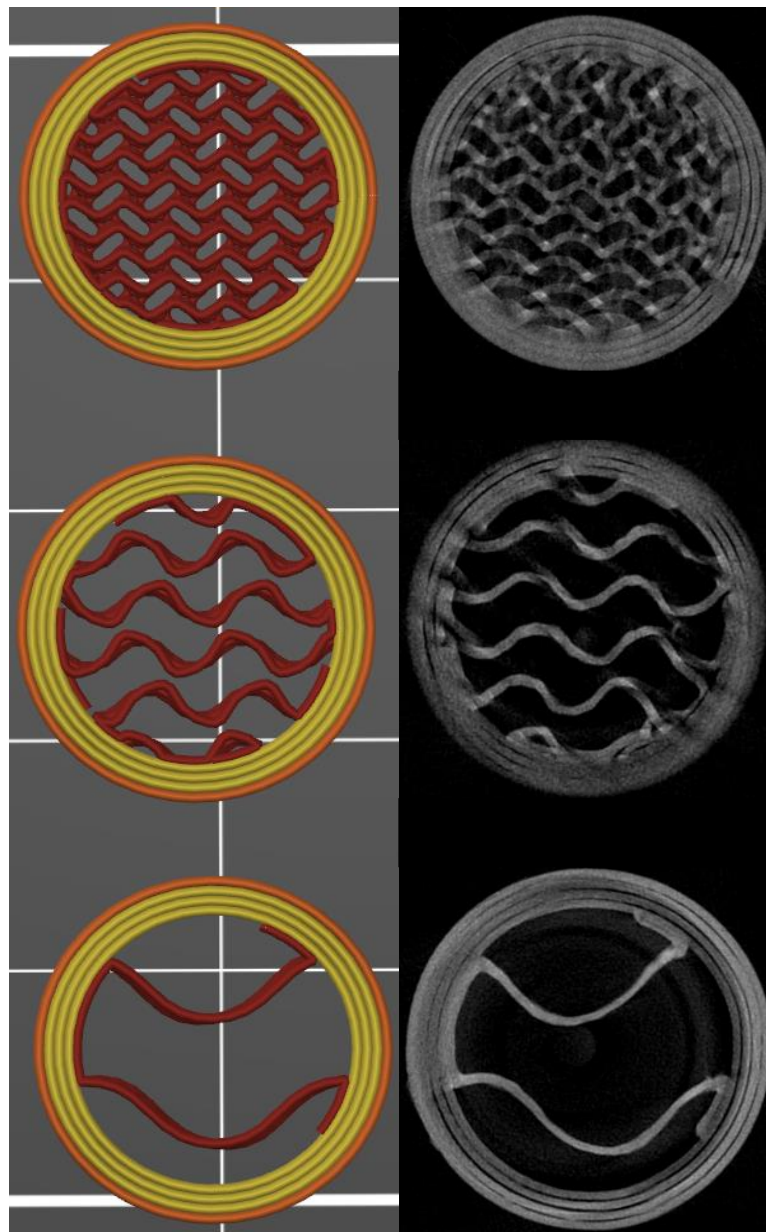


Figure 5-10: Singular slice of a gyroidal unit cell at infill percentages of 50, 25 and 10 from top to bottom and in Prusa slicer CAD (Left) and reconstructed image (Right).

Morphological evaluation

Consistent with the tissue analysis carried out in section 5.2.4 a number of morphological tools were applied to each sample in a specific order to enhance and obtain data points from the samples. The following steps were applied to each data set individually but with the same values:

- Thresholding was performed with a lower grey threshold of 54 and higher grey threshold of 255. This reduced every slice to a binary representation (Figure 5-10 row 2).
- Despeckle completed on black speckles within the 2D space removing any of a size 20 pixels or smaller.
- Despeckle completed on white speckles within the 2D space removing any of a size 80 pixels or smaller.
- 3D model computed using double-time cubes algorithm applying only to defined ROI. Alongside this a 3D analysis was computed.
- Despeckle function to remove broken pores in the 3D space.
- Invert the image in the ROI to highlight the closed porous structure in the images (Figure 5-10 row 4).
- Bitwise operation where the ROI in the image is defined and the whole image minus the ROI. The image is then reloaded with the new ROI.
- It is then thresholded again with the original values of lower at 54 and upper at 255, and then inverted again.
- The same two despeckle methods are run again as above on black objects at a 20-pixel size and on white at an 80-pixel size and the image is saved as open porosity (Figure 5-10 row 3).

The 3D analysis mentioned above was performed to gather the open and closed porosity percentages as well as: trabecular thickness, thickness distribution, separation, and separation distribution. An example set of images was saved at each stage of the process, a number of which are shown in Figure 5-10, allowing for visual analysis if it was required. For the printed components, trabecular thickness was in relation to the thickness of the interior infill pattern designs, and trabecular separation measured the mean spacing between the print lines when laying down the material. To visually analyse the 3D components of the constructs the reconstructions can be reproduced in CTVox (Bruker Micro-CT, Belgium) as a 3D object.

5.3.3. AM prototyping of tissue substitutes.

The first parameter that needed to be established for the prototyping stage was the unit cells that would be evaluated. Initially, a set of key factors was established from section 5.2 that would be used as measures of unit cell suitability for the first set of prototypes. These Key characteristics of the AM prints are as follows:

Material dynamic response:

- Storage modulus E' matching close to 252 ± 9.32 MPa.
- loss modulus E'' matching close to 52.6 ± 27.8 MPa.

Geometric profiles:

- Porosity and trabecular values similar to those reported in table 5.1 and 5.2.
- Vertical and horizontal traversing pores
- Anisotropic orientation of trabecular pillars with vertical load

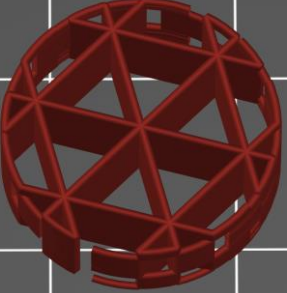
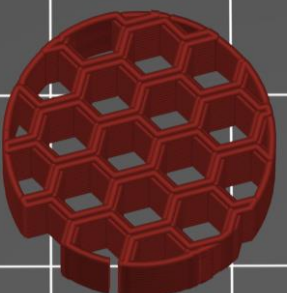
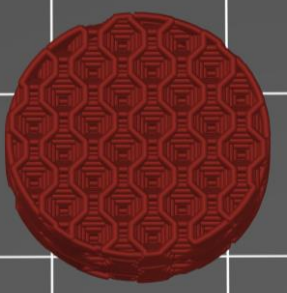
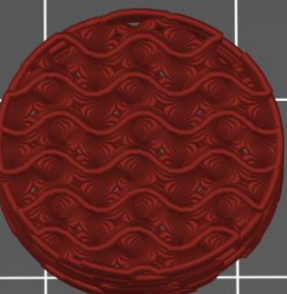
- Internal geometric shape will provide most of the structural load so will be required to be of a strong design.
- As it is common practicing to include a shell within 3D printing research one will be added here but it is not defined to mimic the biological tissue.

5.3.3.1. Initial unit cell evaluation

PrusaSlicer software (Prusa Research a.s., Czech Republic) was used to create 10 options using the provided unit cell designs that is provided with the printer. Custom unit cells designs are an option but are not being evaluated at this stage due to the preliminary point this study is at. The chosen design will be printed and then tested with DMA to gauge their material response to certain loads.

Table 5.3 describes the 4 infill design that were identified as possible contenders for the next stage of analysis and the characteristics that led to the choice. The unit cells that were chosen to progress were: gyroidal, triangular, honeycomb, and 3D honeycomb.

Table 5.3: The 4 unit cells to be evaluated against required key characteristics.

	<p style="text-align: center;">Triangles</p> <ul style="list-style-type: none"> • Strong geometric shape being a triangle but bad interaction with edge of cylinder but only in the lateral domain. • Provides vertical anisotropic strength through consistent print orientation and repetition of the same design triangular shape. • Vertical but no horizontal pores present.
	<p style="text-align: center;">Honeycomb</p> <ul style="list-style-type: none"> • Hexagons provide a geometrically strong in horizontal and vertical orientation. • Vertical but no horizontal pores present • Vertical pillars are present as a result of the hexagonal design. • Double width shell thickness on interior design providing more structural support.
	<p style="text-align: center;">3D Honeycomb</p> <ul style="list-style-type: none"> • Same arguments as above image however with additional comments • Some horizontal pores are present when traversing the design. • Increased horizontal strength through the 3D aspect of the hexagonal design. • Pillar constructs are less obvious in the design.
	<p style="text-align: center;">Gyroidal</p> <ul style="list-style-type: none"> • Provides a flowing porous network that adapts well to the shape it is placed in. • Documented multi-directional loading capacities • Verticality is not linear however continuous segments are present from base to top providing the pillar structures.

5.3.3.2. Design and AM of first round prototype cylindrical cores

The target of the initial run of printed concepts was to check for suitability of the chosen unit cells previously mentioned before any further testing progressed. As this was meant as quick evaluation Micro-CT was not performed on this initial set of AM components. An additional mentioned parameter was altered during this set of evaluations, being the infill percentage, and was set to be at 50%, 25% and 10% for all variations of unit cell.

Table 5.4: Shorthand definitions of testing specimens for future results.

		Unit cell design			
		Gyroidal	Triangular	Honeycomb	3D Honeycomb
Infill %	10	Gyroid10	Triang10	Honey10	3DHoney10
	25	Gyroid25	Triang25	Honey25	3DHoney25
	50	Gyroid50	Triang50	Honey50	3DHoney50

To aid in ease of understanding, the following shorthand definitions of the unit cells have been used for the rest of the evaluation of this chapter: gyroidal infill as gyroid, triangular infill as triangle, honeycomb as honey, and 3D honeycomb as 3Dhoney. Percentages have also been attached to these as 50, 25 and 10 respectively, for clarity and reference these are displayed in Table 5.4. All unit cells and infill percentages were created as CAD models and sliced using PrusaSlicer and are shown in Figure 5-11. The spacings that are visible in the centre of the cylinders were included to allow attachment to the set-up for DMA testing (section 4.2.3).

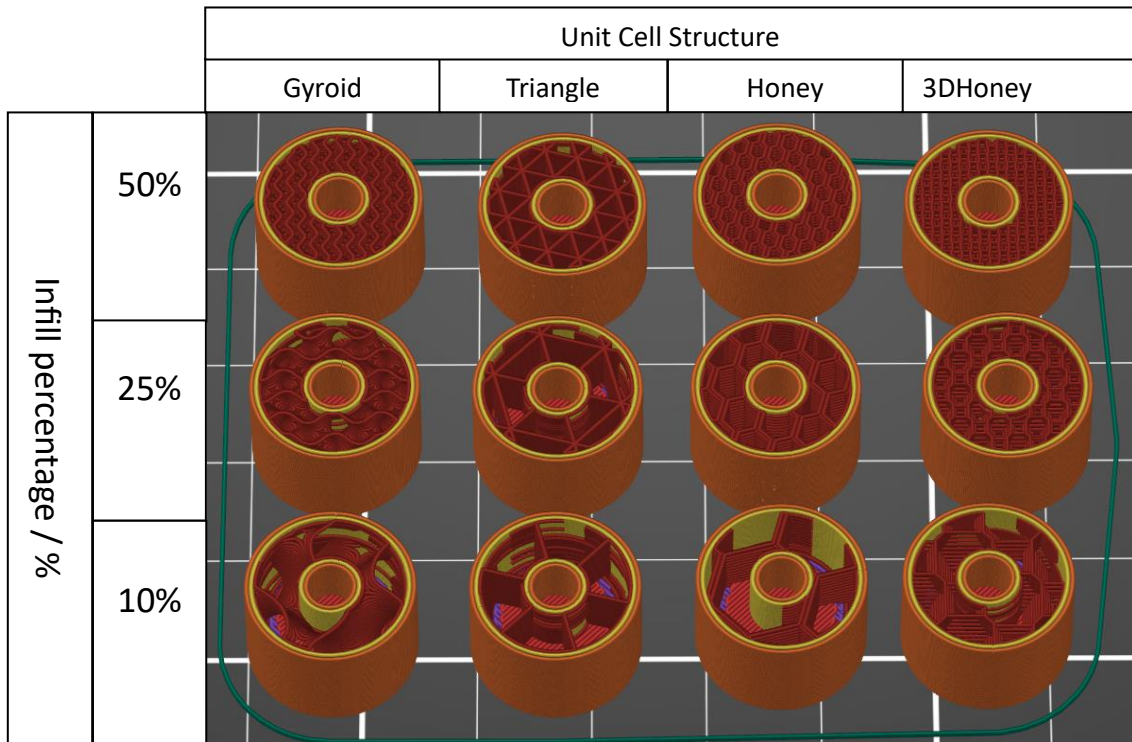


Figure 5-11: PrusaSlicer sliced cad models of the four chosen unit cells for initial iteration of prints. From left to right represents the unit cell designs of: Gyroidal, Triangle, Honeycomb, 3D Honeycomb. From top to Bottom represents the infix percentages of 50%, 25% and 10% for each of the unit cells above.

5.3.3.3. DMA of first round prototypes

To test each printed part's feasibility in its ability to mimic the tissue core, DMA was performed on each unit as described in section 4.3.2.

Storage Modulus

The storage modulus results can be initially analysed through their mean value which is reported in Table 5.5 and the complete data being shown in Figure 5-12.

The range of value obtained was from 38.31 MPa up to 60.80 MPa. Under only one condition did the highest percentage of infill (50%) result in the highest storage modulus. This was in the case of the honeycomb unit cell.

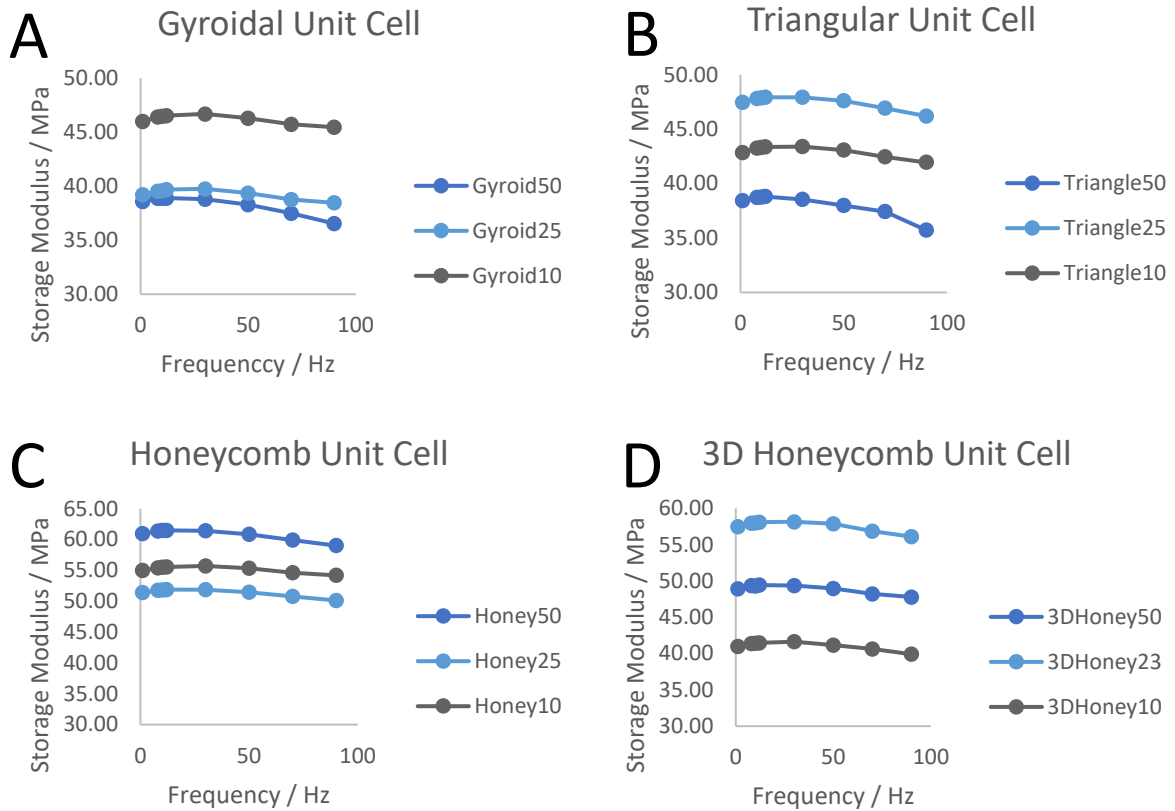


Figure 5-12: Storage modulus outputs for the AM printed cylindrical unit with the four graphs representing: A) Gyroidal unit cell, B) Triangular unit cell, C) Honeycomb unit cell, and D) 3D Honeycomb unit cell. Each graph contains the three results for 50%, 25% and 10% infill percentage as well.

Table 5.5: Mean \pm STD for storage modulus values obtained from the initial prototypes. These are the same values displayed graphically in Figure 5.12.

Mean Storage Modulus across frequency / MPa				
Infill	Gyroidal	Triangular	Honeycomb	3D Honeycomb
50%	38.29 \pm 0.80	38.05 \pm 0.95	60.80 \pm 0.84	48.94 \pm 0.57
25%	39.30 \pm 0.43	47.47 \pm 0.57	51.39 \pm 0.59	57.59 \pm 0.68
10%	46.21 \pm 0.40	42.95 \pm 0.48	55.16 \pm 0.50	41.08 \pm 0.53

The highest storage modulus values were for the honeycomb and 3D honeycomb unit cells at 60.80 and 57.59 MPa respectively, with the lowest being the 50 % infill of gyroidal and triangular with 38.29 and 38.05 respectively (Figure 5-13, Figure 5-14). Unexpected trends of storage modulus were seen in gyroidal and triangular where the 50% infill was the least stiff percentage tested which is an illogical outcome.

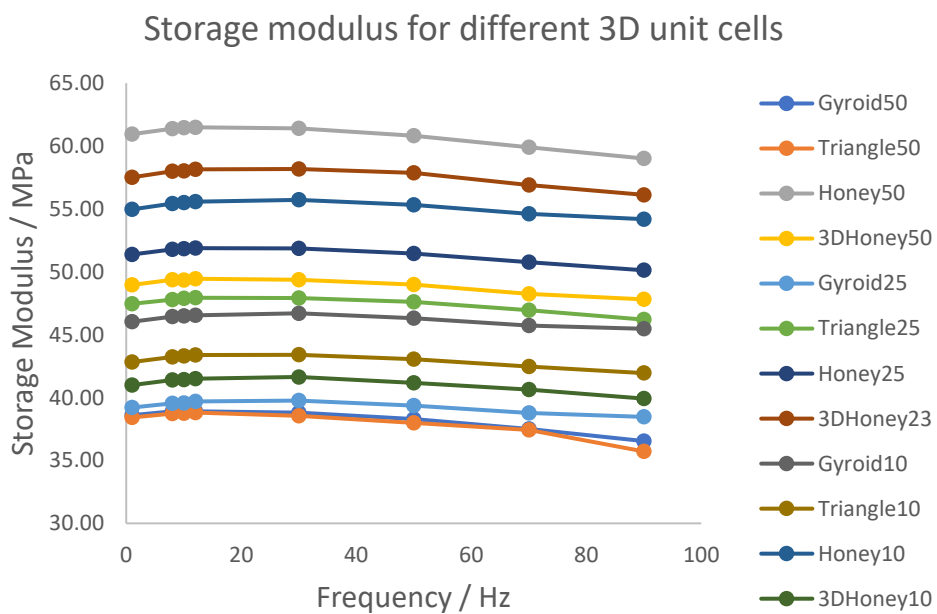


Figure 5-13: All storage modulus values from Figure 5-12 compared against each other. All samples are shown to follow a logarithmic trend with regards to frequency over the range of 1 to 90 Hz.

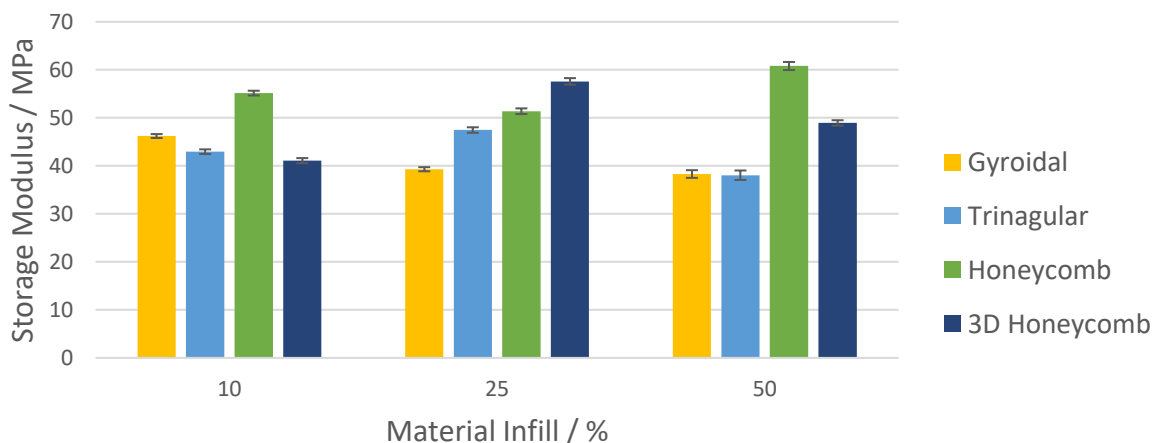


Figure 5-14: Mean storage modulus for each percentage infill comparing the produced prototype unit cells.

Loss Modulus

Table 5.6: Mean values for loss moduli of the AM samples with sample 4 excluded (SD: Standard Deviation).

	Frequency / Hz							
	1	8	10	12	30	50	70	90
Loss Modulus Mean \pm SD / MPa	0.76 \pm 0.13	1.84 \pm 0.27	2.16 \pm 0.32	2.51 \pm 0.38	5.47 \pm 0.86	8.84 \pm 1.33	12.03 \pm 1.92	15.25 \pm 2.54

All the loss modulus values are reported in Figure 5-15 with all samples following a similar trend. E'' is confirmed to be frequency dependent and increases at frequency does up to the tested value of 90 Hz. For all variations the initial loss moduli was consistent at 1 Hz at 0.76 ± 0.13 MPa and by 90 Hz once there was a visible spread the mean was still within a reasonable margin of error at 15.25 ± 2.54 MPa. All values for the mean loss moduli are shown in Table 5.8. Due to the similarity of the loss moduli across all samples this will not be part of the consideration for the next iteration of the study.

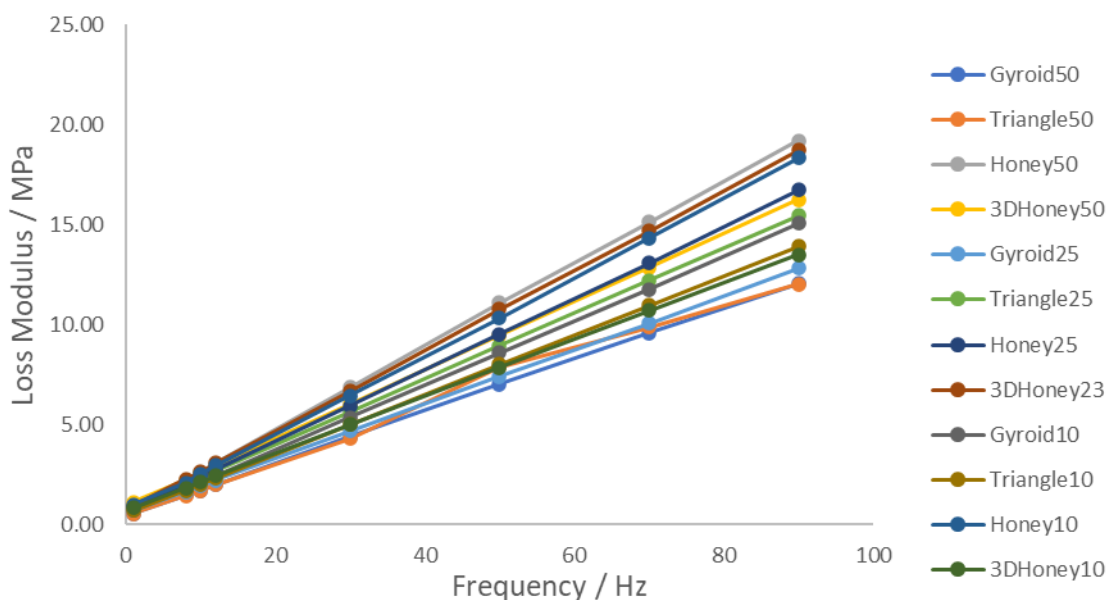


Figure 5-15: Loss modulus outputs for the AM printed cylindrical units for all of the different designs: Gyroidal, Triangular, Honeycomb and 3D Honeycomb. Sample are labelled numerically as defined in Table 4.

Table 5.7: Score allocation for print viability of initial prototyping

		Gyroidal	Triangular	Honeycomb	3D Honeycomb
Infill / %	10	3	2	4	1
	25	1	2	3	4
	50	2	1	4	3
Total Score		6	5	11	8

Taking this into account and grading the unit cell design on their maximal values a simplistic score grading system was used to identify the weakest option at the current stage. Each gained 3 scores, 1 for each infill percentage and then a total score calculated, these scores are displayed in Table 5.7.

5.3.3.4. First round print viability analysis

Analysis of unit cell designs demonstrated that the Honeycomb and 3D Honeycomb design were more effective at storing greater quantities of energy than the other options for unit cell design. When inspecting the geometry, and how the unit cells 'performed' during slicing (Figure 5-11), it was seen that some were more suitable than others. The honeycomb design had difficulty in matching the geometry of the cylinders resulting in many broken hexagons in both 3D and normal unit cells Figure 5-16. To a lesser extent triangles also had this issue, but this is arguably more

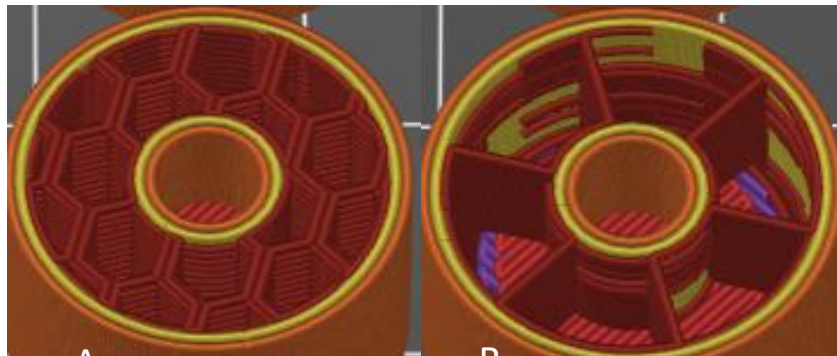


Figure 5-16: A) Honey25 print with incomplete hexagons shown as part of the interior slice. B) Traing10 print where there are no complete triangles present.

important due to the strength of the triangular format coming from its completion. Noticeable different to the rest of the unit cells, the downwards trend of the triangular design is steeper and has a larger range of peak to trough in the obtained results (Figure 5-13). It also reported either the second lowest or lowest output in all three of the infill percentages tested.

The triangular unit cell was found to lead to internal triangles of the interior constructs which were interrupted by the cylindrical exterior shell and attachment point Figure 5-16. This is especially visible in the 10% infill where there are no complete triangular components to provide the expected stiffness present as seen in Figure 5-11. For these reasons the triangular unit cell design was excluded from the second iteration of prototyping. Although gyroidal performed poorly compared to the other two options as well, the most effective design performed within the same boundaries as the optimal honeycomb and 3D honeycomb results, thus gyroidal will still be included. The three progressing will be: Gyroidal, Honeycomb and 3D Honeycomb.

Due to some of the unexpected trends that were highlighted within the results section, a hypothesis was made that the parts may not be printing with the expected and defined geometry. For the second round, internal geometries of the printed components will be analysed through micro-CT scans. Samples will be excluded from analysis if their print quality does not fall within expected boundaries. This will hopefully produce more expected trends within the samples. The resolution of the print was defined by the nozzle we had currently available being the 0.15 mm. It was decided that if print quality became a limiting factor of the build, then the nozzle resolution would be re-visited at a later date. The infill percentage and outer shell diameter will be two of the main parameters that are varied during this study.

5.3.3.5. Design and AM of second round prototype cylindrical cores

The unit cells that were progressed to the second round were gyroidal, honeycomb, and 3D honeycomb. In this iteration the following parameters will be varied alongside these unit cells in the prints: Infill, and outer shell thickness. The variations in infill will stay the same at 10, 25 and 50% respectively and the exterior shell will be altered from 0.8 mm to either a value of 2.6 mm (6 layers for the circumference) or 1.7 mm (4 layers) providing data on 2 equally spaced shell thicknesses (Figure 5-17). In this iteration, the attachment point was omitted from the AM component as we were aware it could be producing artefacts in our results data. Due to the interest in the interior components and how this affected the biocompatibility of printed AM in other studies [174], [175], [193], an additional analytical component of this section will be to micro-CT the components. This will also provide the ability to confirm the internal geometry is as expected within the samples. The same print specifications were used as outlined in (section 5.3.3.2).

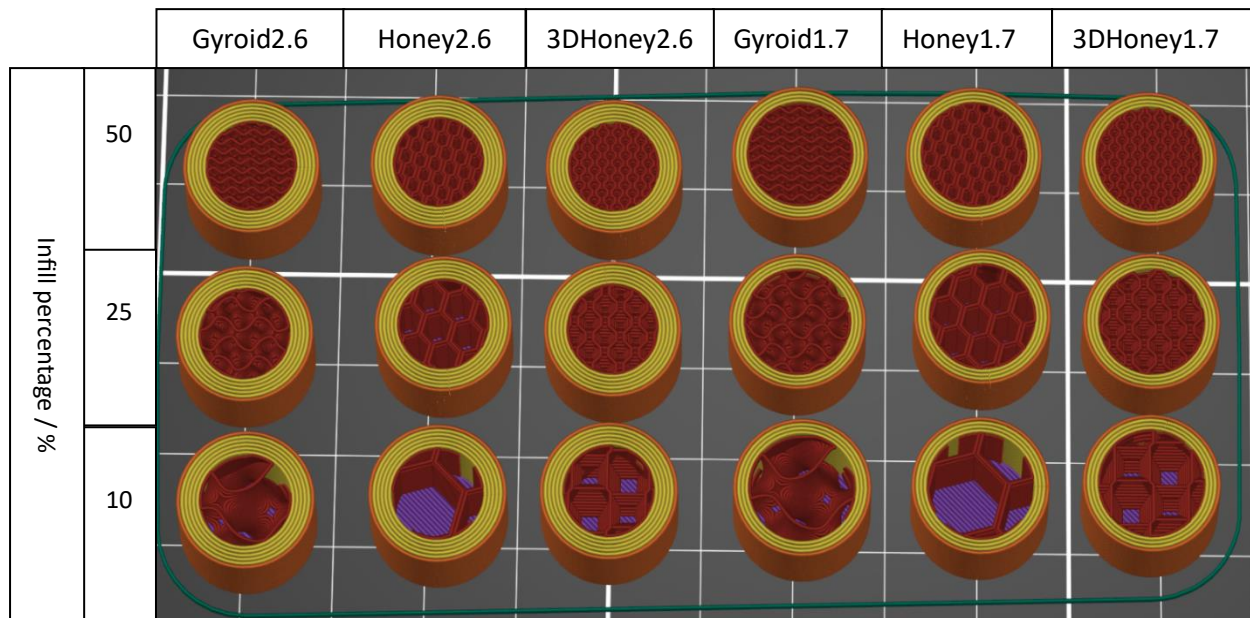


Figure 5-17: PrusaSlicer sliced CAD models of the second iteration of chosen unit cells. From left to right represents the unit cell designs of: Gyroidal, Honeycomb, 3D Honeycomb at 2.6 mm shell thickness and then the same again at 1.70 mm shell thickness. From top to Bottom represents the infill percentages of 50%, 25% and 10% for each of the conditions above.

5.3.3.6. DMA of second iteration of AM Prototypes

The same parameters were used for the DMA tests as used in section 5.3.3.3. A total of 18 samples were tested combining all variations of the three infill percentages, three unit cells and 2 shell thickness.

Removal of incorrect samples:

Of the values that are presented in Figure 5-21 some are now going to be discounted from further analysis based on geometric anomalies found within the structures. Examples and reasons for each expulsion will be given per case. The first sample to be excluded is the Honeycomb pattern and 50% infill with a shell thickness of 2.6 mm. When examining the micro-CT analysis of the sample, many print inconsistencies were identified through the layers. Multiple cracks were present throughout the interior design across multiple slices as seen by the black spaces between the infill segments in Figure 5-18A. When comparing output Figure 5-18A.

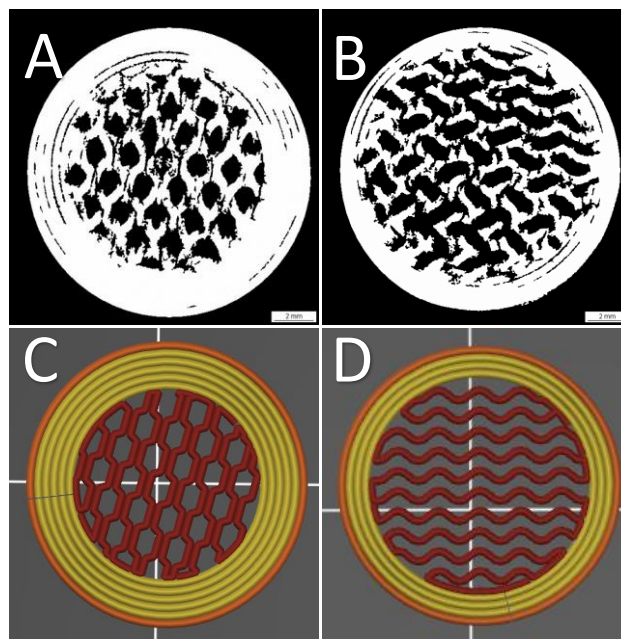


Figure 5-18: Example slice of irregularities found in A) Honey_50_2.6 B) Gyroid_50_1.7. Expected outcome in print specification for A) Honey_50_2.6 B) Gyroid_50_1.7

to expected Figure 5-18C these breakages in the interior design are not present demonstrating the failure to match geometry. There are also many thin tram line disparities present within the exterior shell which could also contribute to the lesser stiffness value. These errors demonstrate that the design was not printed as expected and this these results are excluded from future analysis.

Looking at the Gyroid 1.7 mm Shell 50% infill sample similar issues are present in the internal geometry. The main component of the structural design, the wavy pattern, is broken in half at multiple points and in multiple layers. When comparing this damage to the expected output in Figure 5-18D it is clear this is unintended. Also, present in many of the CT scan slices is the damage to the exterior shell structure in its tram lines, as seen in Figure 5-18B.

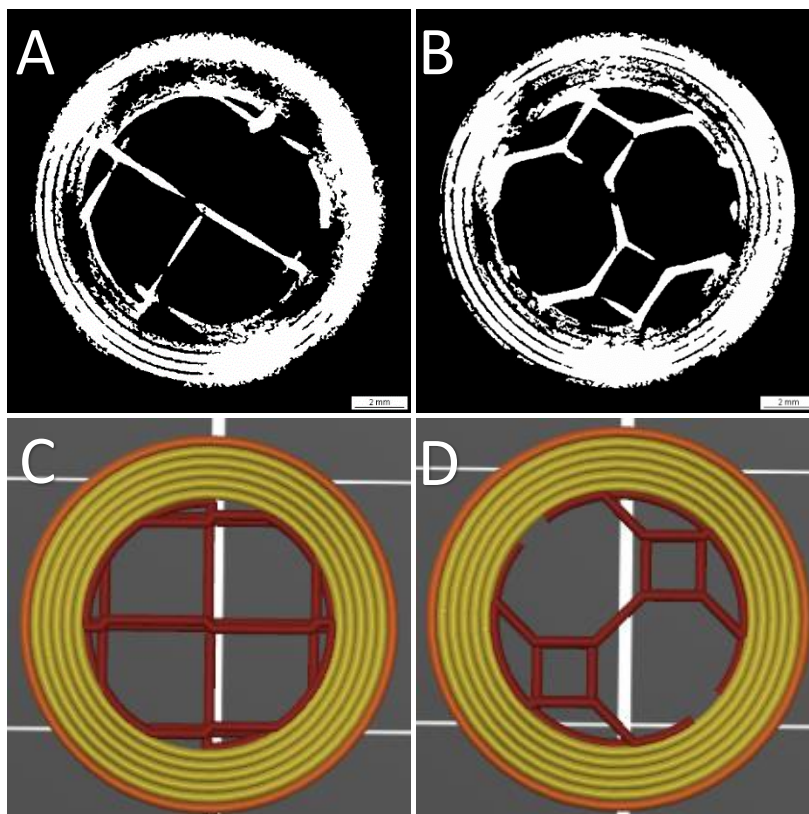


Figure 5-19: Two example slice of irregularities found in 3DHoney_10_2.6 (A, B) and expected outcome in print specification for 3DHoney_10_2.6 (C, D)

Two other samples that are going to be excluded from the results analysis are 3DHoney_10_2.6 and 3DHoney_10_1.7. Multiple slices of expected and actual outcome of 3DHoney_10_2.6 is displayed in Figure 5-19 and of 3DHoney_10_1.7 in Figure 5-20. Both these samples have clear issues of cohesion between the internal infill design and surrounding shell resulting in the black open spaces and unclear shell structure seen in Figure 5-20A-D. The internal pattern was also unable to be accurately replicated by the printer resulting in spacing between lines of polymer as seen by the breaks between the expected and achieved designs.

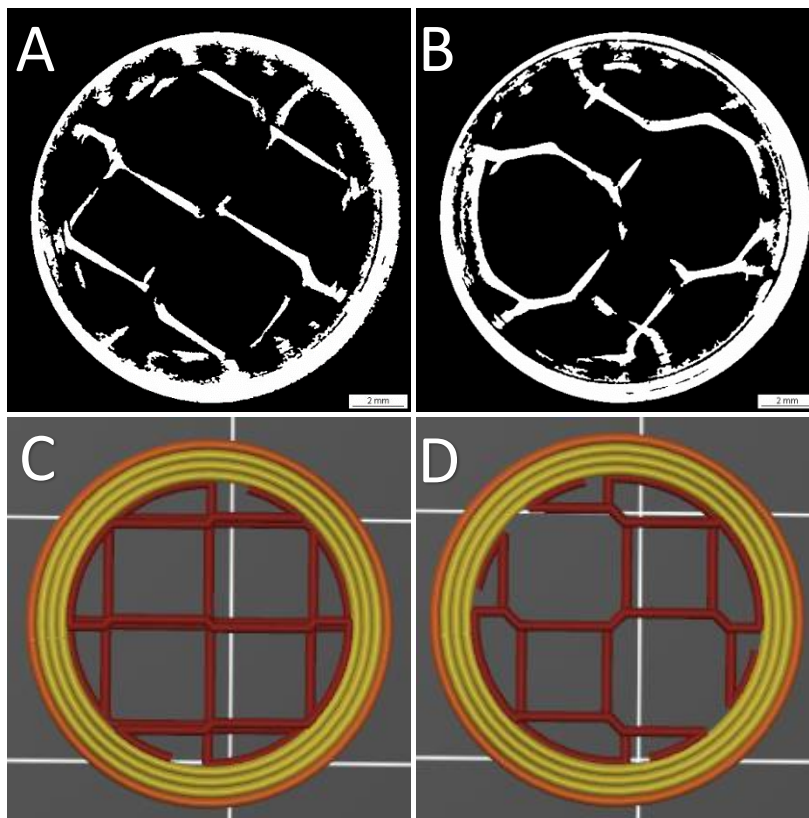


Figure 5-20: Two example slice of irregularities found in 3DHoney_10_1.7 (A, B) and expected outcome in print specification for 3DHoney_10_1.7 (C, D)

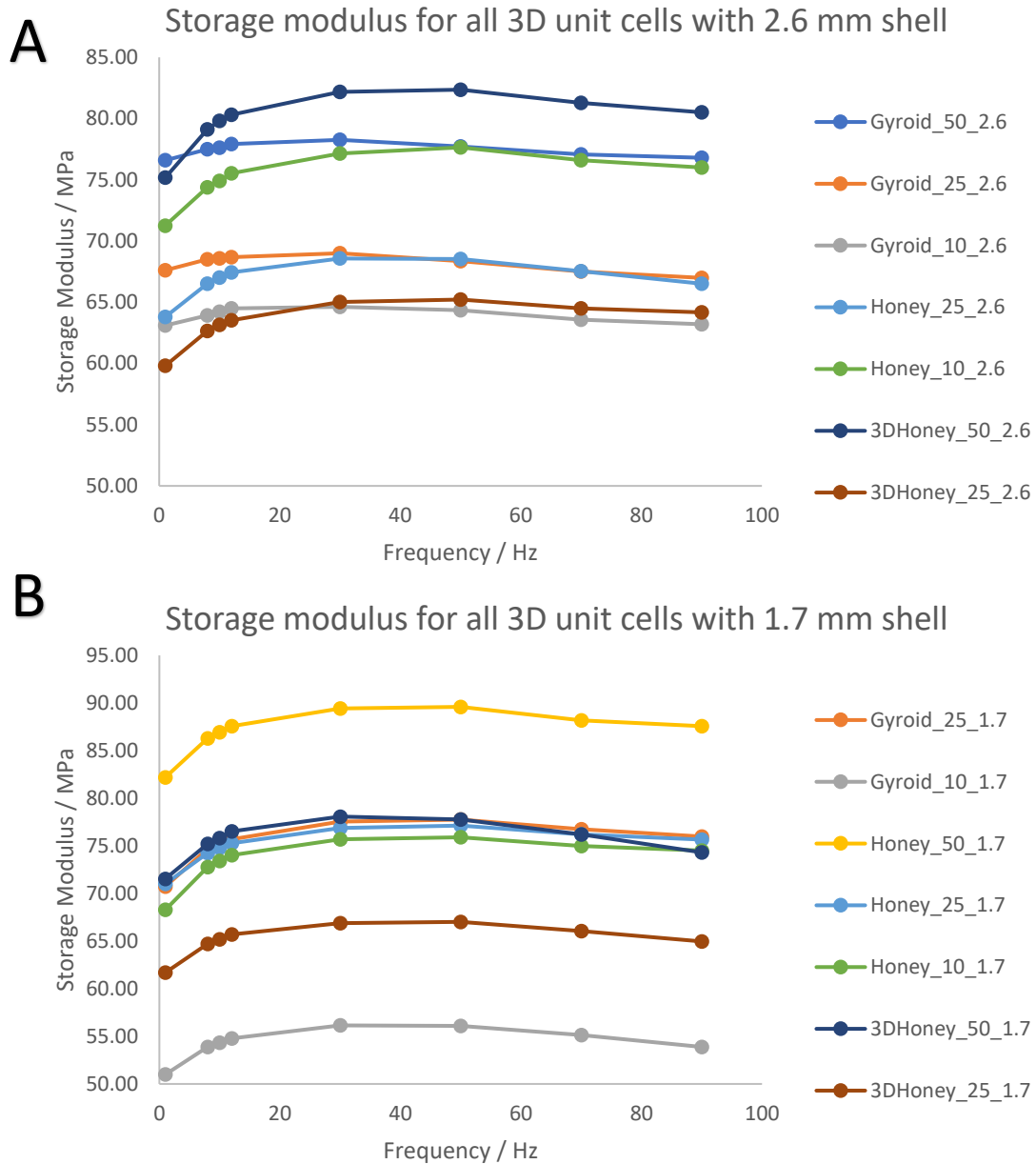


Figure 5-21: Storage modulus outputs for the AM printed cylindrical unit sorted according to their shell thickness: A) 2.6 mm shell and B) 1.7 mm shell.

Storage modulus:

All values obtained for storage modulus are displayed on the graphs in Figure 5-21, and in Figure 5-22 the outputs are sorted by unit cell and shell thickness. The design that produced the stiffest storage modulus when the shell thickness was 2.6 mm was 3Dhoney_50 (80.09 ± 2.13 MPa), and when the shell was at 1.7 mm, Honey_50

(87.22 ± 2.17 MPa) with a difference in their means of 7.1 MPa. 3Dhoney_10 produced the lowest value for the 2.6 mm shell and Gyroid_10 for the 1.7 mm shell. The range of average stiffness seen across the tests was not that dissimilar between the different shell thicknesses as, for 2.6 mm the range was 63.5 – 80.09 MPa and for 1.7 mm it was 54.4 – 87.2 MPa. There was also an increase in E' across the board in comparison to the prototypes from section 5.3.3.4, with the maximum value being increased by 27 MPa and the minimum by 12 MPa (cf. $87.22 - 60.08$ MPa and $50.28 - 38.05$ MPa, respectively).

The gyroidal infill design (Figure 5-22A and B) had a coefficient of variation of 0.081 when the shell was thicker at 2.6 mm than at 1.70 mm where it was 0.163. This implies that the change in infill percentage had a larger impact on the mechanical output than the change in shell thickness due to potentially there being less available space for the unit cell to fill and thus provide support. Increasing the shell thickness also resulted in a more flattened logarithmic relationship between frequency and modulus. The results that produced the lowest storage modulus (E'), were in both cases, the prints that were at 10% infill. This shows that at a low coverage the pattern is significantly less effective especially as the difference between 10% and 25% infill is much greater in the thinner shell sample. The top result for the 2.6 mm shell was 50 % infill (77.44 ± 0.54 MPa), however, for the 1.70 mm shell, 25% infill produced the largest mean storage modulus (75.55 ± 2.08).

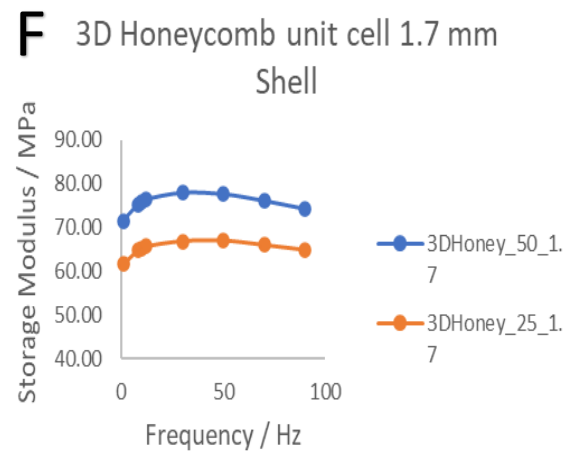
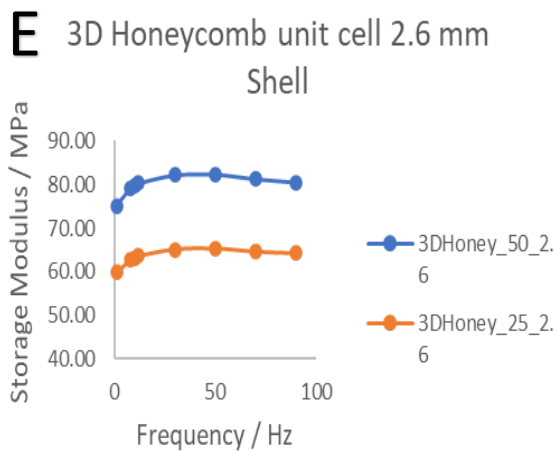
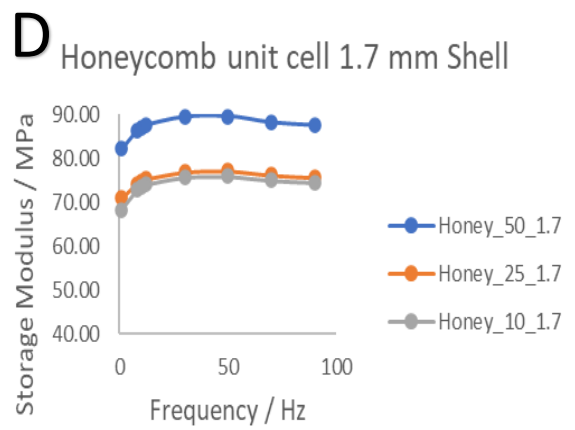
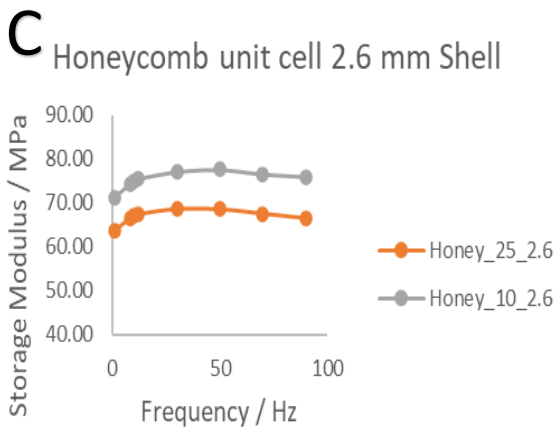
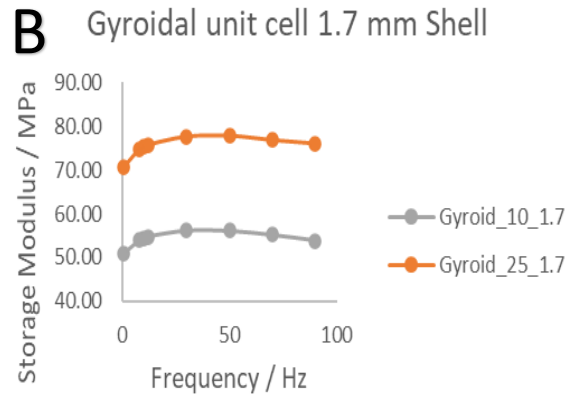
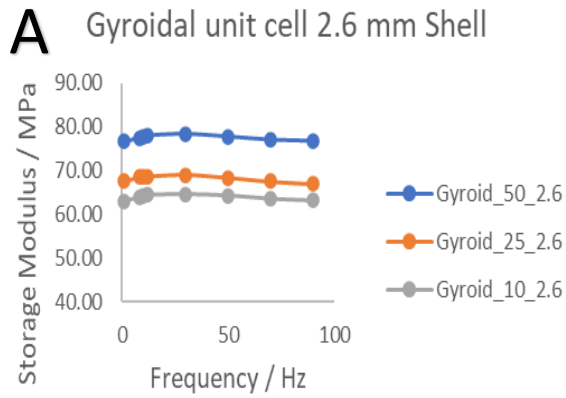


Figure 5-22: Storage modulus outputs for the AM printed cylindrical unit with the six graphs representing: Gyroidal unit cell with A) 2.6mm or B) 1.70 mm shell, Honeycomb unit cell with either C) 2.6 mm or D) 1.70 mm shell, and 3D Honeycomb unit cell with either E) 2.6 mm or F) 1.70 mm shell. Each graph contains the three results for 50%, 25% and 10% infill percentage as well.

Table 5.8: Mean \pm SD for storage modulus values obtained from the second round of prototypes. These are the same values displayed graphically in Figure 5-23.

Mean Storage Modulus across frequency / MPa						
Infill	Gyroid_2.6	Gyroid_1.7	Honey_2.6	Honey_1.7	3DHoney_2.6	3DHoney_1.7
10%	63.93 \pm 0.55	54.41 \pm 1.53	75.44 \pm 1.88	73.69 \pm 2.27	Na	Na
25%	68.15 \pm 0.65	75.55 \pm 2.08	66.99 \pm 1.41	75.15 \pm 1.81	63.50 \pm 1.63	65.27 \pm 1.57
50%	77.44 \pm 0.54	Na	Na	87.22 \pm 2.17	80.09 \pm 2.13	75.68 \pm 1.94

When evaluating the honeycomb unit cells, the 2.6 mm shell samples produce illogical results, where the higher percentage infill produced a less stiff output. This doesn't make sense due to the expectance that more material would results in a stiffer sample when using the same design. The 2.6 mm shell samples will therefore be excluded from the rest of the analysis as they require further repeats and testing before comparative analysis can occur. The 1.7 mm shell design did follow the expected logical outcome of an increasing storage modulus with respect to infill percentage. An increase of 18% was seen between the 10% and 50% infills with the maximum storage modulus being observed across all samples in the Honey_50_1.7 sample at 77.22 \pm 2.17 MPa.

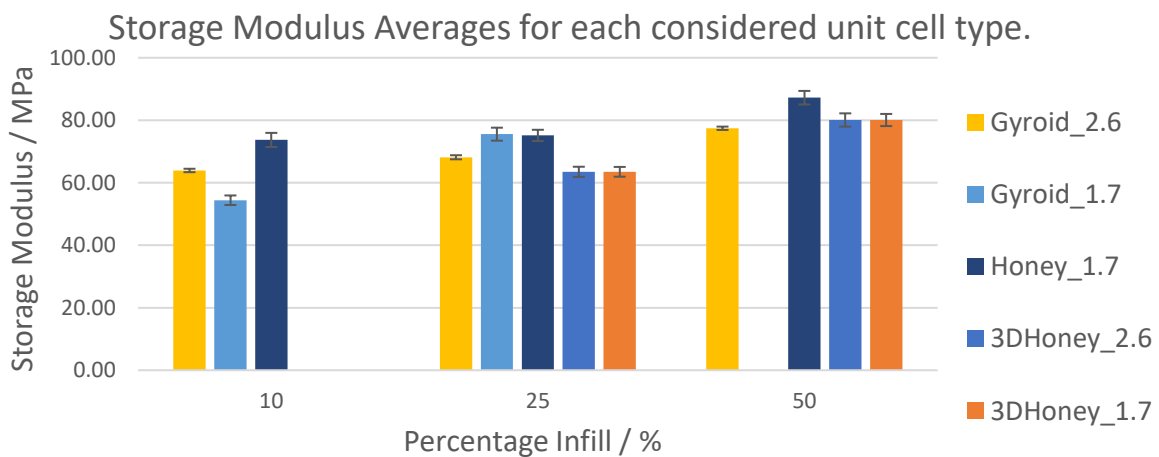


Figure 5-23: Mean storage modulus sorted by percentage infill with means for both 2.6 mm and 1.7 mm in each unit cell design. Error bars represent the 95% CI over all of the frequencies in the frequency sweep.

For the 3D honeycomb (Figure 5-22E & F) the trend was as expected for both 1.7 mm and 2.6 mm as the energy storage capability of the prototypes increased with respect to their infill. When looking at the mean values obtained (Table 5.8, Figure 5-23) there is marginal difference in E' of the prototypes between the 2.6 mm and 1.7 mm shells for both the 25% and 50% infills (25% - 2.8 % difference, 50% - 5.8% difference).

Loss Modulus

The loss modulus values are reported in Figure 5-24 and are split by their shell thickness. Similar to in the first stage of prototyping, all of the samples follow the same trend with regards to frequency.

Table 5.9: Mean values for loss moduli of the second round of prototype AM samples.

	Frequency / Hz							
	1	8	10	12	30	50	70	90
Loss Modulus Mean \pm STD / MPa	2.66 \pm 0.90	4.57 \pm 1.23	5.13 \pm 1.31	5.69 \pm 1.39	10.18 \pm 1.96	15.19 \pm 2.62	20.09 \pm 3.26	25.07 \pm 3.99

Table 5.9 displays the mean values that were obtained across all sample prototypes. The loss modulus results show that the samples were dissipating larger amounts of energy with the new parameter specifications, up from a maximal value of ~15 MPa at 90 Hz to over 30 MPa in some designs. As seen in a comparison of graphs A and B in Figure 5-24 there is very little difference in the range of values that are expressed between a shell of 1.7 mm and a shell of 2.6 mm. There was disparity between which unit cells / infills produced the best combinations. For instance, the Honey_50 sample was the optimal infill/unit cell combination for the 1.7 mm shell but the 3Dhoney_50 was the stiffest for the 2.6 mm shell.

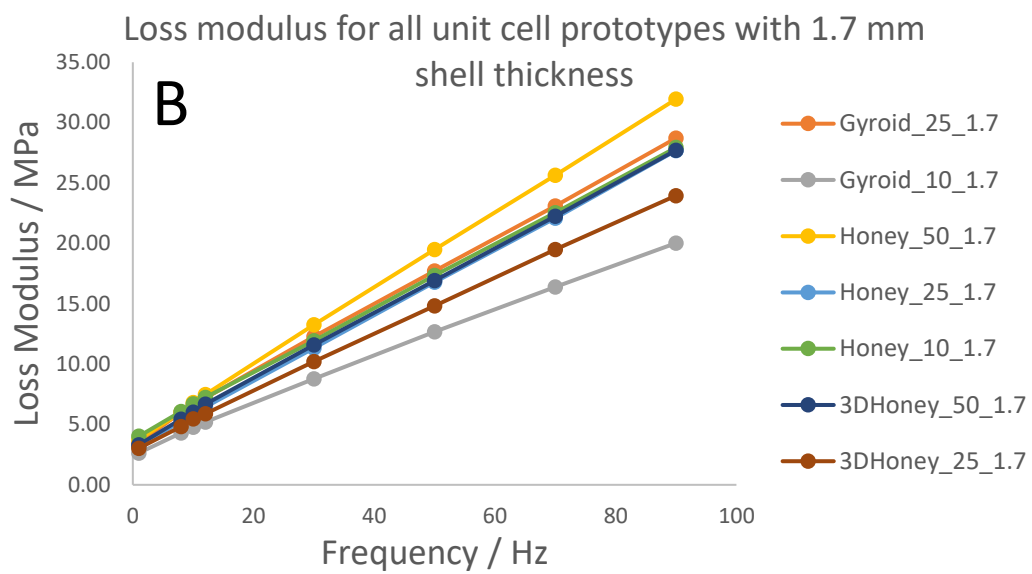
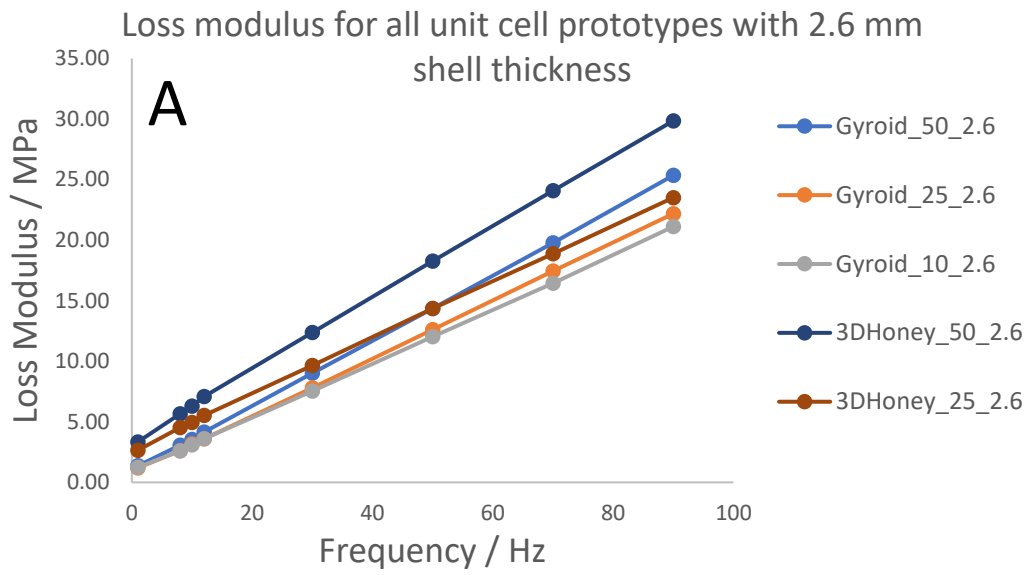


Figure 5-24: Loss modulus outputs for the second prototype of printed cylindrical unit for all of the accepted designs: Gyroidal, Triangular, honeycomb and 3D honeycomb, and infills: 10, 25 and 50. Values are separated by shell thickness with graph A for 2.6 mm shell and B for 1.7 mm.

5.3.3.7. Micro-CT Results – Second set of prototypes

The results obtained through micro-CT analysis were assessed in two different ways: firstly, visually in terms of print feasibility and quality analysis, and secondly, in comparison with the biological data. Images of individual slices representing the various data points being assessed (open & closed porosity) are shown in Figure 5-26 alongside Figure 5-25 containing the complete reconstructions of various samples. Data from sample 'Honey_10_2.6' is excluded from this analysis due to corruption of the files.

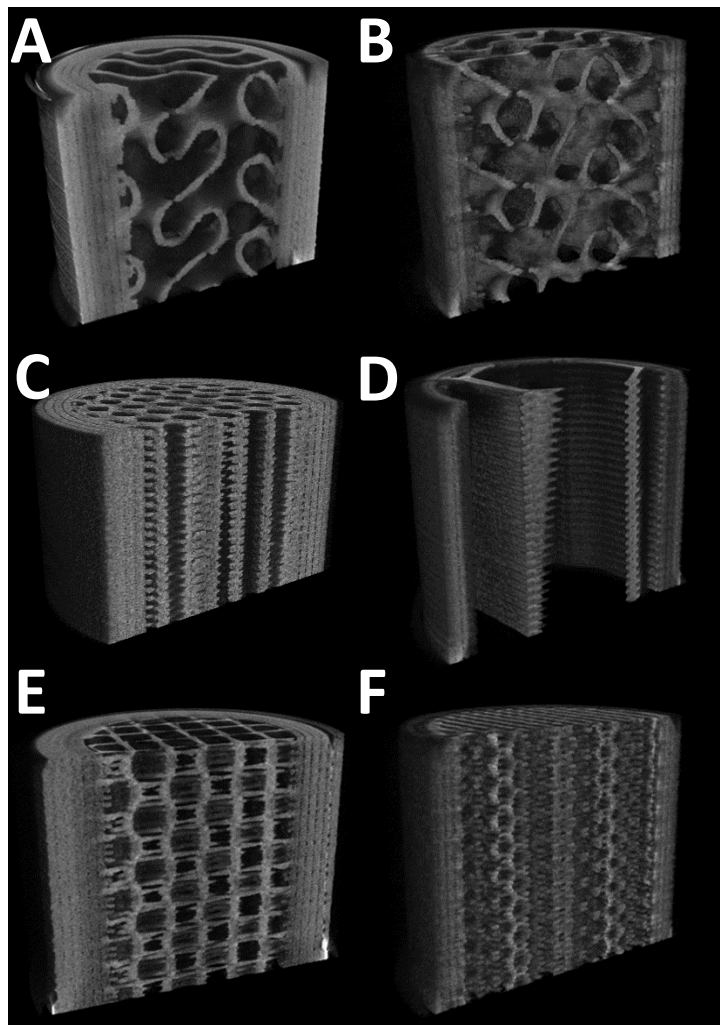


Figure 5-25: 3D renders of the reconstructed prototypes for the following parameter combinations: A) Gyroid_10_2.6, B) Gyroid_25_1.7, C) Honey_50_1.7, D) Honey_10_1.7, E) 3DHoney_25_2.6 and F) 3DHoney_50_1.7. Each image is sliced by a plane to provide an interior look at the samples.

	Thick Shell 25% infil			Thin Shell 25% infil		
	Gyroidal	Honeycomb	3D Honeycomb	Gyroidal	Honeycomb	3D Honeycomb
Grey Scale Bone CT						
Binarised Bone image						
Binary Open Porosity						
Binary Closed Porosity						
Total Porosity / %	55.57	57.34	56.86	75.39	67.21	62.64
Open Porosity / %	53.73	55.87	56.06	74.87	66.71	61.61
Closed Porosity / %	1.84	1.47	0.8	0.52	0.5	1.03

Figure 5-26: Micro CT images for a 25% infill model of each unit cell and of both thin and thick outer shell diameter. From top to bottom of rows: Grey scale original reconstructed images, Thresholded slice images, binarised open pores displayed slice, binarised closed pores displayed slice. Percentages for porosity of the included images are shown at the bottom as well.

The visual analysis was performed on the reconstructed images of each of the samples in conjunction with the data available from the CT analysis output. Although only an example image was shown, a complete analysis of the data sets was performed when evaluating these prototypes by evaluating all three-dimensional reconstructions. As expected, the majority of the open porosity was present within the interior portion of the constructs. However, there were a number of sections where open porosity was highlighted in the exterior shell sections. Examples of this are shown in Figure 5-26, row 3, columns 2, 4 and 6. As all of the samples were solid objects on the exterior some of these can be viewed as thresholding artefacts while others that are closer to the interior wall could be representing larger spaces between the print lines of the shell.

A more in-depth inspection shows that there are multiple breakages within the trabeculae of some of the unit cell structures on the interior of the samples. This is visible in the chosen image slices where the interior had white segments within the black trabeculae, for example row 2 column 5 in Figure 5-26. An observation that was made was also that this became more common as the unit cells became more complicated, or as the infill percentage was raised. This was first identified when excluding original samples, however, the previously excluded had these present throughout the layer rather than at specific intervals.

Images A and B of Figure 5-25 show 2 of the 6 gyroidal designs reproduced in CTVOX, the interior structures are printed effectively, as demonstrated by the clarity of the unit cell design and the complexity is not lost when the infill percentage is increased. There are gaps that can be seen in some of the trabeculae, but they do not appear to be widespread and may just be due to the position of the plane cut.

Table 5.10: Micro-CT results of the second generation of prototypes. With the following data values included: Open porosity percentage, Closed porosity percentage, Trabeculae Thickness (μm) and Trabeculae Separation (μm). Previously excluded samples are marked as Na in this data. Tissue values are included in the last column for comparison.

	Gyroid 50_2.6	Gyroid 25_2.6	Gyroid 10_2.6	Honey 50_2.6	Honey 25_2.6	Honey 10_2.6	3DHoney 50_2.6	3DHoney 25_2.6	3DHoney 10_2.6
Open porosity %	53.73	52.89	56.63	Na	Na	Na	45.74	56.06	Na
Closed porosity %	1.84	0.49	0.85	Na	Na	Na	0.50	0.80	Na
Trabecular Thickness / mm	0.44	1.26	1.02	Na	Na	Na	0.83	0.72	Na
Trabecular Separation / mm	1.79	1.92	2.57	Na	Na	Na	1.86	1.99	Na

	Gyroid 50_1.7	Gyroid 25_1.7	Gyroid 10_1.7	Honey 50_1.7	Honey 25_1.7	Honey 10_1.7	3DHoney 50_1.7	3DHoney 25_1.7	3DHoney 10_1.7	Tissue_Mean
Open porosity %	Na	74.87	70.61	45.31	66.71	80.78	60.88	61.61	Na	51.96
Closed porosity %	Na	0.52	1.07	0.81	0.50	0.25	0.27	1.03	Na	0.15
Trabecular Thickness / mm	Na	0.38	0.65	0.63	0.57	0.33	0.29	0.47	Na	0.25
Trabecular Separation / mm	Na	2.10	2.91	1.60	2.01	3.25	1.64	1.69	Na	0.41

The honeycomb designs follow a more linearly geometric pattern as seen by images C – F in Figure 5-25 and thus was not able to adapt as well to the cylindrical geometry, this being particularly present in the 10% designs (Figure 5-25D). Another issue that was present within both unit cell designs was that the print line troughs between every layer were very visible even at a larger scale.

The porosity of the prototypes varies from a minimum of 45% to a maximum of 81%. For the gyroidal samples, there was no direct correlation between infill and porosity seen in Table 5.11 , with the 25% and 10% samples being within a small margin of each other in both shell thicknesses (7% difference in 2.6 mm shell, 6% difference in 1.7 mm shell). However, it is not always directly linked to the infill percentage of the sample (Table 5.11). Both honeycomb and 3D honeycomb in the 1.7 mm shell did however produce a trend that open porosity increased with a negative correlation to infill percentage. Across all samples the closed porosity was very small, as it was mostly confined to only the shell, with a range of values from 0.29 to 1.84 reported.

The trabeculae thickness within the prototypes is mostly defined by the nozzle attachment at 0.15 mm and the design of the unit cell with all values reported in Table 5.11 row 3. The trabeculae thickness was exaggerated due to the shell being within the ROI of analysis, thus there is an additional measurement of 2.7 mm or 1.7 mm that included in the mean. For trabecular separation the mean for the 50, 25 and 10 percent infills was 1.67 ± 0.13 mm, 1.92 ± 0.13 mm, and 2.70 ± 0.34 mm respectively. All of which are significantly larger than the observed separation in the tissue scans at 0.41 mm.

5.3.3.8. Prototype print viability discussion

DMA results compared to tissue values.

As one of the key aims is to represent human tissue, an adjustment factor of 0.5 is applied to the bovine tissue results to align them with expected human tissue outcomes [31]. From this, the mean storage modulus value for the tissue samples was ~125 MPa (section 5.3.3.6) which is 45% increase over the print unit that produced the stiffest result, 87.22 ± 2.17 MPa. The difference in the loss modulus was much larger at an average of a factor 2.12 when comparing each test frequency individually as seen in Table 5.12.

Table 5.11: Loss modulus comparison of Tissue vs largest printed value with largest loss modulus/ With comparative factor calculated as $E''(\text{tissue})/E''(\text{Printed})$.

	Frequency / Hz								Median of factors
	1	8	10	12	30	50	70	90	
Tissue Loss Modulus / MPa	12.38	14.38	15.42	16.25	24.02	33.35	42.62	52.11	
Printed Loss Modulus MPa	3.34	5.67	6.28	7.08	12.37	18.27	24.08	29.84	
Comparative factor	3.71	2.54	2.45	2.29	1.94	1.83	1.77	1.75	2.12

Micro-CT

A key issue reported in the visual analysis was the print line troughs being highly present in the CT images. This could raise issues in that these segments show that layers of the design are not necessarily flush together, which would result in additional porosity in the prototypes and the introduction of potential weaknesses. It could be a sign of the printer resolution struggling with the complicated nature of the higher infill build specification.

When comparing the obtained open porosity values to the tissue values obtained in section 5.2.3, all of the 50% infill design are within a reasonable margin of the required 51.96% of porosity. As the infill percentage is decreased the similarity to the tissue is diminished, however, the gyroidal unit cell stays the closest in value. For closed porosity a higher mean of 1% was seen in the 2.6 mm shell compared to a mean of 0.58% in the 1.7 mm shell. This logically holds true as introducing two additional layers to the shell width adds two more possible tram lines between print layers where pores can take place. However, closed porosity for all samples (0.25% – 1.84%) falls within an appropriate approximation of the tissue values 0.15%.

There is no clear trend between a change in any of the following: unit cell, shell thickness, and infill percentage, and an increase/decrease in the thickness seen in our outputs. In 4 out of the 6 combinations of unit cell and shell thickness, the largest trabecular thickness was seen when the infill was set to 50%. This could be a results of two things, one as the design becomes more compacted the unit cells become denser resulting in the thicker measurement, or the printer is losing resolution quality as the unit cell complexities increases. For all designs the trabecular thickness is within a reasonable margin of the tissue's reported mean value. Trabecular separations follow a direct trend of decreasing and the infill percentage increase. This was expected as the infill results in a denser unit cell design and thus the pores are smaller in nature.

This disparity in the moduli values and the issues previously raised about the print quality present serious problems to overcome in the aim of developing a synthetic structure. Combing the unit cell designs, or developing new ones could provide the additional stiffness that is required to simulate the desired tissue.

5.3.4. Towards the design of a bio-inspired, multi-layer AM construct

The final stage of this work was to investigate if it was possible to create a hybrid construct that would mimic the different portions of tissue that are present within the osteochondral core. It was decided that mimicking the exact geometry of the components of the osteochondral core would not be completed as the current limitations in resolution would not allow the cartilage section to be both equivalent to its biological thickness and exhibit the correct internal until cell structure and the requirement of a shell that is not biologically accurate. It was therefore decided to include sections of both tissue representation and focus mimicking its mechanical response. Thus, two segments were additively manufactured in the form of ‘towers’, but not by the same ratio of bone to cartilage seen in section 5.2, this allows the individual section as well as the hybrid-crossover section to both be evaluated over a larger portion of printed material. The two sections, however, would be designed to match closest to the bone and cartilage mechanical responses recorded in section 5.2 and other published work. This design would also allow us to investigate if the same printing inconsistencies that rules out previous design in section 5.3.3.6 would be less or more present when both combining unit cell designs and increasing the complexity of the print samples.

5.3.4.1. Tower Specifications

The geometry of the design was decided to be kept simplistic and to combine two copies of the cylinders used in the previous prototypes into a single tower construct. This would also allow two discrete unit cells, infills and shell thicknesses to be used for each portion of the build. Part of the aim of this section was to establish whether

the printer was able to print a part of sufficient quality when combining the different infills, thus micro-CT was used to analyse the interior construct post print. The towers were 30 mm tall and 15 mm in diameter with an interface around the 15 mm mark where the parameters of the print can be altered. These parameters were chosen as it was then a direct combination of the test prints in section 5.3.3.6.

To reduce the likelihood of failure in the combination print, it was decided that the same unit cell would be used for both sections. The chosen unit cell for this prototype was gyroidal as not only did it provide a good range of possible mechanical properties as established in section 5.3.3.8, but structurally it mimicked the porosity of the tissue structure more accurately. As seen in Figure 5-27, different shell thicknesses and infills were used for each section. For the upper segment of the model, a shell thickness of 1.7 mm was used with an infill of 10% and for the

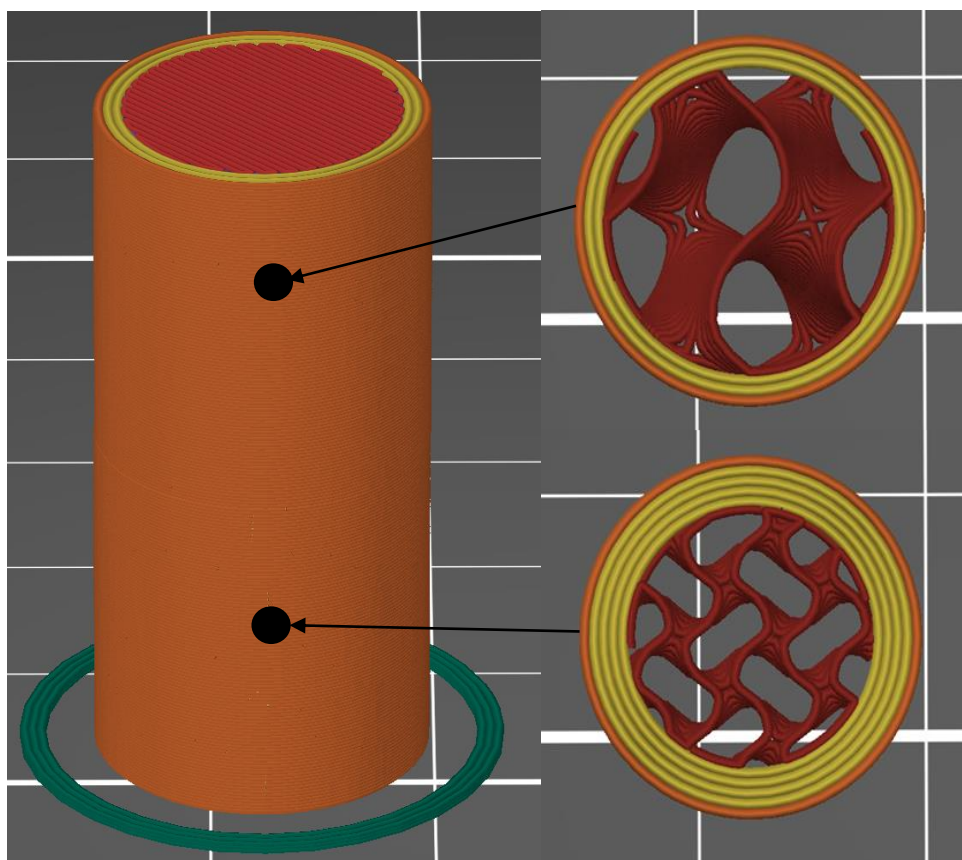


Figure 5-27: CAD designs, sliced in PrusaSlicer, of the AM tower construct with two discrete infills, unit cells and shell thicknesses.

lower segment, a shell thickness of 2.6 mm and an infill of 25%. Three repeats were produced of the tower for repeatability comparison and verification of any outputs gained. DMA was then performed on each of the towers under the same specification as laid out in section 5.2.3 to obtain the material properties of storage and loss modulus that could be compared to our biological data. Micro-CT imaging was also completed to analyse the internal print quality of the prototypes. The same methodology was used as described in section 5.2.4.

5.3.4.2. Tower testing results – Micro CT

All three towers were imaged and then reconstructed to produce 3D models. Figure 5-28 visualises an example of a reconstructed image slice (A) and a 3D model of the same sample (B). The internal structure is clearly visible in image A but also highlights that the transitional zone between the different segments, the area that is approximately at the 50% marker of the tower's height, has not printed accurately. There are visual indications of overlapping segments and incomplete unit cells that will result in structural weakness and reduced overall print quality. The second image (B) demonstrates that the 3D design of the unit cell was able to be printed in both segments, however, there are clear areas of porous black space in the shell and in the trabeculae of the unit cell that could indicate print quality issues as well. These are among the same issues that were identified in the previous prints demonstrating that it may be a limitation of the technology used resulting in a variable outcome of equivalence to print specification. The same micro-geometric anomalies were present across all 3 of the towers tested at inconsistent layers and locations.

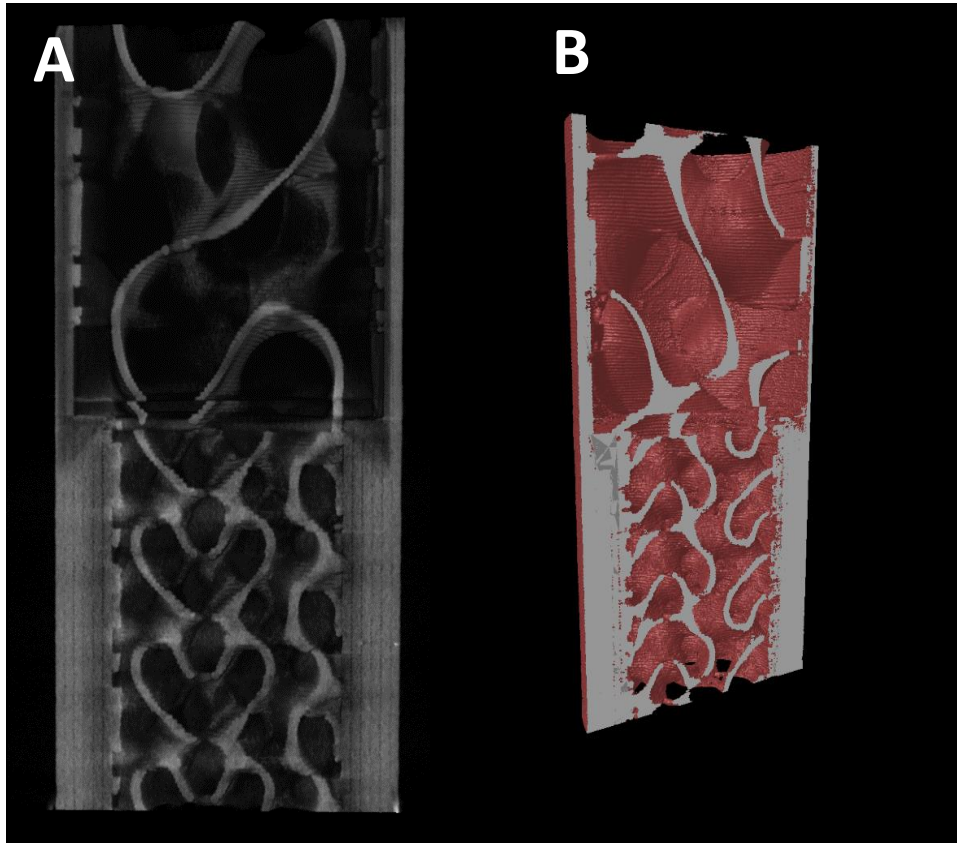


Figure 5-28: A) Reconstructed image of a tower post CT scan produced in CT Vox, B) Reconstructed image model, after morphological operations have been performed on it to calculate the porosity values.

As a result of the transitional zone being highlighted as a weak point of the prototype, further CT analysis was performed on this section individually. A transitional zone of 60 image slices was identified as a focus point and segmented out from the rest of the tower. This was analysed in three portions also: the 20 segments at the base of the zone, 20 transitional, and then the 20 after the transition. A single slice from each of these three sections is shown in their original greyscale format in the first row of Figure 5-29. The same steps of operations that are outlined in section 5.3.3.7 was then performed on each portion of the outlined transitional zone.


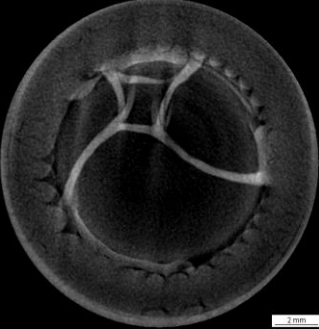
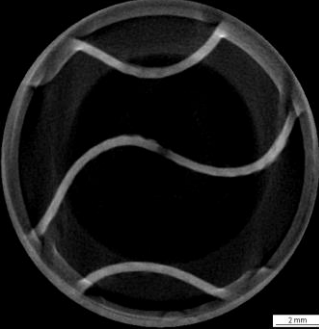




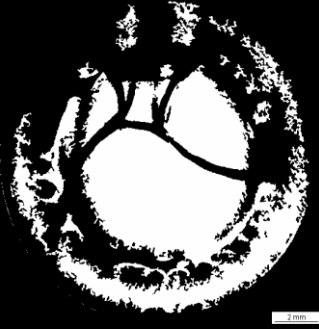

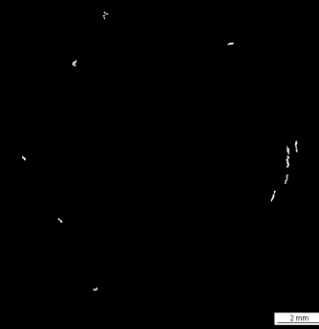
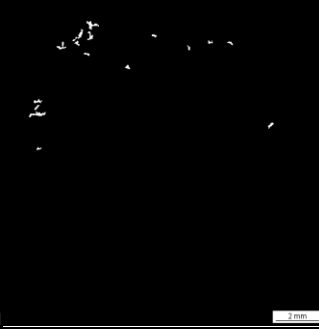
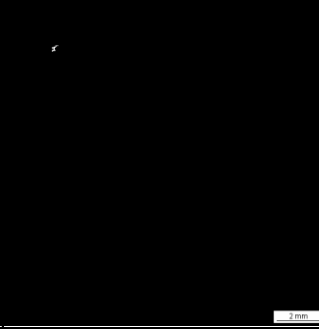
	Transition Zone 60 slice Segment		
	Thick Shell, 25% Gyroidal Infil	Transition segment	Thin Shell, 10% Gyroidal Fill
Grey Scale Bone CT			
Binarised Bone image			
Binary Open Porosity			
Binary Closed Porosity			
Total Porosity / %	41.68	61.94	73.23
Open Porosity / %	41.29	61.88	73.08
Closed Porosity / %	0.39	0.06	0.15

Figure 5-29: Micro CT images, reconstructed and then open and closed porosity image slices for a 60-slice segment of the tower displayed before, at and after the transition zone of the tower construct. From top to bottom of rows: Grey scale original reconstructed images, Thresholded slice images, Binarised open pores displayed slice, Binarised closed pores displayed slice. Percentages for porosity of the included images are shown at the bottom as well.

Visual inspection of Figure 5-29 aids in some initial interpretation, which re-occur from the analysis of the second prototypes. The image shown is of one slice however, the statements made are based on visually analysing all the image slices. Evaluating initially just the binarised image (Row 2, Figure 5-29), the top segment (Column 3, Figure 5-29) that contains the 10% infill 1.7 mm shell seems to have the least amount of corruption gained from being combined with the other prototype. There are a few segments where the shell and trabeculae are not complete, but it is mostly as specified in the 3D model. This is also visible on a larger scale in the reconstruction shown in Figure 5-29B. Moving onto the base portion (Column 1, Figure 5-29), which has the parameters of 25% infill and 2.6 mm shell, the unit cell itself, much like the top section has been completed correctly with some minor defects. However, within the shell of the base section there are clear areas of open porosity where the layers of the shell have not been laid closely enough together. The transitional phase (Column 2, Figure 5-29), has many more issues than those previously mentioned. The unit cell attempted to take on the characteristics of both infill definitions thus printing an incorrect representation of either. This is seen by the incompleteness of the design in the central section of the prototype. Much like in the lower section, the transitional point suffers from a large amount of additional porosity within the shell structure. In this case it is accentuated by the change in the number of shell layers between sections.

The porosity of these sections can be analysed further based on the outputted numeric values as well as the images. Firstly, it is not possible to directly equate the open porosity values to the expected infill percentages due to the exterior shell being a part of the ROI that was analysed in the CT software. It was seen that the open porosity (Row 3, Figure 5-29), the white section of the image, is evident in the shell

section of the images. This is especially prevalent in the transition segment, most likely due to the printer either being unable to differentiate between the two sections or due to significant interference from the alteration of two parameters (shell thickness and infill) at the same time. Creating a discrete transition section in the future with only a singular change may produce cleaner results.

Closed porosity for all three sections was only present within the shell, similar to that seen in the second generation of prototypes (Row 4, Figure 5-29). Although the percentages were low at 0.39%, 0.06% and 0.15% for lower, transition and upper sections, respectively, this highlights that the tram lines between individual applications of the substrate are still present. The issues that have been identified in the transitional zone here are clear indications of the limitations of the printing specification and hardware. As the complexity of the design increased, the accuracy and effective transposition from CAD model to outputted sample is reduced.

5.3.4.3. DMA of prototype towers results

Table 5.12: Storage and Loss modulus results from the three tower prints with mean and SD shown for each frequency tested.

	Frequency (Hz):							
	1	8	10	12	30	50	70	90
Storage Modulus (MPa)	157.82 ± 16.62	167.91 ± 19.45	169.43 ± 20.00	170.58 ± 20.41	174.72 ± 22.17	174.78 ± 22.53	172.43 ± 22.34	170.17 ± 22.23
Loss Modulus (MPa)	9.10 ± 2.27	14.02 ± 3.35	15.39 ± 3.51	16.67 ± 3.78	27.67 ± 5.25	39.96 ± 6.92	52.19 ± 8.69	64.45 ± 10.34

Although there are clear limitations in the printed produced as referenced in the previous section, an analysis of the effectiveness of currently available samples and their mechanical response data is still a useful endeavour to establish a base

standard to work forward from. Figure 5-30 displays the results that were obtained for the DMA of the towers. The mean \pm SD values for E' were 169.7 ± 20.7 MPa and E'' 29.9 ± 18.9 MPa. The full data is available in Table 5.13. Significant variation was seen between samples of the same specification in these tests with the coefficient of variations between the three samples tested being 0.12 for the storage modulus and 0.18 for the loss modulus.

5.3.4.4. Key findings - Comparison to tissue data

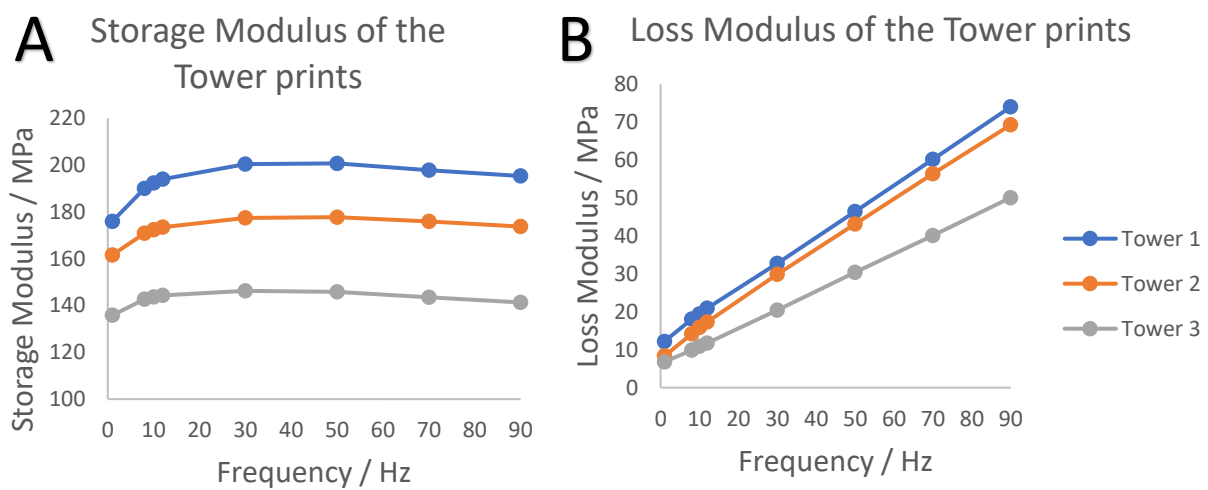


Figure 5-30: Storage (A) and Loss (B) moduli results for the three prototype towers for a frequency sweep of 1 to 90 Hz.

The mean value of the tower constructs storage modulus was 169.7 ± 20.7 MPa which matches the reported bone tissue values by Mountcastle et al. [18] at 170 ± 4.76 MPa, however, the standard deviation of the tower results shows that there is considerable error during the printing process. Even so, these results were also within a reasonable measure of data gathered in section 5.2.5.1 where the bovine storage modulus was 252 ± 9.32 , 50% larger than the printed components. For the loss modulus the difference between are experimental data and tower produced was 76% (cf. $52.6 - 29.9$ MPa, respectively), closer to the expected 2 to 1 ratio.

5.4. Discussion

The aim of this chapter was to establish the feasibility of using additive manufacture to produce a mechanically and structurally accurate prototype of a biological tissue, and for the purposes of this study, an osteochondral core. To provide additional values for our data set, information on mechanical properties and geometric components was gathered through DMA and micro-CT of bovine tissue. Due to the known dynamic nature of articular cartilage this chapter focused on the analysis of tissue before and after DMA compression to identify changes in its material response, which would provide insight to the subsequent analysis. This data would then lead in the construction and analysis of the hierarchical printed components that were then comparatively analysed against the initial studies findings.

Micro-CT of Osteochondral cores pre and post loading

It was established through the Micro-CT analysis that the osteochondral core in bovine tissue has approximately 52% porosity which matches with literature [192]. The micro-CT data gathered on the 5 samples that were DMA tested showed a reduction of 3% (48.87% vs 51.96%), in the porosity post loading with a physiologically representative load (induced stress of 0.75 -1.7 MPa). The set of samples that we tested showed there was a possibility compression of the tissue resulted in permanent deformation and changes to the internal structure. This change to the porosity could be due to the anisotropic nature of trabecula bone by increasing its structural density with the orientation of load [194], [195].

The hypothesis that deformation caused semi-permanent change was also backed up when evaluating the distributions of trabeculae thickness and separation where a

right shift was seen in the thickness post compression and a left shift in the separation. This equated to thicker branches and smaller pores in the tissue post loading. To substantiate these initial findings, the experimental work would need to be evaluated with a further data set and a larger range of load values in future work. There has been evidence of subchondral bone thickening to protect AC against load [196] which would match the trabecular changes identified in our results. It has been suggested that remodelling occurs in both the shape and contour of the subchondral bone [197] when load is applied and also that this is in part done to protect the AC surface [67]. The internal geometry changes were compared using the Micro-CT analysis; however, these can only be taken as preliminary observations due to the small sample size and bovine approximation used. Similar to this adaption of bone, it has already been shown that AC adapts loading capabilities change based on its geometric location and thickness [30], [117], [187]. Both these observations in literature leads us to believe that the osteochondral unit has a complicated mechanical response where its constituent parts responses are intertwined with each other. Thus these parameters are key factors when talking about the osteochondral interface.

AM limitations for manufacturing

The printer used for this study was the Prusa I3 Mk3 (Prusa Research a.s., Czech Republic) and some limitations were identified as a result of this choice. PLA or PETG were the only two filament options, other filaments, or printing materials such as hydrogels have been shown to also be biocompatible [105], [107]. Other printers would have to be investigated to allow use of these. Micro-CT was performed on the

AM components to allow the analysis of the quality of the produced products by looking at tram lines between nozzle runs and overall mimicry of the designed CAD model. The printer that was utilised in our study provided us the ability for a high throughput of prints with an ease to print design changes and allowed quick assessment.

The imperfections that were highlighted in chapter 5.3.3.6 with the samples that were excluded demonstrated a limitation of the printer. Repetition of the study where repeat samples are produced that would help identify whether there are inherent issues in the unit cell design that cause the print errors or whether it is a printer technology deficit. These issues were identified as a result of the micro-CT imaging and were present again in the tower structures that contained a combination of unit cell designs such as in Figure 5-29 as well as additional resolution issues, however, the results from section 5.3.3.6 provided initial insight into the fact that it was able to mimic the structural properties of tissue with some success. The grooves between print lines were clearly visible in our study (Figure 5-26 and Figure 5-29) and have previously been associated mechanical weakness[198]. with techniques developed by Allum et al. [199], [200] developed to counter this and provide stronger mechanical performance that have potential to be utilised in combination with our study.

The irregularities that were a condition for exclusion from the study were more prevalent in the honeycomb and 3D honeycomb designs than the gyroidal. It is postulated that this occurs when the shell is providing the main structural component, however, to explain the reduction in stiffness as the infill is increased is trickier. A hypothesis is that when the infill complexity is increased with percentage more interaction with the interior shell occurs. As we have seen in Figure 5-26 and

Figure 5-29 this can cause irregularities from the CAD and printing issues in reality. What we suggest is that this causes the shell to be weakened and thus results in the lower storage capability that we saw in the results.

Tissue representation utilising AM

Through the stages of prototyping that were performed, it was clear that there are a number of issues that need to be addressed in the next stage of the research.

However, the following observations were made with the conditionals mentioned. It was seen that a large range of control was possible on the material properties of the printed designs through the variation in the parameters that were tested. Across all the prototypes a storage modulus range of 50 – 90 MPa was obtained and a loss modulus range of 0.7 to 35 MPa. All the trends observed in Figure 5-21 are similar to those seen in previous studies for AC [18], [24]. However, the values are closer to that of AC rather than bone when looking at the values obtained. This is demonstrated by the fact that when the bovine-human factor is accounted for at a value of 2:1 [31] the moduli obtained are able to get within a reasonable representation AC tissue responses reported in other studies [18], [23].

For the tower constructs, it was highlighted in section 5.3.4.4 that they were able to mimic the results obtained in the earlier tissue experiments by a factor of 1.5 in the storage modulus and 1.75 in the loss modulus. However, it also demonstrated that there was a huge amount of variability in the outputted product as a result of the consistent print inconsistencies across all samples. Other printers and materials may result in a better resolution or accuracy, but this is not guaranteed due to the stochastic nature of AM. Also a change of material would change the material response properties of any printed units.

With regards to geometry, similar characteristics were identified between the bovine tissue data and the AM produced prototypes in porosity with gyroidal unit cells performing the best producing percentages in the range of 52 – 56% compared to the osteochondral core's porosity value of 51.96%. Both honeycomb and 3D honeycomb were also able to replicate the porosity but to a lesser extent.

A representative geometric design was not necessarily a requisite for the mechanical analysis performed but will be analysed anyway. The effectiveness of this analysis is also hindered by the current design of having a solid exterior shell as this does not allow for perforation. It should be taken into consideration as other studies on AM design has shown tissue-integration on the micro-scale to be a major factor in implant feasibility [201], [202]. Autograft and allograft procedures for osteochondral replacements are regularly used as cartilage replacements operations [6], [203] and designs for AM unit have started to appear in literature [204], [205]. However, these AM approaches do not account for the mechanical properties of the surrounding tissue. PLA is used in this study and has not only been shown to meet the criteria of biocompatibility in other medical applications [108], [109], [206] but also to be able to mimic the mechanics and internal geometrics of the AC and underlying subchondral bone individually (Sections 2.2 and 5.2.7). This produces good possibilities for PLA-AM constructs to be further evaluated for use as a hierarchical replacement for osteochondral cores.

The final goal of this study was to replicate the multi-layered tissue construct that is the osteochondral core with an additively manufactured prototype. Although the mean of the storage moduli for the towers produced was very close to reported findings [18] and some of our own, a number of issues were raised, with one being deviation observed in the results. A difference of 50 MPa was seen between two of

the towers of the same parameter specification highlighting other parameters outside of those defined were at play. The transitional zone that was created to simulate the multilayer tissue demonstrated that the print quality was lacking in reproducing the CAD designs. Incomplete unit cells and large open porosity were both present in this zone (Figure 5-29). A higher resolution of CT scan would provide additional insight into these observed shortcomings. The tower samples highlighted and reinforced the inconsistent print quality in the currently used technology and demonstrated that significant problems need to be overcome before the work can proceed. The first section of the chapter will be used to enhance the simulations that are run in Chapter 3. It highlighted the possibility that the structural properties should change with regards to the progression of the loading profile within any simulations of the osteochondral tissue.

5.5. Conclusion

In conclusion, this chapter aimed to evaluate both the mechanical changes observed in loaded osteochondral tissue and the possibility of creating an additively manufactured reproduction of this structure that was able to mechanically represent how its material response. The work presented shows that there is potential for permanent changes to occur during the natural loading sequence of cartilage that is yet to have been documented, however, further repeats are required to quantitatively prove this. The second section showed that it is feasible to obtain a large range of biologically relevant material properties from the DMA of an AM unit by the variation of certain parameters. A caveat to this was identified though that print quality can vary when combining specifications so the aim of replicating the entire osteochondral

unit was deemed to have scope for improvement, particularly around the manufacture quality and reducing the stochastic nature of the print for this composite construct.

The values obtained for the prototypes in round 2 after the exclusion of inaccurate prints, however, produced storage and loss moduli that matches to AC results reported elsewhere. With regards to the aim of physiologically representing the tissue as well, this was able to be done by showing that a porous internal structure could be printed that still had a close approximation to literature values and experimental results for both AC and subchondral bone storage and loss modulus. This has its own limitation in that the required shell of the print is both biologically inaccurate and is providing an unknown quantity of stiffness to the samples, which would need to be addressed and quantified in future studies. The current specification of hybrid AC/Bone representative construct was within a reasonable range of the biological tissue values, however, with the caveats mentioned in section 5.4. Alternative AM device evaluation of the same designs and more repetitions would provide additional data point to establish the next stages of the work.

Chapter 6. Thesis discussion and overall conclusions

6.1. Thesis discussion

This thesis has focused on the dynamic mechanical behaviour of AC. The dynamics of AC are critical in better analysing AC under non-equilibrium loading states; these are relevant loading states as they link to activities such as walking and running, as well as trauma [19], [24]. AC dynamics is an underexplored area of study with most studies focusing characterisation on equilibrium or quasi-static based loading conditions - this limits the precision with which we can characterise and distinguish the mechanical behaviour of healthy and OA cartilage, and the ability to develop novel replacement constructs. With the work presented in this thesis, two key outputs are presented: firstly, a computational framework by which to enable frequency domain viscoelastic characterisation to be available for time-domain FEA studies; secondly, AM has been exploited to develop test procedures to evaluate and mimic the mechanics of AC.

Chapter 3 focused on increasing the through put and accuracy of producing computational models and material parameters for a tissue specimen, in our case AC. Chapter 4 and 5 focused on macro and micro scale evaluation of cartilage material mechanics respectively through DMA and our ability to mimic them with artificially manufactured constructs, exploiting AM. Chapter 3 utilised human tissue in its work as data was wanted which a synthetic construct would be looking to mimic. Chapter 4 and 5 were more exploratory and thus more readily available animal tissue was used as a substitute.

Chapter 3 produced an automated system that could utilise mechanical data from DMA tests to fit material response parameters that were solved through optimisation.

There were two main components to this chapter, the design and production of the automated modelling system, and the case study on AC. This part of the work presented focused on producing a system that was modular in nature and not tissue specific. Through the analysis of the code base, this design philosophy was seen to be followed with each of the main portions of the modelling process being written in separate code files. This also extended to the material optimisation where the definitions of the 'fitness' functions, which is unique to which material model is being used, was portioned out into a separately definable file. A new technique for the establishing the fitness of a material optimisation solution was developed by allowing geometric models to be created for each possible material solution, and then evaluating the output of said models when compressed under a physiological load. This allowed the direct evaluation of how these material parameters would perform in a mechanical test. It also showed that an interface between the utilisation of Matlab and python's control scripts was a simplistic and effective way to utilise the optimal characteristics of available coding languages.

As far as the design specification goes, the system matched them all by being modular, with important components easily altered. Components of the system that handed load, geometry, boundary conditions, material characterisation, and optimisation algorithm choice were all segmented out into individual functions that allow them to be individually tweaked to the desired specifications of a user. With regards to the genetic algorithm, a separate function that handles the generational mutation was written as this is highly problem specific and would need coding expertise to alter. With the ability to make these changes the system could be used to evaluate other synthetic and tissue material characterisations under dynamic simulation.

The finding presented in the case study in chapter 3 on AC showed that an accurate material approximation can be gained from the system. The evaluation focused on assessing the difference between both the depth of generations performed in the genetic algorithm and the order of the Prony series that were used. Between the two generational depths tested, the majority of the effectiveness of the genetic algorithm was seen in the first 20 iterations with errors in the range of 17% to 24% depending on loading region. However, improvement, was seen across the board when it was raised from 20 to 50 iterations with a reduction of around 0.3% at maximum. If the number of iterations were increased even further this could so further improvement but whether the computational time it would take is worth it is in question. The order of approximation of the Prony series also was seen to alter the results, with $N = 3$ producing the best computational time to accuracy result. This showed that only a singular tweak to the main term of $N = 1$ was required to get a big alteration to the optimal value. For each of the loading sequences the difference between $N = 1$ and $N = 3$ was as follows: ramp - 7% decrease, loading hysteresis section – 25% decrease, and unloading hysteresis section – 3% increase. Although the unloading portion produced a slightly worse results at $N = 3$, the loading and ramp portion meant to the overall approximation was at its lowest in $N = 3$. The percentages changes are much lower in $N = 3$ to $N = 5$ so it was not as optimal, and it also reduces the likelihood of unnecessary terms and overfitting occurring.

Chapter 4 was designed to highlight the limitations in current mechanical testing procedures and their lack of physiological representation on the macro scale. Cartilage specimens obtained from bovine humeral heads were subjected to a sinusoidal cyclic compressive load whilst being held under tension on a contoured platen. AM was used to better mimic the contour otherwise it would not easily be

reproduced, and the tension was applied to return the tissue to an approximation of its natural tensile state in vivo. The results demonstrated that there was a statistical difference seen in both the storage and loss stiffness values between the contoured platens and the flat control. It also demonstrated that the steeper the slope of the contour, the greater the energy dissipation which occurred. This was the case during the cyclic loading across all frequencies tested, at almost a rate of 2:1 when comparing the 30° slope to the 7° slope at 0.77 mJ and 0.41 mJ, respectively. This lines up with observation by Barker and Seedhom that noted that cartilage may adapt based on the load it receives[69]. This could explain part of why cartilage has been shown to vary its mechanical response based on region[116], [117] as the geometry of said region changes in contour.

Chapter 5 focussed on a micro-scale analysis of the osteochondral core to understand its internal geometric structure and how it changes dynamic load. It presents a feasibility study on whether a hierarchical tissue structure can be generated with AM [6], [205]. The factors used to evaluate this feasibility were the geometrical structure and also the mechanical response via DMA; again noting the importance of focusing any constructs on non-equilibrium states of motion. Firstly, a comparison of micro-CT analysis of osteochondral cores pre- and post- DMA loading was performed. Although statistical tests found no significant difference in the changes observed, there was a 3% reduction in the porosity post DMA and a change of between 20 - 30 μm in the trabecular separation. A clear shift in the trabecular distributions in Figure 5-8 alongside the porosity changes lead to the hypothesis that there is permanent change occurring during the short loading cycles. The change that is seen in trabecular separation could be an indicator of subchondral bone aiding in the protection of cartilage [196] under load.

Chapter 5 also aimed to assess whether it is feasible to produce a hierarchical AM construct, which is inspired by an osteochondral core. A set of three constructs were produced with an interior porous structure that would allow for tissue integration[201], [202] as well producing a material response that was close to reported literature values[18], [23]. Tissue integration into implants using implanted growth factors or surface post-processing within scaffold structures[207] has been demonstrated to be an effective tool in studies by Ilea et al.[208], Man et al.[209] and others[210] on titanium constructs. This permeability/porosity of any designed constructs has been shown to enable integration into the subchondral bone and may allow ion transfer within the surrounding cartilage, however, this would need further study. The mean storage modulus was 169.7 ± 20.7 MPa compared to literature[18] at 170 ± 4.76 MPa and experimental bovine obtained in the earlier study presented in chapter 5 at 252 ± 9.32 MPa. For the loss modulus the difference was reported at 13% with trends that differ from previous studies, we hypothesise that this is due to an effect of the differing platen material of PLA having an effect on the energy dissipation ability within the experiment compared to metal substrate platens.

A number of samples were excluded from analysis during the evaluation phase due to the ineffectiveness of the printer to reproduce the respective CAD models.

Incomplete and damaged unit cells were identified when the unit was incomplete for the space it was aimed to fill or too complex in geometry between each layer applied.

This was especially highlighted in the tower complexes. The range of stiffness values that were able to be produced through varying the AM parameters. This combined with the information gained in chapter 4 about regional variation could be combined into creating an AM component that can provide the range of response across its surface. With the use of AM came a lot of control with macro scale

parameters such as joint shape being no issue to replicate. Micro scale geometries are harder to mimic with them limited by the diameter of the print nozzle, accuracy of the CAD design, and resolution of the printer. However, variability present in physical testing rigs provide a huge amount of variance and thus possibility in these parameters too. The faults of the current technology being used were pointed out in section 5.4, but even with the limitations a print within that produced results, although questioned in validity through lack of repeats, within a reasonable margin of biological relevance was produced.

A main limitation of this thesis was that the studies in chapter 4 and 5 were both performed on bovine cartilage/osteocondral cores rather than human. This results in adjustments to the finding having to be made to compensate and allow comparison to other human tissue studies. An extension to this is that even though the data utilised in chapter 3 was from human tissue, human tissue tends not to be otherwise young/healthy. Other factors also effect the physiological accuracy of data as many studies ignore natural tension when setting up experiment designs. This was mediated in our work in chapter 4 with our clamp design to apply a pre-stress condition that was physiologically relevant to the sample. These issues can result in a large amount of variability between data sets which means validation of material characterisation is even more important.

The results of the preliminary work from chapter 5 and the experiment in chapter 4 has shown the feasibility of producing an AM osteochondral model that would be both macro and microscopically representative of cartilage and provide similar properties to AC when materially characterised in a dynamic loading environment. With further evaluation of parameter combination and the possible increase in resolution other printer units would bring this could be further developed into an

entire joint epiphysis. If the AM components can be shown to be an accurate representation of human tissue this would reduce the need for biological samples in testing environment where on the material response analysis is required.

Additionally, chapter 3 showed that the development of an accurate computational model is also possible with the additional of more biological data. Thus, the thesis has met its aims set out in chapter 1.

6.2. Future work

As a results of the work presented in this thesis there are portions of work and stated hypothesis that could be researched further, These are laid out below:

1. Further the abilities of the automated system in the characterisations it can perform. This will allow it to be utilised for other biomaterials and synthetic constructs. Inclusion of further data sets of tissue from human/bovine samples that has been loaded in a dynamic environment will allow the optimisation to improve its accuracy.
2. There is potential to adapt the software to include a substrate below the evaluated FE model. This would not only allow the comparison of the properties seen at the macro scale parameter analysis within chapter 4 but also aid in the investigation of how these substrate's effect the AC. This, in part has already been looked at experimentally by Burgin and Aspden [211] and Crolla et al.[155] but as of yet has not been simulated to best of our knowledge.
3. Progressing from the above point, an investigation into the ability of AM to provide testing substrates that are biologically relevant would be beneficial in future dynamic environment loading studies.

4. Perform a study that further investigates the phenomena of physiological changes to bone geometrics pre and post dynamic loading. Elongation of the loading cycle or changing the amount of load could provide further insight into why the changes are being seen and what effect they are having within the osteochondral setting.
5. Perform further refinement of the AM osteochondral units design. This can be done by the investigation of further AM parameter variations and the testing of other manufacturing possibilities. If the designs can be enhanced to the point of accurate biological representation, investigating the possibility of making the osteochondral units patient specific in their material characterisation would be very beneficial for translation to a medical implant design.

6.3. Thesis conclusions

The work in this thesis has furthered research into AC being a dynamic 'structure' and demonstrates this characterisation. It has also been shown how AM can be used to both develop better testing procedures for characterisation; and also that it has future development potential for material response accurate replacement units.

The overall new research findings for the thesis are outlined below:

- 1) Using an automated approach to gain material parameters can remove not only the human bias in data selection but also provide additional control through the modular design. This enables hyper-viscoelastic approximation in a dynamic modeling environment that is unavailable elsewhere.
- 2) The Prony series approximation solved with a genetic algorithm and used for articular cartilage provides material parameters for a computational model of

said tissue with a mean error between 17% to 24% compared to human test tissue data.

- 3) When comparing the storage modulus of cartilage testing on a contoured plane versus a flat platen, a significant difference was found in for both values in at least one of the regression parameters. The mean values were for, 0° at 1118.5 N/mm, 7° at 1307.9 N/mm and 30° at 935.7 N/mm.
- 4) Cartilage when dynamically loaded on a contoured platen at 30° dissipates almost twice as much energy as if the same sample was loaded on a shallow 7° or flat platen (0.77 mJ, 0.42 mJ, 0.41 mJ, respectively).
- 5) There is preliminary evidence to suggest that permanent geometric changes are seen in bone tissue after a dynamic load between 0.75 MPa and 1.7 MPa at a frequency sweep of 1, 8, 10, 12, 30, 50, 70 and 90 is applied within its porosity percentage (pre load, 51.96%, post load 84.87%), trabecular thickness distributions (peak pre load - 243.4 μm , post load - 270.5 μm .) and trabecular separation distribution (peak pre load - 432.8 μm , post load - 378.7 μm .).
- 6) It is feasible to reproduce a range of material responses, storage modulus between 50 – 90 MPa and loss between 8 – 25 MPa) that lie within bone and cartilage experimental values by altering the interior parameters of the AM design, including unit cell, infill percentage and shell thickness.
- 7) PLA filament was able to be used to additively manufacture a multi-component construct that produced storage and loss modulus results in line with literature and also had geometric characteristics consistent with osteochondral tissue but with limitation that need to be addressed in future studies.

Bibliography:

- [1] J. K. Suh, Z. Li, and S. L. Y. Woo, 'Dynamic behavior of a biphasic cartilage model under cyclic compressive loading', *J Biomech*, vol. 28, no. 4, pp. 357–364, Apr. 1995, doi: 10.1016/0021-9290(94)00103-B.
- [2] D. E. T. Shepherd and B. B. Seedhom, 'The "instantaneous" compressive modulus of human articular cartilage in joints of the lower limb', 1999. [Online]. Available: <https://academic.oup.com/rheumatology/article/38/2/124/1783577>
- [3] A. J. S. Fox, A. Bedi, and S. A. Rodeo, 'The Basic Science of Articular Cartilage: Structure, Composition, and Function', 2009, doi: 10.1177/1941738109350438.
- [4] Arthritis Research UK, 'Osteoarthritis in general practice - Data and Perspectives - Arthritis Research UK', *Med Press*, vol. 222, pp. 253–258, 2013.
- [5] R. C. Lawrence *et al.*, 'Estimates of the prevalence of arthritis and other rheumatic conditions in the United States. Part II', *Arthritis Rheum*, vol. 58, no. 1, pp. 26–35, Jan. 2008, doi: 10.1002/art.23176.
- [6] A. Di Martino *et al.*, 'Osteochondral autograft transplantation versus autologous bone-cartilage paste grafting for the treatment of knee osteochondritis dissecans', *Int Orthop*, vol. 45, pp. 453–461, 2021, doi: 10.1007/s00264-020-04804-6/Published.
- [7] R. Brittain *et al.*, 'NJR statistical analysis, support and associated services National Joint Registry | 19th Annual Report'. [Online]. Available: www.njrcentre.org.uk
- [8] Baker C., 'Obesity statistics', Jan. 2023.
- [9] B. Raud *et al.*, 'Level of obesity is directly associated with the clinical and functional consequences of knee osteoarthritis', *Sci Rep*, vol. 10, no. 1, Dec. 2020, doi: 10.1038/s41598-020-60587-1.

- [10] M. Olive *et al.*, 'Preliminary evaluation of an osteochondral autograft, a prosthetic implant, and a biphasic absorbable implant for osteochondral reconstruction in a sheep model', *Veterinary Surgery*, vol. 49, no. 3, pp. 570–581, Apr. 2020, doi: 10.1111/vsu.13373.
- [11] M. T. Frassica and M. A. Grunlan, 'Perspectives on Synthetic Materials to Guide Tissue Regeneration for Osteochondral Defect Repair', *ACS Biomaterials Science and Engineering*, vol. 6, no. 8. American Chemical Society, pp. 4324–4336, Aug. 10, 2020. doi: 10.1021/acsbiomaterials.0c00753.
- [12] B. G. X. Zhang, D. E. Myers, G. G. Wallace, M. Brandt, and P. F. M. Choong, 'Bioactive coatings for orthopaedic implants-recent trends in development of implant coatings', *International Journal of Molecular Sciences*, vol. 15, no. 7. MDPI AG, pp. 11878–11921, Jul. 04, 2014. doi: 10.3390/ijms150711878.
- [13] P. H. Kuo *et al.*, 'Laser coating of bioactive glasses on bioimplant titanium alloys', *Int J Appl Glass Sci*, vol. 10, no. 3, pp. 307–320, Jul. 2019, doi: 10.1111/ijag.12642.
- [14] X. Bai, M. Gao, S. Syed, J. Zhuang, X. Xu, and X. Q. Zhang, 'Bioactive hydrogels for bone regeneration', *Bioactive Materials*, vol. 3, no. 4. KeAi Communications Co., pp. 401–417, Dec. 01, 2018. doi: 10.1016/j.bioactmat.2018.05.006.
- [15] V. C. Mow, S. C. Kuei, W. M. Lai, and C. G. Armstrong, 'Biphasic creep and stress relaxation of articular cartilage in compression: Theory and experiments', *J Biomech Eng*, vol. 102, no. 1, pp. 73–84, 1980, doi: 10.1115/1.3138202.
- [16] W. M. Lai, J. S. Hou, and V. C. Mow, 'A triphasic theory for the swelling and deformation behaviors of articular cartilage', *J Biomech Eng*, vol. 113, no. 3, pp. 245–258, 1991, doi: 10.1115/1.2894880.

- [17] J. M. Huyghe, W. Wilson, and K. Malakpoor, 'On the thermodynamical admissibility of the triphasic theory of charged hydrated tissues', *J Biomech Eng*, vol. 131, no. 4, p. 044504, Apr. 2009, doi: 10.1115/1.3049531/459854.
- [18] S. E. Mountcastle *et al.*, 'Dynamic viscoelastic characterisation of human osteochondral tissue: Understanding the effect of the cartilage-bone interface', *BMC Musculoskelet Disord*, vol. 20, no. 1, p. 575, Nov. 2019, doi: 10.1186/s12891-019-2959-4.
- [19] D. E. T. Shepherd and B. B. Seedhom, 'A technique for measuring the compressive modulus of articular cartilage under physiological loading rates with preliminary results', *Proc Inst Mech Eng H*, vol. 211, no. 2, pp. 155–165, 1997, doi: 10.1243/0954411971534278.
- [20] C. R. Henak, A. L. Kapron, A. E. Anderson, B. J. Ellis, S. A. Maas, and J. A. Weiss, 'Specimen-specific predictions of contact stress under physiological loading in the human hip: Validation and sensitivity studies', *Biomech Model Mechanobiol*, vol. 13, no. 2, pp. 387–400, 2014, doi: 10.1007/s10237-013-0504-1.
- [21] K. E. Keenan, S. Pal, D. P. Lindsey, T. F. Besier, and G. S. Beaupre, 'A viscoelastic constitutive model can accurately represent entire creep indentation tests of human patella cartilage', *J Appl Biomech*, vol. 29, no. 3, pp. 292–302, 2013, doi: 10.1123/jab.29.3.292.
- [22] X. Zhang, Y. Zheng, G. Y. Li, Y. L. Liu, and Y. Cao, 'Indentation creep tests to assess the viscoelastic properties of soft materials: Theory, method and experiment', *Int J Non Linear Mech*, vol. 109, pp. 204–212, Mar. 2019, doi: 10.1016/j.ijnonlinmec.2018.12.005.
- [23] N. L. A. Fell *et al.*, 'The role of subchondral bone, and its histomorphology, on the dynamic viscoelasticity of cartilage, bone and osteochondral cores', *Osteoarthritis Cartilage*, vol. 27, no. 3, pp. 535–543, Mar. 2019, doi: 10.1016/j.joca.2018.12.006.

- [24] H. Sadeghi, D. M. Espino, and D. E. Shepherd, 'Variation in viscoelastic properties of bovine articular cartilage below, up to and above healthy gait-relevant loading frequencies', *Proc Inst Mech Eng H*, vol. 229, no. 2, pp. 115–123, Feb. 2015, doi: 10.1177/0954411915570372.
- [25] R. M. Aspden and A. A. Cederlund, 'Walking on water: revisiting the role of water in articular cartilage biomechanics in relation to tissue engineering and regenerative medicine', *J R Soc Interface*, vol. 19, p. 20220364, 2022, doi: 10.1098/rsif.2022.0364.
- [26] Reddy J N, *An Introduction to The Finite Element Method*, 3rd ed. New York, 2005.
- [27] V. Klika, E. A. Gaffney, Y. C. Chen, and C. P. Brown, 'An overview of multiphase cartilage mechanical modelling and its role in understanding function and pathology', *Journal of the Mechanical Behavior of Biomedical Materials*, vol. 62. Elsevier Ltd, pp. 139–157, Sep. 01, 2016. doi: 10.1016/j.jmbbm.2016.04.032.
- [28] R. K. Korhonen, P. Julkunen, L. Li, and C. C. Van Donkelaar, 'Computational models of articular cartilage', *Computational and Mathematical Methods in Medicine*, vol. 2013. p. 254507, 2013. doi: 10.1155/2013/254507.
- [29] B. M. Lawless, H. Sadeghi, D. K. Temple, H. Dhaliwal, D. M. Espino, and D. W. L. Hukins, 'Viscoelasticity of articular cartilage: Analysing the effect of induced stress and the restraint of bone in a dynamic environment', *J Mech Behav Biomed Mater*, vol. 75, pp. 293–301, Nov. 2017, doi: 10.1016/j.jmbbm.2017.07.040.
- [30] D. M. Espino, D. E. Shepherd, and D. W. Hukins, 'Viscoelastic properties of bovine knee joint articular cartilage: Dependency on thickness and loading frequency', *BMC Musculoskeletal Disord*, vol. 15, no. 1, pp. 1–9, Jun. 2014, doi: 10.1186/1471-2474-15-205/TABLES/5.
- [31] D. K. Temple, A. A. Cederlund, B. M. Lawless, R. M. Aspden, and D. M. Espino, 'Viscoelastic properties of human and bovine articular cartilage: a comparison of frequency-dependent

- trends', *BMC Musculoskelet Disord*, vol. 17, no. 1, pp. 1–8, Oct. 2016, doi: 10.1186/s12891-016-1279-1.
- [32] J. S. Bell, C. P. Winlove, C. W. Smith, and H. Dehghani, 'Modeling the steady-state deformation of the solid phase of articular cartilage', *Biomaterials*, vol. 30, no. 31, pp. 6394–6401, Oct. 2009, doi: 10.1016/j.biomaterials.2009.08.026.
- [33] C. R. Henak, G. A. Ateshian, and J. A. Weiss, 'Finite element prediction of transchondral stress and strain in the human hip', *J Biomech Eng*, vol. 136, no. 2, p. 021021, Feb. 2014, doi: 10.1115/1.4026101.
- [34] M. Olive *et al.*, 'Preliminary evaluation of an osteochondral autograft, a prosthetic implant, and a biphasic absorbable implant for osteochondral reconstruction in a sheep model', *Veterinary Surgery*, vol. 49, no. 3, pp. 570–581, Apr. 2020, doi: 10.1111/vsu.13373.
- [35] J. N. Fu *et al.*, 'Scaffold-Based Tissue Engineering Strategies for Osteochondral Repair', *Frontiers in Bioengineering and Biotechnology*, vol. 9. Frontiers Media S.A., Jan. 11, 2022. doi: 10.3389/fbioe.2021.812383.
- [36] van Loon C J, de Waal Malefijt M C, Buma P, Verdonschot N, and Veth R P, 'Femoral bone loss in total knee arthroplasty. A review', *Acta Orthop Belg*, vol. 65, no. 2, pp. 154–163, 1999.
- [37] J. Palacio-Torralba *et al.*, 'Quantitative diagnostics of soft tissue through viscoelastic characterization using time-based instrumented palpation', *J Mech Behav Biomed Mater*, vol. 41, pp. 149–160, Jan. 2015, doi: 10.1016/j.jmbbm.2014.09.027.
- [38] S. Park, A. L. Chien, I. D. Brown, and J. Chen, 'Characterizing viscoelastic properties of human melanoma tissue using Prony series', *Front Bioeng Biotechnol*, vol. 11, 2023, doi: 10.3389/fbioe.2023.1162880.

- [39] W. Li, D. E. T. Shepherd, and D. M. Espino, 'Investigation of the Compressive Viscoelastic Properties of Brain Tissue Under Time and Frequency Dependent Loading Conditions', *Ann Biomed Eng*, vol. 49, no. 12, pp. 3737–3747, Dec. 2021, doi: 10.1007/s10439-021-02866-0.
- [40] G. Musumeci, 'The Effect of Mechanical Loading on Articular Cartilage', *Journal of Functional Morphology and Kinesiology Editorial*, doi: 10.3390/jfmk1020154.
- [41] M. Oliveira Silva, J. L. Gregory, N. Ansari, and K. S. Stok, 'Molecular Signaling Interactions and Transport at the Osteochondral Interface: A Review', *Front Cell Dev Biol*, vol. 8, p. 750, Aug. 2020, doi: 10.3389/FCELL.2020.00750/BIBTEX.
- [42] S. Ghosh, J. Bowen, K. Jiang, D. M. Espino, and D. E. T. Shepherd, 'Investigation of techniques for the measurement of articular cartilage surface roughness', *Micron*, vol. 44, no. 1, pp. 179–184, Jan. 2013, doi: 10.1016/j.micron.2012.06.007.
- [43] M. E. Cooke, B. M. Lawless, S. W. Jones, and L. M. Grover, 'Matrix degradation in osteoarthritis primes the superficial region of cartilage for mechanical damage', *Acta Biomater*, vol. 78, pp. 320–328, Sep. 2018, doi: 10.1016/j.actbio.2018.07.037.
- [44] J. Martel-Pelletier *et al.*, 'Osteoarthritis', *Nature Reviews Disease Primers 2016 2:1*, vol. 2, no. 1, pp. 1–18, Oct. 2016, doi: 10.1038/nrdp.2016.72.
- [45] Buckwalter J A and Mankin H J, 'Articular cartilage Part I', *Journal of Bone and Joint Surgery*, vol. 79, no. 4, p. 600, 1997.
- [46] S. L. Woo and J. A. Buckwalter, 'AAOS/NIH/ORS workshop. Injury and repair of the musculoskeletal soft tissues. Savannah, Georgia, June 18-20, 1987.', *J Orthop Res*, vol. 6, no. 6, pp. 907–931, 1988, doi: 10.1002/JOR.1100060615.
- [47] Athanasiou Kyriacos A., Darling Eric M., Hu Jerry C., DuRaine Grayson D., and Reddi A. Hari, *Articular Cartilage*, vol. 1. 2013.

- [48] C. J. Moger *et al.*, 'Regional variations of collagen orientation in normal and diseased articular cartilage and subchondral bone determined using small angle X-ray scattering (SAXS)', *Osteoarthritis Cartilage*, vol. 15, no. 6, pp. 682–687, Jun. 2007, doi: 10.1016/j.joca.2006.12.006.
- [49] J. C. Mansfield, C. P. Winlove, J. Moger, and S. J. Matcher, 'Collagen fiber arrangement in normal and diseased cartilage studied by polarization sensitive nonlinear microscopy', *J Biomed Opt*, vol. 13, no. 4, p. 044020, 2008, doi: 10.1117/1.2950318.
- [50] H. L. Stewart and C. E. Kawcak, 'The importance of subchondral bone in the pathophysiology of osteoarthritis', *Frontiers in Veterinary Science*, vol. 5, no. AUG. Frontiers Media S.A., Aug. 28, 2018. doi: 10.3389/fvets.2018.00178.
- [51] G. Li *et al.*, 'Subchondral bone in osteoarthritis: insight into risk factors and microstructural changes'. [Online]. Available: <http://arthritis-research.com/content/15/6/223>
- [52] S. Milz and R. Putz, 'Quantitative morphology of the subchondral plate of the tibial plateau', 1994.
- [53] J. M. Deneweth, E. M. Arruda, and S. G. Mclean, 'Hyperelastic modeling of location-dependent human distal femoral cartilage mechanics', *Int J Non Linear Mech*, pp. 1–11, 2014, doi: 10.1016/j.ijnonlinmec.2014.06.013.
- [54] C. Wex, S. Arndt, A. Stoll, C. Bruns, and Y. Kupriyanova, 'Isotropic incompressible hyperelastic models for modelling the mechanical behaviour of biological tissues: A review', *Biomedizinische Technik*, vol. 60, no. 6, pp. 577–592, Dec. 2015, doi: 10.1515/BMT-2014-0146/XML.
- [55] R. W. Ogden, *Non-linear elastic deformations*, Illustrated., vol. 1. E. Horwood, 1984, 195AD.

- [56] R. Northeast *et al.*, 'Mechanical testing of glutaraldehyde cross-linked mitral valves. Part one: In vitro mechanical behaviour', *J Engineering in Medicine*, vol. 235, no. 3, 2021, doi: 10.1177/0954411920975894.
- [57] K. Yoganandam *et al.*, 'Investigation of Dynamic, Mechanical, and Thermal Properties of Calotropis procera Particle-Reinforced PLA Biocomposites', *Advances in Materials Science and Engineering*, vol. 2021, 2021, doi: 10.1155/2021/2491489.
- [58] M. L. Roemhildt, K. M. Coughlin, G. D. Peura, B. C. Fleming, and B. D. Beynnon, 'Material properties of articular cartilage in the rabbit tibial plateau', doi: 10.1016/j.jbiomech.2005.07.017.
- [59] E. Comellas, S. I. Valdez, S. Oller, and S. Botello, 'Optimization method for the determination of material parameters in damaged composite structures', *Compos Struct*, vol. 122, pp. 417–424, Apr. 2015, doi: 10.1016/j.compstruct.2014.12.014.
- [60] Menard K. P. and Menard N. R., *Dynamic Mechanical Analysis*, 3rd ed., vol. 1. 2020.
- [61] B. Paschke, R. June, and E. Johnson, 'The effects of dynamic viscosity on cartilage mechanics', 2017, doi: 10.1016/j.joca.2017.02.206.
- [62] F. H. Silver, G. Bradica, and A. Tria, 'Elastic energy storage in human articular cartilage: estimation of the elastic modulus for type II collagen and changes associated with osteoarthritis', *Matrix Biology*, vol. 21, no. 2, pp. 129–137, Mar. 2002, doi: 10.1016/S0945-053X(01)00195-0.
- [63] L. Edelsten, J. E. Jeffrey, L. V. Burgin, and R. M. Aspden, 'Viscoelastic deformation of articular cartilage during impact loading', *Soft Matter*, vol. 6, no. 20, pp. 5206–5212, Oct. 2010, doi: 10.1039/C0SM00097C.

- [64] I. S. Kovach, 'A molecular theory of cartilage viscoelasticity', *Biophys Chem*, vol. 59, no. 1–2, pp. 61–73, Mar. 1996, doi: 10.1016/0301-4622(95)00115-8.
- [65] W. C. Hayes and L. F. Mockros, 'Viscoelastic properties of human articular cartilage.', *J Appl Physiol*, vol. 31, no. 4, pp. 562–568, 1971, doi: 10.1152/jappl.1971.31.4.562.
- [66] G. R. Fulcher, D. W. L. Hukins, and D. E. T. Shepherd, 'Viscoelastic properties of bovine articular cartilage attached to subchondral bone at high frequencies', *BMC Musculoskelet Disord*, vol. 10, no. 1, pp. 1–7, Jun. 2009, doi: 10.1186/1471-2474-10-61/FIGURES/3.
- [67] F. Malekipour, C. Whitton, D. Oetomo, and P. V. S. Lee, 'Shock absorbing ability of articular cartilage and subchondral bone under impact compression', *J Mech Behav Biomed Mater*, vol. 26, pp. 127–135, Oct. 2013, doi: 10.1016/j.jmbbm.2013.05.005.
- [68] A. Verteramo and B. B. Seedhom, 'Effect of a single impact loading on the structure and mechanical properties of articular cartilage', *J Biomech*, vol. 40, no. 16, pp. 3580–3589, Jan. 2007, doi: 10.1016/J.JBIOMECH.2007.06.002.
- [69] M. K. Barker and B. B. Seedhom, 'The relationship of the compressive modulus of articular cartilage with its deformation response to cyclic loading: Does cartilage optimize its modulus so as to minimize the strains arising in it due to the prevalent loading regime?', *Rheumatology*, vol. 40, no. 3, pp. 274–284, 2001, doi: 10.1093/rheumatology/40.3.274.
- [70] W. Ehlers and B. Markert, 'A Viscoelastic Two-phase Model for Cartilage Tissues', in *IUTAM Symposium on Theoretical and Numerical Methods in Continuum Mechanics of Porous Materials*, Kluwer Academic Publishers, 2005, pp. 87–92. doi: 10.1007/0-306-46953-7_12.
- [71] G. Li, J. Gil, A. Kanamori, and S. L. Y. Woo, 'A validated three-dimensional computational model of a human knee joint', *J Biomech Eng*, vol. 121, no. 6, pp. 657–662, Dec. 1999, doi: 10.1115/1.2800871.

- [72] D. M. Pierce, T. Ricken, and G. A. Holzapfel, 'A hyperelastic biphasic fibre-reinforced model of articular cartilage considering distributed collagen fibre orientations: Continuum basis, computational aspects and applications', *Comput Methods Biomech Biomed Engin*, vol. 16, no. 12, pp. 1344–1361, Dec. 2013, doi: 10.1080/10255842.2012.670854.
- [73] W. M. Lai, J. S. Hou, and V. C. Mow, 'A Triphasic Theory for the Swelling and Deformation Behaviors of Articular Cartilage', *J Biomech Eng*, vol. 113, no. 3, pp. 245–258, Aug. 1991, doi: 10.1115/1.2894880.
- [74] D. L. Robinson, M. E. Kersh, N. C. Walsh, D. C. Ackland, R. N. de Steiger, and M. G. Pandy, 'Mechanical properties of normal and osteoarthritic human articular cartilage', *J Mech Behav Biomed Mater*, vol. 61, pp. 96–109, Aug. 2016, doi: 10.1016/J.JMBBM.2016.01.015.
- [75] D. Lacroix, J. A. Planell, and P. J. Prendergast, 'Computer-aided design and finite-element modelling of biomaterial scaffolds for bone tissue engineering', *Philosophical Transactions of the Royal Society A: Mathematical, Physical and Engineering Sciences*, vol. 367, no. 1895. Royal Society, pp. 1993–2009, May 28, 2009. doi: 10.1098/rsta.2009.0024.
- [76] D. G. ; Owen, D. C. ; De Oliveira, E. K. ; Neale, D. E. T. ; Shepherd, and D. M. Espino, 'Numerical modelling of blood rheology and platelet activation through a stenosed left coronary artery bifurcation', 2021, doi: 10.1371/journal.pone.0259196.
- [77] O. Faris and J. Shuren, 'An FDA Viewpoint on Unique Considerations for Medical-Device Clinical Trials', *New England Journal of Medicine*, vol. 376, no. 14, pp. 1350–1357, Apr. 2017, doi: 10.1056/NEJMra1512592.
- [78] M. A. Kraus, M. Schuster, J. Kuntsche, G. Siebert, and J. Schneider, 'Parameter identification methods for visco- and hyperelastic material models', *Glass Structures and Engineering*, vol. 2, no. 2, pp. 147–167, Oct. 2017, doi: 10.1007/s40940-017-0042-9.

- [79] L. Coluccino, C. Peres, R. Gottardi, P. Bianchini, A. Diaspro, and L. Ceseracciu, 'Anisotropy in the Viscoelastic Response of Knee Meniscus Cartilage', *J Appl Biomater Funct Mater*, vol. 15, no. 1, pp. 77–83, Jan. 2017, doi: 10.5301/jabfm.5000319.
- [80] B. Szabo and I. Babuska, *Finite element analysis*. New York: John Wiley & Sons, 1991. doi: 10.1007/978-3-319-20777-3_4.
- [81] A. Erdemir, T. M. Guess, J. Halloran, S. C. Tadepalli, and T. M. Morrison, 'Considerations for reporting finite element analysis studies in biomechanics', *Journal of Biomechanics*, vol. 45, no. 4. Elsevier, pp. 625–633, Feb. 23, 2012. doi: 10.1016/j.jbiomech.2011.11.038.
- [82] D. C. de Oliveira *et al.*, 'A toolbox for generating scalable mitral valve morphometric models', *Comput Biol Med*, vol. 135, p. 104628, Aug. 2021, doi: 10.1016/J.COMPBIOMED.2021.104628.
- [83] R. Dingreville, R. A. Karnesky, G. Puel, and J. H. Schmitt, 'Review of the synergies between computational modeling and experimental characterization of materials across length scales', *J Mater Sci*, vol. 51, no. 3, pp. 1178–1203, Feb. 2016, doi: 10.1007/s10853-015-9551-6.
- [84] P. Pathmanathan, R. A. Gray, V. J. Romero, and T. M. Morrison, 'Applicability Analysis of Validation Evidence for Biomedical Computational Models', *J Verif Valid Uncertain Quantif*, vol. 2, no. 2, Jun. 2017, doi: 10.1115/1.4037671.
- [85] A. E. Anderson, B. J. Ellis, S. A. Maas, C. L. Peters, and J. A. Weiss, 'Validation of finite element predictions of cartilage contact pressure in the human hip joint', *J Biomech Eng*, vol. 130, no. 5, p. 051008, Oct. 2008, doi: 10.1115/1.2953472.
- [86] G. Bastos, L. Sales, N. Di Cesare, A. Tayeb, and J.-B. Le Cam, 'Inverse-PageRank-particle swarm optimisation for inverse identification of hyperelastic models: a feasibility study', *Journal of Rubber Research*, vol. 24, no. 3, pp. 447–460, Sep. 2021, doi: 10.1007/s42464-021-00113-8.

- [87] Connolly S., Mackenzie D., and Comlekci T., 'Multi-objective optimization of hyperelastic material constants: A feasibility study', in *The 10th European Conference on Constitutive Models for Rubber (ECCMR X)*, 2017.
- [88] H. Shipley *et al.*, 'Optimisation of process parameters to address fundamental challenges during selective laser melting of Ti-6Al-4V: A review', *Int J Mach Tools Manuf*, vol. 128, pp. 1–20, May 2018, doi: 10.1016/J.IJMACHTOOLS.2018.01.003.
- [89] M. R. Jacobs, 'Optimisation of antimicrobial therapy using pharmacokinetic and pharmacodynamic parameters', *Clinical Microbiology and Infection*, vol. 7, no. 11, pp. 589–596, Nov. 2001, doi: 10.1046/J.1198-743X.2001.00295.X.
- [90] X. Ying, 'An Overview of Overfitting and its Solutions', in *Journal of Physics: Conference Series*, IOP Publishing, Feb. 2019, p. 022022. doi: 10.1088/1742-6596/1168/2/022022.
- [91] G. Venter, 'Review of Optimization Techniques', *Encyclopedia of aerospace engineering*, 2010.
- [92] A. Wiberg, J. Persson, and J. Ölvander, 'Design for additive manufacturing – a review of available design methods and software', *Rapid Prototyping Journal*, vol. 25, no. 6. Emerald Group Holdings Ltd., pp. 1080–1094, Aug. 21, 2019. doi: 10.1108/RPJ-10-2018-0262.
- [93] S. Yang and Y. F. Zhao, 'Additive manufacturing-enabled design theory and methodology: a critical review', *International Journal of Advanced Manufacturing Technology*, vol. 80, no. 1–4. Springer London, pp. 327–342, Sep. 19, 2015. doi: 10.1007/s00170-015-6994-5.
- [94] E. George, P. Liacouras, F. J. Rybicki, and D. Mitsouras, 'Measuring and Establishing the Accuracy and Reproducibility of 3D Printed Medical Models', <https://doi.org/10.1148/rg.2017160165>, vol. 37, no. 5, pp. 1424–1450, Aug. 2017, doi: 10.1148/RG.2017160165.

- [95] Chua Chee Kai, Wong Chee How, and Yeong Wai Yee, *Standards, Quality Control, and Measurement Sciences in 3D Printing and Additive Manufacturing*. 2017.
- [96] Prusa Research a.s., 'Prusa'. Prusa, Czech Republic, 2017.
- [97] K. C. Wong, '3D-printed patient-specific applications in orthopedics', *Orthop Res Rev*, vol. 8, pp. 57–66, 2016, doi: 10.2147/ORR.S99614/DORR_A_99614_MED0001.AVI.
- [98] H. G. Yi *et al.*, 'A bioprinted human-glioblastoma-on-a-chip for the identification of patient-specific responses to chemoradiotherapy', *Nature Biomedical Engineering* 2019 3:7, vol. 3, no. 7, pp. 509–519, Mar. 2019, doi: 10.1038/s41551-019-0363-x.
- [99] Y. Tian *et al.*, 'A Review of 3D Printing in Dentistry: Technologies, Affecting Factors, and Applications', *Scanning*, vol. 2021, 2021, doi: 10.1155/2021/9950131.
- [100] A. A. Zadpoor and J. Malda, 'Additive Manufacturing of Biomaterials, Tissues, and Organs', *Ann Biomed Eng*, vol. 45, no. 1, pp. 1–11, 2017, doi: 10.1007/s10439-016-1719-y.
- [101] J. Domínguez-Robles *et al.*, '3D Printing of Drug-Loaded Thermoplastic Polyurethane Meshes: A Potential Material for Soft Tissue Reinforcement in Vaginal Surgery', *Pharmaceutics* 2020, Vol. 12, Page 63, vol. 12, no. 1, p. 63, Jan. 2020, doi: 10.3390/PHARMACEUTICS12010063.
- [102] I. Bácskay, Z. Ujhelyi, P. Fehér, and P. Arany, 'The Evolution of the 3D-Printed Drug Delivery Systems: A Review', *Pharmaceutics*, vol. 14, no. 7, Jul. 2022, doi: 10.3390/PHARMACEUTICS14071312.
- [103] H. E. Burton *et al.*, 'The design of additively manufactured lattices to increase the functionality of medical implants', *Materials Science and Engineering: C*, vol. 94, pp. 901–908, Jan. 2019, doi: 10.1016/J.MSEC.2018.10.052.

- [104] F. E. Freeman *et al.*, '3D bioprinting spatiotemporally defined patterns of growth factors to tightly control tissue regeneration', *Sci Adv*, vol. 6, no. 33, pp. 5093–5107, Aug. 2020, doi: 10.1126/SCIADV.ABB5093.
- [105] M. Pekař *et al.*, 'Hydrogel-Based Bioinks for 3D Bioprinting in Tissue Regeneration', *Frontier in Materials*, vol. 7, 2020, doi: 10.3389/fmats.2020.00076.
- [106] J. Gunnar Hilborn *et al.*, 'Hydrogels for Bioprinting: A Systematic Review of Hydrogels Synthesis, Bioprinting Parameters, and Bioprinted Structures Behavior', *Frontiers in Bioengineering and Biotechnology* | www.frontiersin.org, vol. 1, p. 776, 2020, doi: 10.3389/fbioe.2020.00776.
- [107] J. Li, C. Wu, P. K. Chu, and M. Gelinsky, '3D printing of hydrogels: Rational design strategies and emerging biomedical applications', *Materials Science and Engineering: R: Reports*, vol. 140, p. 100543, Apr. 2020, doi: 10.1016/J.MSER.2020.100543.
- [108] J. R. G. Carvalho *et al.*, 'Biocompatibility and biodegradation of poly(lactic acid) (PLA) and an immiscible PLA/poly(ϵ -caprolactone) (PCL) blend compatibilized by poly(ϵ -caprolactone-*b*-tetrahydrofuran) implanted in horses', *Polym J*, vol. 52, no. 6, pp. 629–643, Jun. 2020, doi: 10.1038/s41428-020-0308-y.
- [109] Y. Ramot, M. Haim-Zada, A. J. Domb, and A. Nyska, 'Biocompatibility and safety of PLA and its copolymers', *Adv Drug Deliv Rev*, vol. 107, pp. 153–162, Dec. 2016, doi: 10.1016/J.ADDR.2016.03.012.
- [110] M. H. Hassan *et al.*, 'The potential of polyethylene terephthalate glycol as biomaterial for bone tissue engineering', *Polymers (Basel)*, vol. 12, no. 12, pp. 1–12, Dec. 2020, doi: 10.3390/polym12123045.

- [111] B. Pearson and D. M. Espino, 'Effect of hydration on the frequency-dependent viscoelastic properties of articular cartilage', *Proc Inst Mech Eng H*, vol. 227, no. 11, pp. 1246–1252, Nov. 2013, doi: 10.1177/0954411913501294.
- [112] A. Oloyede and N. Broom, 'Stress-sharing between the fluid and solid components of articular cartilage under varying rates of compression', *Connect Tissue Res*, vol. 30, no. 2, pp. 127–141, 1993.
- [113] Harrigan T. P. and Mann R. W., 'State variables for modelling physical aspects of articular cartilage', *Int J Solids Struct*, vol. 23, no. 9, pp. 1205–1218, 1987.
- [114] J. M. Fick and D. M. Espino, 'Articular cartilage surface rupture during compression: Investigating the effects of tissue hydration in relation to matrix health', *J Mech Behav Biomed Mater*, vol. 4, no. 7, pp. 1311–1317, Oct. 2011, doi: 10.1016/J.JMBBM.2011.04.018.
- [115] J. M. Fick and D. M. Espino, 'Articular cartilage surface failure: An investigation of the rupture rate and morphology in relation to tissue health and hydration', <http://dx.doi.org/10.1177/0954411912439824>, vol. 226, no. 5, pp. 389–396, Mar. 2012, doi: 10.1177/0954411912439824.
- [116] D. E. T. Shepherd and B. B. Seedhom, 'The "instantaneous" compressive modulus of human articular cartilage in joints of the lower limb.', *Rheumatology*, vol. 38, no. 2, pp. 124–132, Feb. 1999, doi: 10.1093/RHEUMATOLOGY/38.2.124.
- [117] J. Hashemi *et al.*, 'The geometry of the tibial plateau and its influence on the biomechanics of the tibiofemoral joint', *Journal of Bone and Joint Surgery - Series A*, vol. 90, no. 12, pp. 2724–2734, Dec. 2008, doi: 10.2106/JBJS.G.01358.
- [118] Z. A. Cohen *et al.*, 'Knee cartilage topography, thickness, and contact areas from MRI: in-vitro calibration and in-vivo measurements', *OsteoArthritis Research Society*, vol. 7, p. 1063, 1999.

- [119] R. Agarwal and A. J. García, 'Biomaterial strategies for engineering implants for enhanced osseointegration and bone repair', *Advanced Drug Delivery Reviews*, vol. 94. Elsevier B.V., pp. 53–62, Nov. 01, 2015. doi: 10.1016/j.addr.2015.03.013.
- [120] D. D. Bikle and B. P. Halloran, 'The response of bone to unloading', *J Bone Miner Metab*, vol. 17, pp. 233–244, 1999.
- [121] P. K. Tomaszewski, N. Verdonchot, S. K. Bulstra, J. S. Rietman, and G. J. Verkerke, 'Simulated bone remodeling around two types of osseointegrated implants for direct fixation of upper-leg prostheses', *J Mech Behav Biomed Mater*, vol. 15, pp. 167–175, 2012, doi: 10.1016/j.jmbbm.2012.06.015.
- [122] Z. Jin, 'Fundamentals of computational modelling of biomechanics in the musculoskeletal system', in *Computational Modelling of Biomechanics and Biotribology in the Musculoskeletal System: Biomaterials and Tissues*, Elsevier Inc., 2014, pp. 3–11. doi: 10.1533/9780857096739.1.3.
- [123] L. Ren and Z. Qian, 'Finite element modeling in the musculoskeletal system: Generic overview', in *Computational Modelling of Biomechanics and Biotribology in the Musculoskeletal System: Biomaterials and Tissues*, Elsevier Inc., 2014, pp. 12–38. doi: 10.1533/9780857096739.1.12.
- [124] D. M. C. de Oliveira, N. Abdullah, N. C. Green, and D. M. Espino, 'Biomechanical Assessment of Bicuspid Aortic Valve Phenotypes: A Fluid–Structure Interaction Modelling Approach', *Cardiovasc Eng Technol*, vol. 11, no. 4, pp. 431–447, Aug. 2020, doi: 10.1007/s13239-020-00469-9.
- [125] R. L. Winslow, N. Trayanova, D. Geman, and M. I. Miller, 'Computational medicine: Translating models to clinical care', *Science Translational Medicine*, vol. 4, no. 158. Oct. 31, 2012. doi: 10.1126/scitranslmed.3003528.

- [126] L. P. Li, J. Soulhat, M. D. Buschmann, and A. Shirazi-Adl, 'Nonlinear analysis of cartilage in unconfined ramp compression using a fibril reinforced poroelastic model', *Clinical Biomechanics*, vol. 14, no. 9, pp. 673–682, Nov. 1999, doi: 10.1016/S0268-0033(99)00013-3.
- [127] J. C. Fialho, P. R. Fernandes, L. Eça, and J. Folgado, 'Computational hip joint simulator for wear and heat generation', *J Biomech*, vol. 40, no. 11, pp. 2358–2366, Jan. 2007, doi: 10.1016/j.jbiomech.2006.12.005.
- [128] D. L. McDowell and F. P. E. Dunne, 'Microstructure-sensitive computational modeling of fatigue crack formation', *Int J Fatigue*, vol. 32, no. 9, pp. 1521–1542, Sep. 2010, doi: 10.1016/j.ijfatigue.2010.01.003.
- [129] H. Delingette, 'Toward realistic soft-tissue modeling in medical simulation', *Proceedings of the IEEE*, vol. 86, no. 3, pp. 512–523, 1998, doi: 10.1109/5.662876.
- [130] X. S. Yang, S. Koziel, and L. Leifsson, 'Computational optimization, modelling and simulation: Smart algorithms and better models', *Procedia Comput Sci*, vol. 9, pp. 852–856, 2012, doi: 10.1016/j.procs.2012.04.091.
- [131] P. Refaeilzadeh, L. Tang, and H. Liu, 'Cross-Validation', in *Encyclopedia of Database Systems*, Springer, New York, NY, 2016, pp. 1–7. doi: 10.1007/978-1-4899-7993-3_565-2.
- [132] Dassault Systemes, 'Topology and Shape Optimization with Abaqus', pp. 1–41, 2011.
- [133] J. J. Kang, A. A. Becker, and W. Sun, 'Determining elastic–plastic properties from indentation data obtained from finite element simulations and experimental results', *Int J Mech Sci*, vol. 62, no. 1, pp. 34–46, Sep. 2012, doi: 10.1016/J.IJMECSCI.2012.05.011.
- [134] S. P. Soe, N. Martindale, C. Constantinou, and M. Robinson, 'Mechanical characterisation of Duraform® Flex for FEA hyperelastic material modelling', *Polym Test*, vol. 34, pp. 103–112, 2014, doi: 10.1016/j.polymertesting.2014.01.004.

- [135] D. W. Abueidda, M. Almasri, R. Ammourah, U. Ravaioli, I. M. Jasiuk, and N. A. Sobh, 'Prediction and optimization of mechanical properties of composites using convolutional neural networks', *Compos Struct*, vol. 227, Nov. 2019, doi: 10.1016/j.compstruct.2019.111264.
- [136] T. Gentils, L. Wang, and A. Kolios, 'Integrated structural optimisation of offshore wind turbine support structures based on finite element analysis and genetic algorithm', *Appl Energy*, vol. 199, pp. 187–204, 2017, doi: 10.1016/j.apenergy.2017.05.009.
- [137] T. K. Mulenga, A. U. Ude, and C. Vivekanandhan, 'Techniques for modelling and optimizing the mechanical properties of natural fiber composites: A review', *Fibers*, vol. 9, no. 1. MDPI AG, pp. 1–17, Jan. 01, 2021. doi: 10.3390/fib9010006.
- [138] Z. H. Zhang, Y. S. Qi, B. G. Wei, H. R. C. Bao, and Y. S. Xu, 'Application strategy of finite element analysis in artificial knee arthroplasty', *Frontiers in Bioengineering and Biotechnology*, vol. 11. Frontiers Media S.A., 2023. doi: 10.3389/fbioe.2023.1127289.
- [139] P. Allen, 'Automated-Modelling-System', *Automated-Modelling-System*. GitHub Repository, 2022.
- [140] S. Miramini, K. L. Fegan, N. C. Green, D. M. Espino, L. Zhang, and L. E. J. Thomas-Seale, 'The status and challenges of replicating the mechanical properties of connective tissues using additive manufacturing', *J Mech Behav Biomed Mater*, vol. 103, p. 103544, Mar. 2020, doi: 10.1016/J.JMBBM.2019.103544.
- [141] M. Szarko, K. Muldrew, and J. E. Bertram, 'Freeze-thaw treatment effects on the dynamic mechanical properties of articular cartilage', *BMC Musculoskelet Disord*, vol. 11, no. 1, p. 231, Dec. 2010, doi: 10.1186/1471-2474-11-231.

- [142] R. J. Lewis, A. K. MacFarland, S. Anandavijayan, and R. M. Aspden, 'Material properties and biosynthetic activity of articular cartilage from the bovine carpo-metacarpal joint', *Osteoarthritis Cartilage*, vol. 6, no. 6, pp. 383–392, Nov. 1998, doi: 10.1053/JOCA.1998.0142.
- [143] G. R. Fulcher, D. W. L. Hukins, and D. E. T. Shepherd, 'Viscoelastic properties of bovine articular cartilage attached to subchondral bone at high frequencies', *BMC Musculoskelet Disord*, vol. 10, no. 1, p. 61, Dec. 2009, doi: 10.1186/1471-2474-10-61.
- [144] T. McCormack and J. M. Mansour, 'Reduction in tensile strength of cartilage precedes surface damage under repeated compressive loading in vitro', *J Biomech*, vol. 31, no. 1, pp. 55–61, Nov. 1997, doi: 10.1016/S0021-9290(97)00103-6.
- [145] B. M. Lawless, 'Biostability of an orthopaedic device and its long-term implantable biomaterials', *University of Birmingham Ph.D*, 2019, Accessed: Oct. 11, 2022. [Online]. Available: <https://etheses.bham.ac.uk/id/eprint/8845/>
- [146] J. Q. Yao and B. B. Seedhom, 'Mechanical conditioning of articular cartilage to prevalent stresses', *Rheumatology*, vol. 32, no. 11, pp. 956–965, Nov. 1993, doi: 10.1093/rheumatology/32.11.956.
- [147] W. Li, D. E. T. Shepherd, and D. M. Espino, 'Investigation of the Compressive Viscoelastic Properties of Brain Tissue Under Time and Frequency Dependent Loading Conditions', *Ann Biomed Eng*, vol. 49, no. 12, pp. 3737–3747, Dec. 2021, doi: 10.1007/S10439-021-02866-0/FIGURES/7.
- [148] I. Pólik and T. Terlaky, 'Interior Point Methods for Nonlinear Optimization', *Lecture Notes in Mathematics*, vol. 1989, pp. 215–276, 2010, doi: 10.1007/978-3-642-11339-0_4.
- [149] P. Bhattacharya and M. Viceconti, 'Multiscale modeling methods in biomechanics', *Wiley Interdiscip Rev Syst Biol Med*, vol. 9, no. 3, p. e1375, May 2017, doi: 10.1002/wsbm.1375.

- [150] H. B. Henninger, S. P. Reese, A. E. Anderson, and J. A. Weiss, 'Validation of computational models in biomechanics', doi: 10.1243/09544119JEIM649.
- [151] M. Fernanda, P. Costa, and C. Ribeiro, 'Parameter Estimation of Viscoelastic Materials: A Test Case with Different Optimization Strategies', 2011, doi: 10.1063/1.3636846.
- [152] K. Wierzbanski, J. Tarasiuk, and A. Lodini, 'Optimization of material properties using genetic algorithms', *Materials Science Forum*, vol. 652, pp. 1–6, 2010, doi: 10.4028/WWW.SCIENTIFIC.NET/MSF.652.1.
- [153] B. M. Chaparro, S. Thuillier, L. F. Menezes, P. Y. Manach, and J. v. Fernandes, 'Material parameters identification: Gradient-based, genetic and hybrid optimization algorithms', *Comput Mater Sci*, vol. 44, no. 2, pp. 339–346, Dec. 2008, doi: 10.1016/J.COMMATSCI.2008.03.028.
- [154] H. Mahmood, D. E. T. Shepherd, and D. M. Espino, 'Surface damage of bovine articular cartilage-off-bone: The effect of variations in underlying substrate and frequency', *BMC Musculoskelet Disord*, vol. 19, no. 1, p. 384, Oct. 2018, doi: 10.1186/s12891-018-2305-2.
- [155] J. P. Crolla, B. M. Lawless, A. A. Cederlund, R. M. Aspden, and D. M. Espino, 'Analysis of hydration and subchondral bone density on the viscoelastic properties of bovine articular cartilage', *BMC Musculoskelet Disord*, vol. 23, no. 1, p. 288, Dec. 2022, doi: 10.1186/s12891-022-05169-0.
- [156] H. Li, J. Li, S. Yu, C. Wu, and W. Zhang, 'The mechanical properties of tibiofemoral and patellofemoral articular cartilage in compression depend on anatomical regions', *Scientific Reports /*, vol. 11, p. 6128, 123AD, doi: 10.1038/s41598-021-85716-2.
- [157] A. C. Swann and B. B. Seedhom, 'Improved techniques for measuring the indentation and thickness of articular cartilage', *Proceedings of the Institution of Mechanical Engineers, Part H:*

- Journal of Engineering in Medicine*, vol. 203, no. 3. SAGE PublicationsSage UK: London, England, pp. 143–150, Sep. 05, 1989. doi: 10.1243/PIME_PROC_1989_203_026_01.
- [158] P. G. Bullough, P. S. Yawitz, L. Tafra, and A. L. Boskey, 'Topographical variations in the morphology and biochemistry of adult canine tibial plateau articular cartilage', *Journal of Orthopaedic Research*, vol. 3, no. 1, pp. 1–16, Jan. 1985, doi: 10.1002/JOR.1100030101.
- [159] H. Iijima *et al.*, 'Immature articular cartilage and subchondral bone covered by menisci are potentially susceptible to mechanical load', *BMC Musculoskelet Disord*, vol. 15, no. 1, Mar. 2014, doi: 10.1186/1471-2474-15-101.
- [160] J. K. Loudon, 'Biomechanics and Pathomechanics of the Patellofemoral Joint', *The International Journal of Sports Physical Therapy |*, vol. 11, no. 6, p. 821, 2016.
- [161] S. Nie, J. Chen, H. Zhang, P. Zhao, W. Yan, and W. Huang, 'Tibial Spine Height Measured by Radiograph is A Risk Factor for Non-Contact Anterior Cruciate Ligament Injury in Males: A Retrospective Case-Control Study', 2022, doi: 10.21203/rs.3.rs-2081381/v1.
- [162] J. M. Patel, B. C. Wise, E. D. Bonnevie, and R. L. Mauck, 'A Systematic Review and Guide to Mechanical Testing for Articular Cartilage Tissue Engineering', *Tissue Engineering - Part C: Methods*, vol. 25, no. 10. Mary Ann Liebert Inc., pp. 593–608, Oct. 01, 2019. doi: 10.1089/ten.tec.2019.0116.
- [163] C. Herberhold *et al.*, 'In situ measurement of articular cartilage deformation in intact femoropatellar joints under static loading', *J Biomech*, vol. 32, no. 12, pp. 1287–1295, Dec. 1999, doi: 10.1016/S0021-9290(99)00130-X.
- [164] M. D. Buschmann, J. Soulhat, A. Shirazi-Adl, J. S. Jurvelin, and E. B. Hunziker, 'Confined compression of articular cartilage: Linearity in ramp and sinusoidal tests and the importance of interdigitation and incomplete confinement', *J Biomech*, vol. 31, no. 2, pp. 171–178, May 1997, doi: 10.1016/S0021-9290(97)00124-3.

- [165] W. C. Hayes, L. M. Keer, G. Herrmann, and L. F. Mockros, 'A mathematical analysis for indentation tests of articular cartilage', *J Biomech*, vol. 5, no. 5, pp. 541–551, Sep. 1972, doi: 10.1016/0021-9290(72)90010-3.
- [166] J. Eschweiler *et al.*, 'life The Biomechanics of Cartilage-An Overview', 2021, doi: 10.3390/life11040302.
- [167] S. Shen, P. Z. Wang, X. Y. Li, X. Han, and H. L. Tan, 'Pre-operative simulation using a three-dimensional printing model for surgical treatment of old and complex tibial plateau fractures', *Sci Rep*, vol. 10, no. 1, Dec. 2020, doi: 10.1038/s41598-020-63219-w.
- [168] CNC Kitchen, 'Comparing Pla, Petg & Asa - Feat. Prusament', <https://www.cnckitchen.com/blog/comparing-pla-petg-amp-asa-feat-prusament>.
- [169] S. D. Taylor, E. Tsiridis, E. Ingham, Z. Jin, J. Fisher, and S. Williams, 'Comparison of human and animal femoral head chondral properties and geometries', in *Proceedings of the Institution of Mechanical Engineers, Part H: Journal of Engineering in Medicine*, Proc Inst Mech Eng H, Jan. 2012, pp. 55–62. doi: 10.1177/0954411911428717.
- [170] D. L. Vaux, F. Fidler, and G. Cumming, 'Replicates and repeats-what is the difference and is it significant? A brief discussion of statistics and experimental design', *EMBO Rep*, vol. 13, no. 4, pp. 291–296, Apr. 2012, doi: 10.1038/EMBOR.2012.36.
- [171] R. M. Aspden, 'Constraining the lateral dimensions of uniaxially loaded materials increases the calculated strength and stiffness: application to muscle and bone', *J Mater Sci Mater Med*, vol. 1, pp. 100–104, 1990.
- [172] D. E. T. Shepherd and B. B. Seedhom, 'Thickness of human articular cartilage in joints of the lower limb', *Ann Rheum Dis*, vol. 58, no. 1, pp. 27–34, 1999, doi: 10.1136/ard.58.1.27.

- [173] C. G. Carlson, A. Chen, K. Patterson, and R. H. Alove, 'Glenohumeral Cartilage Thickness: Implications in Prosthetic Design and Osteochondral Allograft Transplantation', *Cartilage*, p. 194760352311545, Feb. 2023, doi: 10.1177/19476035231154504.
- [174] C. Bergmann *et al.*, '3D printing of bone substitute implants using calcium phosphate and bioactive glasses', *J Eur Ceram Soc*, vol. 30, no. 12, pp. 2563–2567, Sep. 2010, doi: 10.1016/J.JEURCERAMSOC.2010.04.037.
- [175] M. Lowther *et al.*, 'Clinical, industrial, and research perspectives on powder bed fusion additively manufactured metal implants', *Addit Manuf*, vol. 28, pp. 565–584, Aug. 2019, doi: 10.1016/J.ADDMA.2019.05.033.
- [176] S. Tadimalla, M. C. Tourell, R. Knott, and K. I. Momot, 'Quantifying collagen fibre architecture in articular cartilage using small-angle X-ray scattering', *Biomed Spectrosc Imaging*, vol. 6, no. 1–2, pp. 37–57, May 2017, doi: 10.3233/BSI-170164.
- [177] O. Démarteau, L. Pillet, A. Inaebnit, O. Borens, and T. M. Quinn, 'Biomechanical characterization and in vitro mechanical injury of elderly human femoral head cartilage: comparison to adult bovine humeral head cartilage', *Osteoarthritis Cartilage*, vol. 14, no. 6, pp. 589–596, Jun. 2006, doi: 10.1016/j.joca.2005.12.011.
- [178] C. Lubombo and M. A. Huneault, 'Effect of infill patterns on the mechanical performance of lightweight 3D-printed cellular PLA parts', *Mater Today Commun*, vol. 17, pp. 214–228, Dec. 2018, doi: 10.1016/J.MTCOMM.2018.09.017.
- [179] S. Al Hassanieh, A. Alhantoobi, K. A. Khan, and M. A. Khan, 'Mechanical properties and energy absorption characteristics of additively manufactured lightweight novel re-entrant plate-based lattice structures', *Polymers (Basel)*, vol. 13, no. 22, Nov. 2021, doi: 10.3390/polym13223882.

- [180] A. Chauhan and A. D. Bhatt, 'Effect of unit cell features on mechanical properties of lattice structures at constant porosity levels: A general mixture rule based interpretation', *Mater Today Proc*, vol. 56, pp. 1–8, Jan. 2022, doi: 10.1016/j.matpr.2021.11.323.
- [181] S. F. Cobos, C. J. Norley, S. I. Pollmann, and D. W. Holdsworth, 'Cost-effective micro-CT system for non-destructive testing of titanium 3D printed medical components', *PLoS One*, vol. 17, no. 10 October, Oct. 2022, doi: 10.1371/journal.pone.0275732.
- [182] A. Du Plessis, I. Yadroitsev, I. Yadroitsava, and S. G. Le Roux, 'X-Ray Microcomputed Tomography in Additive Manufacturing: A Review of the Current Technology and Applications', *3D Print Addit Manuf*, vol. 5, no. 3, pp. 227–247, Sep. 2018, doi: 10.1089/3dp.2018.0060.
- [183] G. M. Campbell and A. Sophocleous, 'Quantitative analysis of bone and soft tissue by micro-computed tomography: applications to ex vivo and in vivo studies', *Bonekey Rep*, vol. 3, Aug. 2014, doi: 10.1038/bonekey.2014.59.
- [184] J. N. Clark, S. Tavana, B. Clark, T. Briggs, J. R. T. Jeffers, and U. Hansen, 'High resolution three-dimensional strain measurements in human articular cartilage', *J Mech Behav Biomed Mater*, vol. 124, Dec. 2021, doi: 10.1016/j.jmbbm.2021.104806.
- [185] A. du Plessis, C. Broeckhoven, A. Guelpa, and S. G. le Roux, 'Laboratory x-ray micro-computed tomography: A user guideline for biological samples', *GigaScience*, vol. 6, no. 6. Oxford University Press, Jun. 01, 2017. doi: 10.1093/gigascience/gix027.
- [186] T. D. Ngo, A. Kashani, G. Imbalzano, K. T. Q. Nguyen, and D. Hui, 'Additive manufacturing (3D printing): A review of materials, methods, applications and challenges', *Compos B Eng*, vol. 143, pp. 172–196, Jun. 2018, doi: 10.1016/J.COMPOSITESB.2018.02.012.

- [187] T. Nishii, K. Kuroda, Y. Matsuoka, T. Sahara, and H. Yoshikawa, 'Change in knee cartilage T2 in response to mechanical loading', *Journal of Magnetic Resonance Imaging*, vol. 28, no. 1, pp. 175–180, Jul. 2008, doi: 10.1002/JMRI.21418.
- [188] S. H. McBride and M. J. Silva, 'Adaptive and injury response of bone to mechanical loading', *Bonekey Rep*, vol. 1, p. 192, Oct. 2012, doi: 10.1038/bonekey.2012.192.
- [189] A. G. Robling and C. H. Turner, 'Mechanical Signaling for Bone Modeling and Remodeling', 2009.
- [190] S. Raja *et al.*, 'Optimization of 3D Printing Process Parameters of Polylactic Acid Filament Based on the Mechanical Test', 2022, doi: 10.1155/2022/5830869.
- [191] K. Mys *et al.*, 'Quantification of 3D microstructural parameters of trabecular bone is affected by the analysis software', *Bone*, vol. 142, p. 115653, Jan. 2021, doi: 10.1016/J.BONE.2020.115653.
- [192] E. F. Morgan, G. U. Unnikrisnan, and A. I. Hussein, 'Annual Review of Biomedical Engineering Bone Mechanical Properties in Healthy and Diseased States', 2018, doi: 10.1146/annurev-bioeng-062117.
- [193] J. D. Boerckel, D. E. Mason, A. M. Mcdermott, and E. Alsberg, 'Microcomputed tomography: approaches and applications in bioengineering', *Stem Cell Res Ther*, vol. 5, p. 144, 2014, [Online]. Available: <http://stemcellres.com/content/5/6/144>
- [194] G. Osterhoff, E. F. Morgan, S. J. Shefelbine, L. Karim, L. M. McNamara, and P. Augat, 'Bone mechanical properties and changes with osteoporosis', *Injury*, vol. 47, no. Suppl 2, p. S11, Jun. 2016, doi: 10.1016/S0020-1383(16)47003-8.

- [195] V. S. Cheong, V. Kadiramanathan, and E. Dall'Ara, 'The Role of the Loading Condition in Predictions of Bone Adaptation in a Mouse Tibial Loading Model', *Front Bioeng Biotechnol*, vol. 9, Jun. 2021, doi: 10.3389/FBIOE.2021.676867.
- [196] K. A. Staines *et al.*, 'Conditional deletion of E11/podoplanin in bone protects against load-induced osteoarthritis', *BMC Musculoskelet Disord*, vol. 20, no. 1, Jul. 2019, doi: 10.1186/s12891-019-2731-9.
- [197] S. R. Goldring, 'Alterations in periarticular bone and cross talk between subchondral bone and articular cartilage in osteoarthritis', *Ther Adv Musculoskelet Dis*, vol. 4, no. 4, p. 249, 2012, doi: 10.1177/1759720X12437353.
- [198] J. Allum, A. Moetazedian, A. Gleadall, and V. V. Silberschmidt, 'Interlayer bonding has bulk-material strength in extrusion additive manufacturing: New understanding of anisotropy', *Addit Manuf*, vol. 34, Aug. 2020, doi: 10.1016/j.addma.2020.101297.
- [199] J. Allum *et al.*, 'Extra-wide deposition in extrusion additive manufacturing: A new convention for improved interlayer mechanical performance', *Addit Manuf*, vol. 61, Jan. 2023, doi: 10.1016/j.addma.2022.103334.
- [200] J. Allum, J. Kitzinger, Y. Li, V. V. Silberschmidt, and A. Gleadall, 'ZigZagZ: Improving mechanical performance in extrusion additive manufacturing by nonplanar toolpaths', *Addit Manuf*, vol. 38, Feb. 2021, doi: 10.1016/j.addma.2020.101715.
- [201] E. A. Guzzi and M. W. Tibbitt, 'Additive Manufacturing of Precision Biomaterials', *Advanced Materials*, vol. 32, no. 13, p. 1901994, Apr. 2020, doi: 10.1002/ADMA.201901994.
- [202] S. Miramini, K. L. Fegan, N. C. Green, D. M. Espino, L. Zhang, and L. E. J. Thomas-Seale, 'The status and challenges of replicating the mechanical properties of connective tissues using additive manufacturing', *J Mech Behav Biomed Mater*, vol. 103, p. 103544, Mar. 2020, doi: 10.1016/J.JMBBM.2019.103544.

- [203] A. J. Guzman *et al.*, 'Arthroscopic Osteochondral Autograft Transfer System Procedure of the Lateral Femoral Condyle with Donor-Site Backfill Using Osteochondral Allograft Plug', *Arthrosc Tech*, vol. 10, no. 12, pp. e2683–e2689, Dec. 2021, doi: 10.1016/j.eats.2021.08.012.
- [204] S. E. Doyle *et al.*, '3D Printed Multiphasic Scaffolds for Osteochondral Repair: Challenges and Opportunities', *Int J Mol Sci*, vol. 22, no. 22, Nov. 2021, doi: 10.3390/IJMS222212420.
- [205] D. Kilian, T. Ahlfeld, A. R. Akkineni, A. Bernhardt, M. Gelinsky, and A. Lode, '3D Bioprinting of osteochondral tissue substitutes – in vitro-chondrogenesis in multi-layered mineralized constructs', *Sci Rep*, vol. 10, no. 1, Dec. 2020, doi: 10.1038/s41598-020-65050-9.
- [206] X. Wang, G. Li, Y. Liu, W. Yu, and Q. Sun, 'Biocompatibility of biological material polylactic acid with stem cells from human exfoliated deciduous teeth', *Biomed Rep*, vol. 6, no. 5, pp. 519–524, May 2017, doi: 10.3892/br.2017.881.
- [207] Gleadall Andy and Ruiz Laura, 'Transplantable scaffolds', in *3D Printing in Medicine and Surgery*, Woodhead Publishing Series in Biomaterials, 2021, pp. 199–222.
- [208] A. Ilea *et al.*, 'Osseointegration of titanium scaffolds manufactured by selective laser melting in rabbit femur defect model', *J Mater Sci Mater Med*, vol. 30, no. 2, Feb. 2019, doi: 10.1007/s10856-019-6227-9.
- [209] K. Man *et al.*, 'Development of a Bone-Mimetic 3D Printed Ti6Al4V Scaffold to Enhance Osteoblast-Derived Extracellular Vesicles' Therapeutic Efficacy for Bone Regeneration', *Front Bioeng Biotechnol*, vol. 9, Oct. 2021, doi: 10.3389/fbioe.2021.757220.
- [210] H. Zhao, S. Shen, L. Zhao, Y. Xu, Y. Li, and N. Zhuo, '3D printing of dual-cell delivery titanium alloy scaffolds for improving osseointegration through enhancing angiogenesis and osteogenesis', *BMC Musculoskelet Disord*, vol. 22, no. 1, Dec. 2021, doi: 10.1186/s12891-021-04617-7.

- [211] L. V Burgin and R. M. Aspden, 'Impact testing to determine the mechanical properties of articular cartilage in isolation and on bone'.
- [212] K. M. Fischenich, J. A. Wahlquist, R. L. Wilmoth, L. Cai, C. P. Neu, and V. L. Ferguson, 'Human articular cartilage is orthotropic where microstructure, micromechanics, and chemistry vary with depth and split-line orientation', *Osteoarthritis Cartilage*, vol. 28, no. 10, pp. 1362–1372, Oct. 2020, doi: 10.1016/j.joca.2020.06.007.
- [213] S. Suri and D. A. Walsh, 'Osteochondral alterations in osteoarthritis', *Bone*, vol. 51, no. 2, pp. 204–211, Aug. 2012, doi: 10.1016/j.bone.2011.10.010.
- [214] D. Chappard, M. F. Baslé, E. Legrand, and M. Audran, 'New laboratory tools in the assessment of bone quality', *Osteoporosis International*, vol. 22, no. 8, pp. 2225–2240, Aug. 2011. doi: 10.1007/s00198-011-1573-6.
- [215] Z. A. Qureshi, S. A. B. Al Omari, E. Elnajjar, F. Mahmoud, O. Al-Ketan, and R. A. Al-Rub, 'Thermal characterization of 3D-Printed lattices based on triply periodic minimal surfaces embedded with organic phase change material', *Case Studies in Thermal Engineering*, vol. 27, Oct. 2021, doi: 10.1016/j.csite.2021.101315.
- [216] White T and Folkens P, *The Human Bone Manual*, 1st ed., vol. 1. Academic Press 2005, 2005.